Renato Quagliani

Study of Double Charm B Decays with the LHCb Experiment at CERN and Track Reconstruction for the LHCb Upgrade

Springer

Springer Theses

Recognizing Outstanding Ph.D. Research

Aims and Scope

The series "Springer Theses" brings together a selection of the very best Ph.D. theses from around the world and across the physical sciences. Nominated and endorsed by two recognized specialists, each published volume has been selected for its scientific excellence and the high impact of its contents for the pertinent field of research. For greater accessibility to non-specialists, the published versions include an extended introduction, as well as a foreword by the student's supervisor explaining the special relevance of the work for the field. As a whole, the series will provide a valuable resource both for newcomers to the research fields described, and for other scientists seeking detailed background information on special questions. Finally, it provides an accredited documentation of the valuable contributions made by today's younger generation of scientists.

Theses are accepted into the series by invited nomination only and must fulfill all of the following criteria

- They must be written in good English.
- The topic should fall within the confines of Chemistry, Physics, Earth Sciences, Engineering and related interdisciplinary fields such as Materials, Nanoscience, Chemical Engineering, Complex Systems and Biophysics.
- The work reported in the thesis must represent a significant scientific advance.
- If the thesis includes previously published material, permission to reproduce this must be gained from the respective copyright holder.
- They must have been examined and passed during the 12 months prior to nomination.
- Each thesis should include a foreword by the supervisor outlining the significance of its content.
- The theses should have a clearly defined structure including an introduction accessible to scientists not expert in that particular field.

More information about this series at http://www.springer.com/series/8790

Renato Quagliani

Study of Double Charm B Decays with the LHCb Experiment at CERN and Track Reconstruction for the LHCb Upgrade

Author
Dr. Renato Quagliani
LHCb group, LPNHE, CNRS
Université Paris-Saclay
Paris, France

Supervisors
Drs. Yasmine Amhis
LAL
University of Paris-Sud, CNRS/IN2P3,
    Université Paris-Saclay
Orsay, France

Dr. Jonas Rademacker
H. H. Wills Physics Laboratory
University of Bristol
Bristol, UK

Dr. Patrick Robbe
LAL
University of Paris-Sud, CNRS/IN2P3,
    Université Paris-Saclay
Orsay, France

To my family and people who love me.

Supervisors' Foreword

The Standard Model of particle physics has been highly successful in describing the fundamental constituents of matter and their interactions. It passed numerous experimental tests. Its most recent triumph was the discovery of the Higgs particle, verifying a crucial Standard Model prediction. However, the Standard Model also predicts an almost empty universe, in blatant contradiction to cosmological evidence, and the fact that this thesis, and someone who reads it, exist. It also fails to describe gravity, and the nature of dark matter and dark energy. There must be physics beyond the Standard Model. The central aim of particle physics research today is to find and characterise this "new physics". Nearly, all alternatives to the Standard Model that address its shortcomings predict the existence of new, heavy particles. Particle colliders such as the Large Hadron Collider at CERN aim to produce these new particles by converting some of the collision energy E into mass m using Einstein's famous $E = mc^2$ relation. The mass of these new particles is therefore limited by the collision energy. Renato's research focuses on an alternative approach that does not suffer from this limitation and lets us see beyond the "energy frontier".

Quark flavour physics is the precision study of quarks changing "flavour", i.e. changing from one type to another through the weak interaction. New heavy particles can affect flavour changes as virtual particles. Crucially, there is no kinematic cut-off for the masses of virtual particles, their mass is not limited by $E = mc^2$. In the past, the flavour physics approach has been extremely successful. For example, the observation of charge-parity (CP) violation in Kaon decays led to the prediction of the third, heaviest generation of quarks (top and bottom), long before they could be produced directly in colliders—an achievement recognised with the 2008 Nobel Prize for Kobayashi and Maskawa. The bottom quarks they predicted have approximately the mass of a He atom, exist after production for about 1ps (which is long in particle physics terms) and can now be produced in large numbers. They, and the "B hadrons" they form by combining with other quarks, turn out to be ideal for flavour physics, with many opportunities for virtual particles to affect their

decays to lighter particles. The LHC produces by far the largest number of B hadrons in the world. LHCb is the experiment at the LHC optimised to study them.

The effect of virtual particles on B hadron decays is subtle. The key to reaching maximal sensitivity to heavy "new physics" particles is precision. In this field, high precision requires large data samples. The more data, the more precision, the further we can see. The first part of Renato's thesis is dedicated to improving the precision achievable in flavour physics by preparing LHCb for an upgrade that constitutes a step change in the ability of the experiment to record vast numbers of B hadron events. A key element of the upgraded LHCb detector is the scintillating fibre tracker ("SciFi"), which implements a new detector technology. It consists of millions of fibres that emit light when a charged particle (possibly the decay product of a B hadron) passes through them. The emitted light is turned into an electronic signal and recorded. Renato had to put all these signals together to reconstruct the original tracks caused by each particle as it passes through the detector. With typically about 100 tracks per collision, and 30,000,000 collisions per second, this is a formidable task. Renato created a tracking algorithm for the SciFi that has unprecedented efficiency, purity, and—crucially—is fast enough to cope with 30 million collision events per second. With this, Renato played a decisive part in deploying a new detector technology for the LHCb upgrade, which will have substantial impact on the future of flavour physics.

Renato also performed the first study of the decay $B^0 \rightarrow D\overline{D}K^*$ using LHCb data. The $D/\overline{D}$ particles are mesons with a charm and anti-charm quark, respectively, and the K^* contains an anti-strange quark. This decay is of the utmost interest for many reasons. It is highly suited for finding and studying new, "exotic" charm resonances, of which many new and unexpected ones have been discovered recently. It also allows the study "charm loops". These might affect the angular distribution in other decays such as $B^0 \rightarrow K^*\mu\mu$, which have been the source of great excitement recently because of the indications of physics beyond the Standard Model seen in these decays. If these indications turn into a discovery, this would be a major upheaval in the field—the first evidence of the long-sought "new physics" would finally have been found. In order to distinguish this from "fake" signals due to difficult-to-predict (but still Standard Model) effects induced by the aforementioned charm loops, the studies of $B^0 \rightarrow D\overline{D}K^*$ that Renato instigated in his thesis are hugely important. Renato used and optimised highly sophisticated statistical methods, and combined them with his deep understanding of the underlying physics and the LHCb detector, to achieve high data selection efficiency, background rejection. He also developed data-driven methods to evaluate reconstruction efficiencies and background contamination, both crucial for this measurement.

Renato is also an exceptional LHCb citizen, who also spent a substantial amount of time training younger colleagues in generic as well as LHCb-specific computing and software skills in several formal training events that he co-organised and ran.

Renato's exceptional contribution to the LHCb experiment, in particular his pioneering work on the tracking algorithm for the LHCb upgrade, earned him LHCb's Early Career Scientist Achievement Award in 2017.

Renato is the first student of the joint particle physics Ph.D. programme from the Université Paris-Sud (Laboratoire de l'Accélérateur Linéaire in Orsay) and the University of Bristol. He had supervisors from both institutes and spent just under 50% of his time at each (and the remaining time at CERN). He received his Ph.D. degree jointly from both institutions. We are delighted that this cross-European cooperation got off to such a good start with an exceptional student producing original scientific work of the highest quality.

Orsay, France	Drs. Yasmine Amhis
	Co-Directrice
Bristol, UK	Dr. Jonas Rademacker
	Director
Orsay, France	Dr. Patrick Robbe
October 2018	Director

Abstract

Double-charmed B meson decays are dominated by the Cabibbo-favoured $b \rightarrow c(W^- \rightarrow \bar{c}s)$ transition. This thesis presents the study of $B^0 \rightarrow D^0\overline{D}^0K^{*0}$ decay which has never been observed so far. The branching ratio is quoted with respect to the $B^0 \rightarrow D^{*-}D^0K^+$ decay mode. No K^{*0} mass window selection is applied in $B^0 \rightarrow D^0\overline{D}^0K^{*0}$, reconstructing the $K\pi$ system as a K^{*0}. The invariant mass of the $K\pi$ system is selected to be in full allowed phase space: $m(K) + m(\pi) < m(K\pi) < m(B) - 2m(D^0)$. D^0 mesons are reconstructed through the Cabibbo-favoured $D^0 \rightarrow K^-\pi^+$ mode and the K^{*0} as $K^+\pi^-$. The integrated luminosity of 3 fb^{-1} collected by LHCb during LHC Run 1 are used to select and reconstruct $B0 \rightarrow D^0\overline{D}^0K^{*0}$ leading to a preliminary branching ratio corresponding to:

$$\frac{\mathscr{B}(B0 \rightarrow D^0\overline{D}^0K^{*0})}{\mathscr{B}(B^0 \rightarrow D^{*-}D^0K^+)} = (12.83 \pm 1.80\,(\text{stat})\,)\%$$

A major upgrade of LHCb is foreseen for 2020. At that time, LHCb will operate at five times larger luminosity than Run I reaching the value of $\mathscr{L} = 2 \times 10^{33}$ cm^{-2} s^{-1}. An increased pile-up level is expected leading to higher detector occupancy as well as harsher radiation environment. A new trigger strategy will be adopted to take advantage of the higher luminosity to collect at least 5 fb^{-1} per year.

The hardware-based trigger strategy used during Run I and Run II will be completely removed, and a fully-based software trigger strategy will be adopted. Therefore, software applications performing trigger selection will be executed at collision rate.

Such strategy requires the replacement of all the read-out electronics in all the subsystem, and in order to guarantee high track reconstruction performance, all the tracking sub-detectors will be replaced. The tracker placed downstream the LHCb

dipole magnet will be replaced by a scintillating fibre tracker (SciFi) made of layers of scintillating fibres read-out by Silicon Photomultiplier.

This thesis presents the LHCb upgrade, the LHCb upgrade tracking strategy as well as the development of the stand-alone track reconstruction algorithm using only information from the SciFi. This algorithm plays a crucial role in the reconstruction of particles originating from decaying b and c hadrons as well as particles originating from long-lived particles such as K_s^0 and Λ^0. The algorithm strongly enhances the overall expected performance for the upgrade leading to a large improvement in reconstruction efficiency, fake tracks rejection and execution time.

Acknowledgements

Contents

Chapter 1
Introduction to Theory

The Standard Model (SM) of particle physics and general relativity (GR) are the two main modern theories used to describe fundamental interactions in Nature. The former is able to describe experimental data in a consistent framework regarding electromagnetic, weak and strong interactions while the latter describes the gravitational one. In this thesis only the Standard Model of particle physics will be described. Particular attention will be made on the quark sector, providing a description of the weak interaction structure of the heavy flavour sector of particle physics. The heavy flavour sector is encoded in the SM through the Cabibbo–Kobayashi–Maskawa (CKM) matrix. This is the main domain of study at the LHCb experiment (see Chap. 2).

The Standard Model of particle physics is a quantum field theory describing the fundamental interactions between elementary particles and it is the theory currently accepted to describe the elementary blocks of matter building the universe. Although the SM has been introduced in the 70s, the experimental discoveries supporting the theory were observed decades later. However, it is known that the SM is not the ultimate theory of Nature. Several aspects about the fundamental structure of matter and cosmological observations cannot be explained within the SM: dark matter, dark energy, matter-antimatter asymmetry in the universe are only few of them.

High energy physics experiments has the ultimate goal to break down the SM, looking for discrepancies between experimental observations and SM prediction. Two main approaches are experimentally followed: direct observations and precision measurements. The former aims at producing on-shell new particles not predicted by the SM and performing direct observation of their behaviour (e.g. SM forbidden decay modes), the latter aims at observing experimental discrepancies with theory prediction which can only be explained introducing new physics (NP) effects. Nowadays, efforts are made to search for signal of NP, taking advantage of particle accelerators or cosmological observations.

1.1 A Subatomic Particle Classification

Within the SM, a subatomic fundamental particle is defined as a physical object which does not have an internal structure (point-like particle) or at least, a particle for which an internal structure has never been experimentally observed so far. In the SM, particles are described by quantum fields and the physical particles correspond to excitations of the corresponding fields, e.g. electrons are described as excitations of a Dirac field and photons are described as excitations of an electromagnetic field.

   In general, subatomic particles are divided into groups of similar characteristics and behaviours using their spin (see Fig. 1.1) properties:

- Fermions are half-integer spin particles: these particles satisfy the Fermi–Dirac statistics (in QFT the quantization of fields is made using anti-commutator relation) and their quantum behaviour is encoded in the Dirac equation, which is the equation for free fermion field of spin $\frac{1}{2}$:

$$(i\gamma^\mu \partial_\mu - m)\psi(\overrightarrow{x}) = 0, \tag{1.1}$$

   where $\psi(\overrightarrow{x})$ is the 4 component Dirac field, γ^μ ($\mu = 0, 1, 2, 3$) are the 4×4 Dirac matrices and m is the mass term of the Dirac field.
- Particles with integer spin are bosons: these particles satisfy the Bose–Einstein statistics (in QFT the quantization of fields is made using commutation relation) and their free evolution behaviour is described by the Klein–Gordon equation (spin 0 case):

$$(\partial_\mu \partial^\mu + m^2)\Phi(\overrightarrow{x}) = 0, \tag{1.2}$$

   where $\Phi(\overrightarrow{x})$ is the boson field and m its mass.

Dirac and Klein–Gordon equations are derived imposing the relativistic dispersion relation $E^2 = m^2 + p^2$ ($c = 1$) for spin $\frac{1}{2}$ and 0 representations of the Lorentz group. The solutions of Eqs. (1.1) and (1.2) determine a field (ψ and Φ in this case) whose excitations correspond to particles. To better understand the concept of field excitation, as example, one can consider the QFT description of a reticular lattice.
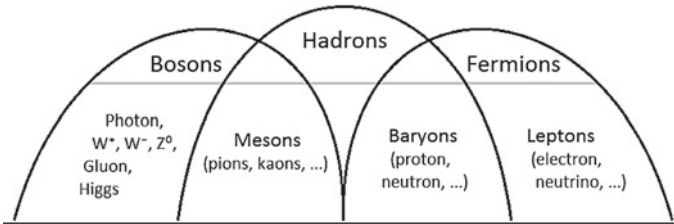
Fig. 1.1 Subatomic particles classification depending on their spin. Mesons and baryons are composite particles while the remaining fermions and bosons in the picture are fundamental particles

The lattice vibrations are described through the field defined by the many individual reticular point undergoing a quantum coherent collective motion. This collective excitation in the periodic, elastic arrangement of atoms (or molecules) defines the quasiparticle called phonon. The phonon is an excited state of the modes of vibration (described by a field) of the interacting atoms (or molecules) in the lattice. For the SM particle physics theory the concept is the same: excitations of a Dirac field corresponds to the presence of spin $\frac{1}{2}$ particles in the system.

The most interesting aspect of a quantum field theory is the interacting behaviour of particles rather than the free behaviour which has been discussed up to now. Indeed, the great success of the Standard Model is related to the fact that it is capable in a consistent QFT formalism to describe at the same time three out of the four fundamental interactions. An extraordinary achievement of the SM is that interactions between different fundamental particle fields are introduced in the theory imposing gauge symmetries, i.e. invariance of the theory under local transformations of the fields. The Lagrangian of the SM can be derived "simply" imposing a set of symmetries to the theory. Grossly speaking, once a symmetry is imposed in the theory (such as CPT, rotation, translation, Lorentz transformation), only limited set of terms can be added to the Lagrangian describing the underlying physics processes. Symmetries in particle physics are classified as local (e.g., a local phase transformation of the field $\psi \rightarrow e^{i\phi(x)}\psi$) and global (e.g., $\psi \rightarrow e^{i\phi}\psi$). The imposition of a local phase transformation symmetry (gauge-symmetry) for the fundamental particle fields described by either the Klein–Gordon or the Dirac equation implies the introduction of a covariant derivative term embedding a massless bosonic field to preserve the symmetry. These fields, depending on the gauge symmetry imposed, are able to describe the electromagnetic, weak and strong interactions and they represents the force-mediating particles of the theory. Therefore, a gauge theory is a theory where the interactions are derived from a fundamental principle: the invariance of physics laws under local gauge transformation of fundamental particle fields.

Concerning the SM, fundamental interactions appear imposing $U(1)$ (Abelian symmetry group for the electromagnetic force), $SU(2)$ (non-Abelian for weak force), $SU(3)$ (non-Abelian for the strong force) group gauge symmetry to the free dirac and bosonic Lagrangian.[1] The fundamental particles of the SM are leptons, quarks, the Higgs Boson and the gauge fields of the interactions. Electromagnetic and weak interactions are unified thanks to the Spontaneous Symmetry Breaking (SSB) mechanism which requires the Higgs Boson to be introduced in the theory. The fundamental particles mass term is introduced in the gauge invariant Lagrangian through the Higgs Mechanism and the mass term value is related to the coupling between fundamental particle fields and the Higgs Boson. A nutshell representation of the elementary constituents of the SM, their interactions and the Higgs Boson role in the SM is shown in Fig. 1.2.

---

[1] Gravity is not included in the model; the gravitational force is negligible in particle physics domain. Furthermore, at the currently accessible energies in the laboratory, gravitational force effects would be too small to be observed.
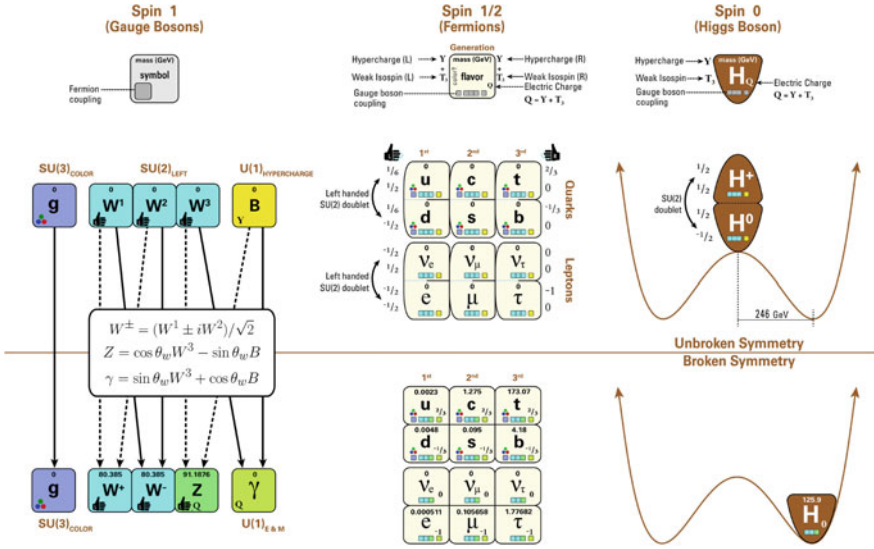
Fig. 1.2 Elementary particles of the SM: gauge bosons are shown on the left, the three generation Spin-$\frac{1}{2}$ fundamental matter particles (quarks and leptons) on the centre, and the Higgs boson on the right. A summary of their names, spins, charges, masses and interactions are provided. The brown horizontal line shows how the Spontaneous Symmetry Breaking, i.e. the choice of a minimum for the Higgs field in the electroweak gauge symmetry representation, acts on the various particles and gauge bosons (at the top in the unbroken symmetry and the broken symmetry case on the bottom). Figure taken from [1]

Although all experimental results in many different facilities (ATLAS, CMS, LHCb, BaBar, Belle, TeVatron, LEP and many others) are largely in agreement with the SM predictions so far, it is well known that the Standard Model is not the ultimate theory of Nature. Indeed, SM is not able to provide candidates for Dark Matter, it fails to explain the dark energy and the observed asymmetry of matter and antimatter in the universe and moreover, the theory does not include gravity. Coming back to the building blocks of the Standard Model, elementary particles are classified into matter particles and force-mediating (or force-messenger) particles. It happens that elementary matter particles in Nature are fermions and they are classified into leptons (electron, muon, tau and their corresponding neutrinos) and quarks (up, down, charm, strange, top, bottom or beauty).

The Dirac equation solutions allow negative energy solutions which are interpreted as anti-particles. Indeed, each elementary particle has its corresponding antiparticle characterized by having the same mass but opposite charges (this is the most important prediction of the Dirac equation). The charge of a particle has sense to be defined only in presence of an interaction which allows the particle to couple to a force-mediating particle. Each of the three different interactions implies the existence of three different charges to be defined for each fundamental particles.

The organization of fundamental particles of matter in leptons (l) and quarks (q) are directly linked to their interacting behaviour: leptons and quarks are charged from the electromagnetic and weak-interaction point of view (therefore they can interact weakly and electromagnetically). Nevertheless, from the strong interaction point of view, leptons are neutral (therefore they do not interact strongly) while quarks are charged (quarks carry the so-called colour charge). Exceptions are made for neutrinos which only interact weakly.

The most common organization of fundamental particles of the Standard Model is obtained dividing them into three flavour generations. This classification is related to the weak interaction structure of the Standard Model, their mass hierarchy and the historical development of the Standard Model:

$$l = \begin{pmatrix} v_e \\ e \end{pmatrix}, \begin{pmatrix} v_\mu \\ \mu \end{pmatrix}, \begin{pmatrix} v_\tau \\ \tau \end{pmatrix} \quad q = \begin{pmatrix} u \\ d \end{pmatrix}, \begin{pmatrix} c \\ s \end{pmatrix}, \begin{pmatrix} t \\ b \end{pmatrix}$$

The fundamental particle field is written as an irreducible representation of the Poincaré group which is the group of Lorentz transformations, rotations and translations. A representation of a group is an object having specific properties under the transformation laws of the group. The Poincaré group representations are classified by spin. Dirac spinors are the spin $\frac{1}{2}$ representation of the Poincaré group and two types of spinors are identified depending on their transformation behaviours: left-handed (fundamental) and right-handed (anti-fundamental) ones. The four dimensional Dirac spinor is a direct sum of a left- and right-handed 2-component spinors. The SM is a chiral theory, i.e. different representations of the Lorentz group transform differently not only under the Lorentz group itself, but also with respect to the SM $SU(3) \times SU(2) \times U(1)$ gauge group. The chirality of a spin $\frac{1}{2}$ particle refers to whether it is in the fundamental or anti-fundamental representation of the Poincaré group while the helicity is referred to the direction of the spin along the direction of motion.

NP theories which attempt to solve the problems of the Standard Model (beyond the standard model theories, also called BSM), use as starting point the SM considered as an effective theory and attempts are made adding extra symmetries to the theory (which result in the introduction of new particles and interactions). The most interesting one is the super symmetry theory ($SUSY$). It adds a symmetry to the SM between fermionic and bosonic spaces leading to the existence of super-symmetric partners of SM fundamental particles which are able to solve at the same time several problems of the SM. Notably, one of the main goal of the LHC is the direct and indirect observation of such particles. Indirect observations of NP relies on the fact that extra contributions (w.r.t. to SM ones) would appear at the loop level.[2]

---

[2] $SUSY$ provide candidates (neutralinos, the super-symmetric partner of neutrinos) to the dark matter and solve some problems of the Standard Model, so, maybe, one day, the current picture of fundamental particles will be extended including *sleptons* and *squarks*.

1.2   The Fundamental Interactions of the SM

The force-mediating particles between the fundamental particles of the SM are bosons (spin 1 representation of the Lorentz-group). Interactions in the SM are described by force-mediating particles which are exchanged between the elementary matter particles. Depending on the interaction we can identify:

- The photon (γ) is the electromagnetic interaction force-carrier particle. Electrically charged particles interact each other exchanging a virtual photon. The photon (γ) turns out to be massless and electrically neutral and it appears imposing the Abelian $U(1)$ gauge symmetry to the theory.
- The Z^0 and $W^\pm$ are the force-carriers of the weak interaction. Weak interaction is responsible of natural radioactivity. The three gauge-bosons are massive and they have spin equal to 1. The Z^0 is electrically neutral and its mass is measured to be (91.1876 ± 0.0021) GeV/c^2 [2] while the $W^\pm$ are electrically charged and their masses have been measured to be (80.358 ± 0.015) GeV/c^2 [2]. The weak interaction can be derived imposing the gauge symmetry associated to the group $SU(2)$. Only this would not be enough to explain the massive properties of these force-carriers. In such context, the Higgs Mechanism of Spontaneous Symmetry Breaking (SSB) allows the gauge fields of weak interaction to dynamically acquire mass. The SSB of the SM mechanism also permits the unification of weak and electromagnetic interaction, and this is also one of the reason why the gauge bosons of weak interaction carry electric charge.
- Gluons g are the force-carrier of the strong interaction. Strong interaction is responsible of the binding and confinement of quarks inside hadrons. A total of 8 massless and electrically neutral gluons are exchanged by particles carrying colour charge. The possible colour charge for quarks are three and also the gluons carry a colour-anticolour charge. Therefore, gluons are allowed to interact with each other (self-coupling terms between gluon fields appear in the Lagrangian). Leptons (electron, muon, tau and the neutrinos) do not interact strongly because they do not carry colour charge; leptons belong to a singlet representation of the $SU(3)$ colour group while quarks belong to the fundamental triplet representation of the colour group and gluons to the octet one. The gauge symmetry group related to the strong interaction is the non-Abelian $SU(3)$ group and the strong interaction theory is called Quantum Chromo Dynamic (QCD).

The last and fundamental ingredient of the Standard Model is the Higgs Boson. The Higgs Boson has been directly observed by two experiments at the Large Hadron Collider (LHC) at CERN: ATLAS [3] and CMS [4] in 2012 observed experimentally for the first time a candidate consistent with the Higgs Boson predicted in 1964. The Higgs Boson is extremely important in the Standard Model for several reasons. First of all, its coupling to fermions is introduced in the theory through a Yukawa coupling term; the interaction between fermions and the Higgs Field allows fundamental particles to acquire a mass term. Furthermore, the Higgs particle plays a crucial role in the Higgs Mechanism of SSB of the electroweak gauge symmetry

Table 1.1 The four fundamental forces in Nature and the relative intensities

Force	Relative strength	Force-mediating particle	Charge
Strong	1	Gluons(8)	Colour
Electromagnetic	10^{-2}	Photon γ	Electric charge
Weak	10^{-5}	$W^\pm$ and Z^0	Hypercharge (Y)

$(SU(2)_L \times U(1)_Y \xrightarrow{SSB} U(1))$. The Higgs Mechanism is able to explain the existence of massive Z^0 and $W^\pm$ gauge fields and provide a unification principle between weak and electromagnetic interactions, namely the electroweak interaction.[3]

The relative strength between the four fundamental forces in Nature is summarized in Table 1.1. Masses of fundamental particles are so small that gravitational interaction is completely negligible (10^{-42} relative strength scale). A short review of the three fundamental forces encoded in the SM of particle physics theory is presented in Sects. 1.2.1 (strong), 1.2.2 (electromagnetic), 1.2.3 (weak).

1.2.1 The Strong Interaction

The fundamental particles in the SM carrying the colour charge of the strong interaction are quarks and gluons. The typical interaction time scale of strong interactions is of the order of 10^{-23}s. Gluons are the messenger particles of strong interaction; they are massless and they carry colour, therefore gluon-gluon and gluon-quark interactions are possible. Three different colour charge states are predicted by the theory, i.e. red (R), green (G) and blue (B) and the corresponding anti-colour charges. Within the SM, the strong interaction is described by a $SU(3)$ gauge-symmetry group. In a $SU(N)$ symmetry group the number of generators of the symmetry are $N^2 - 1$, which from a physical point of view corresponds to $N^2 - 1$ force-mediator fields (i.e. particles from its excitation). Therefore, eight different gluons are predicted by a gauge invariant $SU(3)$ theory. The quarks are embedded in the theory as a singlet representation of the field (they carry either a colour charge or an anti-colour charge), while gluons belong to the octet representation (they carry a combination of colour and anti-colour charges).

The most important aspects of the theory are the gauge invariance and the theory renormalization.[4] In a quantum field theory the terms appearing in the Lagrangian are not a priori physically observable quantities. Indeed, any experimental physical observable can be calculated as a function of the theory free parameters. Therefore, one can reformulate the theory such that a physical observable is written as a function of the other(s). This reformulation is known as renormalization. QCD redefinition

---

[3]Unification of theories in physics is not a novel concept. As example for unification of theories, the Lorentz tensor $F_{\mu\nu}$ was able to unify magnetic and electric forces under the same picture.

[4]Also factorization and infrared safety in theoretical predictions play a crucial role.

of the strength of the force (i.e. the coupling constant) at any given energy scale is affected by the non-Abelian structure of the associated $SU(3)$ colour group. It turns out that the strong interaction coupling constant is very large when coloured object are at a very large distance (or small energy scales), i.e. $\alpha_s(q^2)$ (q is the energy scale of the process under study) is large at small q^2 while it is small at small distances, i.e. large q^2. Therefore, if the energy scale of the processes studied is large enough, perturbation theory holds and can be applied, while at low energy scale, α_s becomes too large for perturbation theory to be used.

The outcome of the QCD renormalization process is the introduction of the so-called running coupling constant which is nothing different than a rescaling of the interaction strength observed experimentally depending on the energy regime of the process itself. Nevertheless, if the rescaled coupling constant is too large, perturbation theory cannot be applied. It is important to underline that any analytic Standard Model calculation is performed through perturbation theory. Nevertheless, even if the QCD calculation at low energy scale cannot provide trust-worthy predictions, successful attempts and continuous progresses are made thanks to lattice QCD computations which contrary to Effective Field theory uses as Lagrangian of the system the SM one rather than an effective one where the first principles does not appear straightforwardly.

Grossly speaking, the bridge between nuclear physics (low energy QCD regime) and particle physics (Standard Model of particle physics) is not yet mature enough and completely understood and there are several experiments and possible measurements which could help to improve the current knowledges. Furthermore, precise measurements of QCD effects in a given physical system can always be re-used to reduce uncertainties in theoretical prediction and also as experimental input (measurements using this scheme are called model independent). Double charmed B meson decays can indeed lead to improvements to our current understanding of how quarks bound among themselves within hadrons as well as improve our understanding of underlying non perturbative QCD effects.

The two regimes identified in QCD resulting from the running of the coupling constant are:

- **Confinement**: the strength of the strong force increases with the distance separating two coloured objects. Perturbation theory does not hold and effective field theories are employed.
- **Asymptotic Freedom**: coloured objects interaction strength is smaller as the energy scale increases (smaller distances). Quarks are considered as quasi-free particles and perturbation theory holds.

The confinement regime explains why quarks are not observed as free particles: quarks organize and interact among themselves in such a way to form colourless objects. A colourless object is translated in the theory to a $SU(3)$ singlet representation. A singlet representation of the $SU(3)$ group can be achieve in the simplest case through the sum of a quark and an anti quark ($R + \overline{R}$ for example) or the sum of three quarks or three anti-quarks ($R + G + B$) leading to mesons and baryons, respectively. Colourless objects can also be obtained in other more complex ways

(4 or 5 quark states). These particles are called exotics. From a phenomenological point of view when two quarks are brought away from each other, the energy stored in their interaction is so big that new particles can be created forming new hadrons in a process called hadronization. Hadronization is used to describe the creation of jets in hadronic collisions such as the TeVatron and LHC. At large energy scales, quarks can be considered as quasi-free particles and SM perturbative approaches work well to compute cross sections and lifetimes. According to the quark model, hadrons can be organized in multiplets following the $SU(N)$-flavour symmetry group of isospin (I), where N is the number of constituent quarks involved.

The important conserved quantum number in strong interactions are the isospin I and the hypercharge Y (related to the flavour conservation). Hadrons inside a $SU(N)$-flavour multiplet are characterized by the isospin and the hypercharge Y, being defined as the sum of the baryonic number (B) and the other quantum numbers describing the constituent-quark content of the hadron: strangeness S, charm C, bottomness B' and topness T, i.e. $Y = S + C + B' + T + B$. Different multiplets for different values of the total angular momentum J are predicted by the quark-model. As an example, the K and K^* systems have the same quark content but $J = 0$ and $J = 1$ respectively. In Nature, the $SU(N)$ (for $N > 2$) flavour symmetry is not an exact symmetry; the direct consequence of its explicit breaking is the observation of very different hadrons masses within the same hadron multiplet.

1.2.2 The Electromagnetic Interaction

Electromagnetism acts on particles carrying electric charge: quarks and leptons. The typical lifetime of a particle decaying electromagnetically is of the order of 10^{-20}s. The electromagnetic interaction conserves the lepton number and the quark flavour, meaning that a photon can only couple with leptons or quarks of the same type.

The quantum field theory describing electromagnetism is the Quantum Electrodynamics (QED). As for the QCD, the renormalization of the theory leads to a running coupling constant α which describes the variation of the electromagnetic processes strength at different energy scales. Since QED is obtained from an Abelian gauge theory ($U(1)$), the behaviour of QED is opposite to QCD, i.e $\alpha(q^2)$ becomes smaller at high distances and low q^2. In the limit of $q^2 \to 0$, electrons and in general electrically charged particles are observed as free objects. The asymptotic value ($\alpha(0)$) is known as the fine structure constant, measured as $\alpha(0) = \dfrac{1}{137}$. Its value increases as the energy of the electromagnetic processes (q) involved increase.

1.2.3 The Weak Interaction

All the fundamental particles of matter of the Standard Model interact weakly. Weak interaction and its unification with electromagnetism is provided by the SSB of the

electroweak gauge symmetry $SU(2) \times U(1) \to U(1)$ and it will be described in Sect. 1.4.

In 1932, Fermi [5] proposed a field theory similar to QED to explain nuclear β-decays where a neutron decays into a proton, an electron and an electronic antineutrino, i.e. $n \to pe^-\overline{\nu_e}$. The crossed form of the process is $e^+n \to p\overline{\nu_e}$, and starting with the QED formalism used to describe the electron-proton scattering, Fermi was able to introduce the weak interaction theory. The QED formalism for electron-proton scattering ($e^-p \to e^-p$ at tree level, i.e. the $1st$ non-vanishing term in perturbation theory) leads to the transition amplitude:

$$
\begin{aligned}
\mathcal{M} &= \left(e\overline{u_p}\gamma^\mu u_p\right)\left(\frac{-1}{q^2}\right)\left(-e\overline{u_e}\gamma_\mu u_e\right) \\
&= -\frac{e^2}{q^2}\left(\overline{u_p}\gamma^\mu u_p\right)\left(-\overline{u_e}\gamma_\mu u_e\right) \\
&= -\frac{e^2}{q^2}\left(j^{em,\mu}\right)_p\left(j^{em}_\mu\right)_e
\end{aligned}
\tag{1.3}
$$

where $u(p)$ is a Dirac spinor depending on the 4-momentum p of the associated particle (solution of the Dirac equation), γ^μ are the Dirac matrices, j^{em} is the electromagnetic current and $\left(\frac{-1}{q^2}\right)$ is the electromagnetic propagator associated to the virtual exchanged photon carrying momentum q. In the scattering process, the q^2 value is the transferred momentum between e and p while for the crossed process where $e^+e^- \to p\overline{p}$, the q^2 value of the virtual photon corresponds to the centre of mass energy of the e^+e^- system.

In general, for a quantum field theory, interaction at tree level is given by the sum of amplitudes contributing to the process and each amplitude is expressed as the product of currents circulating at the vertices of the interaction and the propagator of the interaction "connecting" interacting currents. The general formalism and how it is derived can be found in any Quantum Field Theory book. Analogously to QED, Fermi described the weak β-decay using a punctual interaction (no propagators involved) and the amplitude of the process became

$$
\mathcal{M} = G_F\left(\overline{u_n}\gamma^\mu u_p\right)\left(\overline{u_{\nu_e}}\gamma_\mu u_e\right)
\tag{1.4}
$$

where G_F is the weak coupling factor called Fermi constant.

We should underline that the amplitude of the process written in (1.4) is a scalar product of two currents. Both currents transform as vectors under Lorentz transformation, therefore parity (P, defined in Sect. 1.3) is conserved in such formalism. Some years after the Fermi effective theory was introduced, the theory has evolved and has been modified to include parity violation in weak processes. The weak interaction theory will be discussed in more details in Sect. 1.4.

1.3 Symmetries and Quantum Number Conservation

In particle physics and generally in physics, symmetries and conservation laws play a crucial and central role. Indeed, the Standard Model Lagrangian can be written down simply imposing symmetries to the theory and including in the theory a list of allowed terms matching the symmetry requirements. Grossly speaking, the logic is to add to the Lagrangian whatever term not forbidden by the conservation laws of the theory. Symmetries are related to transformation of the physics system. These transformations can be continuous and discrete. The former are parametrized by a set of continuous parameters ($\overrightarrow{\theta}$ and $\overrightarrow{\beta}$ for instance for rotations and Lorentz transformations, respectively) while the latter are parametrized by discrete values ($+1$ and -1 for instance). The continuous group of Lorentz transformation and its representations are the building blocks from where the Dirac (1.1) and the Klein–Gordon equation (1.2) for free fermions and free bosons Lagrangians are derived. Imposing additional symmetries, all the Standard Model can be derived. Then, the main question to address to have a complete picture of the theory is to understand which symmetries one should consider in order to build the theory of Nature; to answer this question experimental discoveries and observations played and will continue to play for NP searches a fundamental role.

In particle physics, three discrete symmetries are of fundamental importance:

- Parity (P) or space inversion: the parity operator revert the sign of spatial coordinates.
- Charge Conjugation (C): it changes a particle p into its antiparticle $C(p) = \overline{p}$.
- Time Reversal (T): it reverse the direction of time progression. For a given process it consists in swapping the initial and final states.

P and C are unitary transformations, while T is anti-unitary and the interest about these three discrete symmetries is that the combination of the three transformations, CPT, is an exact symmetry of Nature [6] (if CP is violated also T is violated). The weak interactions do not conserve individually C and P and also CP is violated. The rules and conservation laws of the Standard Model interactions are summarized in the Table 1.2.

In addition to symmetries, quantum numbers of fundamental particles set the selection rules for a given process. The total angular momentum J, the electric charge Q, baryonic number B and the lepton number L are, as the energy and momentum conserved by all the Standard Model interactions. Flavour is not conserved in weak interaction and it almost explains all the phenomenology of $c-$, $b-$, $s-$ hadron decays with some QCD corrections to be taken into account. Finally, the Isospin I quantum number is conserved only by the strong interaction.

Table 1.2 Fundamental interactions and their conservation laws

Symmetry or Quantum number	Strong	Electromagnetic	Weak
CPT	✓	✓	✓
P	✓	✓	X
C	✓	✓	X
CP or T	✓	✓	X
Q (Electric charge)	✓	✓	✓
B (Baryonic number)	✓	✓	✓
L (Lepton number)	✓	✓	✓
$Flavour$	✓	✓	X
I (isospin)	✓	X	X
J	✓	✓	✓

1.4 The Electroweak Theory of Weak Interaction

In the early 50s particles containing a strange (s) quark were experimentally observed. At that time they were named τ and θ. Despite the two particles had the same mass and lifetime, their decay modes were observed to be different: $\theta^+ \rightarrow \pi^+\pi^0$ and $\tau^+ \rightarrow \pi^+\pi^-\pi^+$ (here the τ is not the fermion of the third lepton family). The two decaying modes have opposite parity and at that time parity was considered to be conserved in all interactions; therefore, the two particles were not initially associated to the same state. In 1956, Lee and Yang [7] solved the problem supposing that the two particles were actually the same one, called K meson.

Parity violation in weak interaction was confirmed in 1957 by C.S. Wu et al. [8] in the famous experiment of β-transition of polarized ^{60}Co nuclei studying the transition ^{60}Co→^{60}Ni$^*e^-\overline{\nu_e}$. The nuclear spin in the ^{60}Co atom was aligned with an external magnetic field and if parity was conserved the electrons would have been emitted in the same or opposite direction of the nuclear spin in equal amounts. The experimental observation that electrons are emitted preferentially in a direction opposite to the nuclear spin direction lead to the discovery of Parity violation in weak interactions. Goldhaber M. et al. [9] in 1958 showed that neutrinos have negative helicity, where the helicity of a given particle is defined as the projection of the spin onto the momentum direction

$$h = \frac{\overrightarrow{S} \cdot \overrightarrow{p}}{|\overrightarrow{p}|}.$$

Helicity is not a Lorentz invariant quantity by definition since it is always possible to boost the system such that the momentum reverts its direction. For massless particle, such as neutrinos, helicity and chirality coincide. Historically, the experimental observation of the left-handed only nature of the neutrinos (and only right-handed anti-neutrino) and the parity violation in weak β decays, leads to the definition of the CP-symmetry (product of Parity and Charge conjugation) as fundamental symme-

try of Nature (later discovered to be a broken symmetry as well). Strictly speaking, charge conjugation deals with particles and anti-particles, while CP deals with matter and anti-matter. Indeed, left-handed neutrinos become right-handed anti-neutrino under CP transformation and not simply via C transformation.

At that point, the Eq. (1.4) encoding the Fermi theory of weak interaction was modified to accommodate P and C violation. This was achieved replacing the γ^μ terms with $\gamma^\mu \left(1 - \gamma^5\right)$ changing the structure of the interaction of currents from vector-vector to vector-axial (V-A).

The modified Fermi theory for β-decay including P violation was reformulated and the amplitude of the neutron decay was rewritten as:

$$\mathcal{M} = \frac{G_F}{\sqrt{2}} \left[\overline{u_n}\gamma^\mu \left(1 - \gamma^5\right) u_p\right] \left[\overline{u_{\nu_e}}\gamma_\mu \left(1 - \gamma^5\right) u_e\right] \tag{1.5}$$

Indeed, the $(1 - \gamma^5)$ term is the left-handed projection operator for Dirac fields while $(1 + \gamma^5)$ is the right-handed projection operator. The Fermi theory implementing the vector-axial (V-A) structure at this stage was still considered as a point-like interaction because the energy scale of the processes studied was too small to observe effects from virtual particles exchanged in the interaction.

QED description contains the γ propagator, being the messenger of the interaction. Within the Fermi theory, the Fermi Constant G_F is used. Nevertheless, to fully describe the weak interaction from a more fundamental point of view a particle (or particles), interpreted as propagator of the interaction should be introduced. The Gargamelle Bubble Chamber experiment demonstrated the existence of the neutral weak currents where the Z^0 particle is used as mediator [10] while in all $\beta^\pm$ processes the W^+ and the W^- were introduced as mediator. In the case of charged current ($W^\pm$ as mediator), the amplitude of the process becomes:

$$\mathcal{M} = \left[\frac{g}{\sqrt{2}}\overline{u_n}\gamma^\mu \frac{1}{2} \left(1 - \gamma^5\right) u_p\right] \left(\frac{1}{M_W^2 - q^2}\right) \left[\frac{g}{\sqrt{2}}\overline{u_{\nu_e}} \frac{1}{2}\gamma_\mu \left(1 - \gamma^5\right) u_e\right] \tag{1.6}$$

where g is the dimensionless coupling constant, M_W is the $W^\pm$ boson mass and q is its 4-momentum, while the $\frac{1}{2}$ factors are inserted for normalisation purpose.

The same strategy of introducing a propagator to the weak interaction can be done for the neutral current where the boson exchanged is the Z^0. The analogy with the QED photon propagator becomes straightforward at this point. To quantitatively estimate the coupling, in the limit of $q^2 \ll M_W^2$, which corresponds to the limit in which the weak interaction can be considered punctual, we find the important relation linking the Fermi Constant G_F to the mass of the $W^\pm$.

$$\frac{G_F}{\sqrt{2}} = \frac{g^2}{8M_W^2} \tag{1.7}$$

Looking at (1.7) and (1.5), the weak interactions are not weak because of the coupling g is small compared to the electromagnetic one (e), but simply because the masses of the exchanged bosons (M_W or M_Z) are large. Indeed, within the "final" electroweak theory it turns out that $g \approx e$ allowing the unification of weak and electromagnetic forces above the unification energy scale of 100 GeV. The energy translates to 10^{15} K, a temperature exceeded shortly after the Big Bang.

As the electric field and the magnetic field are unified thanks to the electromagnetism, something similar conceptually but fundamentally different in physical reason is done for the weak interaction and electromagnetism. The unification of the two forces was proposed by Glashow in 1961 [11]. Unification of the two theories requires the introduction of the weak isospin and the weak hypercharge (Y) quantum numbers and the introduction of the $SU(2)_L \times U(1)_Y$ group symmetry. The $SU(2)_L$ is the symmetry group for the weak isospin involving only left-handed states, while the $U(1)_Y$ corresponds to the weak hypercharge Y group involving both left- and right-handed states. The presence of the $U(1)_Y$ symmetry group helps to incorporate the electromagnetism in the weak interaction theory when the $SU(2)_L \times U(1)_Y$ gauge-symmetry is spontaneously broken by the Higgs mechanism [12, 13] with the introduction of the Higgs Boson. The electroweak theory predicts in this way that a mass term for the Z^0 and the $W^{\pm}$ should appear, while the γ remains massless after the SSB mechanism. The theory was developed by Glashow, Weinberg in 1967 [14] and Salam in 1968 [15].

$SU(2)_L \times U(1)_Y$ gauge group theory implies the introduction of a triplet of gauge fields W^i_μ (from the $SU(2)_L$) coupled with strength g to the weak isospin current J^i_μ and a single gauge field B_μ (from $U(1)_Y$) coupled to the weak hypercharge current j^Y_μ with a strength conventionally taken as $g'/2$. The introduction of these four gauge fields[5] leads to a new Lagrangian for the theory. Therefore, the definition of the basic electroweak interaction operator becomes:

$$- i g \left(J^i \right)^\mu W^i_\mu - i \frac{g'}{2} \left(j^Y \right)^\mu B_\mu \tag{1.8}$$

The massive and physical $W^{\pm}_\mu$ and Z^0_μ together with the massless A_μ (photon) are connected to the W^i_μ and B_μ. The link is the following:

$$W^{\pm}_\mu = \sqrt{\frac{1}{2}} \left(W^1_\mu \mp i W^2_\mu \right) \tag{1.9}$$

$$Z_\mu = -B_\mu \sin\theta_W + W^3_\mu \cos\theta_W \tag{1.10}$$

$$A_\mu = B_\mu \cos\theta_W + W^3_\mu \sin\theta_W, \tag{1.11}$$

---

[5]In gauge theory, the interaction field are achieved by substitution of the partial derivative with a covariant derivative, allowing to preserve the gauge symmetry.

where θ_W is the Weinberg angle or weak mixing angle. Thus, the physical gauge field of weak and electromagnetic interaction are obtained through a rotation of fields in the $SU(2)_L \times U(1)_Y$ space.

The resulting electroweak neutral interaction coupling between currents and exchanged bosons is expressed as:

$$- i g J_\mu^3 \left(W^3 \right)^\mu - i \frac{g'}{2} j_\mu^Y B^\mu \tag{1.12}$$

$$- i \left(g \sin \theta_W J_\mu^3 + \frac{g'}{2} \cos \theta_W j_\mu^Y \right) A^\mu \qquad - i \left(g \sin \theta_W J_\mu^3 - \frac{g'}{2} \cos \theta_W j_\mu^Y \right) Z^\mu \tag{1.13}$$

where the first term corresponds to the electromagnetic interaction and the second one to the weak neutral current interaction.

In order to recover the electromagnetic interaction with coupling e, we find that

$$g \sin \theta_W = g' \cos \theta_W = e. \tag{1.14}$$

The unification of electroweak theory is then given by Eq. (1.14), through the Weinberg angle θ_W. There is another relation related to the Weinberg angle and the masses of the gauge bosons Z^0 and $W^\pm$. Such a relation can be derived as a consequence of the unification of the electromagnetism and weak interaction and assuming that the responsible of the mass terms for the Z^0 and $W^\pm$ is the Higgs Mechanism of SSB and it corresponds to:

$$\frac{M_W^2}{M_Z^2 \cos^2 \theta_W} = 1. \tag{1.15}$$

Equations (1.15), (1.7), (1.14) describe and constrain the theory. Any experimental disagreement with these predictions is NP.

The full Standard Model Lagrangian is obtained adding the QCD and the whole theory is described by a $SU(2)_L \times U(1)_Y \times SU(3)$ gauge symmetry, where $SU(2)_L$ correspond to the weak isospin for left-handed particles, $U(1)_Y$ the weak hypercharge and the $SU(3)$ is the colour symmetry group applied to the matter particles. The weak interaction bosons can dynamically acquire a mass term thanks to the Spontaneous Symmetry Breaking mechanism. This requires the introduction of the Higgs Boson. The role of the Higgs Boson is not only related to the massive nature of the weak interaction mediators, but it can also couple to SM matter-particles providing them a mass term in the Lagrangian.

The structure of the Standard Model Lagrangian implies that left-handed particles can be written as doublets in the fundamental representation (equivalent to the spin $\frac{1}{2}$ representation of the $SU(2)$ group) of the weak isospin symmetry group $SU(2)_L$ while the right-handed particles are in a singlet representation (right-handed neutrinos

Table 1.3 Quantum numbers for Standard Model quarks and leptons of the first family. Q is the electric charge, Y is the weak hypercharge and I_3 the third component of the weak isospin

Quantum numbers	Quarks				Leptons		
	u_L	d_L	u_R	d_R	e_L^-	ν_e	e_R^-
Q	2/3	−1/3	2/3	−1/3	−1	0	−1
Y	1/3	1/3	4/3	−2/3	−1	−1	−2
I_3	1/2	−1/2	0	0	−1/2	1/2	0

are not included). The quantum numbers of Standard Model matter-particles are summarized in the Table 1.3.

Quarks are arranged in three different families: u-type quarks (u, c and t quarks) have the same quantum numbers than u_R and u_L particles in Table 1.3, same is true for d-type quarks (d, s and b quarks). All quarks are massive while for leptons, neutrinos are considered massless in first approximation. Neutrino oscillations have been observed and this implies that flavour eigenstates have different masses. Therefore neutrinos are massive even tough their absolute values have not been measured yet being too small. The neutrino mass term can be included in the Standard Model without breaking the SM: considering the neutrino as a Majorana particle or considering it as a Dirac particle (like all the other particles) but accepting that right handed neutrino interactions are at least 26 orders of magnitude weaker than the ordinary neutrinos.[6] To explain the various mass terms in the Lagrangian for the fundamental matter particles, a Yukawa coupling between the Higgs field and the lepton one leads to the mass term in the Lagrangian when considering the vacuum expectation value of the Higgs Field.

The Standard Model free parameters are 18, where 9 of them are related to the Higgs Yukawa coupling to the 9 massive fermions present in the theory (3 for the leptons and 6 for quarks). The quark mixing which will be explained in the next section and which is responsible of the heavy flavour transitions adds to the Standard Model a total of 4 free parameters. The remaining parameters are related to the interaction coupling constants: α_s for QCD, e, G_F and θ_W for the electroweak sector. The last free parameter of the Standard Model is the Higgs boson mass m_H. The measurement of the Higgs mass is indeed the main reason why LHC has been built.

The full Standard Model Lagrangian can be written down (no QCD accounted here):

---

[6]Although the Dirac neutrino approach fits well with the SM picture of mass generation via Higgs mechanism, it also suggests that Higgs-neutrino interaction is 12 orders of magnitude weaker than that of the top quark. In such picture, the hierarchy of masses of SM particles is still an open question in physics.

$$\mathcal{L} = -\frac{1}{4}\mathbf{W}_{\mu\nu} \cdot \mathbf{W}^{\mu\nu} - \frac{1}{4}B_{\mu\nu}B^{\mu\nu}$$

$\left.\begin{array}{l} \text{W}^\pm, \text{Z}, \gamma \text{ kinetic} \\ \text{energies and} \\ \text{self-interactions} \end{array}\right.$

$$+\bar{L}\gamma^\mu \left(i\partial_\mu - g\frac{1}{2}\boldsymbol{\tau} \cdot \mathbf{W}_\mu - g'\frac{Y}{2}B_\mu\right) L$$
$$+\bar{R}\gamma^\mu \left(i\partial_\mu - g'\frac{Y}{2}B_\mu\right) R$$

$\left.\begin{array}{l} \text{lepton and quark} \\ \text{kinetic energies} \\ \text{and their} \\ \text{interactions with} \\ \text{W}^\pm, \text{Z}, \gamma \end{array}\right.$

$$+\left|\left(i\partial_\mu - g\frac{1}{2}\boldsymbol{\tau} \cdot \mathbf{W}_\mu - g'\frac{Y}{2}B_\mu\right)\phi\right|^2 - V(\phi)$$

$\left.\begin{array}{l} \text{W}^\pm, \text{Z}, \gamma, \text{ and Higgs} \\ \text{masses and} \\ \text{couplings} \end{array}\right.$

$$-(G_1\bar{L}\phi R + G_2\bar{L}\phi_c R + \text{hermitian conjugate}).$$

$\left.\begin{array}{l} \text{lepton and quark} \\ \text{masses and} \\ \text{coupling to Higgs} \end{array}\right.$

where $\overline{L}$ is the left handed component of fermions and ϕ is the Higgs field. In the formulation of the Lagrangian the spin-1 field strength tensor is also included:

$$F^a_{\mu\nu} = \partial_\mu A^a_\nu - \partial_\nu A^a_\mu + gf^{abc}A^b_\mu A^c_\nu \tag{1.16}$$

where A is the gauge field, g is the coupling constant and $\boldsymbol{\tau}$ are the Pauli matrices, i.e. the generators of the $SU(2)$ group in the doublet representation. The quantity f^{abc} is the structure constant of the gauge group considered and it is defined by the group generators t_a commutation relation $[t_a, t_b] = if^{abc}t_c$.

For an Abelian gauge theory such as $U(1)$, the third term of (1.16) disappears, i.e. $F_{\mu\nu} = \partial_\mu A^a_\nu - \partial_\nu A^a_\mu$ while for a non-Abelian gauge theory such as $SU(2)$ and $SU(3)$ the third term is responsible of the self-coupling of gauge bosons, given that the gauge field dynamic Lagrangian is proportional to the contraction of two field strength tensors.

In order to include QCD in the previous formulation we just have to add the contraction of the field strength tensor $G_{\mu\nu}$ relative to the $SU(3)$ color group and introduce the corresponding covariant $SU(3)$ derivative in the Dirac equation for the quarks.

1.5 The Higgs Boson Role in the Standard Model

Fundamental particles in the Standard Model are massive. Before the introduction of the Higgs Boson in the theory, masses were added to the theory as a dimensional parameter. The Higgs mechanism allows to let particles acquire masses via Yukawa coupling leading to the presence of mass terms in the Lagrangian. The Lagrangian mass term, without considering the Higgs Boson in the theory is written as:

$$m\overline{\psi}\psi = m\left(\overline{\psi}_R\psi_L + \overline{\psi_L}\psi_R\right) \tag{1.17}$$

where $\psi_L(\psi_R)$ is the left(right)-handed component of the dirac spinor ψ. The presence in the Lagrangian of such term, explicitly breaks the $SU(2)_L$ gauge symmetry because the left-handed component belongs to a doublet representation of weak isospin while right-handed component behaves as a singlet under $SU(2)$ transformation. A similar problem arises in adding a mass term in the Lagrangian for the gauge bosons To overcome this problem and avoid the explicitly breaking of the gauge symmetries, the Higgs mechanism of spontaneous symmetry breaking has been introduced. The mechanism is able to *dynamically* generate masses for the particles and gauge bosons through an interaction term. The prize to pay is the introduction of a new Spin-0 field, the Higgs field.

The Higgs mechanism generates gauge invariant mass terms through spontaneous symmetry breaking of $SU(2)_L \times U(1)_Y \xrightarrow{SSB} U(1)_{E.M}$ symmetry of the Standard Model Lagrangian. The resulting Lagrangian, introducing the Spin-0 Higgs field ϕ, is:

$$\begin{aligned}\mathscr{L} &= \left(\partial_\mu\phi\right)^\dagger\left(\partial^\mu\phi\right) - V(\phi) \\ &= \left(\partial_\mu\phi\right)^\dagger\left(\partial^\mu\phi\right) - \mu^2\phi^\dagger\phi - \lambda\left(\phi^\dagger\phi\right)^2,\end{aligned} \tag{1.18}$$

where the terms with derivatives are related to the dynamic of the field. The famous *Mexican Hat Potential* is obtained considering $\mu^2 < 0$ in (1.18). The potential $V(\phi)$ has its minimum for

$$\phi^\dagger\phi = \frac{-\mu^2}{2\lambda}. \tag{1.19}$$

The field configuration encoded in (1.19) represents a group of points invariant under $SU(2)_L$ transformations. Note that when $\mu^2 > 0$, a unique minima exists, while for $\mu^2 < 0$ a degenerate set of minima arises, and the choice of a specific configuration leads to the spontaneous symmetry breaking mechanism.

The Lagrangian in (1.18) preserves all the symmetries of the Standard Model and even if a minimum is chosen as the vacuum of the theory, any other minimum point can be reached by a simple gauge transformation, a rotation in $SU(2)$. The choice of the minima is made in such a way that:

$$\phi_0 = \sqrt{\frac{1}{2}}\begin{pmatrix} 0 \\ v + H(x) \end{pmatrix} \tag{1.20}$$

where v is the vacuum expectation value and $H(x)$ is a perturbative expansion around this minimum value. The choice of expanding around the second component is made because the vacuum is expected to be electrically neutral, but in principle, excitations of the field can be electrically charged.

The choice made for the Higgs field ground state has a strong impact in the Lagrangian, the following terms appear naturally when taking into account the weak isospin $SU(2)_Y$ doublets:

$$- G_e \left[(\overline{\nu_e}, e)_L \begin{pmatrix} \phi^+ \\ \phi_0 \end{pmatrix} e_R + \overline{e}_R \left(\phi^-, \overline{\phi^0} \right) \begin{pmatrix} \nu_e \\ e \end{pmatrix}_L \right]$$

$$= - \frac{G_e}{\sqrt{2}} v \left(\overline{e}_L e_R + \overline{e}_R e_L \right) - \frac{G_e}{\sqrt{2}} \left(\overline{e}_L e_R + \overline{e}_R e_L \right) H \qquad (1.21)$$

$$= - m_e \overline{e} e - \frac{m_e}{v} \overline{e} e H$$

where G_e is an arbitrary constant (different for all the other massive fermions) interpreted as the interaction strength between the Higgs and fermion fields and being proportional to the fermion mass. As a consequence, a mass term is introduced in the Lagrangian for the fundamental fermions: $m_e = \dfrac{G_e v}{\sqrt{2}}$. Additionally, a Yukawa interaction term between the fermion (e in the example) and the Higgs scalar field H appears. The interaction strength between them is equal to $\dfrac{m_e}{v}$, i.e. the Higgs-fermion coupling is always proportional to the particle mass. The same happens for all the other fermions and for each of them a different G_l is introduced. Therefore, a total of 9 free parameters appear in the SM without taking into account neutrino masses. For the vector bosons associated to the electroweak interactions, once the minimum is chosen and the gauge fields are introduced through the covariant derivative, the Lagrangian assumes the following form:

$$\left(\frac{1}{2} v g \right)^2 W_\mu^+ W^{-\mu} + \frac{1}{8} v^2 \left[g W_\mu^3 - g' B_\mu \right]^2 + m_\gamma \left[g' W_\mu^3 + g B_\mu \right], \qquad (1.22)$$

where the interaction terms of gauge and Higgs fields are not shown. The $W^\pm$ and Z^0 mass terms appear as:

$$m_{W^\pm} = \frac{1}{2} v g$$

$$m_Z = \frac{1}{2} v \sqrt{g^2 + g'^2}.$$

Doing the calculation properly, thanks to the spontaneous symmetry breaking the term m_γ in (1.22) is predicted to be equal to 0.

The Spontaneous Symmetry Breaking of electroweak theory and a mechanism able to provide a mass term for fermions has been presented. The introduction of the Higgs Boson is crucial within the Standard Model since it allows to introduce in an elegant way gauge invariant mass terms which would be impossible to introduce without explicit break the gauge symmetries. Furthermore, a self coupling term for the H field appears and, once the minimum is chosen, a mass term for the H appears and can be identified as

$$m_H = \sqrt{2v^2 \lambda}.$$

The mass of the Higgs boson is also unknown and needs to be fixed experimentally because both λ and v are free parameters of the theory.

It is not surprising that the direct observation of the Higgs particle has been the goal of the last 50 years of experiments in particle physics. The particle and the mechanism were predicted in 1964 by three groups of physicists: F. Englert and R. Brout [16], P. Higgs [13, 17], G. Guralnik, C. Hagen and T. Kibble [18]. In July 2012, the ATLAS and CMS collaborations, using the 12 fb^{-1} of data collected in proton-proton collisions during 2011 and 2012, observed for the first time in several different decay channels a particle with the Higgs characteristics [3, 4]. The Higgs boson mass was measured to be around $125\,GeV/c^2$. In March 2013 new results showed that the observed particle has $J^P = 0^+$ as predicted in Ref. [19]. Additional properties of this particle to further validate that the observed state is exactly the Higgs boson predicted by the theory have been measured. Furthermore, since the Higgs field is very sensitive to NP effects, it is very important to continue its study, either to find discrepancies to the theory and to set limits in order to discard NP models.

In any case, the Higgs mechanism enforces the validity of the Standard Model and the predictive strength of the physics theories during the last century. Before its direct observation, the main input about its existence was deduced by the strong constrain put by the SSB on the ratio between the $W^{\pm}$ and Z^0 boson masses.

1.6   The Flavour Structure of the Standard Model

The electron was discovered in 1897 by J.J. Thomson [20] and the other particles composing the atoms were discovered in the following years: the proton was discovered by E. Rutherford in 1919 and J. Chadwick [21] discovered the neutron in 1932. These discoveries highlight the fact that the atom has an internal structure. In 1933 the positron was discovered by C.D. Anderson [22] as well as the muon and the anti-muon in 1936 [23]. In 1947 it was the time of the π particle, theoretically predicted by H. Yukawa in 1935 [24] as the mediator of strong interaction. At that time, the whole picture of subatomic particles began to be quite complicated and in the same year (1947) new particles were observed studying cosmic rays, such as the K meson and the Λ baryon. These last two particles (the Kaon K and the Λ baryon) were called strange particles because they were produced via strong interaction but they were observed decaying with a very long lifetime ($\mathcal{O}(10^{-10})$ s) which is the typical lifetime of weakly decaying particles. In order to explain such effect a new additive quantum number was introduced: the strangeness (S) being conserved in strong interaction and violated in weak one. In the following years, new particles with the same characteristics were observed, such as the Σ and the Ξ. All the observed particles were classified in a $SU(3)$ isospin symmetry group. Therefore, in order to complete the isospin multiplet, the Ω particle was predicted to exist and experimentally observed in 1964.

The large number of observed particles points to the conclusion that underlying structures are present for hadrons and mesons. The quark representation was proposed by Gell-Mann [25] and Zweig [26] in 1964 with the goal to describe in a coherent way

the observed zoology of particles: the up (u), down (d) and strange (s) quarks were introduced. Also the isospin symmetry was introduced and imposed to be conserved in strong interaction and violated in weak one. u and d quarks were associated to be a doublet representation of the isospin symmetry group while the s was associated to a singlet representation. In such a way, the u and d were allowed to interact with each other but no interaction of u and d quarks with the s was predicted. The observation of $K^- \rightarrow \mu^- \bar{\nu}_\mu$ decay mode implies that the quarks in the K system (s and $\bar{u}$) should annihilate in order to produce the observed final state. As a consequence, the theory requires the introduction of some mechanism allowing the s quark and the isospin doublet u and d to interact with each other.

The solution to the problem was the introduction of the mixing of quarks, introduced for the first time by N. Cabibbo in 1963 [27]. In his work he proposed a mechanism in which both the d and s quarks were allowed to interact weakly with the u. The key point of the mixing is the distinction between weak interaction eigenstates and mass eigenstates of the Hamiltonian, connected through a rotation of the isospin doublet. As a consequence, an isospin doublet given by u and d' and a singlet s' were defined:

$$\begin{pmatrix} d' \\ s' \end{pmatrix} = \begin{pmatrix} \cos\theta_C & \sin\theta_C \\ -\sin\theta_C & \cos\theta_C \end{pmatrix} \begin{pmatrix} d \\ s \end{pmatrix} \tag{1.23}$$

where θ_C (or $\sin(\theta_C) = \lambda$ in the CKM matrix) is the Cabibbo angle experimentally found to be $\theta_C \sim 13°$. In this way, the interaction between the u and s quark became possible and the physics interpretation is that the weak interaction eigenstates are an admixture of d and s quark. As a consequence the coupling at the vertex of the interaction between u and s quarks is $G_F \sin\theta_C$, which is smaller than the coupling of u and d quark ($G_F \cos\theta_C$). The $u \rightarrow d$ transition is called Cabibbo favored, while $u \rightarrow s$ Cabibbo suppressed. The quark mixing allows the weak interaction coupling to be universal. Although the quark mixing from Cabibbo could explain why strange particles are allowed to decay weakly to u quarks, new problems arose.

According to the quark mixing theory from Cabibbo, also flavour changing neutral currents were predicted. Indeed, the allowed couplings for neutral current between the proposed states are:

$$u\bar{u} + d\bar{d}\cos^2\theta_c + s\bar{s}\sin^2\theta_c + (d\bar{s} + s\bar{d})\cos\theta_C\sin\theta_C, \tag{1.24}$$

i.e. the theory predicts also the presence of $d \rightarrow s$ transition which were not observed experimentally. This problem was solved by Glashow, Illiopolis and Maiani in 1970 with the introduction of the *GIM mechanism* [28]. The *GIM mechanism* predicts the existence of a fourth quark, the *charm* (c). In this way, a second family of quarks was introduced: the (c, s) family. The two families take part to the weak interaction transitions as two separate doublets $(u, d')^T$ and $(c, s')^T$ where:

$$\begin{pmatrix} u \\ d' \end{pmatrix} = \begin{pmatrix} u \\ d\cos\theta_C + s\sin\theta_c \end{pmatrix}, \quad \begin{pmatrix} c \\ s' \end{pmatrix} = \begin{pmatrix} c \\ s\cos\theta_C - d\sin\theta_c \end{pmatrix}. \tag{1.25}$$

In this way the neutral couplings become $u\bar{u} + d\bar{d} + c\bar{c} + s\bar{s}$ and the flavour changing neutral current (FCNC) processes become forbidden at the leading order (tree level).

The experimental observation of the c quark was obtained at the same time at Brookhaven National Laboratory and at SLAC in 1974 [29, 30], through the observation of the J/ψ resonance, being interpreted as a bound state of $c\bar{c}$ quarks. The observation of CP violation in K^0 system was observed in 1964 leading to the introduction of a third family of quarks (t, b), as it will be more clear later in the section. The K^0 meson was in fact observed to decay weakly into two different CP eigenstate modes: $\pi^+\pi^-$ and $\pi^+\pi^-\pi^0$. Therefore, the K^0 meson was described as an admixture of two CP eigenstates, CP-even K_s^0 and the CP-odd K_L^0. The former has a short lifetime and the latter a long one because of the different available phase space in their decay (2π and 3π).

Christenson et al. [31], while attempting to measure the angular distribution of the K_L^0 decay products observed the CP violating decay $K_L^0 \to \pi^+\pi^-$. The direct consequence of CP violation is that a particle and its own antiparticle do not decay in the same way. CP violation can be embedded in the theory through the introduction of a complex phase in the weak coupling of quarks. In a 2-quark family picture the Cabibbo rotation matrix modifying the couplings of weak interaction according to the flavour of the quarks involved is a unitary 2×2 matrix with a single angle as free parameter (θ_C). Thanks to the introduction of a third quark family, a total of three rotation angles and an extra irreducible complex phase appears straightforwardly, allowing the presence of CP violation in the theory.

The introduction of a third family of quarks to explain the observed CP violation in K decays was introduced by M. Kobayashi and T. Maskawa in 1973 [32]. The confirmation of the existence of a third family of quarks occurred in 1977 at Fermilab with the discovery of the b quark. Similarly to the c quark discovery, the observation of the Υ resonance [33] was interpreted as a bound state of $b\bar{b}$. The top (t) quark decay was first seen in 1994 by the CDF and DØ Collaborations [34]. Differently from the other quarks, the t one has a decay time which is smaller than the hadronization time scale, meaning that the t quark never hadronizes.

The flavour structure of the Standard Model and the weak interaction description in the quark sector is then completely encoded in the so-called CKM 3×3 unitary matrix (more details in Sect. 1.6.1). Over-constrained and precise-measurements of the CKM matrix parameters have been the main purposes of experiments such as BaBar and Belle and it is the main goal of the LHCb experiment. Regarding the lepton sector, three families of leptons are encoded in the SM and a similar scenario appears. The analogous of the CKM matrix in the lepton sector is called PMNS matrix introduced by Pontecorvo–Maki–Nakagawa–Sakata [35–37]. The PMNS matrix is able to explains the neutrino flavour oscillations, and, also in this case a single CP violating phase appears. Nevertheless, no experiments have been able to measure CP violation in neutrino oscillations so far.

1.6.1 The CKM Matrix

The CKM matrix encodes the CP violation in weak interactions and it is able to describe weak decay processes and oscillation of neutral mesons such as the $B^0 - \overline{B}^0$, $B_s^0 - \overline{B}_s^0$, $K^0 - \overline{K}^0$ oscillations. The charged weak interaction processes mediated by the $W^{\pm}$ vector boson appear in the Standard Model Lagrangian as:

$$-\frac{g}{\sqrt{2}} \left(\overline{u}_L, \overline{c}_L, \overline{t}_L\right) \gamma^{\mu} W_{\mu}^{+} V_{CKM} \begin{pmatrix} d_L \\ s_L \\ b_L \end{pmatrix}. \tag{1.26}$$

The L sub-script in (1.26) stands for left-handed component of the Dirac spinor, g is the universal weak interaction coupling constant and the non-universality of weak interaction in the quark sector is totally encoded in the CKM matrix (V_{CKM} [32]):

$$V_{CKM} = \begin{pmatrix} V_{ud} & V_{us} & V_{ub} \\ V_{cd} & V_{cs} & V_{cb} \\ V_{td} & V_{ts} & V_{tb} \end{pmatrix}. \tag{1.27}$$

Different possible parametrizations of the CKM matrix are available in literature. Chau and Keung [38] proposed a standard parameterisation of V_{CKM} which is obtained by the product of three (complex) rotation matrices and one irreducible phase δ_{13}:

$$V_{CKM} = \begin{pmatrix} c_{12}c_{13} & s_{12}c_{13} & s_{13}e^{-i\delta_{13}} \\ -s_{12}c_{23} - c_{12}s_{23}s_{13}e^{i\delta_{13}} & c_{12}c_{23} - s_{12}s_{23}s_{13}e^{i\delta_{13}} & s_{23}c_{13} \\ s_{12}s_{23} - c_{12}c_{23}s_{13}e^{i\delta_{13}} & -c_{12}s_{23} - s_{12}c_{23}s_{13}e^{i\delta_{13}} & c_{23}c_{13} \end{pmatrix}, \tag{1.28}$$

where $s_{ij} = \sin\theta_{ij}$ and $c_{ij} = \cos\theta_{ij}$, with $i, j = 1, 2, 3$ and $i \neq j$. The θ_{ij} are the mixing angles between the three quark generations and δ_{13} is the irreducible complex phase which allows CP violation in weak interaction.

The presence of CP violation in the theory can be clearly seen from the fact that $V_{CKM} \neq V_{CKM}^*$. The subscripts i and j refer to the quark families: 1 is assigned to the lightest one (u, d), 2 for (c, s) and 3 for heaviest one of b and t. Therefore θ_{12} is the Cabibbo angle (θ_C), responsible for the $u - s$ quark mixing. Experimentally s_{12} is measured to be 0.22. The other two angles θ_{13} and θ_{23} are found to be smaller than the Cabibbo one: $s_{23} \sim 10^{-2}$ ($c - b$ mixing), $s_{13} \sim 10^{-3}$ ($u - b$ mixing) and $c_{23} \sim c_{13} \sim 1$.

The magnitudes of the matrix elements highlight the existence of a hierarchy which allows a more physical parametrization expressed in terms of four parameters: λ, A, ρ and η. The parametrization was introduced for the first time by L. Wolfenstein in 1983 [39]:

$$s_{12} = \lambda \quad , \quad s_{23} = A\lambda^2 \quad \text{and} \quad s_{13}e^{-i\delta_{13}} = A\lambda^3(\rho - i\eta). \tag{1.29}$$

Expanding in powers of $\lambda = |V_{us}| \sim \sin\theta_C$, the V_{CKM} matrix expressed up to the order λ^6 terms is read as:

$$V_{CKM} = \begin{pmatrix} 1 - \dfrac{\lambda^2}{2} - \dfrac{\lambda^4}{8} & \lambda & A\lambda^3(\rho - i\eta) \\ -\lambda + \dfrac{A^2\lambda^5}{2}(1 - 2\rho) - iA^2\lambda^5\eta & 1 - \dfrac{\lambda^2}{2} - \lambda^4\left(\dfrac{1}{8} + \dfrac{A^2}{2}\right) & A\lambda^2 \\ A\lambda^3\left(1 - \left(1 - \dfrac{\lambda^2}{2}\right)(\rho + i\eta)\right) & -A\lambda^2\left(1 - \dfrac{\lambda^2}{2}\right)(1 + \lambda^2(\rho + i\eta)) & 1 - \dfrac{A^2\lambda^4}{2} \end{pmatrix} + O(\lambda^6).$$
$$(1.30)$$

The real parameters of the matrix are now λ, A and ρ while the imaginary part is represented by a unique variable: η. When $\eta \neq 0$ CP violation becomes possible. The λ parameter encodes the relative strength of the interactions between different quark families: diagonal terms (interaction within the same quark family) are close to 1, transition between the first and the second family (second and third family) [first and third] is of the order $\lambda(\lambda^2)[\lambda^3]$.

It becomes clear now the importance of $b-$physics and precise measurements of the CKM matrix parameters to fully constrain the theory and test its validity. In fact, while the mixing between the first and the second family is described by the Cabibbo angle (thus the λ parameter), the decays of $b-$hadrons involve CKM matrix elements which are the most sensitive to CP violation. Generally, a $b-$hadron decay is described by terms accounting for vertices of interactions associated to V_{cb} or V_{ub}. V_{CKM} can be seen as a rotation matrix connecting mass eigenstates with the eigenstates of weak interaction. Unitarity of the theory is ensured if the following condition holds:

$$V_{ij}V_{jl}^\dagger = V_{ij}^\dagger V_{jl} = \delta_{il}. \tag{1.31}$$

Nine relations can be obtained from (1.31) and it allows to write down nine independent equations. Using (1.31), it must be true that

$$V_{ud}^* V_{ub} + V_{cd}^* V_{cb} + V_{td}^* V_{tb} = 0. \tag{1.32}$$

Defining

$$\bar\rho = \rho\left(1 - \frac{\lambda^2}{2}\right) \qquad \bar\eta = \eta\left(1 - \frac{\lambda^2}{2}\right), \tag{1.33}$$

and using the Wolfestein parametrization and neglecting $O(\lambda^7)$ terms it is possible to derive the following relations:

$$V_{ud}^* V_{ub} = A\lambda^3(\bar\rho - i\bar\eta) \quad , \quad V_{cd}^* V_{cb} = -A\lambda^3 \quad \text{and} \quad V_{td}^* V_{tb} = A\lambda^3(1 - \bar\rho + i\bar\eta). \tag{1.34}$$

Dividing (1.34) by $A\lambda^3$, the unitarity condition can be represented[7] in the $(\bar\rho, \bar\eta)$ plane as a triangle with summits at C(0, 0), B(1, 0) and A($\bar\rho-\bar\eta$) as shown in Fig. 1.3.

---

[7]It is also possible to use other relations but in all the other relations λ appears to different powers in the unitarity condition.

Fig. 1.3 The unitarity triangle in the $(\overline{\rho}-\overline{\eta})$ plane
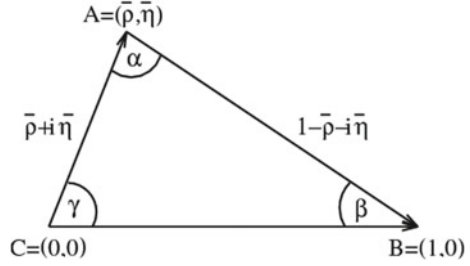
The relevant relations from the unitarity condition up to $\mathcal{O}(\lambda^4)$ terms of the CKM matrix are the following:

$$
\overline{AC} = \frac{\left|V_{ud}V_{ub}^*\right|}{\left|V_{cd}V_{cb}^*\right|} = \sqrt{\overline{\rho}^2 + \overline{\eta}^2} = \frac{1-\dfrac{\lambda^2}{2}}{\lambda}\frac{\left|V_{ub}\right|}{\left|V_{cb}\right|}
$$

$$
\overline{AB} = \frac{\left|V_{td}V_{tb}^*\right|}{\left|V_{cd}V_{cb}^*\right|} = \sqrt{(1-\overline{\rho})^2 + \overline{\eta}^2} = \frac{1}{\lambda}\frac{\left|V_{td}\right|}{\left|V_{cb}\right|}
$$

$$
\overline{CB} = 1.
$$

(1.35)

These relations encode the standard model the *CP* violation in quark sector and precise measurements and cross checks with different processes of the position of A in the $\overline{\rho}-\overline{\eta}$ plane can provide tests and limits of validity of the Standard Model. The sides of the triangle are proportional to matrix elements while angles of the triangle are related to *CP* violation in weak processes. The position of the vertex $(\overline{\rho}, \overline{\eta})$ can be over-constrained measuring independently the sides and the angles. *CP* violation in K, D and B systems must fit together according to the presence of a single phase in the V_{CKM}. The angles of the triangle are labelled in the literature as $\phi_{1,2,3}$ or α, β, γ. The $\overline{AC} = \left|\dfrac{V_{ud}V_{ub}^*}{V_{cd}V_{cb}^*}\right|$ side of the triangle in Fig. 1.4 can be measured using B decays involving $b \to c$ or $b \to u$ transitions, while the $\overline{AB} = \left|\dfrac{V_{td}V_{tb}^*}{V_{cd}V_{cb}^*}\right|$ side involves $B^0 - \overline{B}^0$ oscillation due to the presence of $b \to t$ transitions in the loop.

The angles of the triangle are defined as follows:

$$
\alpha = Arg\left(-\frac{V_{td}V_{tb}^*}{V_{ud}V_{ub}^*}\right)
$$

(1.36)

$$
\beta = Arg\left(-\frac{V_{cd}V_{cb}^*}{V_{td}V_{tb}^*}\right)
$$

(1.37)
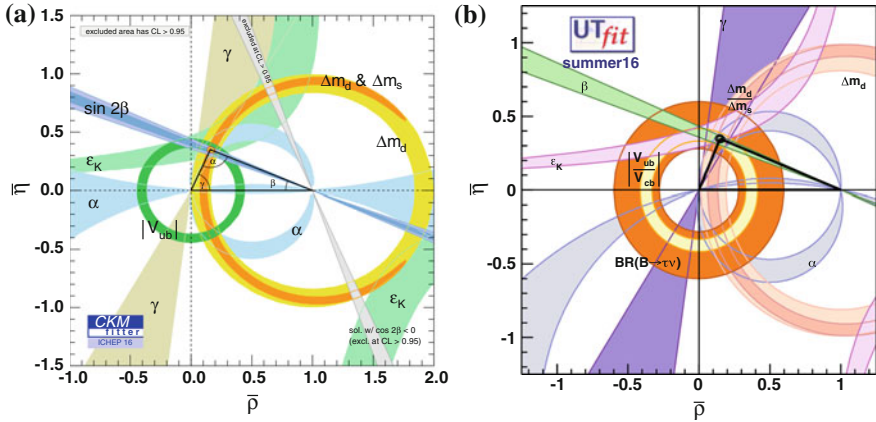
Fig. 1.4 The measured unitarity triangle which constrain the position of A in the $(\overline{\rho}-\overline{\eta})$ plane. The shaded areas have a 95% Confidence Level (CL). The intersection of all of the allowed measurements are consistent with the Standard Model. The results show the state of art in 2016. **a** shows the constrained unitarity triangle using a frequentist approach (CKM fitter) while **b** are the results using a Bayesian approach (UT fit)

$$\gamma = Arg\left(-\frac{V_{ud}V_{ub}^*}{V_{cd}V_{cb}^*}\right) \tag{1.38}$$

All the current measurements (decay rates, oscillation frequency, lifetimes) aiming at over constraining the CKM matrix are consistent with the existence of a unique CP violating phase in the quark sector. Since the asymmetry of matter and anti-matter in the universe predicted by the Standard Model is in discrepancy with the cosmological measured one, one should expect signals of New Physics from this sector. The last point has been one of the main reason why B-factories facilities have been built (Belle, BaBar, LHCb). Indeed, such kind of precision measurement dedicated experiments permit to over-constrain the Standard Model and at the same time are able to search and spot signals for indirect signatures of New Physics effects entering in the processes at loop level.

All the physics measurements aiming at constraining the unitarity triangle are represented as allowed regions in the $(\overline{\rho} - \overline{\eta})$ plane as shown in Fig. 1.4. All the measurements, nowadays, are consistent with the unique picture given by the SM. A huge effort is made to increase the sensitivity and the statistics of measurements, in order to find NP and eventually constrain the SM validity.

The subject of this thesis is the study of the $B^0 \to D^0\overline{D}^0K^{*0}$ and $B^0 \to D^{*-}D^0K^+$ using the Run I data of the LHCb experiment. These decay modes are described by the $b \to c$ and they belongs to the family of $B \to D^{(*)}\overline{D}^{(*)}K^{(*)}$ decays. The $b \to c$ transition is the dominant one in B decays (*CKM* favoured). A comprehensive introduction to doubly charmed B meson decays is provided in Chap. 5.

References

1. M. Borsato, Study of the $B^0 \to K^{*0}e^+e^-$ decay with the LHCb detector and development of a novel concept of PID detector: the Focusing DIRC. Ph.D thesis, Santiago de Compostela U (2015)

2. Particle Data Group, C. Patrignani et al., Review of particle physics. Chin. Phys. **C40**(10), 100001 (2016). https://doi.org/10.1088/1674-1137/40/10/100001

3. ATLAS Collaboration, G. Aad et al., Observation of a new particle in the search for the Standard Model Higgs boson with the ATLAS detector at the LHC. Phys. Lett. **B716**, 1 (2012). https://doi.org/10.1016/j.physletb.2012.08.020, arXiv:1207.7214

4. CMS collaboration, S. Chatrchyan et al., Observation of a new boson at a mass of 125GeV with the CMS experiment at the LHC. Phys. Lett. **B716**, 30 (2012). https://doi.org/10.1016/j.physletb.2012.08.021, arXiv:1207.7235

5. E. Fermi, An attempt of a theory of beta radiation. Z. Phys. **88**, 161 (1934). https://doi.org/10.1007/BF01351864

6. E. Noether, Invariant variation problems. Gott. Nachr. **1918**, 235 (1918). https://doi.org/10.1080/00411457108231446. arXiv:physics/0503066

7. T.D. Lee, C.-N. Yang, Question of parity conservation in weak interactions. Phys. Rev. **104**, 254 (1956). https://doi.org/10.1103/PhysRev.104.254

8. C.S. Wu, Experimental test of parity conservation in beta decay. Phys. Rev. **105**, 1413 (1957). https://doi.org/10.1103/PhysRev.105.1413

9. M. Goldhaber, L. Grodzins, A.W. Sunyar, Helicity of neutrinos. Phys. Rev. **109**, 1015 (1958). https://doi.org/10.1103/PhysRev.109.1015

10. Gargamelle Neutrino, F.J. Hasert et al., Observation of neutrino like interactions without muon or electron in the Gargamelle Neutrino experiment. Nucl. Phys. **B73**, 1 (1974). https://doi.org/10.1016/0550-3213(74)90038-8

11. S.L. Glashow, Partial symmetries of weak interactions. Nucl. Phys. **22**, 579 (1961). https://doi.org/10.1016/0029-5582(61)90469-2

12. P.W. Higgs, Broken symmetries and the masses of Gauge Bosons. Phys. Rev. Lett. **13**, 508 (1964). https://doi.org/10.1103/PhysRevLett.13.508

13. P.W. Higgs, Spontaneous symmetry breakdown without Massless Bosons. Phys. Rev. **145**, 1156 (1966). https://doi.org/10.1103/PhysRev.145.1156

14. S. Weinberg, A model of leptons. Phys. Rev. Lett. **19**, 1264 (1967). https://doi.org/10.1103/PhysRevLett.19.1264

15. A. Salam, Weak and electromagnetic interactions. Conf. Proc. **C680519**, 367 (1968)

16. F. Englert, R. Brout, Broken symmetry and the mass of gauge vector mesons. Phys. Rev. Lett. **13**, 321 (1964). https://doi.org/10.1103/PhysRevLett.13.321

17. P.W. Higgs, Broken symmetries, massless particles and gauge fields. Phys. Lett. **12**, 132 (1964). https://doi.org/10.1016/0031-9163(64)91136-9

18. G.S. Guralnik, C.R. Hagen, T.W.B. Kibble, Global conservation laws and massless particles. Phys. Rev. Lett. **13**, 585 (1964). https://doi.org/10.1103/PhysRevLett.13.585

19. A. Collaboration, Evidence for the spin-0 nature of the Higgs boson using ATLAS data. Phys. Lett. B **726**, 120 (2013)

20. J.J. Thomson, Cathode rays. Phil. Mag. **44**, 293 (1897). https://doi.org/10.1080/14786449708621070

21. J. Chadwick, Possible existence of a neutron. Nature **129**, 312 (1932). https://doi.org/10.1038/129312a0

22. C.D. Anderson, The positive electron. Phys. Rev. **43**, 491 (1933). https://doi.org/10.1103/PhysRev.43.491

23. S.H. Neddermeyer, C.D. Anderson, Note on the nature of cosmic ray particles. Phys. Rev. **51**, 884 (1937). https://doi.org/10.1103/PhysRev.51.884

24. H. Yukawa, On the interaction of elementary particles. Proc. Phys. Math. Soc. Jpn. **17**, 48 (1935)

25. M. Gell-Mann, A schematic model of Baryons and Mesons. Phys. Lett. **8**, 214 (1964). https://doi.org/10.1016/S0031-9163(64)92001-3
26. Zweig, An SU(3) model for strong interaction symmetry and its breaking. Version 1,
27. N. Cabibbo, Unitary symmetry and leptonic decays. Phys. Rev. Lett. **10**, 531 (1963). https://doi.org/10.1103/PhysRevLett.10.531
28. S.L. Glashow, J. Iliopoulos, L. Maiani, Weak interactions with Lepton-Hadron symmetry. Phys. Rev. D **2**, 1285 (1970). https://doi.org/10.1103/PhysRevD.2.1285
29. E598 Collaboration, J.J. Aubert et al., Experimental observation of a heavy particle. J. Phys. Rev. Lett. **33**, 1404 (1974). https://doi.org/10.1103/PhysRevLett.33.1404
30. SLAC-SP-017 Collaboration, J.E. J.Ãugustin et al., Discovery of a narrow resonance in e^+e^- annihilation. Phys. Rev. Lett. **33**, 1406 (1974). https://doi.org/10.1103/PhysRevLett.33.1406
31. J.H. Christenson, J.W. Cronin, V.L. Fitch, R. Turlay, Evidence for the 2π decay of the K_2^0 meson. Phys. Rev. Lett. **13**, 138 (1964). https://doi.org/10.1103/PhysRevLett.13.138
32. M. Kobayashi, T. Maskawa, CP violation in the renormalizable theory of weak interaction. Prog. Theor. Phys. **49**, 652 (1973). https://doi.org/10.1143/PTP.49.652
33. S.W. Herb, Observation of a dimuon resonance at 9.5GeV in 400GeV proton-nucleus collisions. Phys. Rev. Lett. **39**, 252 (1977). https://doi.org/10.1103/PhysRevLett.39.252
34. CDF Collaboration, C. Collaboration, Evidence for top quark production in $\bar{p}p$ collisions at $\sqrt{s} = 1.8$ TeV. Phys. Rev. Lett. **73**, 225 (1994). https://doi.org/10.1103/PhysRevLett.73.225, arXiv:hep-ex/9405005
35. B. Pontecorvo, Mesonium and anti-mesonium. Sov. Phys. JETP **6**, 429 (1957)
36. B. Pontecorvo, Inverse beta processes and nonconservation of lepton charge. Sov. Phys. JETP **7**, 172 (1958)
37. Z. Maki, M. Nakagawa, S. Sakata, Remarks on the unified model of elementary particles. Prog. Theor. Phys. **28**, 870 (1962). https://doi.org/10.1143/PTP.28.870
38. L.-L. Chau, W.-Y. Keung, Comments on the parametrization of the Kobayashi-Maskawa matrix. Phys. Rev. Lett. **53**, 1802 (1984). https://doi.org/10.1103/PhysRevLett.53.1802
39. L. Wolfenstein, Parametrization of the Kobayashi-Maskawa matrix. Phys. Rev. Lett. **51**, 1945 (1983). https://doi.org/10.1103/PhysRevLett.51.1945

Chapter 2
The LHCb Detector at the LHC

2.1 The Large Hadron Collider

The Large Hadron Collider (LHC) [1] at CERN is the most powerful particle collider ever built. The accelerator has a circumference of 27 km and it is installed in a dedicated tunnel placed 100 m underground in the Swiss-France area near Geneva (Switzerland). LHC is designed to accelerate counter-propagating proton beams up to an energy of 7 TeV and collide them at the nominal centre-of-mass energy of 14 TeV. Before injection in the LHC ring, the beams are pre-accelerated by several steps as shown in Fig. 2.1.

The different acceleration steps before the proton beams are injected in the LHC ring are:

1. Protons are obtained by removing electrons from hydrogen atoms and they are first accelerated by the LINear ACcelerator 2 (LINAC 2) up to 50 MeV and then they are injected into the BOOSTER which brings them up to an energy of 1.4 GeV;
2. The Proton Synchrotron (PS) accelerates protons up to 26 GeV and the resulting beam is injected in the Super Proton Synchrotron (SPS);
3. The SPS provides a proton beam with an energy of 450 GeV which is injected clockwise and counter-clockwise in the LHC ring.

A total of 16 Radio-frequency (RF) cavities are placed along the LHC ring and they are used to accelerate the proton beams to the nominal collision energy. In order to bend the proton beam and let it circulate in the LHC ring, 12,300 superconducting Niobium-Titanium dipole magnets are used. The dipole coils are kept at cryogenic temperature of 1.9 K, reached thanks to a helium cooling system. The intensity of the superconducting dipole magnetic field is 8.3 T. The dipole magnets allows to keep the protons in the LHC orbit. Proton beams are also kept stable and focused while propagating thanks to a total of 392 quadrupoles. The counter propagating proton beams are housed in the same cryostat and they share the same yoke such that they can experience the same magnetic field, but in opposite directions. In four of the eight
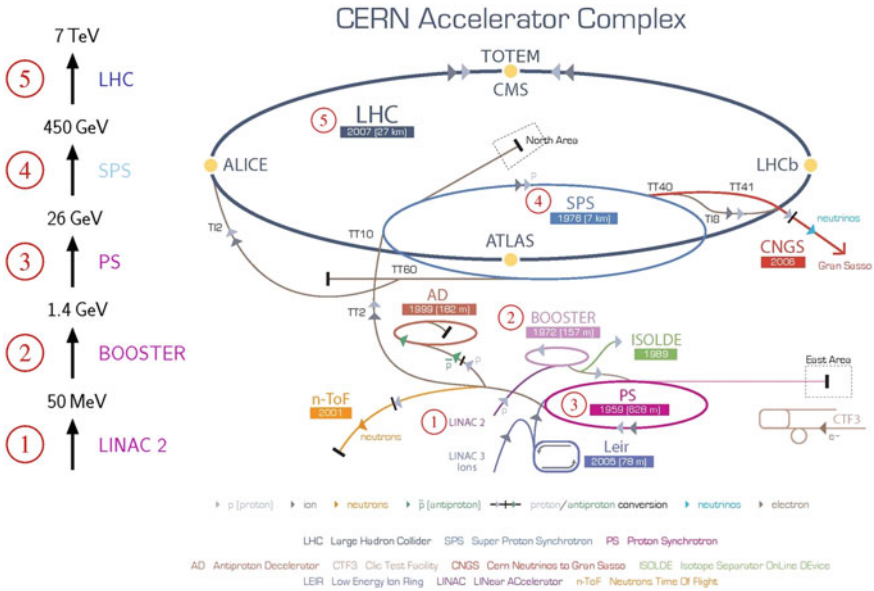
Fig. 2.1 A schematic drawing of the LHC accelerator complex showing the different particles (*p* or *Pb*) acceleration steps. In order to bring protons at 3.5–4 and 6.5–7 TeV during Run I (2011 and 2012) and Run II (2015–2018) data taking periods respectively, *p* are extracted from a Hydrogen source and then accelerated up to 50 MeV by the LINear ACCelerator 2 (LINAC 2). The BOOSTER brings them up to 1.4 GeV and the Proton Synchrotron (PS) accelerates them up to 26 GeV. The Super Proton Synchrotron (SPS) finally brings them to 450 GeV and the output is injected in the LHC ring where they can finally reach the nominal collision energy. Figure taken from [2]

circular sectors defining the LHC ring, the beams are allowed to collide. The collision points are called Interaction Points (IPs). The four IPs are located in the middle of long straight sections of the corresponding circular sector and they are surrounded by a total of seven different high-energy physics experiments aiming at studying the multi- TeV scale particle collision products. Nominal proton bunches circulating in the LHC ring are composed of 1.2–1.4×10^{11} protons separated each other by a distance of 25 ns $\times c$, leading to a nominal expected collision rate of 40 MHz. The designed LHC instantaneous luminosity corresponds to 10^{34} cm^{-2} s^{-1}.

The various experiments at the LHC placed at the IPs can be divided into two main categories: the General-Purpose Detectors (GPDs) and the dedicated physics experiments. The GPDs at LHC are the ATLAS [3] (A Toroidal LHC ApparatuS) and CMS [4] (Compact Muon Solenoid) experiments; both of them have been designed to study collisions producing high transverse momentum (p_T) particles. Their physics program is very wide but the main focus consists on the search and study of the Higgs Boson properties and the search for direct evidences of New Physics (NP). Furthermore, GPDs physics program also covers aspects related to the physics of *b* and *t* quarks, precision measurement in the electroweak sector of the SM and general SM precision measurements. The success of these GPDs can be found in the first

observation of the Higgs Boson [3, 4] which happened right after the beginning of data taking using solely 2011 and 2012 data from both CMS and ATLAS experiments. Nowadays, the main focus regarding the Higgs Boson has moved to the measurement of its properties since the discovered scalar boson is highly sensitive to contribution from Beyond Standard Model (BSM) physics.

The other main experiments (dedicated physics experiments) operating at the LHC are:

1. **LHCb** [7] (Large Hadron Collider beauty): it is a dedicated experiment for heavy flavour physics optimised and designed for the study of c and b hadron decay products. Details will be provided later in this chapter.
2. **ALICE** [8] (A Large Ion Collider Experiment): it is dedicated to the study of quark-gluon plasma (QGP) in heavy ion collisions taking advantage of the LHC runs using Pb ion beams.
3. **TOTEM** [9] (TOTal Elastic and diffractive cross-section Measurement) experiment: it studies the total proton-proton cross-section, elastic scattering and diffractive dissociation and it is also used to monitor the LHC luminosity.
4. **LHCf** [10] (Large Hadron Collider forward): it is used for engineering measurements for astroparticle experiments simulating cosmic rays in laboratory conditions.
5. **MoEDAL** [11] (Monopole and Exotics Detector At the LHC): it looks and searches for magnetic monopole.

The first proton beam was injected in the LHC ring in September 2008, nevertheless the operation was blocked due to an accident which happened few weeks later.[1] Data taking restarted in 2010 and continued in 2011 and 2012; this period is referred to as Run I. During Run I, the centre of mass energy of the colliding protons was 7 TeV in 2011, while in 2012 it has been increased up to 8 TeV (in order to increase the Higgs production cross-section for ATLAS and CMS). Data taking restarted in 2015 (referred to as Run II) with the LHC machine operating at a centre of mass energy of 13 TeV and providing proton bunches at the nominal time spacing separation of 25 ns (it was 50 ns in Run I). The instantaneous luminosity at the LHCb experiment is $\mathscr{L}_{inst} = 4 \times 10^{32}\,\mathrm{cm}^{-2}\,\mathrm{s}^{-1}$ and it is one order of magnitude lower than the one used by the GPDs experiments. The LHCb recorded integrated luminosity during the various data taking period is shown in Fig. 2.2.

2.2 The LHCb Experiment at the LHC

The experimentally observed and Standard Model predicted *CP* asymmetry is not enough to explain the observed matter-antimatter asymmetry in our universe. Therefore, NP effects are expected to appear in *CP* violating processes. In such context,

---

[1]A quench in a superconducting magnet induced a leak of liquid helium in the tunnel damaging the corresponding section of the LHC accelerator.
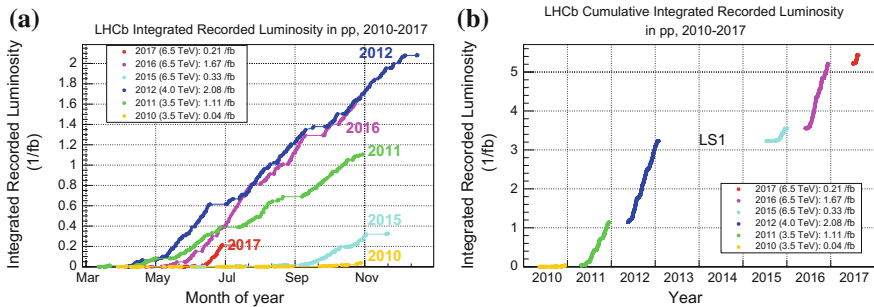
Fig. 2.2 a shows the evolution of the integrated luminosity at LHCb during the various data taking periods. **b** shows the cumulative integrated luminosity at the LHCb experiment until the last data taking in July 2017. Figure from [12]

the LHCb experiment at the LHC has been designed to perform precision measurements using the vast statistics of heavy flavour hadrons produced in *pp* collisions in the forward region. Signals of NP contribution can be indirectly accessed using heavy flavour meson decays at tree and loop level. Differently from GPDs aiming at making direct observations of NP particles, LHCb looks for indirect effects of them in processes such as *CP* violation in *B* and *D* mesons decays and lepton flavour universality violation (LFUV). These NP effects arise mainly from box diagrams and penguin ones, leading to observed quantities being in discrepancy with respect to the SM predictions. Many other aspects are covered at LHCb, such as the dynamic of *B* mesons decays, quarkonium spectroscopy and general *QCD* aspects. In order to study *b* and *c* hadrons, *pp* collisions from the LHC are used. Given the nominal LHCb luminosity of $2 \cdot 10^{32} \, \mathrm{cm^2 \, s^{-1}}$ and the inelastic cross-section σ_{inel} of about 70 mb at 7 TeV [13], the expected *pp* visible collision rate in the detector is about 10 MHz (see Fig. 2.3). The $b\bar{b}$ production cross-section at $\sqrt{s} = 7$ TeV is 300 µb [15]. Therefore, an event containing a *b* hadron is expected to be produced every 230 *pp* interactions on average. The dominant heavy meson production mechanism at the TeV energy scale is the fusion between gluons and partons (see Fig. 2.4).

Because of the $b\bar{b}$ production mechanism characteristics in proton collisions, the angular distribution of $b\bar{b}$ pairs is peaking in the forward and backward directions with respect to the proton beam direction. Therefore, the LHCb detector has been designed as a single-arm forward spectrometer, covering a pseudorapidity (η) range in the forward direction between 1.8 and 4.9. A comparison between LHCb and GPDs (CMS in this case) in terms of pseudorapidity coverage (CMS covers the range $-2.4 < \eta < 2.4$) is shown in Fig. 2.5 where also the angular distribution of $b\bar{b}$ pair produced at $\sqrt{s} = 8$ TeV is shown.

The LHCb coordinate system is defined as follow:

- The origin of the coordinate system is the interaction point.
- The *x*-axis is horizontal, and points from the interaction point towards the outside of the LHC ring.
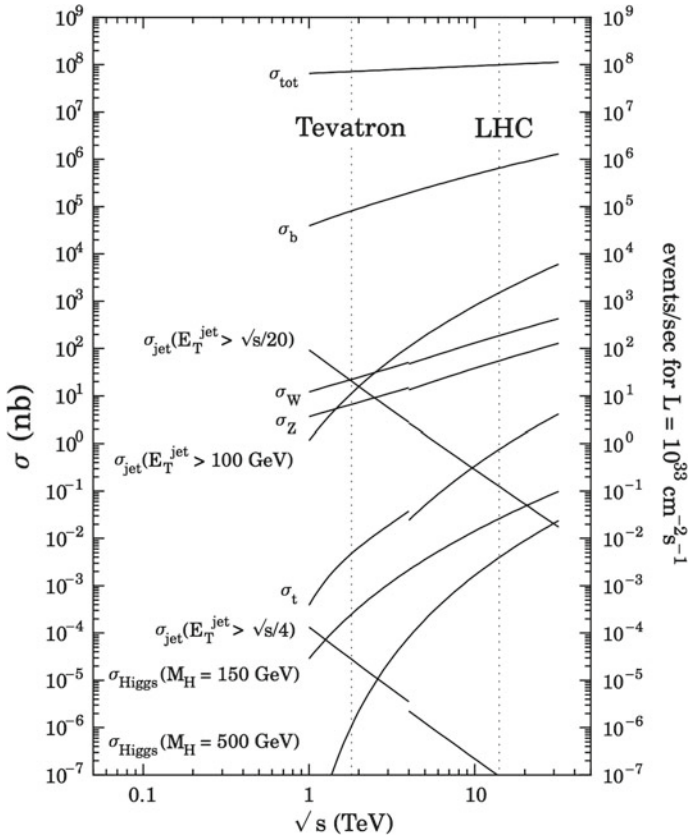
Fig. 2.3 Dependence of various hard scattering process cross-sections as a function of the centre-of-mass energy $\sqrt{s}$. The dashed lines corresponds to the Tevatron energy of $\sqrt{s} = 1.96$ TeV and the nominal LHC energy of 14 TeV. As it can be observed, the ratio of $b\bar{b}$ production (σ_b in the picture) is between 2 and 3 orders of magnitude lower than the total cross-section σ_{tot}. Figure is taken from [15]

- The y-axis is perpendicular to the x-axis and to the beam line. It points upwards and is inclined by 3.601 mrad with respect to the vertical axis.
- The z-axis points from the interaction point towards the LHCb detector and is aligned with the beam direction, to create a right handed Cartesian coordinate system xyz.
- The transverse plane is the $x - y$ one and it is used to define particles transverse quantities such as p_{T} and E_{T}.

Tracks produced at LHCb are bent by a dipole magnet having a bending power of 4 Tm and magnetic field lines along the y direction. Throughout this thesis, a point A is said to be upstream (downstream) a point B if $z_A < (>)z_B$.

The LHCb detector has an angular acceptance of [10,300] mrad in the non-bending plane ($y - z$) and [10, 250] mrad in the bending plane ($x - z$). This allows to capture
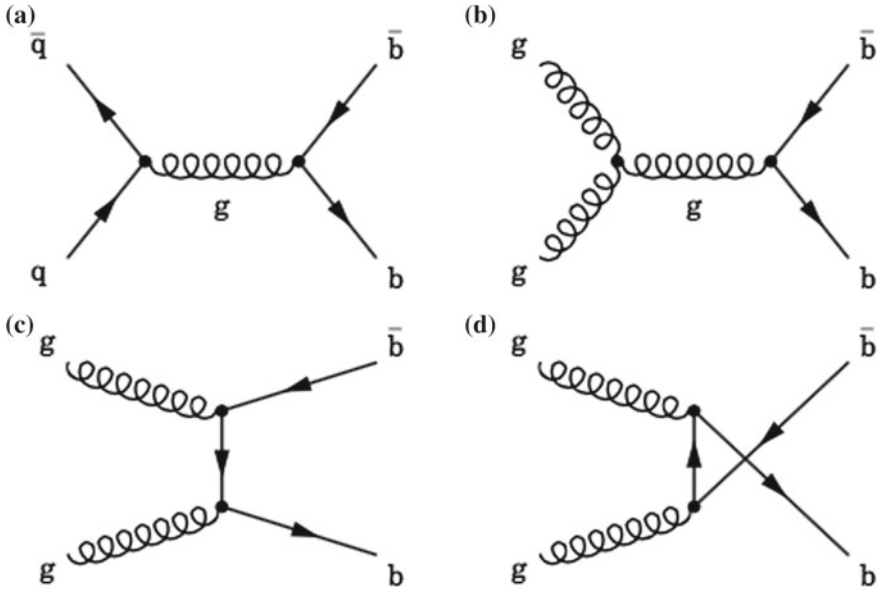
Fig. 2.4 Leading order Feynman diagrams for $b\bar{b}$ production in pp collisions at LHC. **a** shows the leading order diagram $b\bar{b}$ pair creation via $q - \bar{q}$ annihilation, **b**, **c**, **d** show $b\bar{b}$ production through gluon fusion. Figure is taken from [16]
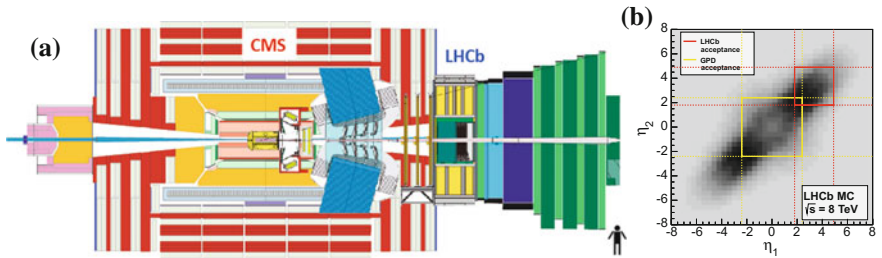
Fig. 2.5 LHCb and GPDs (CMS) angular acceptances comparison. **a** shows the LHCb detector superimposed to the CMS one. Figure taken from [17]. **b** shows the $b\bar{b}$ production as a function of (η_1, η_2) for a centre-of-mass energy of 8 TeV (similar distributions are obtained at $\sqrt{s} = 7$, 13 and 14 TeV). η_1 and η_2 are the pseudorapidities of the produced b and $\bar{b}$, respectively. Yellow (Red) dotted lines mark the GPDs (LHCb) acceptance limits. Figure taken from [18]

27% of the total b or $\bar{b}$ quarks produced in pp collisions at LHC. The LHCb detector design as a forward spectrometer (see Fig. 2.6) combined to the $b\bar{b}$ production mechanism at LHC offers further advantages: the average momentum (p) of the produced b or c mesons is about 80 GeV/c, leading to approximately 1 cm mean travelling distance before decay. Therefore, the signature of events containing heavy hadrons relies on precision measurements of decay vertices position to be distinguished from the others inelastic pp collision.
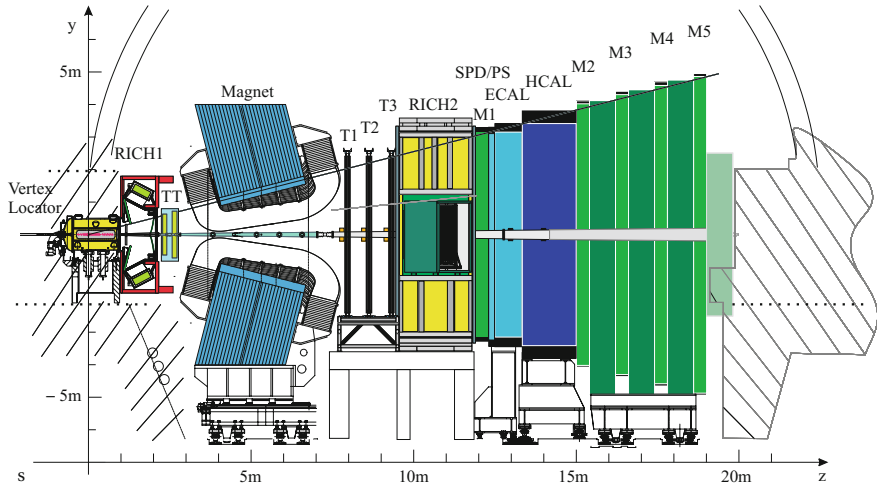
Fig. 2.6 LHCb detector side view. Figure taken from [19]

Therefore, the primary vertex (PV, production point of the $b, c-$hadrons) and secondary vertex (SV, decay position of the $b, c-$hadrons) reconstruction plays an important role in event selection and trigger. Indeed, the vertex resolution achieved thanks to the VErtex LOcator (VELO) detector (see Sect. 2.3.1) is fundamental in the determination of displaced b and c decay vertices which are used to identify the event topology and finally provide very precise measurement of decay times, indispensable for CP violation measurements.

The most important experiments running between 1999 and 2010 leading to a step forward in the understanding of the heavy flavour structure of the SM are BaBar [20] and Belle [21]. These two experiments were installed at $e^{\pm}$ colliders. The asymmetric e^+e^- beam energies were tuned to achieve a centre of mass energy equal to the mass of the $\Upsilon(4S)$ resonance. The produced resonance decays into pairs of charged or neutral B mesons, i.e. (B^+B^-) or $(B^0\overline{B}^0)$ with a boost in the laboratory frame. The boost of the resulting mesons is the result of the asymmetric e^+e^- beam energies and this fact allows the experiments to achieve a similar vertex topology separation strategy as in LHCb. The LHCb experiment, thanks to the pp collisions provided by the LHC can reach much higher cross-sections and all b hadrons species can be produced $(B_s, B_c, \Lambda_b, \ldots)$ and studied. However, a much higher pollution in the final states environment is expected due to inelastic cross section being 2–3 orders of magnitude greater than the $b\bar{b}$ production cross-section. Although the LHCb experiment suffers in terms of b-flavor tagging (i.e. identification of the b hadron flavour at the production point) efficiencies ($\sim$5%) and a low reconstruction efficiency for events containing neutrals (γ, π^0) with respect to $B-$factories, LHCb is currently the leading beauty and charm physics experiment thanks to the world's largest sample of exclusively reconstructed charm and beauty decays. Notably, this result has been achieved using only the Run I data (2011 and 2012).

LHCb excellent performance and data quality in the high-multiplicity hadronic environment provided by LHC collisions can only be achieved thanks to a reduction of the delivered instantaneous luminosity [22] by the LHC aiming at limiting the ageing of the detectors placed close to the interaction point. Indeed, the LHCb instantaneous luminosity is lowered by 2 orders of magnitude (the design one is $2 \times 10^{32} \, \text{cm}^{-2} \, \text{s}^{-1}$) with respect to the CMS and ATLAS experiments and it is kept approximatively constant in time minimizing the effects of luminosity decay during a LHC fill[2] (see Fig. 2.7b). Among all the possible luminosity levelling techniques [23] the LHCb experiment implements the strategy of levelling with offset as sketched in Fig. 2.7b. This strategy avoids head-on collisions separating beams perpendicularly to the collision plane [24]. The luminosity levelling allows to obtain events with few proton-proton interaction per bunch crossing and it allows an excellent identification and reconstruction of the production vertex of the $b\bar{b}$ pairs and the whole decay chain, fundamental for the LHCb physics goals. The average number of visible interactions per bunch crossing (μ_{vis}) and the instantaneous luminosity during Run I data taking for LHCb are shown in Fig. 2.7a.

The separation of beauty and charm hadron decays from the background takes advantage of the vertex signature as mentioned before and of the final state high transverse momentum (p_T). Therefore, an excellent tracking system, particle identification and trigger strategy are the key ingredients for LHCb. The LHCb tracking system is composed by a VErtex LOcator (VELO, details given in Sect. 2.3.1) positioned at few mm from the pp interaction point, a dipole magnet (see Sect. 2.3.2) and tracking stations placed upstream and downstream of the dipole (see Sects. 2.3.3, 2.3.4 and 2.3.5). The tracking system is designed to reconstruct different types of tracks among which the so called `long` track are the most relevant for physics analysis. `Long` tracks leave signatures in the whole spectrometer and they are associated to charged particles produced close to the interaction point flying throughout the whole detector. Other important tracks in LHCb are the `downstream` tracks and they are associated to the large fraction of tracks originating from long-lived particles decay (such as K_S and Λ^0). `Downstream` tracks are produced outside the VELO, therefore they can be reconstructed using only the upstream and the downstream trackers.

Details on the tracking system are provided in Sect. 2.3 while tracking strategies will be provided in the dedicated upgrade section (see Sect. 4.1) when describing the track reconstruction for the upgrade phase. Particle identification (see Sect. 2.4) is ensured for electrons and photons by a silicon pad detector (SPD), a preshower (PS) and an electromagnetic calorimeter (ECAL), while for charged hadrons the hadronic calorimeter is used (HCAL) (see Sect. 2.4.2). Different types of hadrons are distinguished through the two Ring Imaging CHerenkov detectors (see Sect. 2.4.1) placed upstream and downstream of the dipole magnet covering different hadron momentum ranges. Muons are identified by muons stations composed of alternating layers

---

[2]A further advantage of keeping the luminosity constant is that the same trigger configuration can be kept and that the detector occupancy is not changing. This simplifies the analysis of the data and reduces systematic uncertainties.

Fig. 2.7 **a** Instantaneous luminosity during a long (15 h) LHC fill comparison between ATLAS, CMS and LHCb. **b** Pile-up μ_{vis} and peak luminosity recorded at LHCb during Run I data taking period. The violet dashed line corresponds to the designed value ($\mu_{vis} = 0.6$); it has been demonstrated that performances are not degraded if the value is kept at 1.6 (at $\sqrt{s} = 8$ TeV) [25], which is the value used for data taking corresponding to a peak luminosity of 4×10^{32} cm^{-2} s^{-1}. Figures taken from [25]
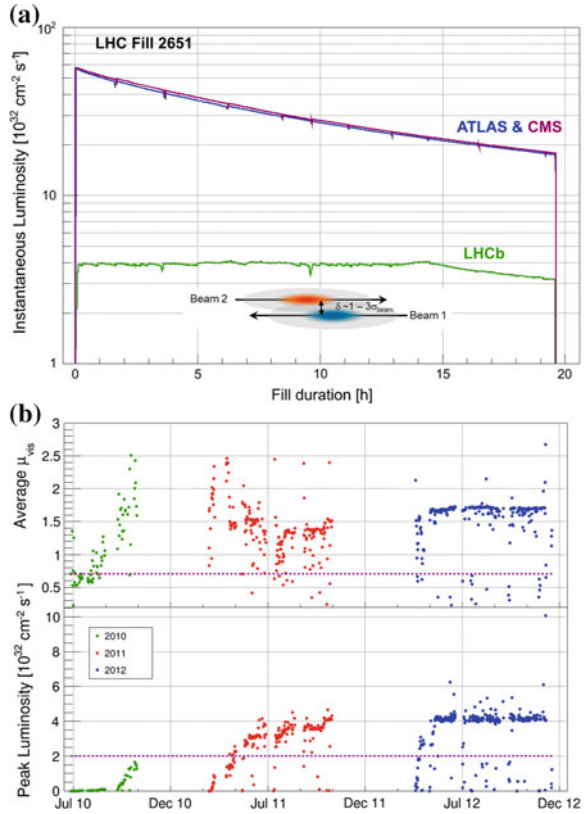
of iron and multiwire proportional chambers (see Sect. 2.4.3) placed downstream the calorimeter system.

Event rate reduction is mandatory in order to efficiently collect interesting events given the high event rate at the LHC. This is achieved by a flexible, versatile and efficient trigger strategy realized through the dedicated fast electronics of the calorimeters and muon stations (L0 trigger, hardware based) and through an Online CPU Farm performing a first fast simplified software event reconstruction (HLT1) followed by a full software event reconstruction (HLT2) at a reduced input rate. Details on the trigger strategy in Run I will be discussed in Sect. 2.4.5 and its evolution in Run II and upgrade will be discussed in Sect. 3.3.

2.3 LHCb Tracking System

Charged tracks produced in *pp* collisions (called prompt) or produced as decay products of *b* and *c* hadrons are reconstructed by the VErtex LOcator (VELO) and they allow to identify and reconstruct the PVs and SVs. Charged particles

originating from decaying b and c hadrons ($p, \overline{p}, e^{\pm}, \mu^{\pm}, K^{\pm}, \pi^{\pm}$) are considered stable particles within the LHCb detector and their momentum is evaluated measuring the bending experienced downstream the VELO. Upstream of the dipole magnet (Sect. 2.3.2) the Tracker Turicensis (TT) (Sect. 2.3.3) is placed, aiming at constraining the track segment upstream the magnet and providing a preliminary momentum estimation capable to predict the expected track position downstream of the magnet. Upstream track segments are then matched to downstream ones which are provided by three tracking stations (named *T1, T2, T3*) allowing for a precise measurement of track momenta (Sects. 2.3.4 and 2.3.5) with a resolution of $\Delta p / p = 0.4\%$ at $p = 5\,\mathrm{GeV/c}$ to $\Delta p / p = 0.6\%$ at $p = 100\,\mathrm{GeV/c}$ and a reconstruction efficiency (for tracks traversing the whole spectrometer) above 96%.

The downstream tracker uses two different technologies: silicon strip sensors in the inner region and straw-gas drift tubes in the outer region.[3] The former is called Inner Tracker (IT) and the latter Outer Tracker (OT). Details are provided in the following sub-sections for each sub-system.

2.3.1   VErtex LOcator

The *VErtex LOcator* (VELO) detector is the closer sub-detector surrounding the beam interaction point. The main goal of the detector is to locate primary vertices (PV), assign tracks to the correct PV and evaluate for each track the impact parameter (IP), defined as the distance of closest approach of a track to a given vertex. PV resolution is fundamental to precisely measure CP parameters, lifetimes of heavy hadrons and oscillation frequencies of heavy mesons (such as B_s oscillation), while IP is useful to fight the combinatorial background coming from candidates in which one track is associated with the wrong decay vertex. Therefore, the most important VELO performance indicators are the PV resolution as a function of the number of tracks (N_{tracks}) composing the vertex (shown in Fig. 2.8) and the IP resolution as a function of the track's transverse momenta (p_T) (shown in Fig. 2.9).

The excellent VELO performances are achieved thanks to its design. The VELO is made of 21 stations[4] made of silicon strips placed perpendicularly to the beam line for a total length of one meter (along z direction) and each of them has a thickness of $300\,\mu\mathrm{m}$. Each station is composed of 2048 silicon strip sensors; the traversing charged particles generate electron-hole pairs in the medium whose charge is collected by the read-out electronics. Among the 21 modules we can distinguish between R- and ϕ-sensors aiming at measuring the radial distance and the azimuthal coordinate of the traversing charged particles, respectively. The third coordinate is known from the z-position of the module itself. Two pile-up sensors (pile-up veto system) are installed upstream the interaction region to guarantee a fast trigger at the hardware level using the measurement of the backward charged track multiplicity and the identification of multiple interaction events. It is also used to improve the

---

[3]Inner (Outer) region corresponds to regions close (far) to the beam-pipe.

[4]Five of them are located upstream the interaction point.
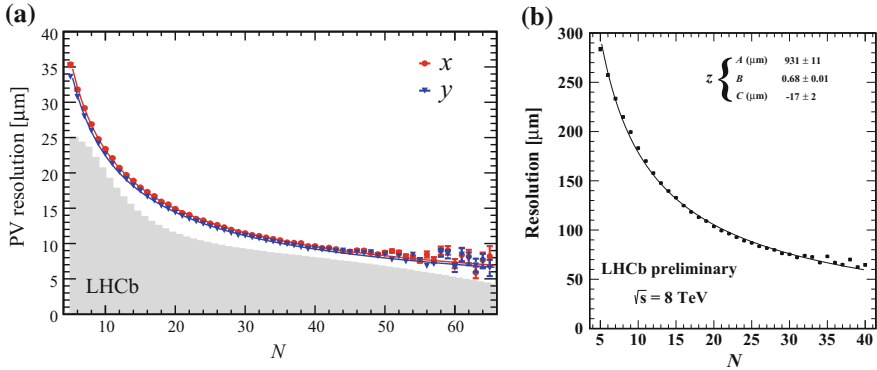
Fig. 2.8 Primary vertex resolution (along x and y on the left, along z on the right) during the 2012 data taking period as a function of the number of tracks (N_{tracks}) composing the vertex. Performances are obtained using events where only one single PV is found. Similar performances are achieved also for events containing two and three PVs and in the 2011 data taking period. Figures are taken from [26]
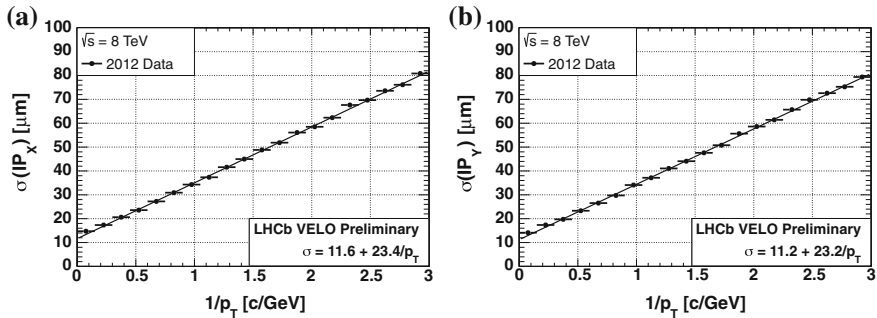
Fig. 2.9 Impact parameter resolution (σ_{IP}) along the x- (**a**) and y-axis (**b**) as a function of the inverse transverse momentum measured on 2012 data (similar performance are achieved for 2011 data and for events with 2 and 3 PVs). Figures taken from [26]

spatial resolution of reconstructed vertices using the tracks produced in the backward direction. Each of the 21 modules is composed by two retractable halves as shown in Fig. 2.10 which allows the VELO to be opened during beam injection. Indeed, the distance of the silicon strips from the beam axis in stable beam condition is 8 mm, which is smaller than the aperture allowed by the LHC during injection. During injection and unstable beam conditions the two halves are separated to each other by a distance of 6 cm, while in stable beam conditions the two halves overlap covering the full acceptance. Furthermore, the retractable layout design limits the ageing of the detector. A scheme of the VELO detector layout is shown in Fig. 2.10. The tracks coming from the interaction point can be reconstructed using the hits in the various VELO planes, and primary vertex candidates can be identified.
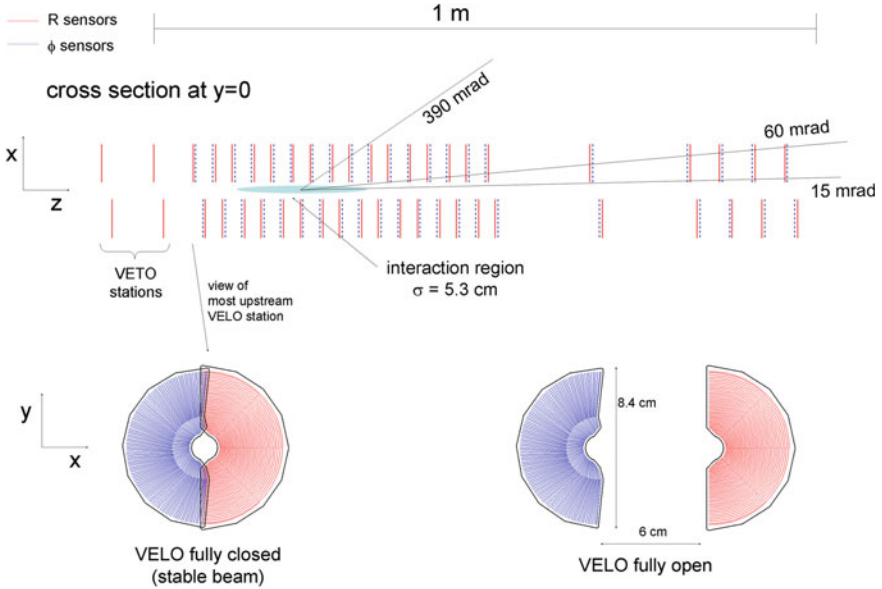
Fig. 2.10 Scheme of the VELO detector layout. The view of the front face of the modules is also illustrated in both the open and closed positions. R and ϕ-sensors are illustrated in red and blue respectively. Figure taken from [26]
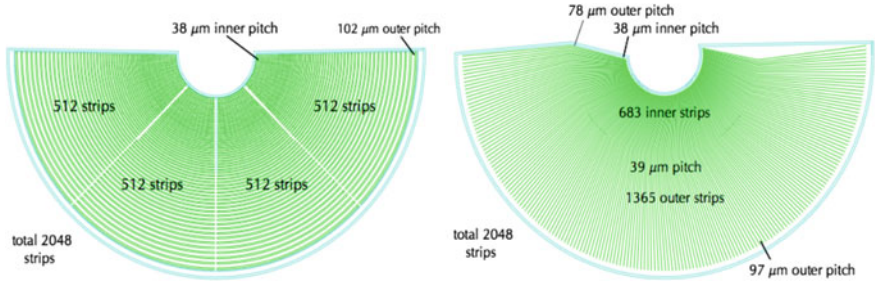
Fig. 2.11 Layout of $R-$(left) and $\phi-$(right) sensors. Details of pitch size and silicon strip geometry are also shown. The hit resolution achieved with this layout is around $4\,\mu$m. Figure is taken from [26]

The R-sensors consist of a semicircular silicon strip segmented into four $45°$ sectors, each of them composed of 512 silicon strips (for a total of 2048 silicon strips). The strip pitch increases linearly as a function of the radius, corresponding to a pitch size of $38\,\mu$m at the inner edge of the sensor and about $102\,\mu$m at the outer edge.

The ϕ-sensors consist of straight silicon strips; they are divided into an inner and an outer region in which the strips are skewed in opposite direction. The outer region is composed of twice as many strips as the inner region. The inner region is composed by 683 inner strips and the pitch size increase linearly as a function of the radius, ranging from 38 to $78\,\mu$m.

The outer regions is composed by 1365 outer strips and the pitch size in the outer region increases linearly with the radial distance ranging from 39 to 97 μm. A sketch of R and ϕ sensors is shown in Fig. 2.11.

The VELO sensors are encapsulated in a secondary vacuum container which is designed to limit the material budget before the first measurement. The separation between the secondary vacuum and the beam vacuum is achieved thanks to a thin aluminium foil called RF foil. Indeed, operation inside the primary vacuum would be impossible due to beam-induced effects in the modules such as pick-up of radio frequency (RF) waves from the beams leading to large correlated noise in the sensors. More details of the mechanical design can be found in Ref. [27].

2.3.2 LHCb Dipole Magnet

LHCb uses a warm dipole magnet with an integrated magnetic field of approximately 4 Tm. The dipole total weight is 1,600 tons operating at ambient temperature.

The magnetic field is provided by two identical coils of conical saddle shape placed mirror-symmetrically to each other in the magnet yoke. Non-uniformities of the field are of the order of 1%. The main $\vec{B}$ field component is along the y-axis, and it allows to bend charged particles in the x-z plane and provide a measurement of their momentum [23]. The knowledge of the magnetic field $\vec{B}(x, y, z)$ and its integral along a track path is essential to determine the expected motion of tracks depending on their charge and momentum. Indeed, the magnetic field map is used in the track fit (Kalman filter) and simplified local-parametrisations are used for pattern recognition algorithms. A sketch of the LHCb dipole magnet and the magnetic field intensity in the y direction is shown in Fig. 2.12.
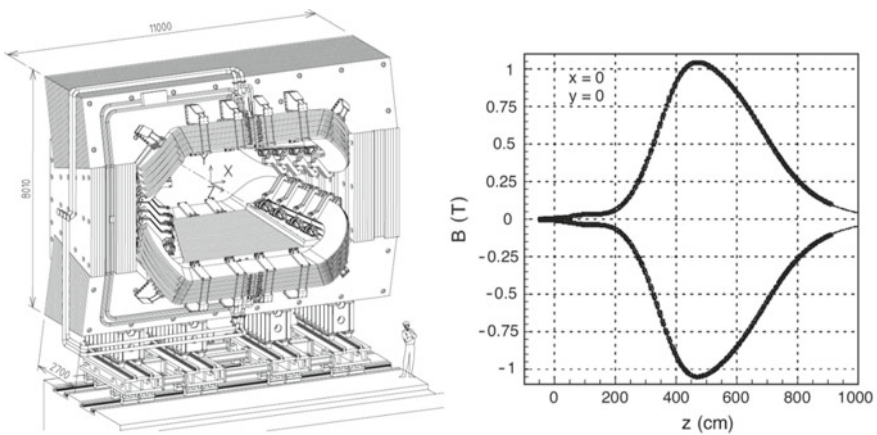
Fig. 2.12 On the left, the scheme of the LHCb dipole magnet. On the right, the magnetic field intensity as a function of z at $(x, y) = (0, 0)$. Figures taken from [23]

Low momentum charged particles experience a large deviation from the magnetic field and they are swept out the LHCb acceptance downstream the dipole. Therefore, only the tracker placed upstream the dipole can be used to find those tracks. Nevertheless, most of the high momentum particles are bent by the magnet and can be detected in the downstream trackers. The magnetic field intensity was measured with a relative precision of few times 10^{-4} and the measurement was achieved through an array of Hall probes. The magnetic field polarity is reversed frequently during data-taking to keep under control systematics due to left-right effects in the detector and to allow a proper calibration of the detectors.

2.3.3   Tracker Turicensis (TT)

The Tracker Turicensis (TT) or Trigger Tracker is located upstream the dipole magnet where a fringe field is present. It consists of four different layers of silicon strip sensors arranged in two stations (TTa, TTb) separated by 27 cm along the z direction (see Fig. 2.13). The four layers are oriented in a stereo-configuration, usually defined as *xuvx* configuration. The first and last layer are oriented in such a way that they provide measurement along the x axis, i.e. silicon strips run perpendicularly to the x-z plane. The $u(v)$ layer is rotated by an angle of $-5°$ $(+5°)$ around the z axis. The combination of u and v measurements allows to extract the $y(z_{layer})$ position of the track and provide a 3D information for track reconstruction.

The total area covered by the detector in the $x - y$ plane is $8.4\,\mathrm{m}^2$. Each sensor (rectangles in Fig. 2.13) covers a total area of $9.44\,\mathrm{cm} \times 9.64\,\mathrm{cm}$ and the sensor's thickness is $0.5\,\mathrm{mm}$. Each sensor is composed by a total of 512 read-out strips and the single silicon strip pitch size is $183\,\mu\mathrm{m}$, leading to an excellent position resolution of $\sim 50\,\mu\mathrm{m}$ in the bending plane. All sensors inside the TT are connected to
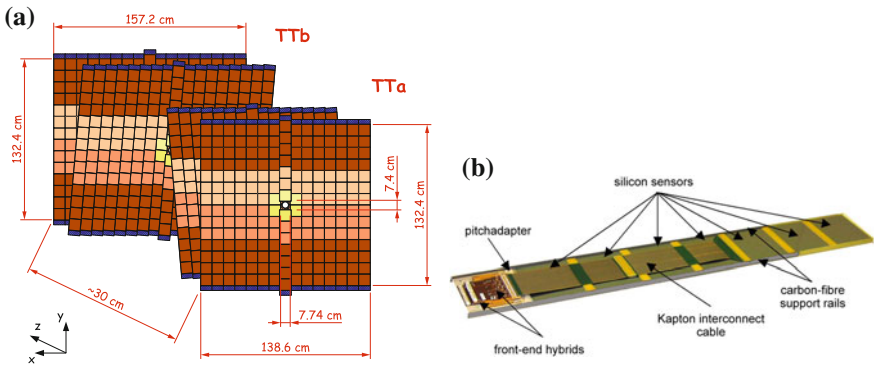
Fig. 2.13 On the left, the layout of the TT sub-system. Colour coding shows the read-out sectors and the grouping of the silicon strip sensors. On the right a sketch of the half module containing a total of seven sensors. Figures taken from [29]

read-out electronics and high and low voltage power supplies. Sensors are grouped into half-modules, and each module contains 7 sensors in a row. A TT layer is composed of about 30 half-modules and within the same module, sensors are grouped into two or three read-out sectors (three read-out sectors are used for central modules) as shown in Fig. 2.13 where the different read-out sectors are highlighted with different colours. Within a read-out sector, the 512 silicon strips of the different sensors are connected strip by strip through wire bonds. As particle flux increases close to the beam pipe, smaller readout sectors (i.e. shorter read-out strips) are required in the central part of the detector to achieve an appropriate hit occupancy. Therefore, the six sensors around the beam pipe are read out separately (yellow marked sensors in Fig. 2.13). Further details can be found in Refs. [30–32].

2.3.4   Inner Tracker (IT)

The Inner Tracker sub-system is located downstream the dipole magnet and it covers the inner region (where higher occupancy is expected) of the three tracking stations *T1, T2, T3*. A sketch of the IT in one of the T-Station can be found in Fig. 2.14. The Inner Tracker consists of silicon strip sensors similar to the ones used in the TT arranged in *xuvx* configuration in each T-Station. The cross-shaped arrangement of the sensors surrounding the beam-pipe is used to guarantee a low hit occupancy (2%) given the high density of tracks expected close to the beam-pipe. Indeed, the IT covers only the 2% of the LHCb acceptance but it contains 20% of the tracks produced in *pp* collisions. In each layer a total of four boxes containing active material can be distinguished: top, bottom, left and right boxes. Top and bottom boxes contain single silicon sensors, while left and right ones contain two rows of silicon sensors.
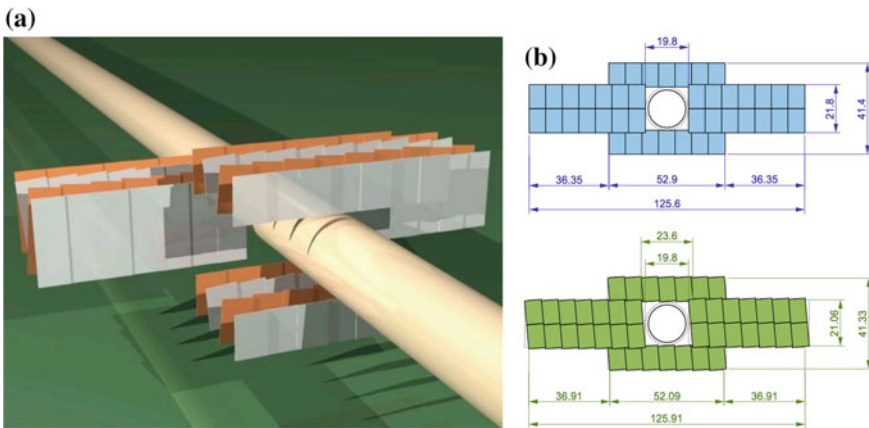
Fig. 2.14   On the left, the isometric view of the Inner Tracker sensitive elements in one of the three T-stations. On the right the layout of *x-layer* (top) and stereo layer (bottom). The lengths provided are in cm and they refer to the active area of the Inner Tracker. Figures taken from [31, 32]

The sensor dimensions are 7.6 cm × 11.0 cm × 320–410 μm[5] (width × length × thickness) containing a total of 384 silicon strips (pitch size of 196 μm) leading to a single hit position resolution of 50 μm. Both IT and TT use the same technology. They are both designed to be light and thermally insulated and a cooling system is used to keep the temperature at 5° to reduce radiation damages and ensure a low noise rate. The signal-to-noise ratio achieved in 2012 was higher than 12. More details about the Inner Tracker mechanical design can be found in Ref. [32].

2.3.5   Outer Tracker (OT)

The Outer Tracker (OT) is placed downstream of the dipole magnet. It follows the same arrangement as the Inner Tracker and it aims at covering the remaining acceptance not covered by the IT. The Outer Tracker, similarly to the Inner Tracker, is composed by three stations with four layers each in the *xuvx* configuration. The Outer Tracker is made of small straw gas drift tubes having an outer (inner) diameter of 5.0 mm (4.9 mm). Each layer of the Outer Tracker is made of a total of 18 modules symmetrically placed defining the left and right halves of the detector and each module contains a total of 128 straw-gas drift tubes. Modules are typically 5 m long and they are electrically divided in the middle (y = 0) to separate the upper and lower regions of the detector. The innermost modules are shorter than 5 m aiming at housing the Inner Tracker. Pairs of consecutive half left/right layers are mounted in the so-called C-frames which can be retracted to perform maintenance works. A sketch of the OT detector and the various layers mounted on the C-Frames is shown in Fig. 2.15 where also a front view of the full T-station *x-layer* (containing OT and IT) is shown.

Each drift tube has a pitch size of 5.25 mm and it is composed by an anode wire supplied by a high voltage potential of 1550 V. The walls of the straws tube are made of conductive material in order to collect the charge produced by the ionization of the gas induced by the traversing charged particle. The 128 straws within the module are organised into two staggered monolayers (64 + 64, relative offset along z is half the pitch) as shown in Fig. 2.16a, aiming at reducing the detector dead regions. Each straws is filled with a gas admixture of Ar/CO_2 (70% : 30%) leading to a maximal drift time of 50 ns. The drift time depends on the distance of the traversing track to the anode wire (see Fig. 2.16b) and thanks to a time to digital converter (TDC), measuring the difference of the arrival time of the ionisation clusters to the wire with respect to the LHCb bunch clock, it is possible to achieve a position resolution of 200 μm in the bending plane for traversing particles. Overall, the Outer Tracker covers a total area of 29 m² per layer and it is instrumented with a total of 53,760 read-out channels. The OT average occupancy during Run I (50 ns bunch spacing) was between 10 and 20% in the innermost detector region.

---

[5]Thicker sensors are used in left and right boxes where two rows of sensors connected in series are present.
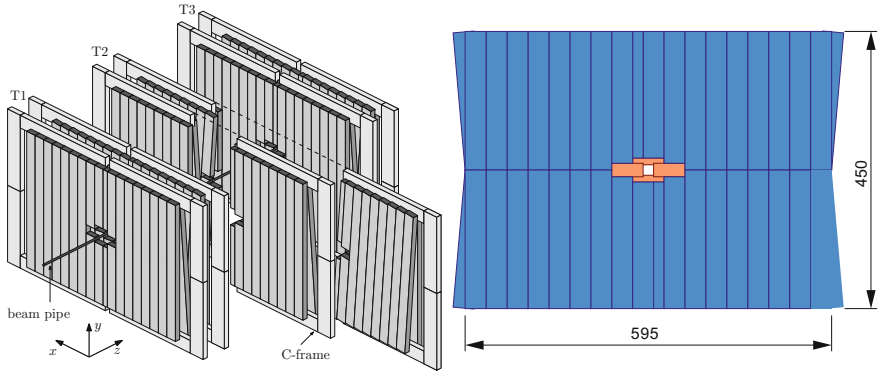
Fig. 2.15 On the left, a view of the Outer Tracker. Each station (*T1, T2, T3*) consists of four layers in the *xuvx* configuration. Consecutive Outer Tracker layers within the same station are mounted in the C-Frames as shown in the picture. In the picture *T2* C-frames are shown in the opened position to allow maintenance. The layout of a single *x-layer* is shown on the right, highlighting in orange the Inner Tracker and in blue the Outer Tracker. The dimensions are in cm and they refer to the sensitive surface of the Outer Tracker. Figures taken from [33]
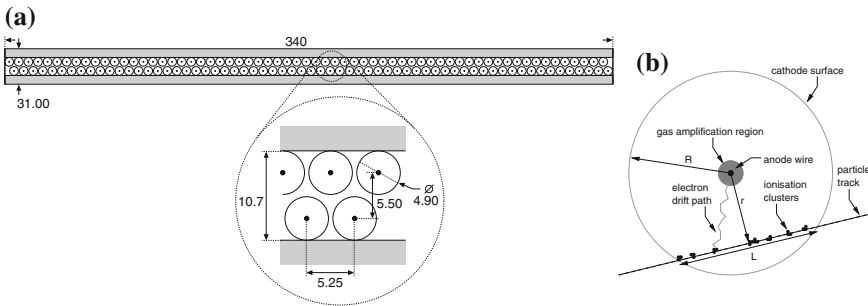
Fig. 2.16 On the left, the cross-section of an Outer Tracker module is shown. On the right the details of a single straw with a traversing particle. Figures taken from [33]

Smaller bunch spacing has an important impact on occupancy due to the drift time having tails up to 50 ns. The last aspect is important when dealing with a higher track multiplicity and it is the main reason why it will be fully replaced for the upgrade (see Sect. 3.2.1.3). Further details about the LHCb Outer Tracker can be found in Refs. [7, 33].

2.4 LHCb Particle Identification System

Particle identification in LHCb is ensured by three detectors: Ring Imaging Cherenkov detectors (RICH), called RICH1 and RICH2 (see Sect. 2.4.1), the calorimeter system (see Sect. 2.4.2) and the muon system (see Sect. 2.4.3).
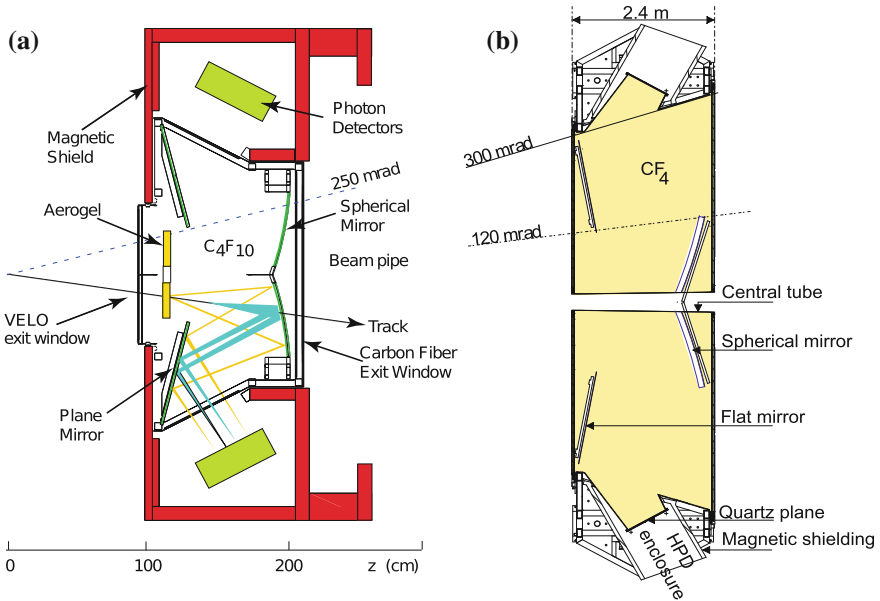
Fig. 2.17 a Side view of the RICH1 detector. The silica aerogel has been removed in Run II.
b Side view of the RICH2 detector. Figures taken from [34]

2.4.1   RICH Detectors

RICH detectors use the Cherenkov light produced by traversing particles to identify
the charged particle species. A charged particle traversing a dielectric medium (also
called radiator) with a refractive index n, with a velocity ($\beta = v/c$) higher than the
speed of light in the medium, emits photons in a cone at a specific angle (θ_C):

$$\cos \theta_C = \frac{1}{n\beta}. \tag{2.1}$$

The effect is observed only if $n \cdot \beta$ is larger than one, therefore, depending on the
medium, one could cover different ranges of β, i.e. different momentum ranges. In
LHCb two Ring Imaging CHerenkov (RICH) detectors are present (see Fig. 2.17),
one is placed upstream the dipole magnet (RICH1) and the other one (RICH2) is
placed downstream the dipole magnet (see Fig. 2.6).

The main goal of the RICH detectors is to distinguish π to K (also p, e, μ) in
different momentum ranges: p between 1 and 60 GeV/c and between 15 GeV/c and
more than 100 GeV/c thanks to RICH1 and RICH2, respectively. The different p
coverage is achieved taking advantage of different radiator materials for RICH1 and
RICH2 (see Fig. 2.18). RICH1, located between the VELO and the TT uses 85 cm
(in z direction) of C_4F_{10} with a refractive index $n = 1.0014$, optimised for particle
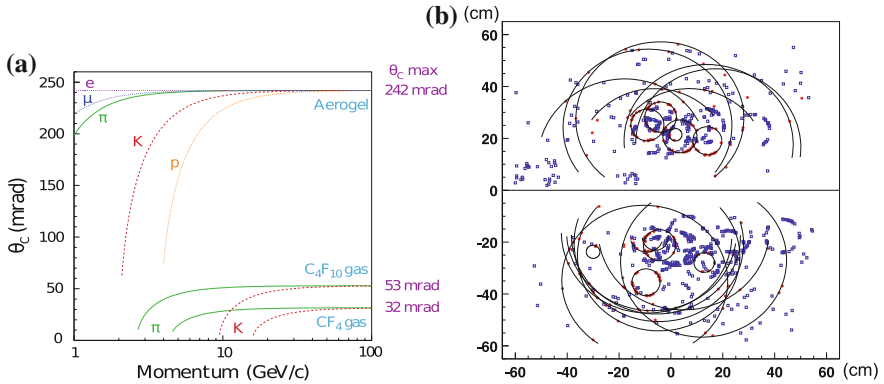
Fig. 2.18 **a** Cherenkov angle as a function of p for various charged particles and the three radiating media used in RICH1 and RICH2. The π/K separation is achieved using the combination of the different media in a wide p range. **b** Typical RICH1 event display during Run I. Rings are detected by the HPDs and reconstructed. For Run II data taking, the Aerogel has been removed from the RICH1. Figures taken from [35]

identification in the momentum range between 1 and 60 GeV/c. RICH1 emitted photons from traversing charged particles are brought outside the LHCb acceptance with a spherical and flat mirror and they are detected by a matrix of Hybrid Photon Detectors (HPDs) with a granularity of 2.5 mm × 2.5 mm aiming at detecting the reflected light cones (detected as rings at the HPDs, see Fig. 2.18). The radius of the ring (whose centre corresponds to the projected interaction point of the track with the RICH medium) is then used to infer the value of θ_C (i.e. β). The combination of β and the track momentum from the track reconstruction permits to assign a mass to the particles, i.e. identify it.

RICH2 working principle is the same as RICH1: spherical and flat mirrors are used to guide the Cherenkov light outside the LHCb acceptance and HPDs are used as well to detect the rings. The radiator material used in RICH2 is CF_4 (with about 5% of CO_2 added to quench scintillation) with a refractive index $n = 1.0005$ optimised to perform excellent particle identification in p range going from 15 GeV/c to above 100 GeV/c. The angular acceptance of RICH1 (RICH2) in the $x - z$ plane is from $\pm 25(12)$ mrad to $\pm 300(120)$ mrad while in the vertical plane ($y - z$) it goes from $\pm 25(12)$ mrad to $\pm 250(100)$ mrad. RICH1 mirrors are made of Carbon Fibre Reinforced polymer rather than glass in order to reduce material interaction and scattering (being placed before the dipole), while the RICH2 mirrors are made of glass since it is placed downstream all the LHCb tracking detectors. Furthermore, in order to reduce noise and guarantee optimal read-out in the HPDs, both RICH mirrors are surrounded by magnetic shielding. More details about RICH detectors can be found in Refs. [34, 35].

2.4.2 Calorimeter System

Photon, electron and hadron identification is achieved by the calorimeter system through the measurement of their energies. The LHCb calorimeter system is composed, in increasing z position, by a Scintillating Pad Detector (SPD), a Preshower (PS), an electromagnetic calorimeter (ECAL) and a hadronic calorimeter (HCAL). Plane scintillator tiles are used in both the SPD and the PS, while a stack of alternating slices of lead absorber and scintillators are used in the ECAL (shashlik-type layout [36, 37]). The HCAL consists of alternating tiles of iron and scintillator. In all the calorimeter sub-systems wavelength shifting fibres are used to transmit the light produced by the particles in the scintillator (from the hadronic or electromagnetic showers) to PhotoMultipliers tubes (PMT).

The PS and SPD are composed by two planes of scintillator pads separated each other by a distance of 56 mm and a 15 mm thick lead plane is placed in between them. The lead placed in between the PS and SPD corresponds to 2.5 electromagnetic interaction lengths (X_0) but only ~0.06 hadronic interaction lengths (λ_I). In such configuration, PS and SPD are used to initiate the electromagnetic shower from electrons and photons, while the hadronic shower is mainly initiated at positions downstream the electromagnetic calorimeter. The calorimeter particle identification logic is sketched in Fig. 2.19. The expected hit density varies by two orders of magnitude over the surface of the calorimeters. In order to match the performance requirements, the PS, SPD and ECAL are designed to have in the transverse plane three different sections (see Fig. 2.20) with different granularity while the HCAL, placed downstream all the other calorimeter sub-systems, is composed only by two sections. The granularity and details of the various calorimeter sub-system is provided in Table 2.1.

The sensitive area of the SPD and PS active surface is 6.6 m wide and 6.2 m high, while the ECAL (HCAL) is 7.8 (8.4) m wide and 6.3 (6.8) m high. ECAL (HCAL) is placed at 12.5 (13.33) m from the interaction point and they are designed to cover an acceptance of 300 (250) mrad in the bending (non-bending) plane matching projectively the tracking system geometry. The ECAL total length in the z direction
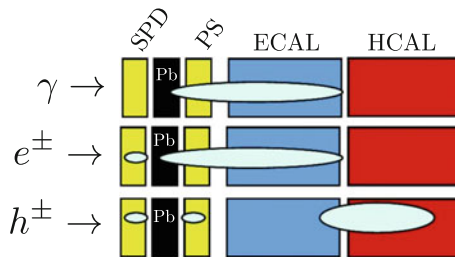
Fig. 2.19 e/γ/hadron identification with the calorimeter system of LHCb. The lead layer placed between the SPD and the PS is used to initiate the electromagnetic shower which is measured in the ECAL. The hadronic shower from hadrons is instead measured in the HCAL. Figures adapted from [38]
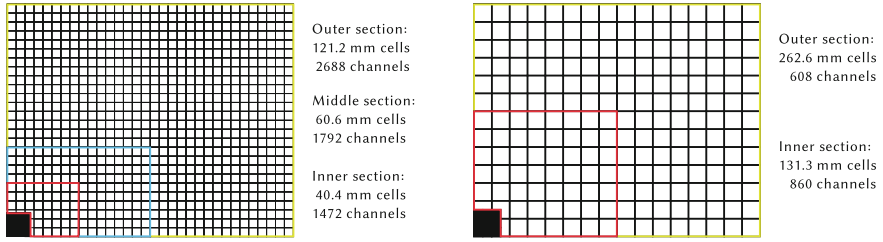
Fig. 2.20 (left) Segmentation of the SPD, PS and ECAL; (right) segmentation of the HCAL. Figures taken from [39]

Table 2.1 Calorimeter system description. Total depth of the calorimeter subsystems along z, corresponding electromagnetic (X_0) and hadronic (λ_I) interaction lengths and segmentation of the different systems are provided

	Depth in z [mm]	Interaction length $X_0 - \lambda_I$	Granularity [mm^2]		
			Inner section	Middle section	Outer section
SPD	180	2.0−0.1	40.4 × 40.4	60.6 × 60.6	121.2 × 121.2
PS	180	2.0−0.1	40.4 × 40.4	60.6 × 60.6	121.2 × 121.2
ECAL	835	25−1.1	40.4 × 40.4	60.6 × 60.6	121.2 × 121.2
HCAL	1650	none−5.6	131.3 × 131.3	None	262.6 × 262.6

is 83.5 cm and it is made of a series of alternating 2 mm thick lead layers and 4 mm thick scintillator tiles covering a total of 25 electromagnetic radiation length such that high energy photon and electrons electromagnetic shower can be fully contained. The HCAL total length in the z direction is 1.65 m.

The calorimeter system is also designed to process data for trigger purposes at 40 MHz rate. In fact, the transverse energy E_T measurement of particles interacting in the calorimeter is employed in the L0 trigger, see Sect. 2.4.5.1. During 2012 data taking, for $B_s^0 \to \phi\gamma$ analysis, where γ is reconstructed with the calorimeter, the invariant mass resolution of the B_s^0 candidates was ∼100 MeV/c^2, while the electron identification efficiency was about 90% accepting a 5% $e \to h$ mis-identification probability. Overall, the ECAL (HCAL) energy resolution corresponds to $\frac{\sigma_E}{E} = \frac{10\%}{\sqrt{E}} \oplus 1\%$ ($\frac{\sigma_E}{E} = \frac{65\%}{\sqrt{E}} \oplus 9\%$), E expressed in GeV. The reason why the HCAL resolution is worse than the ECAL one has to be found in its granularity and on the fact that the light yield in the HCAL is a factor 30 smaller than in the ECAL (the HCAL PMTs operate at higher gain).

During data taking, the calorimeter system is calibrated regularly to maintain a constant trigger rate thanks to the embedded self-calibration system equipped with a ^{137}Cs γ source. Further details on the calorimeter system at LHCb can be found in Ref. [39].

2.4.3   Muon Stations

Muon identification plays an important role in LHCb because muons are present as final states of several *CP*-violating *B* decays, such as $B^0_{(s)} \to J/\psi(\mu^+\mu^-)K^0_s$ and $B^0_s \to J/\psi(\mu^+\mu^-)\phi$. The muon system is readout at 40 MHz and signatures of high p_T muons are computed at hardware level to perform trigger decisions (L0 trigger) while the full muon identification and characterization (p_T, p, ID) is performed in the software trigger.

The LHCb muon system is composed by 5 muon stations (M1–5) located at the downstream end of the LHCb spectrometer. Each station is composed by four quadrants and each quadrant is composed in the transverse plane by four regions (R1–4) of multi-wire proportional chambers (MWPC) with increasing granularity. Exception is made for the inner region (R1) of the first station, M1, placed upstream the calorimeters where triple-GEM detectors are used due to the higher particle flux which causes faster ageing. The triple-GEM (MWPC) detector gas admixture is made of $Ar/CO_2/CF_4$ in the following proportions 45:15:40 (50:40:10). The gas admixture is chosen to allow a fast read-out and signal yield (40 MHz read-out rate) in order to gather detector information within 20 ns with a time-resolution smaller than 4.5 ns.

The muon stations layout is achieved in order to cover an angular acceptance of 306 (258) mrad in the bending (non-bending) plane in a projective way and a total of 1,380 MWPC chambers are employed covering a full active surface of 435 m^2. The station segmentation and granularity is optimised according to the particle flux. The granularity of the muon stations is higher in the x direction than the y one. The granularity and the pad dimensions are summarised in Table 2.2.

M2–M5 stations alternate MWPCs with 80 mm thick iron absorber (called Muon filter 1–4 in Fig. 2.21) such that only penetrating muons having $p > 6$ GeV/c will be able to cross all the 5 muon stations. The total thickness of the muon system and of the calorimeters correspond to 20 interaction lengths.

The binary information provided by a 5-hit coincidence in the five muon stations allows to identify the muons, while the hit positions in the stations are used to measure the p_T of muons. Indeed, high detection efficiency (>99%) is a key feature of the muon system.

The LHCb muon station layout is shown in Fig. 2.21.

Table 2.2 Logical muon pads per station and per region dimensions. Sizes are provided in terms of x-size $\times$ y-size in mm units. The listed dimensions allow to achieve in all muon stations almost uniform occupancy

Region	M1 [mm^2]	M2 [mm^2]	M3 [mm^2]	M4 [mm^2]	M5 [mm^2]
R1	10×25	6.3×31	6.7×34	29×36	31×39
R2	20×50	12.5×63	13.5×34	58×73	62×77
R3	40×100	25×125	27×34	116×145	124×155
R4	80×200	50×250	54×34	231×270	248×309
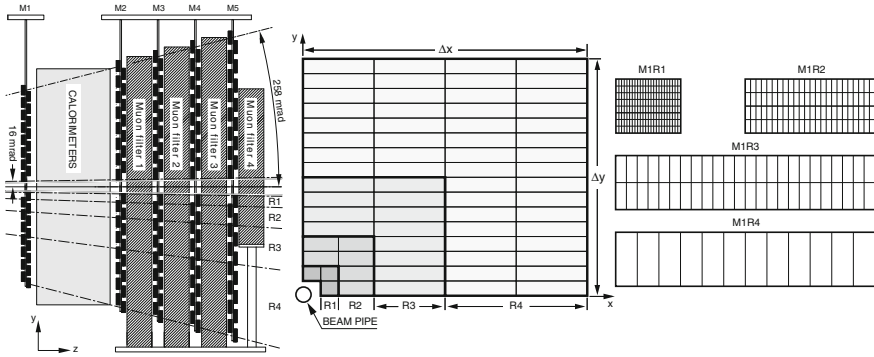
Fig. 2.21 (left) Cross section view of the muon system. (centre) Layout of one quadrant of a single muon station. Each square represents a different muon chamber region (R1–4). (right) Segmentation of the four types of regions in M1. A uniform particle flux and detector occupancy are obtained thanks to the different sizes of the muon chamber regions (R1, R2, R3, R4). The ratio of the dimensions from the inner (R1) to the outer (R4) region is 1:2:3:8. Figure taken from [40]

Muon stations provided excellent performance during 2012 data taking: muon identification efficiency was 97% for a 1–3% $\pi \to \mu$ mis-identification probability. Further details on the muon system at the LHCb experiment can be found in Refs. [40, 41].

2.4.4 Particle Identification Strategy and Performance at LHCb

Particle identification at LHCb is performed by dedicated algorithms combining information from the RICH1, RICH2, calorimeters and muon stations. Hadrons are identified thanks to the PS, SPD and HCAL and the π/K separation is obtained using the RICH's detectors. $e^{\pm}$ and γ identification is provided combining information from the ECAL, PS and SPD while μ are identified by the muon stations.

Once all the reconstructed tracks are available, their *PID* information is provided by the algorithms into a combined log-likelihood difference defined as:

$$\Delta LL = \ln \mathscr{L}(h) - \ln \mathscr{L}(t) = \ln \left(\frac{\mathscr{L}(h)}{\mathscr{L}(tr)} \right), \tag{2.2}$$

where t is the reconstructed track and h is the particle hypothesis (e/γ, K, π, p and μ). Equation (2.2) expressing the difference in log-likelihood for a given track to be compatible with a particle hypothesis.

The likelihood hypothesis is evaluated depending on the particle type and it is computed multiplying sub-detector contributions:
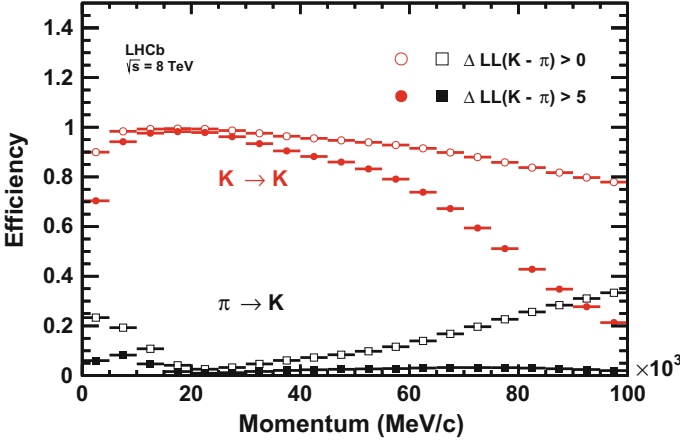
Fig. 2.22 *PID* performance for Kaon. The Kaon identification efficiency (in red, $K \to K$) and pion misidentification rate (in black $\pi \to K$) measured on 2012 data are shown as a function of track momentum. Two different *PID* selections are shown: $\Delta LL_{K/\pi} > 0$ (open markers) and $\Delta LL_{K/\pi} > 5$ (filled marker), resulting in different performances, especially at high and low momentum. Figure from [42]

$$\begin{aligned}
\mathcal{L}(K) &= \mathcal{L}^{\mathrm{RICH}}(K_{hypo}) \cdot \mathcal{L}^{\mathrm{CALO}}(!e_{hypo}) \cdot \mathcal{L}^{\mathrm{MUON}}(!\mu_{hypo}) \\
\mathcal{L}(\pi) &= \mathcal{L}^{\mathrm{RICH}}(\pi_{hypo}) \cdot \mathcal{L}^{\mathrm{CALO}}(!e_{hypo}) \cdot \mathcal{L}^{\mathrm{MUON}}(!\mu_{hypo}) \\
\mathcal{L}(\mu) &= \mathcal{L}^{\mathrm{RICH}}(\mu_{hypo}) \cdot \mathcal{L}^{\mathrm{CALO}}(!e_{hypo}) \cdot \mathcal{L}^{\mathrm{MUON}}(\mu_{hypo}),
\end{aligned} \tag{2.3}$$

where $\mathcal{L}^{\mathrm{CALO}}(!e_{hypo})$ is the likelihood from the Calorimeter system for the given particle of not being an electron. Similarly the $\mathcal{L}^{\mathrm{MUON}}(!\mu_{hypo})$ is defined as the likelihood from the Muon systems for the particle of not being a μ.

Charged hadrons *PID* variables expressing the probability of being $h = K, \pi, e$ or μ are computed with respect to the π hypothesis as follows:

$$PID(K, \pi, e, \mu) = \Delta LL_{(K,\pi,e,\mu)/\pi} = \ln\left(\frac{\mathcal{L}(K, \pi, e, \mu)}{\mathcal{L}(\pi)}\right) \tag{2.4}$$

where $\mathcal{L}(h)$ and $\mathcal{L}(\pi)$ are evaluated from (2.3) according to the $h-$hypothesis. The π/K separation performance depends on the track momentum and pseudo rapidity (η) as shown in Fig. 2.22 (only p dependence shown). The *PID* performances during Run I are excellent: for $\Delta LL_{K/\pi} > 0$ the average identification efficiency for K ($K \to K$) is measured to be 95% with an average π misidentification rate of 10%.

In order to boost the *PID* offline performances, LHCb has introduced a neural-net based *PID* variable, called *ProbNN*. This quantity is evaluated taking into account tracking, ECAL, HCAL, muon stations and RICH informations. Such variable is more powerful than the $\Delta LL_{K/\pi}$ since it takes into account correlations among the various sub-detectors and various ΔLL. The multivariate classifier is

trained on Monte Carlo events and it considers all the tracks in the events including also fakes (*ghost*). Separate networks are trained for e, μ, π, K, p and *ghosts*. Therefore, the final *PID* selections can be performed applying requirements to its $ProbNN(K, \mu, e, \pi, p, ghost)$. Two different tunings of the $ProbNN$ are available for Run I data. In the analysis presented in this thesis, both the available versions have been used: $ProbNN$V2 and $ProbNN$V3. $ProbNN$V3 adds more kinematic regions and the neural net training is obtained removing the fake tracks. Further details on the particle identification performance and strategy can be found in Refs. [42, 43].

2.4.5 LHCb Trigger System

A three stage trigger strategy is employed in LHCb. The three stage approach aims at reducing the 40 MHz input rate (the bunch crossing rate from the LHC translates into 10 MHz of visible interactions for LHCb) to 5 kHz, which is the rate at which data can be stored to disk. The trigger strategy used during Run I data taking period is schematically summarised in Fig. 2.23.

The earliest stage is the hardware trigger (L0 trigger) which takes advantage of the calorimeter system, muon system and the VELO pile-up system. The main goal of the hardware trigger is to reduce the bunch crossing rate of 40 MHz down to 1.1 MHz, which is the rate at which all the remaining sub-detectors (tracking system and RICH) can be read-out. The second and the third trigger stages are taking advantage of all the sub-detector informations and event-recording decisions are taken based on a first partial event reconstruction performed by the HLT1 trigger. HLT1 aims at reducing the 1.1 MHz input rate to 80 kHz which is the rate at which the full event reconstruction is performed. After the online reconstruction, the trigger rate is reduced to 5 kHz thanks to a set of inclusive and exclusive event selections. The final 5 kHz rate is the rate at which data are stored to disk and become available for later off-line analysis. It is important to underline that the bandwidth is configured to match the computing resources available for the experiment.

Since the HLT is a software trigger based on C++ applications, it guarantees enough flexibility to meet the experimental needs, adjusting the bandwidth according to physics priorities and avoid technological obsolescence during the lifetime of the experiment. HLT1 and HLT2 performances are evaluated on "no bias" samples, which are special events recorded without any trigger requirements. The events are then selected and reconstructed using the full offline reconstruction software. Further selections are applied according to the specific analysis.

In LHCb all measurements of the sub-detectors have a unique identifier, and these identifiers are written in a trigger report in the data stream. Those unique identifiers are used to classify the event in three non-exclusive categories:

- TOS (Trigger On Signal): a final candidate (or trigger object) is classified as TOS if the trigger objects (measurement in the detector) being associated with the signal candidate are sufficient to trigger the event (w.r.t. to that given trigger selection).

Fig. 2.23 LHCb trigger scheme during the 2012 data taking period. Figure taken from [44]
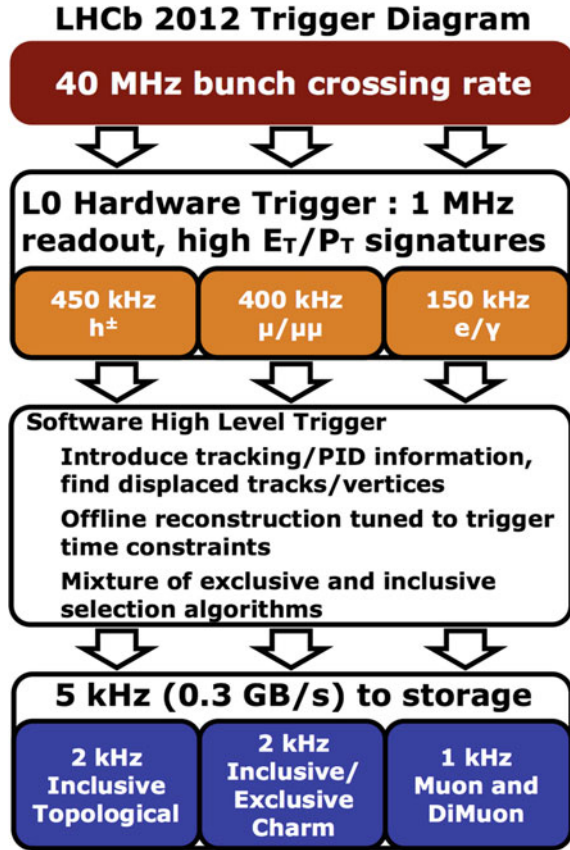
- TIS (Trigger Independent of Signal): a final candidate (or trigger object) is classified as TIS if the event could have been triggered also by objects being not associated with the signal. TIS events are triggered unbiased w.r.t. the searched signal except for correlations between the signal decay and the rest of the event.
- DEC (Trigger Decision): events which are triggered either by signal trigger (TOS) or by the trigger independent of the signal (TIS) or by a combination of the two.

Given the definition, an event or a candidate can be associated to both TIS and TOS simultaneously and this fact is used to extract the trigger efficiencies. TOS efficiencies are measured as $\epsilon_{TOS} = N^{TIS\&TOS}/N^{TIS}$ where N^{TIS} is the number of events classified as TIS and $N^{TIS\&TOS}$ is the number of events classified simultaneously as TIS and TOS.

2.4.5.1 Level 0 Trigger (L0)

Custom made electronics in the calorimeter, muon system and VELO pile-up sensors allows to perform an hardware based decision synchronously with the 40 MHz

bunch crossing clock. *B* hadrons studied by LHCb have masses larger than 5 GeV/c^2, therefore, final states will be characterized by a large p_T or E_T. In order to efficiently trigger on interesting events it would be enough to identify events which are not too busy containing at least one or pairs of high p_T or E_T final states. The former task is achieved thanks to the VELO pile-up system and SPD multiplicity measurements, while the latter is achieved by the calorimeter and muon triggers. The calorimeter trigger system reconstructs and selects the highest E_T electron, photon and hadron in the current event while the muon trigger system reconstructs the highest p_T muon (L0Muon) or the highest muon pairs p_T^{12}, where $p_T^{12} = \sqrt{p_T^{highest} \times p_T^{2^{nd} highest}}$.

In particular, the VELO pile-up system is made of the 2 *R* sensors placed upstream the interaction region. It aims at identifying events with single and multiple visible interactions. In fact, only the radial position of backward tracks and the backward tracks position extrapolation to the beam axis allows to identify primary vertices with a resolution of 3 mm. Events with more than one visible interaction can also be vetoed but such solution has never been applied because of the excellent performance of both detector hardware and trigger system in higher pile-up environment. Indeed, the LHCb original plan was to run with a pile-up level $\mu = 0.4$, but data have been recorded at $\mu = 1.6$ and no veto has been applied.

The calorimeter trigger system searches for high E_T particles where the E_T is evaluated out of the clustering algorithm, implemented in the Front-End board using FPGA devices. The algorithm builds up 2 × 2 cells calorimeter clusters and selects the one containing the highest deposit providing an information on the highest E_T particle in the event. Depending on the location among the various calorimeter elements (SPD, PS, ECAL, HCAL) the highest E_T, e, γ or hadron candidate is identified together with its measured E_T. Also the total E_T in the HCAL and the total SPD hit multiplicity of the event are computed. The SPD multiplicity is related to the charged track multiplicity in the event and it allows to remove very busy events which are not suitable for offline analysis and would imply an important slow-down of the event reconstruction in the HLT.

Muon stations informations are used to perform a stand-alone muon track reconstruction selecting in each quadrant of the muon station the highest p_T muon track or the two highest p_T muon tracks. The p_T resolution from the L0 muon trigger is ~20%. No magnetic field is expected in the muon station region, therefore a straight line search is enough to identify muon candidates. All the five muon stations are required to contain hits to build a muon candidate. Hits generating the muon candidates are firstly looked for in M3. A constraint is applied forcing the track to point towards the interaction region and under straight-line assumption other hits are looked for in M2, M4 and M5 in specific field of interest search windows. Extrapolation of hits in M2 and M3 is used to find matching ones in M1. The first two stations (M1 and M2), separated each other by the calorimeter system, provides the p_T measurement under the assumption that the track candidates originate from the interaction point.

At 40 MHz rate, the various L0 trigger informations are sent to the L0 Decision Unit which performs operations to combine them. Overlap between different decisions (logical OR) and pre-scaling is allowed and the L0 decision is sent to the Read Out Supervisor, responsible of taking the decision of accepting the event or not

Table 2.3 Different set of configuration cut values for the L0 trigger decisions during 2011 and 2012 data taking periods. For `L0DiMuon`, p_T^{12} is defined as $p_T^{12} = \sqrt{p_T^{highest} \times p_T^{2nd\,highest}}$

L0 decision	2011 Thresholds	2012 Thresholds	SPD multiplicity
`L0Muon`	$p_T > 1.48\,\text{GeV/c}$	$p_T > 1.76\,\text{GeV/c}$	<600
`L0DiMuon`	$p_T^{12} > 1.296\,\text{GeV/c}$	$p_T^{12} > 1.6\,\text{GeV/c}$	<900
`L0Hadron`	$E_T > 3.6\,\text{GeV}$	$E_T > 3.5 - 3.74\,\text{GeV}$	<600
`L0Electron`	$E_T > 2.5\,\text{GeV}$	$E_T > 2.5 - 2.86\,\text{GeV}$	<600
`L0Photon`	$E_T > 2.5\,\text{GeV}$	$E_T > 2.5 - 2.96\,\text{GeV}$	<600
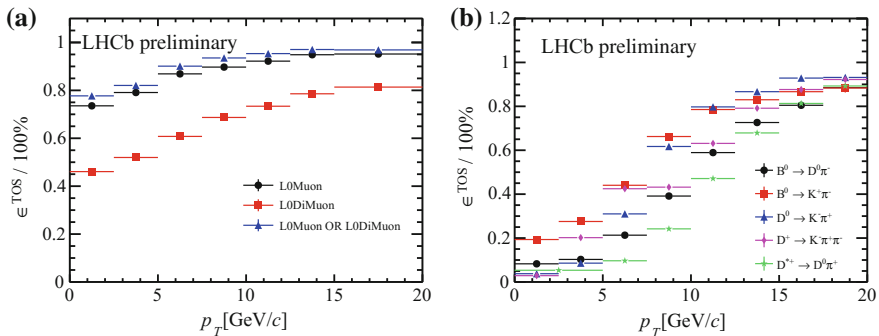
Fig. 2.24 L0 TOS efficiencies for the 2012 data taking period. **a** L0 muon TOS efficiencies evaluated for $B^\pm \to J/\psi(\to \mu^+\mu^-)K^\pm$ as a function of the B candidate p_T. **b** L0 hadron TOS efficiencies as a function of the beauty or charm candidate p_T evaluated in different decay modes. Figures taken from [45]

depending on the status of the other sub-detectors components preventing overflows. The time elapsed between a proton-proton interaction and the delivery of the L0 decision to the Front-End electronics is fixed to be $4\,\mu\text{s}$[6] resulting in solely $3.5\,\mu\text{s}$ left for the L0 data processing.

Trigger selections in the L0 are stored and can be assigned to the final B meson signal candidate. As an example, once the final B meson signal candidate is built, it is said to be `L0Hadron` TOS if the signal decay mode contains at least one reconstructed track used to make the trigger decision. Depending on the various trigger lines listed in Table 2.3, objects are recognised as hadronic, electromagnetic, muon and dimuon objects.

The L0 trigger efficiencies for data taken during 2012 are shown in Fig. 2.24 and the L0 trigger configurations for muon, dimuon, hadron, electrons and photon selection used during Run I data taking are listed in Table 2.3.

---

[6]The $4\,\mu\text{s}$ latency also includes the cable and electronic delays and the time the particle spent to travel through the full detector.

2.4.5.2   High Level Trigger I (HLT1)

A quick confirmation of the L0 trigger decision is achieved through a partial software event reconstruction (HLT1) reducing the 1.1 MHz input rate from the L0 by a factor 30. Confirmation or rejection of the L0 trigger decisions are achieved through C++ applications running asynchronously on the CPUs composing the Event Filter Farm (EFF). The time budget during Run I for an event to be processed by the HLT was 30 ms as a result of the available computing power resources for LHCb.

Generally speaking, the HLT1 strategy is to find high p_T and p tracks in the event. Therefore, it is enough at this stage that tracking algorithms reconstruct only high p and p_T tracks which in turn allows to execute a fast reconstruction sequence in HLT1, which is achieved with a dedicated tuning of the event reconstruction algorithms. The impact parameter with respect to the primary vertex (IP) for the HLT1 reconstructed tracks is measured and it is used to reject events. The tracks reconstructed by the HLT1 tracking sequence allows to identify the presence of secondary vertices in the event and events are rejected based on the vertex properties and track-pair invariant mass measurements.

A fast muon identification is performed as well, matching muon chamber hits to `Velo` tracks. The reconstruction sequence present in the HLT1 consists in the reconstruction of tracks in the VELO and the determination of the primary vertices (PV) in the event. In order to allow a fast execution of the reconstruction sequence and to fit in the timing budget available from the computing power resources, `Velo` tracks are selected based on their impact parameter and their quality and their track-segment in the T-stations is searched for to determine their momentum. Tracks traversing the full spectrometer are searched for in HLT1 through a *forward* tracking approach: `Velo` tracks are used as "seed" to find matching hits in the tracker downstream the magnet. The higher is the required momentum the smaller is the size of the search windows in T-stations, leading to a fast execution. The final decision for the event is based on the existence of at least one track satisfying p_T, p and IP requirements.

The HLT1 line used for this thesis is called `HLT1TrackAllL0` which is a generic trigger selection being executed for all events accepted by the L0 trigger. The line relies on the existence of at least one track in the event having an impact parameter with respect to every PV in the event greater than 0.1 mm and having $p_T > 1.6$ GeV/c. A similar line is used for muons (`Hlt1TrackMuon`), which selects good quality muon candidates having p_T greater than 1 GeV/c and being displaced from the PV. Dimuon candidates are also selected by requiring the corresponding invariant mass to be greater the 2.5 GeV/c^2 without any track displacement requirement or based on track displacement requirements but without any invariant mass cut.

The performances of the HLT1 most relevant trigger lines are shown in Fig. 2.25.

2.4.5.3   High Level Trigger II (HLT2)

Events surviving the HLT1 trigger decision are fully reconstructed and data are stored to disk. The full event reconstruction in the HLT2 is performed on events passing the
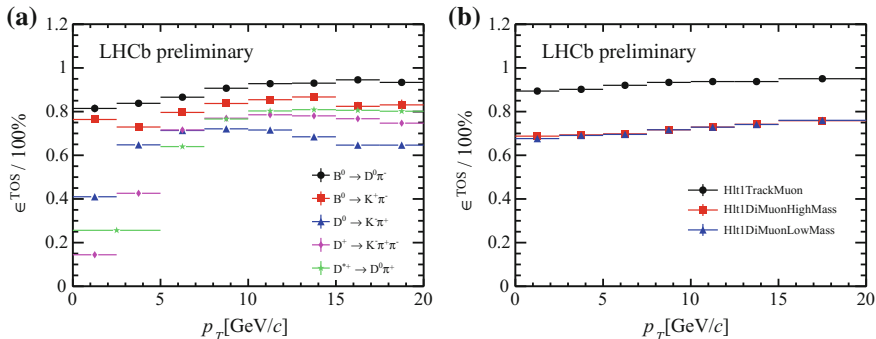
Fig. 2.25 HLT1 TOS efficiencies during 2012 data taking period. **a** shows the `Hlt1TrackAllL0` TOS performance for various channels as a function of the beauty or charm hadron p_T. **b** shows the HLT1 muon trigger lines TOS performances for the decay mode $B^+ \rightarrow J/\psi(\rightarrow \mu^+\mu^-)K^+$ as a function of the B p_T. Figures taken from [45]

HLT1 trigger, and the whole detector information is used. Exclusive decay modes or inclusive ones are selected and stored (eventually also scaled to reduce data size) by specific HLT2 trigger lines. For example, inclusive selections rely on the presence in the events of heavy displaced two-, three-, four-prongs vertices. Indeed, the HLT2 is mainly based on three topological lines aiming at covering all the possible B decays with a displaced vertex and at least two charged particles in the final state.

The inclusive nature of the trigger lines allows to achieve high efficiency for any B decays with at least two charged particles as final states, and the lines are designed to achieve excellent timing performance and background rejection. Inclusive triggers selections are not allowed to use quantities such as the B mass candidates and the agreement of B candidate reconstructed momentum direction with respect to the line joining the secondary vertex (SV, decay position of the b or c hadron) to the primary vertex (PV). An efficient trigger selection for B decays containing D mesons as intermediate state (or in general for B decays where long-lived resonances are present) should avoid cuts based on the vertices qualities, nevertheless very loose selection are applied in the trigger selection. Due to the timing budget available for HLT2, the algorithms, finding T-station segments out of VELO track input, are configured to find and search for tracks having p_T greater than 500 MeV/c and p greater than 5 GeV/c.

The HLT2 lines used in analysis of this thesis are called `HLT2Topo(2,3,4)BodyBBDT` which relies on a Bonsai Boosted Decision Tree [16]. The topological inclusive B trigger relies on the presence of a significantly displaced vertex, significantly displaced track(s) with high p_T and within the displaced vertex other extra 1, 2, 3 tracks having a high sum of p_T. Therefore, to allow the trigger to be as inclusive as possible the trigger decision is made on partially reconstructed B candidates. Details of the implementation of the topological lines can be found in Refs. [47, 48]. The most important variable employed in the Boosted Decision Tree for the topological line is the corrected mass defined as $m_{corr} = \sqrt{m + \left|p_T^{miss}\right|^2} + \left|p_T^{miss}\right|$ where
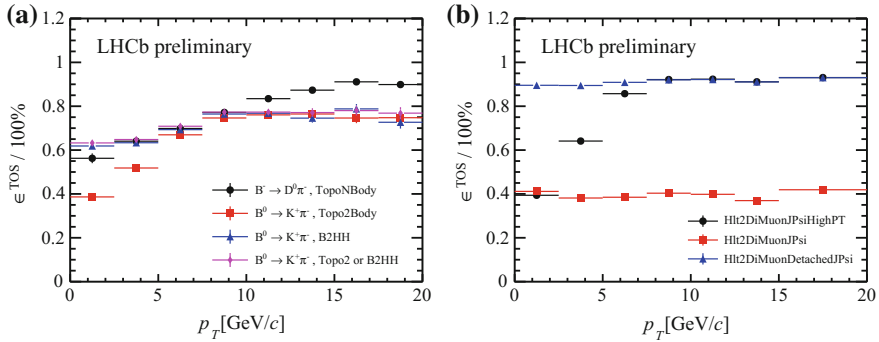
Fig. 2.26 HLT2 TOS efficiencies during 2012 data taking period. **a** shows the HLT2 topological lines trigger performance on different decay modes. Also the efficiency for the exclusive $B^0 \rightarrow K^+\pi^-$ is provided (named B2HH). **b** shows the HLT2 TOS trigger performance for the J/ψ trigger lines. Figures taken from [45]

p_T^{miss} is the missing transverse momentum to the flight direction of the B candidate and its value is obtained using the primary and secondary vertex information.

In addition to the topological lines, HLT2 contains a set of lines exploiting tracks being identified as muons by the algorithm dedicated to muon identification or as electrons using ECAL clusters. Dimuon candidates are also formed and, depending on their mass, cuts are applied on the flight distance and p_T of the dimuon candidate. Single muon candidates are accepted either requiring large p_T, or a combination of IP χ^2 and p_T cuts, where the IP χ^2 is defined as the difference in χ^2 of the PV reconstructed with and without the track under consideration. Also in this case Boosted Decision Tree based trigger selections containing muons are used. Exclusive selection lines are also used in the HLT2 requiring that all the particles of the exclusive decay are reconstructed. In the majority of the cases these lines are dedicated to exclusive channels containing muons in the final state or for prompt charm hadron production studies.

During Run I data taking the performance of the HLT2 trigger was excellent looking to different decay modes as it can be seen in Fig. 2.26. Since 2012 a deferred HLT has been implemented [49]. The goal of this deferred trigger is to use the inter-fill periods of the LHC machine to process data temporarily stored on disk allowing to increase the efficiency of the trigger and optimize the CPU resource utilization.

2.4.6 Real Time Alignment and Calibration in Run II

LHCb has introduced a novel real-time detector alignment and calibration strategy for LHC Run II which will be also employed for the upgrade phase. Data collected at the start of the fill is processed in a few minutes and used to update the alignment, while the calibration constants are evaluated for each LHC run. LHC "fill" is defined

Table 2.4 Run I and Run II timing budget comparison in the HLT resulting from a larger Event Filter Farm available in Run II

Trigger step	Output rate (Run I → Run II)	Time budget (Run I → Run II)
HLT1	(80 → 150) kHz	(20 → 35) ms/event
HLT2	(5 → 12.5) kHz	(150 → 650) ms/event

from the start of collision to the dump of the beam. LHC "Run" is a one hour data collection (up to 10–20) time interval. The procedure aims at improving the quality of the online selection and the performance stability. The required computing time constraints are met thanks to a new dedicated framework using the multi-core farm infrastructure for the trigger. During Run II, the LHCb computing power has been increased leading to a different timing budget for the different trigger steps in the HLT as summarised in Table 2.4.

The online event reconstruction in Run I was simpler and faster than the one used offline and it did not take into account of the latest alignment and calibration constants. During Run I data-taking, calibration and alignment were performed on already triggered events and data were reprocessed at the end of the year. The detector real-time alignment and calibration in Run II allows to reduce the discrepancy between offline and online selections allowing to perform direct physics analysis on the trigger output. This is achieved thanks to the so called "turbo stream" [50].

Sub-detectors alignment and calibration constants are evaluated at regular intervals, i.e., per LHC fill, per run or, in some cases, less frequently. A dedicated data sample for each sub-detector calibration and alignment task is collected with specific trigger selections from HLT1 and the updated alignment and calibration constants become available in a few minutes. If the automatic procedure finds a significant variation of the constants with respect to the ones used previously (each run has a baseline set of constants), a new run is triggered and the updated constants are used in the trigger (HLT1 and HLT2) and for further offline processing. Otherwise, the events are processed with the baseline calibration constants. Once the updated alignment and calibration constants becomes available, they are used to feed the event reconstruction in the HLT system in real-time and to update the HLT1 parameters.

2.4.6.1   Framework

Two main activities are defined: alignment and calibration. The former takes advantage from the multi-core infrastructure of the Event Filter Farm (EFF) while the latter is mainly executed on a single node of the EFF (except for the π^0 calorimeter calibration). The different activities are coordinated and guaranteed by a dedicated framework which exploits the power of the multi-core infrastructure. The central component of the framework is the analyser, performing a massive parallelized (on ~1700 nodes) track reconstruction based on the alignment constants provided by the iterator. The iterator, running on a single node, collects the analyser output and evaluates the constants for the next iteration. Depending on the task, the constants

are evaluated in different ways: minimizing a Kalman filter χ^2 calculated from the residuals of reconstructed tracks for the tracking system alignment or fitting monitoring histograms. The iterative procedure is interrupted when the variation of the χ^2 or the fit quality of the monitoring histograms are below a given threshold.

2.4.6.2 VELO, Trackers and Muon System Alignment

The tracking system alignment is evaluated for every fill. It is based on the minimization of a Kalman filter χ^2 calculated from the residual of already reconstructed tracks [51, 52]. The Kalman filter fit allows to take into account multiple scattering, energy loss and magnetic field effects and provide alignment for multiple sub-detectors at once. Moreover, mass and vertex constraints can be used to avoid global distortion of the resulting alignment constants. Each sub-detector element alignment constant is constrained, depending on the detector status, to the nominal, surveyed or previously aligned position as starting point for the iterative alignment procedure. The iterative alignment procedure aiming at providing the updated alignment constants is stopped when the χ^2 variation is below threshold. Alignment of the trackers (upstream and downstream ones) is executed every fill after the VELO alignment. The constants might change during data taking due to magnet polarity switches, thus updates of the constants are expected every few weeks. Alignment constants for the muon stations are not expected to vary in time and the alignment procedure output is only used as monitoring.

2.4.6.3 RICH Mirror Alignment

The RICH mirror alignment is executed every one or two fills and is used as monitoring. It relies on the parallelized track reconstruction and the Cherenkov rings reconstruction on the Hybrid Photon Detector (HPD) plane. Both tasks are performed by the analyser while the fit to the analyser output histograms to evaluate the alignment constants is performed by the iterator. The Cherenkov light produced by particles entering the RICH radiators is reflected by a spherical and a flat mirror to the HPD plane. The Cherenkov light cone produced is detected as a ring (with radius proportional to the Cherenkov opening angle θ_{Ch}) cantered at the reflected image of the intersection point between the incoming track and the radiator material.

In case of misalignment of mirrors, the projected reconstructed track coordinate will not correspond to the observed Cherenkov ring center. Therefore, the Cherenkov opening angle varies as a function of the azimuthal angle (ϕ) in the HPD plane. Misalignment of mirrors are encoded in the values of θ_x and θ_y which can be fitted for using $\Delta\theta_{Ch} = \theta_{Ch} - \theta_0 = \theta_x \cdot \cos\phi + \theta_y \cdot \sin\phi$, where θ_0 is the Cherenkov angle calculated from the momentum of the selected tracks of a given unambiguous PID assignment from other sub-detectors and from the refractive index of the radiator.

2.4.6.4   Online Calibration for RICH, OT and Calorimeters

The HLT1 output of the online reconstruction and monitoring histograms are used to calibrate the RICH, OT timing offset t_0 and the calorimeter systems. *PID* performance depends on the variation of the gas admixture, temperature and pressure of RICH radiators since they imply a variation of their refractive index. For each run, a fit for the difference between the reconstructed and the expected Cherenkov angle is performed and correction factors for the refractive index are extracted. The distance between the reconstructed track position and the wire position in the OT is proportional to the known drift time. Therefore a global offset of the drift time residual distribution for OT hits is used to correct the time-offset t_0 of read-out electronics with respect to the LHCb clock. The calibration is performed every run and the t_0 offset constant is updated if the observed shift is above a given threshold.

Calorimeter calibration is achieved through relative and absolute methods consisting of adjustments of the photomultipliers (PMTs) HV settings. The relative method consists of a LED monitoring system aiming at detecting ageing of PMTs and it is performed for both ECAL and HCAL. The absolute calibration method uses a reconstructed di-photon invariant mass spectrum peaking around the π^0 nominal value. Per-cell calibration coefficients are computed in order to adjust the π^0 reconstructed invariant mass to its nominal value.

2.4.7   LHCb Software Framework and Applications

The GAUDI [53] framework is used to execute the LHCb software. The LHCb software is mainly written in C++ which can be configured through Python scripts. As an example, reconstruction algorithms to be run in a reconstruction sequence can be modified, configured and re-arranged using simple Python scripts. Within the framework, several applications with specific tasks are used:

1. GAUSS: it is used for the generation and simulation of decays of interests. PYTHIA is used to generate events (*pp* collisions), the EVTGEN package is used to generate decay chains of interest and the interaction of final states particles with the material and tracks propagation in the magnetic field is achieved thanks to GEANT4.

2. BOOLE: the energy deposits in the sub-detectors are converted to a read-out output within BOOLE. It basically allows to simulate the detector response corresponding to a given detector sensitive area. The conversion of energy deposits into what would be the read-out output for a given sub-detector is usually called digitisation. In order to tune the effects of sub-detectors (read-out delays, detector inefficiencies, signal attenuation, thresholds in the read-out, electronic noise, etc.. . .) and implement a proper simulation of the sub-systems, test-beam data and real-data are used to let the simulation be as close as possible to the properties of real-data.

3. BRUNEL: it contains the event reconstruction packages. Hit level information (after digitisation) are used to reconstruct the fundamental objects to be used in physics

analysis: tracks. Particle identification algorithms are run for the reconstructed tracks and the result is written out on disk.

4. MOORE: it is the application used to run the trigger. The application is able to run the event reconstruction (BRUNEL instances on the Event Filter Farm) and store the trigger decisions. The application is used both in the computing farm and for trigger emulation on simulated events.

5. DAVINCI: it is the physics analysis software of LHCb. It combines the final states for which p, p_T, IP and *PID* algorithm output are assigned to provide a candidate for a given decay chain of interest. Several selection cuts are defined for the specific chain of interest and data are written to summary data file. This process is called Stripping. Therefore, data stripping means that all the selection lines from analysts are executed centrally and the selected candidates stored to disk such that any analyst can read directly the candidate of interest and store the relevant candidate, final state, event information to ROOT tuple.

The software framework used at LHCb during Run I and Run II is not designed to run multi-thread applications in the trigger farm. The GAUDI framework was originally designed to exploit the power of single processors rather than use more CPUs at once to execute the event reconstruction sequence. The goal of the upgrade phase of LHCb (see Chap. 3) is to convert the core framework and all the relevant applications in a thread-safe software such that the same event can be handled by the framework and the different algorithms composing the reconstruction sequence can be executed simultaneously in different CPU cores. In such a way the optimal usage of CPU resources would be achieved increasing the overall throughput of the HLT, defined as the amount of events processed per second taking into account the resources available in the Event Filter Farm.

References

1. L. Evans, P. Bryant, LHC machine. JINST **3**, S08001 (2008). https://doi.org/10.1088/1748-0221/3/08/S08001
2. C. Lefèvre, The CERN accelerator complex. Complexe des accélérateurs du CERN, Dec 2008
3. ATLAS Collaboration, G. Aad et al., The ATLAS experiment at the CERN large hadron collider. JINST **3**, S08003 (2008). https://doi.org/10.1088/1748-0221/3/08/S08003
4. CMS Collaboration, S. Chatrchyan et al., The CMS experiment at the CERN LHC. JINST **3**, S08004 (2008). https://doi.org/10.1088/1748-0221/3/08/S08004
3. ATLAS Collaboration, G. Aad et al., Observation of a new particle in the search for the Standard Model Higgs boson with the ATLAS detector at the LHC. Phys. Lett. B **716**, 1 (2012). https://doi.org/10.1016/j.physletb.2012.08.020, arXiv:1207.7214
4. CMS Collaboration, S. Chatrchyan et al., Observation of a new boson at a mass of 125 GeV with the CMS experiment at the LHC. Phys. Lett. B **716**, 30 (2012). https://doi.org/10.1016/j.physletb.2012.08.021, arXiv:1207.7235
7. LHCb Collaboration, A.A. Alves Jr. et al., The LHCb detector at the LHC. JINST **3**, S08005 (2008). https://doi.org/10.1088/1748-0221/3/08/S08005
8. ALICE Collaboration, K. Aamodt et al., The ALICE experiment at the CERN LHC. JINST **3**, S08002 (2008) https://doi.org/10.1088/1748-0221/3/08/S08002

9. TOTEM Collaboration, G. Anelli et al., The TOTEM experiment at the CERN Large Hadron Collider. JINST **3**, S08007 (2008). https://doi.org/10.1088/1748-0221/3/08/S08007

10. LHCf Collaboration, O. Adriani et al., The LHCf detector at the CERN Large Hadron Collider. JINST **3**, S08006 (2008). https://doi.org/10.1088/1748-0221/3/08/S08006

11. MoEDAL Collaboration, J. Pinfold et al., Technical design report of the MoEDAL experiment. Technical report, CERN-LHCC-2009-006, MoEDAL-TDR-001, Jun 2009

12. LHCb Collaboration, Large Hadron Collider beauty experiment public results website, http://lhcb-public.web.cern.ch/lhcb-public/

13. LHCb, R. Aaij et al., Measurement of the inelastic pp cross-section at a centre-of-mass energy of $\sqrt{s} = 7$ TeV. JHEP **02**, 129 (2015). https://doi.org/10.1007/JHEP02(2015)129, arXiv:1412.2500

15. LHCb Collaboration, R. Aaij et al., Measurement of $\sigma(pp \rightarrow b\bar{b}X)$ at $\sqrt{s} = 7$ TeV in the forward region. Phys. Lett. B **694**, 209 (2010). https://doi.org/10.1016/j.physletb.2010.10.010, arXiv:1009.2731

15. M.L. Mangano, G. Altarelli, CERN workshop on standard model physics (and more) at the LHC (2000), http://cds.cern.ch/record/425440

16. J. Nardulli, Reconstruction of two-body B decays in LHCb. Ph.D. thesis, Vrije U. Amsterdam, Amsterdam, 2007, Presented on 04 Oct 2007

17. LHCb Collaboration, For LHCb talks, Jul 2012, https://cds.cern.ch/record/1463546. General Photo

18. LHCb Collaboration, $b\bar{b}$ Production angles public plots, http://lhcb.web.cern.ch/lhcb/speakersbureau/html/bb_ProductionAngles.html. General Photo

19. R. Lindner, LHCb layout, Feb 2008, https://cds.cern.ch/record/1087860. LHCb Collection

20. BaBar, B. Aubert et al., The BaBar detector. Nucl. Instrum. Methods A479, 1 (2002). https://doi.org/10.1016/S0168-9002(01)02012-5, arXiv:hep-ex/0105044

21. A. Abashian, The Belle detector. Nucl. Instrum. Methods **A479**, 117 (2002). https://doi.org/10.1016/S0168-9002(01)02013-7

22. R. Jacobsson, Future wishes and constraints from the experiments at the LHC for the Proton-Proton programme, in *Proceedings, ICFA Mini-Workshop on Beam-Beam Effects in Hadron Colliders (BB2013): CERN, Geneva, Switzerland, 18–22 March 2013* (2014), pp. 167–176. https://doi.org/10.5170/CERN-2014-004.167, arXiv:1410.3663

23. B. Muratori, T. Pieloni, Luminosity levelling techniques for the LHC, in *Proceedings, ICFA Mini-Workshop on Beam-Beam Effects in Hadron Colliders (BB2013): CERN, Geneva, Switzerland, 18–22 March 2013* (2014), pp. 177–181. https://doi.org/10.5170/CERN-2014-004.177, arXiv:1410.5646

24. F. Follin, D. Jacquet, Implementation and experience with luminosity levelling with offset beam, in *Proceedings, ICFA Mini-Workshop on Beam-Beam Effects in Hadron Colliders (BB2013): CERN, Geneva, Switzerland, 18–22 March 2013* (2014), pp. 183–187. https://doi.org/10.5170/CERN-2014-004.183, arXiv:1410.3667

25. LHCb Collaboration, R. Aaij et al., LHCb detector performance. Int. J. Mod. Phys. A **30**(07), 1530022 (2015). https://doi.org/10.1142/S0217751X15300227, arXiv:1412.6352

26. LHCb Collaboration, VELO approved conference plots, https://lbtwiki.cern.ch/bin/view/VELO/VELOConferencePlots

27. L. Collaboration, LHCb VELO (VErtex LOcator): technical design report. Technical Design Report LHCb, CERN, Geneva, 2001

23. LHCb Collaboration, LHCb magnet: technical design report, CERN-LHCC-2000-007. LHCb-TDR-001, http://cdsweb.cern.ch/search?p=CERN-LHCC-2000-007&f=reportnumber&action_search=Search&c=LHCb+Reports

29. LHCb Collaboration, LHCb silicon tracker - material for publications, http://www.physik.unizh.ch/groups/lhcb/public/material/

30. LHCb Collaboration, LHCb reoptimized detector design and performance: technical design report, CERN-LHCC-2003-030. LHCB-TDR-009, http://cdsweb.cern.ch/search?p=CERN-LHCC-2003-030&f=reportnumber&action_search=Search&c=LHCb+Reports

31. L. Collaboration, The LHCb detector at the LHC. J. Instrum. **3**(08), S08005 (2008)

32. LHCb Collaboration, LHCb inner tracker: technical design report, CERN-LHCC-2002-029. LHCB-TDR-008, http://cdsweb.cern.ch/search?p=CERN-LHCC-2002-029&f=reportnumber&action_search=Search&c=LHCb+Reports

33. LHCb Outer Tracker Group, R. Arink et al., Performance of the LHCb outer tracker. JINST **9**(01), P01002 (2014). https://doi.org/10.1088/1748-0221/9/01/P01002, arXiv:1311.3893

34. LHCb Collaboration, LHCb RICH: technical design report, CERN-LHCC-2000-037. LHCB-TDR-003, http://cdsweb.cern.ch/search?p=CERN-LHCC-2000-037&f=reportnumber&action_search=Search&c=LHCb+Reports

35. M. Adinolfi et al., Performance of the LHCb RICH detector at the LHC. Eur. Phys. J. C **73**, 2431 (2013). https://doi.org/10.1140/epjc/s10052-013-2431-9, arXiv:1211.6759

36. G. David et al., Performance of the PHENIX EM calorimeter. IEEE Trans. Nucl. Sci. **43**, 1491 (1996). https://doi.org/10.1109/23.507090

37. J. Badier et al., Shashlik calorimeter: beam test results. Nucl. Instrum. Methods **A348**, 74 (1994). https://doi.org/10.1016/0168-9002(94)90844-3

38. A. Martin Sanchez, CP violation studies on the $B^0 \to DK^{*0}$ decays and hadronic trigger performance with the LHCb detector at CERN, CERN-THESIS-2013-311, http://cdsweb.cern.ch/search?p=CERN-THESIS-2013-311&f=reportnumber&action_search=Search&c=LHCb+Theses

39. LHCb Collaboration, LHCb calorimeters: technical design report, CERN-LHCC-2000-036. LHCB-TDR-002, http://cdsweb.cern.ch/search?p=CERN-LHCC-2000-036&f=reportnumber&action_search=Search&c=LHCb+Reports

40. LHCb Collaboration, LHCb muon system: technical design report, CERN-LHCC-2001-010. LHCB-TDR-004, http://cdsweb.cern.ch/search?p=CERN-LHCC-2001-010&f=reportnumber&action_search=Search&c=LHCb+Reports

41. LHCb Collaboration, X. Cid Vidal, Muon identification in the LHCb experiment, arXiv:1005.2585

42. LHCb RICH Group, M. Adinolfi et al., Performance of the LHCb RICH detector at the LHC, Eur. Phys. J. C **73**, 2431 (2013). https://doi.org/10.1140/epjc/s10052-013-2431-9, arXiv:1211.6759

43. A. Powell et al., Particle identification at LHCb. PoS **ICHEP2010**, 020 (2010). LHCb-PROC-2011-008, https://cdsweb.cern.ch/record/1322666?ln=en

44. LHCb Collaboration, LHCb trigger schemes webpage, https://lhcb.web.cern.ch/lhcb/speakersbureau/html/TriggerScheme.html

45. LHCb HLT Project, J. Albrecht, V.V. Gligorov, G. Raven, S. Tolk, Performance of the LHCb high level trigger in 2012. J. Phys. Conf. Ser. **513**, 012001 (2014). https://doi.org/10.1088/1742-6596/513/1/012001, arXiv:1310.8544

16. V.V. Gligorov, M. Williams, Efficient, reliable and fast high-level triggering using a bonsai boosted decision tree. JINST **8**, P02013 (2013). https://doi.org/10.1088/1748-0221/8/02/P02013, arXiv:1210.6861

47. M. Williams et al., The HLT2 topological lines. Technical report, LHCb-PUB-2011-002, CERN-LHCb-PUB-2011-002, CERN, Geneva, Jan 2011

48. V.V. Gligorov, C. Thomas, M. Williams, The HLT inclusive B triggers, Technical report, LHCb-PUB-2011-016, CERN-LHCb-PUB-2011-016, LHCb-INT-2011-030, 2011

49. M. Frank et al., Deferred high level trigger in LHCb: a boost to CPU resource utilization. J. Phys. Conf. Ser. **513**(1), 012006 (2014)

50. S. Benson, V. Gligorov, M.A. Vesterinen, J.M. Williams, The LHCb turbo stream. J. Phys. Conf. Ser. **664**(8), 082004 (2015)

51. W. Hulsbergen, The Global covariance matrix of tracks fitted with a Kalman filter and an application in detector alignment. Nucl. Instrum. Methods **A600**, 471 (2009). https://doi.org/10.1016/j.nima.2008.11.094, arXiv:0810.2241

52. J. Amoraal, Application of vertex and mass constraints in track-based alignment. Nucl. Instrum. Methods **A712**, 48 (2013). https://doi.org/10.1016/j.nima.2012.11.192, arXiv:1207.4756

53. G. Barrand et al., GAUDI - the software architecture and framework for building LHCb data processing applications, in *Proceedings, 11th International Conference on Computing in High-Energy and Nuclear Physics (CHEP 2000): Padua, Italy, 7–11 February 2000* (2000), pp. 92–95

Chapter 3
The LHCb Upgrade

The LHCb experiment key objectives are the observation of effects of NP and the study of the underlying NP phenomena. Although LHCb has been able to collect efficiently data in Run I (2011–2012) and Run II (from 2015 to 2018) measuring a wide range of processes in heavy flavour decays, it is still limited by the instantaneous luminosity levelling which implies a data rate collection of about $1\,\text{fb}^{-1}$/year. Currently, the maximum luminosity LHCb can operate at is limited by the detector rather than the capabilities of the LHC. Operating at a higher luminosity would have huge physics program benefits, reducing current uncertainties and gaining the possibility to study highly suppressed decay modes highly sensitive to NP.

Therefore, LHCb foresees a major upgrade for Run III (2020–2025) characterised by an upgrade of its sub-detectors (the whole tracking system will be replaced) and their read-out system combined to a revolutionary trigger strategy for experiments of such dimensions. The whole detector will be read-out at the collision rate and the trigger will be fully implemented in software running on a vast computing farm. The trigger decision will be based on fully reconstructed, offline-quality events. This leads to a more efficient trigger, and the most flexible trigger scheme at the LHC. These changes will allow LHCb to collect about $5\,\text{fb}^{-1}$ of data per year with an increased efficiency due to the novel trigger strategy. The LHCb upgrade key features are:

1. Detector upgrade: the whole detector will be read-out at $40\,\text{MHz}$ and detector information will be directly processed for triggering. Key components such as VELO, tracking and RICH will undergo substantial upgrades to maintain or improve the detector performances in an environment with significantly increased pile-up and track multiplicity.
2. The L0 hardware based trigger (currently reducing the input rate down to 1.1 MHz) will be completely removed and a full flexible software trigger strategy will be employed.

Physics motivation for the LHCb upgrade will be summarised in Sect. 3.1 while a review of the various sub-detector upgrades will be provided in Sect. 3.2 and the current status for the trigger strategy will be provided in Sect. 3.3.

3.1   Physics Motivation

There are several open questions in the LHC era regarding the SM: is there a fundamental reason why there are only 3 generations of particles? Is there any underlying physics determining the hierarchy of masses of SM particles and the CKM matrix structure? What is the origin of the baryon-antibaryon asymmetry in the universe? These questions can perhaps be answered taking advantage of the enormous statistics of b and c hadrons produced at the LHC. Indeed, flavour physics is a very powerful field of study to reduce the parameter space of NP. For example, *SUSY* Higgs partner particles can be constrained by some key measurements such as $B_s^0 \rightarrow \mu^+\mu^-$, the measurement of $b \rightarrow s\gamma$ transitions and $B^- \rightarrow \tau^-\nu$. Furthermore, NP is expected to affect the helicity structure of the SM processes. High statistics samples are needed to study kinematical effects and angular distributions of processes highly sensitive to the helicity structure of the SM such as the flavour changing neutral current (FCNC) modes: $B \rightarrow K^*\mu\mu$ or in general all decay modes described by $b \rightarrow sll$ transitions. Indeed, some hints of NP have been already observed with the current recorded data [1, 2].

Another key measurement of the LHCb physics program to study underlying effects of NP is the precise measurement of CKM angles among which γ is the least known. If NP particles appear at the TeV energy scale, CP-violating asymmetries (therefore the CKM unitarity condition) would become highly sensitive to them and discrepancies should appear. Nevertheless, current measurements do not show significant deviations from the SM picture, although some interesting hints, especially in $b \rightarrow sll$ transitions, are emerging. This could mean that flavour couplings of NP exhibit peculiar structures which can be exploited solely with higher precision measurements, i.e. collecting more data. The target instantaneous luminosity for the LHCb upgrade is $20 \times 10^{32}\,\mathrm{cm^{-2}s^{-1}}$, which is five times larger than the current one. LHCb upgrade improvements are not simply related to the capability of collecting higher statistics in a shorter time (scaling of precision $\propto \dfrac{1}{\sqrt{N}}$), but they also account for higher efficiencies from the fully software based trigger strategy enhancing the gain achieved solely considering the expected five times larger instantaneous luminosity.

The LHCb physics program can be divided into two main categories: the exploration and precision measurements and a brief summary highlighting the main goals of LHCb program can be found in Table 3.1. The upgraded LHCb experiment physics programme will allow to go far beyond the flavour physics studies: it will permit to perform studies in the lepton sector such as the study of lepton flavour-violating τ decays, search of $\sim 1\,\mathrm{GeV}$ Majorana neutrinos, be competitive in electroweak physics measurements and improve the uncertainties on the effective electroweak mixing angle for leptons. Concerning the electroweak physics measurement, LHCb will be able to reduce systematic uncertainties w.r.t. GPDs concerning the W boson mass measurement and it will be able to measure the forward-backward asymmetry in $Z \rightarrow ll$ decays leading to the measurement of the effective electroweak mixing

Table 3.1 Examples of the LHCb quark flavour physics goals organised in exploration and precision studies for current LHCb highlighting the current and LHCb upgrade physics programme. Table taken and modified from [3]

	Exploration	Precision studies
Current LHCb (5 fb^{-1} at the end of run II)	Measurement of $B_s \to \mu^+\mu^-$ down to SM value	Measure unitarity triangle angle γ to ~4° to permit meaningful CKM tests
	Search for mixing induced CP-violation in B_s system ($2\beta_s$) down to SM value	Search for CP violation in charm
	Look for non-SM behaviour in forward-backward asymmetry of $B^0 \to K^*\mu^+\mu^-$	
	Look for evidence of non-SM photon polarisation in exclusive $b \to s\gamma^{(*)}$	
LHCb upgrade (50 fb^{-1})	Search for $B^0 \to \mu^+\mu^-$	Measure $\mathscr{B}(B_s \to \mu^+\mu^-)$ to a precision of to ~10% of SM value
	Study other kinematical observables in $B^0 \to K^*\mu^+\mu^-$, e.g. $A_T(2)$	Measure $2\beta_s$ to precision <20% of SM value
	CP violation studies with gluonic penguins e.g. $B_s \to \phi\phi$	Measure γ to < 1° to match theoretical precision
	Measure CP-violation in B_s mixing (A^s_{fs})	Charm CP violation search below 10^{-4}
		Measure photon polarisation in exclusive $b \to s\gamma^{(*)}$ to % level

angle for leptons $(\sin^2(\theta_{eff}^{lept}))$.[1] Furthermore, LHCb will be able to search for new long lived particles, perform and continue spectroscopy studies of charmonium and bottomonium as well as perform general QCD studies concerning central exclusive production which are complementary to those performed at GPDs. Lastly but not less important, LHC is the only machine currently running able to perform measurements for B_s, B_c mesons as well as all the $b-$baryons (Ω_b, Λ_b, Σ_b, etc). Particularly relevant in such fields is the B_s time dependent CP violation.

Overall, the upgrade software trigger strategy, which will allow to run event reconstruction at collision rate, exhibits the incredible opportunity to lower the trigger thresholds to low p_T leading to a huge boost of the physics capabilities of the experiment.

---

[1] The forward region detection of $Z \to ll$, allows to determine the direction of the partons producing the Z. Indeed, the Z will follow the valence u (or d) quark direction of motion, since it is produced mostly via collision of $u(d)$-valence and $\bar{u}(\bar{d})$-sea quarks.

3.2   Detector Upgrade: Motivations and Plans

In order to fully exploit the LHC capabilities, LHCb detector optimal running conditions should try to fully benefit from the large cross-sections for $b-$ and $c-$ quark productions, be able to perform analysis in a clean environment (e.g. high signal purity and significance) and maximise as much as possible the trigger efficiencies and capabilities. These three aspects have a strong interplay among each others. For example, one could run LHCb at higher luminosities and take advantages of larger pile-up (μ, measured as the average number of visible interactions per crossing) to increase the physics yield. Nevertheless, the previous statement implies an increased background contamination as well as higher detector occupancies which lead to drop in track reconstruction efficiencies.

The studies performed in 2010 for the proposal of the LHCb upgrade were not yet accounting for the excellent performance shown by the LHCb experiment in Run I. At that time, the nominal luminosity decided for the LHCb upgrade was 10^{33} cm^{-2}s^{-1} with a pile-up of 2.5 and extrapolations were made to account for the spill-over effects of 25 ns bunch spacing, which has been reached only in Run II. At that time also the technological solutions to adopt for the detector upgrade were not yet decided as well as a trigger strategy. Nonetheless, it was already clear that to fully benefit from higher luminosities the LHCb hardware trigger would represent a serious bottleneck to perform optimal triggering of events, especially for hadronic modes. Another important aspect taken into account was the increase of the sub-detector occupancy which implies a limitation in the reconstruction efficiencies for decays where multi-hadron final states are required. In fact in a decay with n final states the final reconstruction efficiency would be proportional to ε^n, where ε is the single track reconstruction efficiency. Going from $\mu = 0.4$ to 2 the Outer Tracker occupancy rises by a factor two while for the other sub-detectors it rises by a factor 1.6. The reconstruction efficiency with the current OT at $\mu = 4$ is reduced by 36% w.r.t. $\mu = 0.4$, destroying all the possibilities to gain in physics yields from running at larger pile-up, especially for multi-hadronic final states decay modes.

The hadronic L0 trigger selection reduces the 40 MHz input rate to 1.1 MHz allowing the read out of all sub-detectors and removes almost half (depending on the number of hadronic final states) of the signal candidates. Studying the trigger yield from different decays of B mesons for different luminosities (see Fig. 3.1) shows how the L0 hardware trigger becomes increasingly inefficient for hadronic events at higher luminosities, with event yields saturating far below the luminosity target of the LHCb upgrade.

The trigger-less strategy (40 MHz read-out) for the upgrade implies a full replacement of the front-end electronics in all subsystems. The whole tracking system will be replaced by new detectors allowing a faster and more (or equally) efficient event reconstruction. Furthermore, the new detectors will be able to cope with the harsher data taking condition: a higher radiation level is expected at the nominal instantaneous luminosity of $\mathscr{L} = 2 \times 10^{33}$ cm^{-2}s^{-1} as well as a pile-up of $\nu = 7.6$, where ν is the average number of interactions per bunch crossing (different from μ which is the number of visible interaction per bunch crossing).
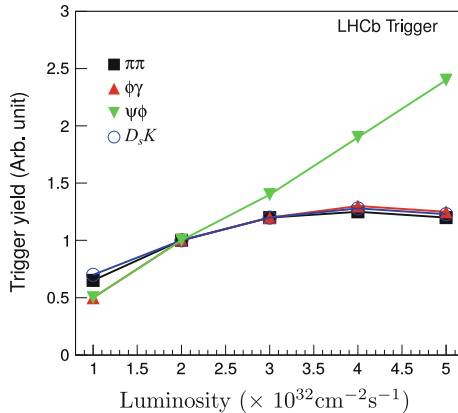
Fig. 3.1 Evaluation of the trigger yields as a function of the instantaneous luminosity at LHCb for some selected decay modes. The green triangles represents the trigger yields scaling as a function of the luminosity for the $B_s \rightarrow J/\psi\phi$ mode for which the muon L0 trigger is used. For all the other modes, the hadronic L0 trigger selection is used. It is clear that the hardware (HW) based L0 trigger for hadronic decays efficiency flattens out at higher luminosity implying an important loss in physics yield. Figure taken from [4]

The PS, SPD and M1 muon station will be removed and the HPD used in RICH will be replaced since it encapsulates the RICH read-out electronics (limited to 1.1 MHz readout). The removal of the aerogel radiator (removed for Run II) allows for a change in the RICH1 optics, improving the Cherenkov angle resolution and reducing the occupancy. A more detailed description of the changes in the sub-detectors are described in the following sections (Sect. 3.2.1 for the tracking detectors and Sect. 3.2.2 for the particle identification ones).

3.2.1 Tracking System Upgrade

The entire tracking system will be substituted for the LHCb upgrade. The current VELO will be replaced and the new hybrid pixel sensors will get to a distance of 5.1 mm from the beam-pipe. An overview of the VELO upgrade is provided in Sect. 3.2.1.1. Both the trackers upstream and downstream of the magnet will be also substituted. The TT will be replaced by four layers of silicon detectors. To cope with the higher occupancy the detector will have higher granularity and cover a larger acceptance in the central region with respect to the current TT. The Inner Tracker and Outer tracker will be removed and a new Scintillating Fibre Tracker (SciFi) will be installed. The SciFi is a homogeneous detector (contrary to IT and OT) made of scintillating fibers read out by silicon photomultipliers outside the LHCb acceptance. The LHCb upgrade tracking system is designed to achieve high tracking performance, to be read out at 40 MHz and allow a simpler and faster track reconstruction.

3.2.1.1   VELO Upgrade

The entire VELO will be replaced to cope with the expected higher detector signal output rate, the exposition to higher luminosity and to be able to operate for the lifetime of the upgraded detector (at least $50\,fb^{-1}$).

The upgraded VELO (VELOPix) will be composed by two retractable halves (as for the current VELO) which in nominal running conditions will place the VELOPix sensor at only 5.1 mm from the beam-pipe (compared to the 8.2 mm for the current VELO). The VELO modules will be replaced by a total of 26 modules oriented perpendicularly to the beam axis and housing pixels sensors. A sketch of the VELOPix layout is shown in Figs. 3.2 and 3.3, a summary of fundamental features and the comparison of the requirements between the VELO and the upgraded VELO are given in Table 3.2.

Sensors and readout chips are cooled at $-20\,^{\circ}C$ using a CO_2 coolant via a microchannel silicon substrate. The cooling is needed due to the heating of the VELOPix chips. The layout of the sensors and the cooling system on the VELOPix module is shown in Fig. 4.15a. A custom readout chip, called VeloPix ASIC [5] will be used for the LHCb VELO upgrade, designed and developed to provide the required readout performance and radiation hardness. The chip is composed by a matrix of 256×256 pixels and the pixel size is $55\,\mu m \times 55\,\mu m$. For each pixel a binary hit information is provided to allow a high data rate output.

The pattern recognition algorithm using the upgraded VELO runs directly over raw data where a mapping of binary information to the (x, y, z) position is performed without intermediate clustering and data packing of the pixel hits. The expected performances of the VELO upgrade are shown in Fig. 3.4 and compared to the current VELO, running at the upgrade conditions. It can be clearly seen that the upgraded VELO outperforms the current one thanks to the closer position to the beam-pipe, the lower material budget and the higher angular coverage of the modules. More details on the LHCb upgrade VELO detector can be found in Ref. [6].
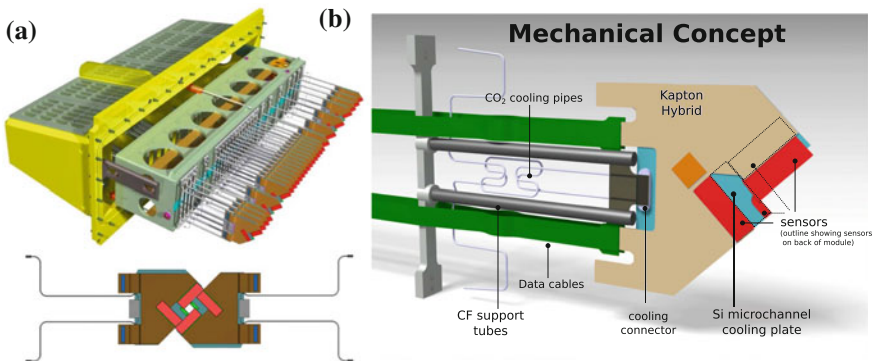
Fig. 3.2 **a**-top Sketch of one half of the VELO upgrade detector. A total of 26 modules are aligned along the beam direction. **a**-bottom Zoom of two modules in the "velo-closed" configuration. In red- the "L-shaped" pixel sensors. **b** 3D model of the mechanical design of a VELO upgrade module
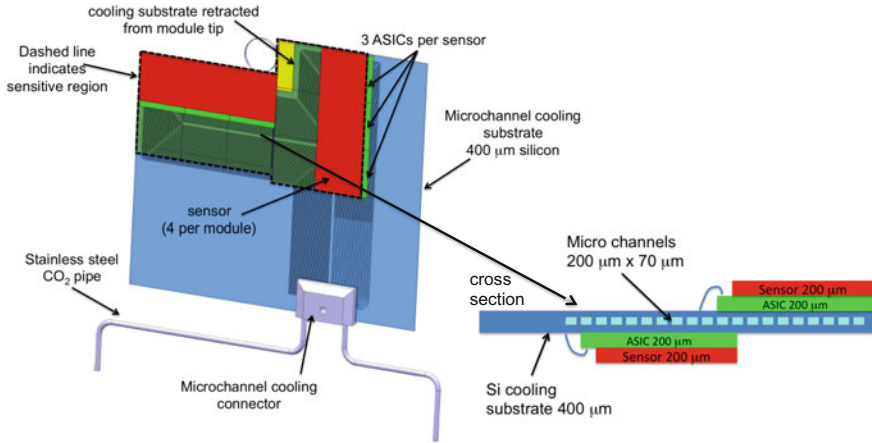
Fig. 3.3 Sketch of the microchannel cooling system for the LHCb VELO upgrade modules. Sensors are placed on both sides with respect to the microchannel cooling substrate and their projective position overlaps to reduce the dead regions and increase the VELO geometrical acceptance

Table 3.2 Summary of the major differences between the current VELO and the VELOPix

Feature	Current VELO	Upgraded VELO
Sensor type	R and ϕ strips	Pixels
Sensors/module	2048 strips	4 x 256×256 pixels
# of modules	42	52
Detector active area	0.22 m^2	0.12 m^2
	~172k strips	~41M pixels
Technology	Electron collecting	Electron collecting
	300 µm thick	200 µm thick
Max fluence	3.9×10^{14}	8×10^{15}
	MeV $\cdot$ n$_{eq}$/cm^{-2}	MeV $\cdot$ n$_{eq}$/cm^{-2}
HV tolerance	500 V	1000 V
ASIC readout rate	1 MHz	40 MHz
Total data rate	~150 Gb/s	1.2 Tb/s
Total power consumption	~1 kW	2.2–2.3 kW

3.2.1.2 Upstream Tracker Upgrade

The current Tracker Turicensis (see Sect. 2.3.3) will be replaced by the Upstream Tracker [7] (UT). The tracker is positioned upstream the dipole magnet at 2.27 to 2.70 m from the interaction region and it is composed by four layers in the *x-u-v-x* configuration. The technology used for the UT will be the same as the current silicon tracker, i.e. silicon strip sensors. The main modifications to the current tracker consist on the following points:
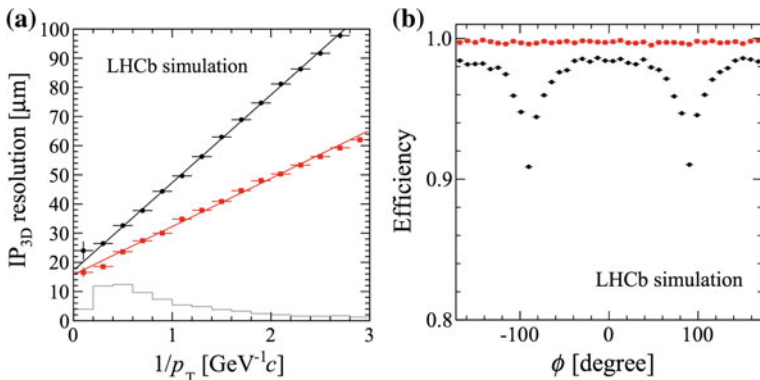
Fig. 3.4 Performance comparison between the upgraded VELO (red) and the current VELO at the upgrade running condition (black). **a** shows the 3D impact parameter (IP) resolution as a function of the inverse p_T of tracks. The gray distribution shows the distribution of $b-$ hadrons daughters in arbitrary units. **b** shows the track reconstruction efficiency as a function of the azimuthal angle for a sample of simulated $B^0 \rightarrow K^{*0}\mu^+\mu^-$ at the upgrade running condition

- Finer granularity to cope with increased particle density.
- Larger geometrical acceptance at small polar angles, to allow faster and more efficient track reconstruction at 40 MHz (innermost cut-out at 34 mm from the beam-pipe).
- Signal processing and digitization performed in proximity of the sensors at 40 MHz rate.
- Improved radiation hardness for at least $50\,\text{fb}^{-1}$ data collection.
- Reduced thickness leading to a reduced budged material ($<5\%\ X_0$).

The main goal of the UT is to provide a fast estimation of p and p_T for tracks with only VELO and UT reconstructed track segments. The fast estimation is used in the software trigger to tighten the search windows for hits in the tracker downstream of the magnet, leading to a large speed-up of the tracking reconstruction sequence. The UT is also used to reconstruct the decay products of long-lived particles such as K_s^0 and Λ^0, which often decay outside the VELO. The UT also provides approximate momentum measurements for very low momentum tracks bent outside the LHCb acceptance by the dipole which cannot be reconstructed downstream of the magnet. The design of the UT tracker is shown in Fig. 3.5. The expected radiation dose in the innermost part of the detector after an integrated luminosity of $50\,\text{fb}^{-1}$ is around 35 Mrad. Indeed, the hit density (ρ_{hit}^{UT}) is expected to be $\rho_{hit}^{UT}(r) = 3.832 \cdot r^{-1.684}$ hits/event· cm^2, leading to a radiation dose decreasing by a factor 10 at a radial distance (r) greater than 15 cm.

The vertical column structure, called "stave", of the current TT will be kept for the UT. The stave is designed to provide the mechanical support and the cooling for the front-end electronics and the sensors. The layout of the UT is the same as for the TT, i.e. four layers in the *x-u-v-x* configuration to provide a full LHCb
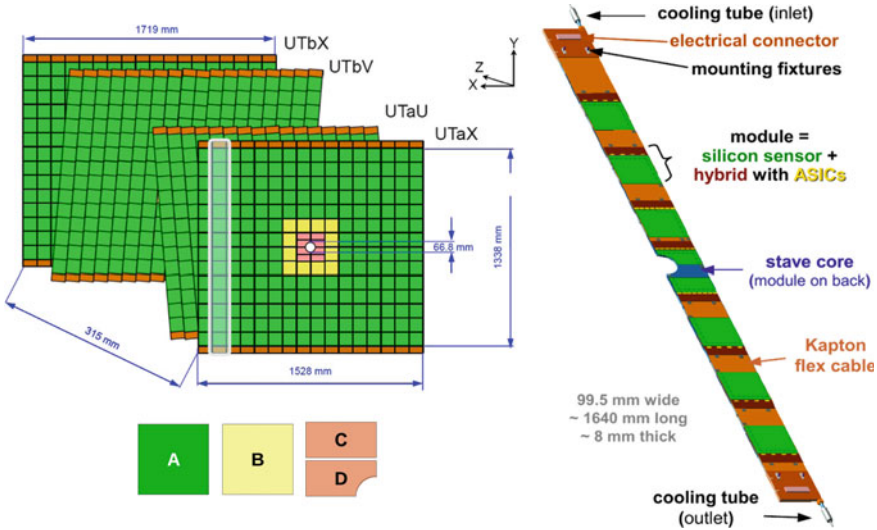
Fig. 3.5 On the left the layout of the UT tracker for the LHCb upgrade with an exploded view of the "stave" containing the UT modules. Different type of modules of different geometry and granularity will be used for the UT (A, B, C, D in the picture)

acceptance coverage. Four types of silicon micro-strip sensors with different read-out strip geometries will be used in each detection layers (named A, B, C and D in Fig. 3.5):

- Type A: they are the majority and they cover the larger active area. They are made of 10 cm long readout strip with strip pitch size of 190 μm.
- Type B: as Type A they are made of 10 cm long readout strip but the strip pitch size is 95 μm. They are placed closer to the beam-pipe.
- Type C: they are the innermost ones and they consist of 5 cm long readout strips with a pitch size of 95 μm.
- Type D: they are shaped with a quadrantal cutout to maximise the coverage in the innermost region. The readout strips are the same as Type C.

All sensors are designed to have 320 μm thickness which is smaller than the current TT. The expected hit resolution for the UT is 50 μm and no better precision is required since the momentum resolution is completely dominated by multiple scattering. The main goal of the UT is to allow a fast and efficient track reconstruction at the 40 MHz collision rate. Simulation studies indicate that using solely the VELO and UT information improves the p_T resolution and reduces the fake track rate compared to the current VELO +TT system. This leads to a large speed up of the track reconstruction: `VeloUT` track segments allow to precisely predict the position of hits in the SciFi reducing the size of the corresponding search window leading to a faster execution of the track reconstruction sequence.

3.2.1.3   Downstream Tracker: Sci-Fi

The current tracker placed downstream of the magnet (IT+OT) will be fully replaced by a homogeneous tracker using as active material 2.5 m long multi cladding wavelength shifting scintillating fibers read out by radiation-hard Silicon Photomultipliers (*SiPM*) outside the LHCb acceptance, cooled down to $-40\,°C$. The harsher radiation environment also leads to an increased neutron fluence which is very dangerous for the *SiPM* ageing. The main contribution to the neutron fluence at the *SiPM* location comes from backsplash event in the calorimeter and to mitigate the impact of neutron irradiation, neutron shielding material will be installed in front of the calorimeter. The chosen material is polyethylene plus a 5% of boron plus additional plates to ensure fire resistance leading to a reduction of fluence by a factor 3.

The current downstream tracker layout will be kept, i.e. a total of three stations with four layers each in *x-u-v-x* configuration will be used as well as the retractable C-frames. The current OT at the LHCb upgrade running condition would experience a too high occupancy leading to a 20–30% drop in tracking efficiencies, hence the necessity of a replacement. The larger occupancy in the OT can be understood taking into account the straw tubes drift time together with the 25 ns bunch spacing and the higher particle flux expected in the T-stations.

The *Scintillating Fiber Tracker* key features are:

- It uses a single technology with high granularity ($250\,\mu m$ fibers diameter).
- The readout electronics is placed outside the LHCb acceptance and is fast.
- A uniform position resolution of $100\,\mu m$ will be achieved.
- It will limit the active material to less than $1\% X_0$ per detection layer.
- High hit detection efficiency is required to be greater than 99%.

The *Scintillating Fiber Tracker* will be described in more details in Sect. 4.2 and further details can also be found in [7].

3.2.2   Particle Identification System Upgrade

The role of particle identification is crucial in achieving the physics goals of the upgraded LHCb experiment. The calorimeters and muon system will continue to be essential in triggering and the RICH will be employed for the final trigger decision before storing data to disk. Indeed particle identification (*PID*) is an important component of the current and upgrade software trigger to perform the final trigger decision. A series of partial upgrades of the current particle identification subsystems are planned for the upgrade to avoid degradation of the *PID* performances at the upgrade running conditions.

3.2.2.1   RICH Upgrade

Both RICH detectors basic layout will be kept for the upgrade. Two major changes are planned:

1. The harsher running condition will lead to a prohibitive peak occupancy (35%) in RICH1. The optical system will be improved to fight the higher occupancy through the replacement of the spherical mirrors with new ones having a larger radius of curvature (from 2710 to 3650 mm) leading to an increased focal length. Also the flat mirrors (made of glass) will be replaced with new ones of higher reflectivity for RICH1 and the whole optical layout will be modified taking into account mechanical constraints. A comparison of the optics for the current RICH1 and the upgraded one is shown in Fig. 3.6.
2. Full replacement of the Hybrid Photon Detectors (HPD) which are currently encapsulating the 1 MHz read-out electronics with Multi Anode PMTs (MaPMT) with external read-out at 40 MHz.

The new RICH readout will be composed by 8×8 pixels MaPMTs distributed over an active area of 23×23 mm^2 or over an active area of 48.5×48.5 mm^2. The former will be employed in the whole RICH1 and the inner region of RICH2, while the latter will be used only in the outer region of the RICH2 where a lower occupancy is expected (thus a lower granularity is required). A time-of-flight detector is proposed to be installed for a potential further upgrade, anticipated to take place several years after the first upgrade. Such a detector would improve particle identification capabilities for particles having a momenta between 1–10 GeV/c. Such detector is currently under development [9]. In absence of such detector a veto requirement will be used for *PID* taking into account the p measured and the thresholds for which particles would have produced Cherenkov light, i.e. if the tracks in the gas radiator of RICH1 is below the kaon threshold of 9.3 GeV/c, any signal produced will assign to those tracks the pion hypothesis.
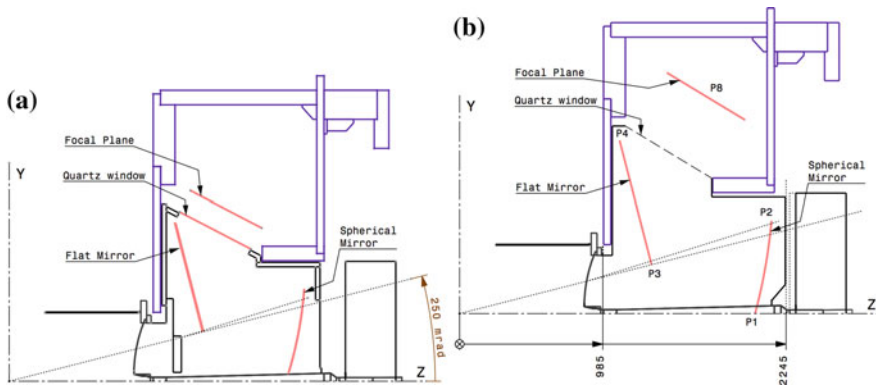
Fig. 3.6 RICH1 optical geometries. **a** is the optics of the current RICH1, **b** the one that will be used for the upgrade. Figures taken from [8]

The external front-end electronics and digital boards are developed to have a channel by channel configurable gain and discriminator threshold, have a low power consumption, be fast and to cope with the expected radiation damages after $50\,\text{fb}^{-1}$. Photon counting will be provided by a custom made ASIC named CLARO [10]. Overall, simulation studies indicate that the expected *PID* performance of the upgraded RICH detectors will allow better *PID* performance than the current detector at the harsher upgrade data taking conditions. More details on the RICH upgrade can be found in Refs. [8, 11].

3.2.2.2 Calorimeter Upgrade

The instantaneous luminosity expected for the upgrade does not require a complete rebuilding of the calorimeter system. The current ECAL and HCAL will be kept as they are except for the read-out electronics which will be fully substituted. Both calorimeters granularity do not show critical issues for the upgrade running conditions and neither do their photomultipliers and HV system. The PS, SPD and the lead converter in between are used mainly for particle identification in L0 trigger decisions for e, γ and hadrons and they will be completely removed. Indeed, the e and γ *PID* becomes too difficult because of the large pile-up (around 10% drop in *PID* performance).

A critical aspect of the calorimeter system at LHCb is the ageing of the PMTs. Indeed, already at the current instantaneous luminosity of $2{\cdot}10^{32}\ \text{cm}^{-2}\text{s}^{-1}$ the high dark current leads to important gain degradation caused by the ageing of the dynode system. To avoid fast ageing, the PMT gain is expected to be reduced by a factor of 5 and the new Front End (FE) boards will implement a preamplifier system with higher gain. The readout of the HCAL and ECAL will be substituted to cope with 40 MHz read-out. Further details on the electronics for the LHCb calorimeter upgrade can be found in Ref. [12]. Ageing studies of the calorimeter system have shown that some modules of the central region of the calorimeter system will need regular replacement during data taking to avoid large degradation of performance due to radiation damage.

3.2.2.3 Muon System Upgrade

The muon system upgrade aims at high reconstruction and identification efficiencies for muons while keeping the $\pi/K/\mu$ misidentification as low as possible. It turns out that the current muon detector exceeds the performance specification requirements, therefore only a few changes are planned for the upgrade:

- The M1 station (the one made of triple-GEM detectors placed upstream the calorimeters) will be removed as its main purpose was its use in the L0 trigger.
- The readout electronics will be substituted to cope with 40 MHz readout and will use a new GigaBitTransfer (GBT) based communication protocol.

- In front of the M2 station additional shielding around the beam pipe will be installed to reduce the amount of background hits and the larger occupancy expected due to the showers in the material close the beam-pipe.

Further details on the muon system upgrade can be found in Ref. [8].

3.2.3   Upgrade Readout and Online

To allow a trigger-less read-out and software event processing, collision events will be recorded and transmitted from the sub-detector's Front-End (FE) electronics to the readout network at 40 MHz. Thus, a multi-Tb/s network is required to provide the fundamental inputs to the software applications performing the trigger decisions. The final output rate of data is expected to be 20 kHz (nominal value). Given that a typical event has a size of 100 kB, the final rate to store on disk is expected to be around 2 GB/s [13]. Nevertheless the expected rate is 2 GB/s, a system able to handle 4 GB/s is required to be able to write and at the same time read the data for checks and copy data to the Grid. Those capacities can be easily acquired at moderate costs already now. Technically, also a system capable to handle 10 GB/s case poses no problem assuming the usage of 10 GB technology for the LAN connection between the LHCb online system and the storage area.

A comparison between the current and the upgrade readout architectures is shown in Fig. 3.7. Each sub-detector will be equipped with trigger-less Front-End (FE) electronics, compressing and transmitting the data packets to the Back-End (BE) electronics. Data compression and transmission will have to happen directly on the FE electronics. Reduced amounts of data links are a critical aspect and each sub-detector FE is required to use the data bandwidth in the most efficient way. The new FE electronics of each sub detector must then implement data compression and packing algorithms to meet the requirements. The LHC clock information, fast commands such as reset and synchronization commands as well as slow control (i.e. the non time-critical setup and monitoring controls) will be transmitted to the FE using the same optical links for the data output. This will be possible thanks to radiation hard bi-directional optical links and the GigaBit Transceiver chipset (GBT) [14], developed at CERN.

The current baseline for the read-out BE uses of a very compact, high density FPGA-based boards able to handle a throughput of more than 0.5 Tb/s. As an example, the FPGA-based readout board for the SciFi will be responsible for performing the clustering, producing encoded clusters. Those encoded clusters are then required to fit in a definite amount of bits to match the bandwidth requirements of the Gigabit Ethernet links, used to connect the BE electronics to the processing farm (where HLT applications will run). It is therefore crucial to identify the key information to send to the HLT to perform efficient event reconstruction.

Although the final goal is to remove entirely the hardware based trigger, a similar version will be also maintained to allow an optimal staging for the installation of
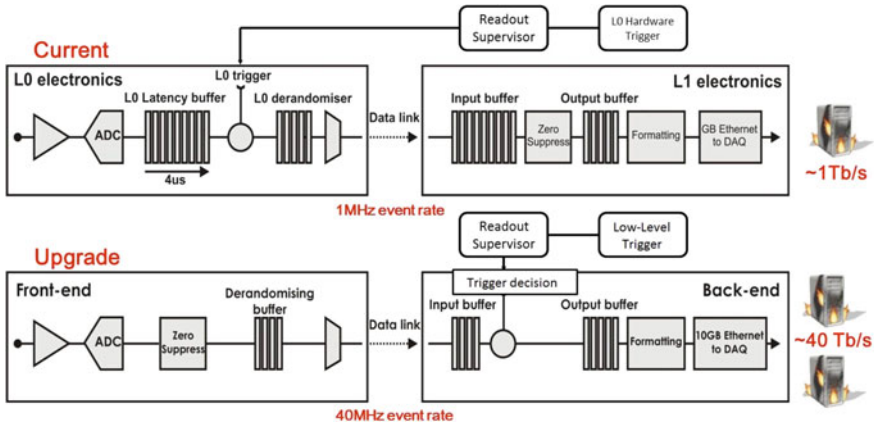
Fig. 3.7 Current (top) and Upgrade (bottom) read-out architecture comparison. Figure taken from [15]

the processing farm. This is commonly called Low-Level-Trigger (LLT) and it will be used to tune the readout rate between the current 1 MHz and the maximum of 40 MHz. Further details on the upgrade readout architecture for the LHCb upgrade can be found in Refs. [13, 16].

3.3 Trigger for the Upgrade

Three main concepts will be employed for the LHCb upgrade trigger:

- Trigger-less readout at 40 MHz of the full detector.
- Full software trigger, i.e., event reconstruction algorithms will run at the collision rate.
- Real-time alignment and calibration of the detector. This concept has been already implemented for the Run II data taking and its working principle will be briefly described in Sect. 2.4.6.

At the upgrade running conditions a pile-up level of $\mu = 5.2$ ($\nu = 7.6$) is expected. Therefore, a much larger fraction of events will contain interesting signals for the LHCb physics program. This means that the trigger strategy for the upgrade should be able, apart from removing useless events, to categorise efficiently the interesting events according to the physics requirements. In order to perform such a task much more information with respect to the ones provided by the low-latency hardware based solutions are needed before taking a trigger decision. The expected output rate to offline storage of interesting events, assuming a 100% trigger efficiency and moderate p_T and vertex displacement requirements, is divided as follows: 27 GB/s for beauty hadrons, 80 GB/s for charm and 27 GB/s for light, long-lived particles.
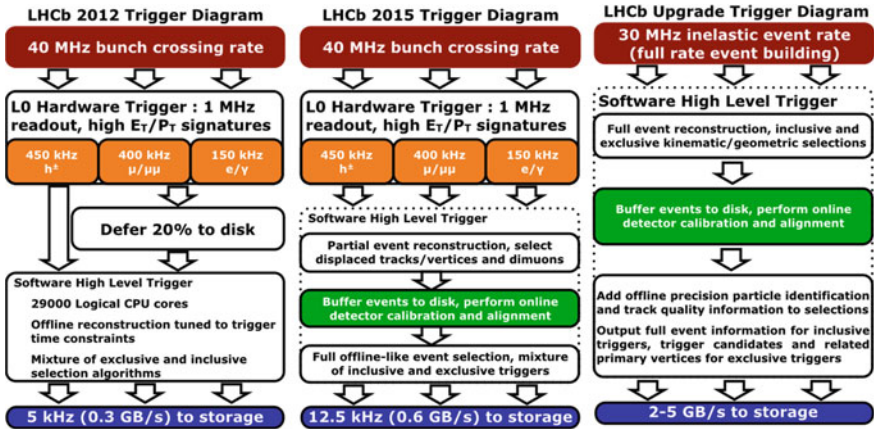
Fig. 3.8 Diagrams of the LHCb trigger data-flow in Run I (left), Run II (center) and the one foreseen for Run III (right)

For Run I, HLT event reconstruction algorithms were running on the Event Filter Farm (EFF) made of ∼29,000 CPU cores. The computing power has been increased for Run II to allow the real-time alignment and calibration tasks. HLT1 triggered events provide the inputs needed for the calibration and alignment tasks. Once these tasks are completed, the updated alignment and calibration constants are used in HLT1 and for the HLT2. Meanwhile the alignment and calibration tasks are executed, events are staged for further processing once the constants become available.

The real time detector alignment and calibration allow to perform offline quality particle identification and align the offline reconstruction (slower) performance to the online (faster) one. Therefore, offline data calibration is no longer needed and physics analysis can be performed directly using data coming from the trigger output. Another advantage of such a strategy is the capability to store on disk pre-scaled high statistics signal modes and remove useless information saving a huge amount of space on disk (almost 90% saved in Run II). The strategy has been employed successfully in Run II data taking (maintaining also the offline one) as proof of principle and it will be completely adopted for the upgrade. A full comparison of the trigger strategies adopted during Run I, Run II and the expected one for the upgrade is shown in Fig. 3.8.

Concerning the upgrade trigger, the tracking strategy has been redesigned to take advantage of the detector real time alignment and calibration strategy adopted in Run II described in Sect. 2.4.6. Therefore, a simplified and fast track reconstruction sequence has been put in place matching the timing requirements (estimated at the Trigger Technical Design Report time), efficiently selecting interesting events and providing the necessary inputs for the real time alignment and calibration.

The main steps for the online tracking sequence in LHCb's 2020 HLT trigger [13] are summarized in Fig. 3.9. The main track reconstruction steps are:
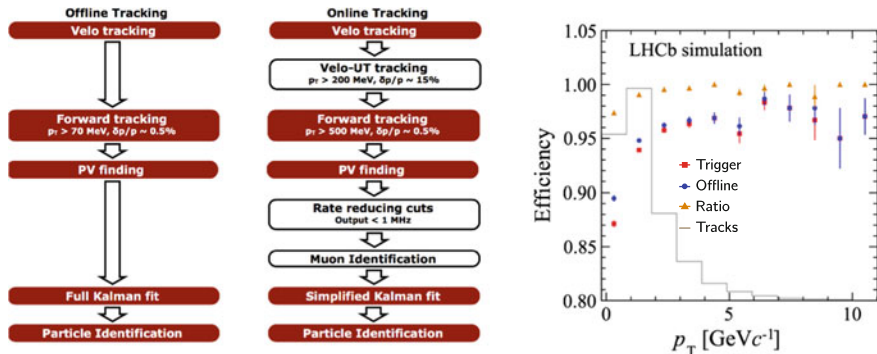
Fig. 3.9 Online and offline tracking sequence comparison for the LHCb upgrade trigger (left). Online and offline tracking performance comparison as a function of the transverse momentum p_T of tracks (right). On the right also the transverse momentum distribution of tracks (in arbitrary scale) in typical LHCb events is shown (gray line)

1. Segments in the VELO are looked for.
2. Each VELO segment is matched with a list of hits in the upstream tracker producing the so called VELO-UT tracks.
3. VELO-UT segments and their momentum and charge estimation are used to look for matching segments in the SciFi in reduced field of interest search windows.
4. PV finding: using the reconstructed tracks, primary vertices (PVs) are searched for.

The timing of the reconstruction sequence for the LHCb upgrade is a critical aspect to take into account for several reasons:

- Depending on the computing resources that can be purchased, timing constraints might impose a loss in physics performance and introduce limitations on the physics program.
- A fast reconstruction software allows to consider the presence of additional, dedicated reconstruction algorithms which could allow to further expand the LHCb physics program.
- Fast and efficient reconstruction software is mandatory for a successful LHCb upgrade. The two aspects are strongly correlated and improvements on both at the same time are usually achieved through the implementation of smarter reconstruction strategies, constant improvement of reconstruction software and exploit the potentiality of using dedicated hardware architectures.

For the trigger Technical Design Report (TDR), the maximal total timing budget for event reconstruction on a single CPU node was estimated from an extrapolation taking into account the growth of computing power before the final purchase of the nodes. The estimated timing budget was $t = 13$ ms/event. This number was obtained using the following formula:

$$t = \frac{g^y \times n \times N}{R},\tag{3.1}$$

where R is the bunch crossing rate with visible interactions (30 MHz), n is the amount of processes per node which can be run, N is the number of nodes available at the upgrade time, g is the performance growth factor for the nodes which can be purchased at equal cost in the upcoming years and y is the number of years before purchasing the nodes.

At the TDR time, assuming a money budget of 2.8 MCHF, the number N of 24 virtual core X5650 nodes which could have been purchased was 1000. The performance growth factor per year at equal cost was estimated to be $g = 1.365$ accounting for the evolution of computing power between 2007 and 2010. Unfortunately, the growth factor rate at equal cost re-evaluated between 2010–2016 shows that the value was overestimated. The measured one is in fact $g = 1.1$. The reason behind such change is to be found in the evolution trend of computing power, which in last years have been moved from having more powerful single core machines to an increasing density of CPU. Therefore, even tough machines fulfilling the trigger TDR extrapolation are available, their price would be too high to be affordable. An updated extrapolation accounting for $g = 1.1$, shows that the current sequence timing must be improved of at least a factor six. Indeed, the LHCb computing software for the upgrade is expected to be completely modified, changing the underlying Gaudi framework from a sequential execution of algorithms to a fully schedulable and parallelizable one. In other words, to maximise the usage of the CPU power available on the nodes, the reconstruction algorithms would not be executed as a plain reconstruction sequence on single nodes, but each algorithm, wherever possible will be scheduled and run on different CPU.

It is therefore important to modify the LHCb software to handle such big change: data-dependencies should be known a priori such that the framework will be able to handle the multi-thread execution of reconstruction sequence pieces, the underlying reconstruction algorithms are not allowed to modify the status of data objects stored in the temporary memory (called Transient Event Store) and algorithms are required to be stateless since multiple instance of it will be run for different event at the same time. A thread-safe software is therefore a starting point for the LHCb upgrade to be able to maximise the computing power resource usage and fully exploit the expected evolution of computing resources. In the upcoming years, it will be very important to benchmark the progresses in reconstruction timing since eventual shortfall which could not be covered with the available money budget, will dictate a review of the trigger strategy. This aspect strongly highlights that the LHCb upgrade physics program will be able to be accomplished if the upgrade LHCb reconstruction software will be significantly improved. Naively speaking, there are two main categories of speed-up for the event reconstruction which can be achieved in next years: one takes advantage of modern programming standards and multi-threading aspects in general, another one is a completely re-design of the reconstruction strategy in a smarter and optimal way. When the latter and the former are not possible to be achieved, a speed-up can still be achieved but accepting a loss in reconstruction efficiency.

References

1. LHCb, R. Aaij et al., Test of lepton universality using $B^+ \to K^+\ell^+\ell^-$ decays. Phys. Rev. Lett. **113**, 151601 (2014). https://doi.org/10.1103/PhysRevLett.113.151601, arXiv:1406.6482
2. LHCb, R. Aaij et al., *Test of Lepton Universality with $B^0 \to K^{*0}\ell^+\ell^-$ Decays*, arXiv:1705.05802
3. Letter of intent for the LHCb Upgrade. Technical report, CERN-LHCC-2011-001. LHCC-I-018, CERN, Geneva (2011)
4. J. Albrecht, C. Fitzpatrick, V. Gligorov, G. Raven, The upgrade of the LHCb trigger system. JINST **9**(10), C10026 (2014). https://doi.org/10.1088/1748-0221/9/10/C10026. arXiv:1410.5012
5. T. Poikela et al., Velopix: the pixel asic for the lhcb upgrade. J. Instrum. **10**(01), C01057 (2015)
6. L. Collaboration, LHCb VELO upgrade technical design report. Technical report. CERN-LHCC-2013-021. LHCB-TDR-013 (2013)
7. LHCb Collaboration, LHCb tracker upgrade technical design report. CERN-LHCC-2014-001. LHCB-TDR-015, http://cdsweb.cern.ch/search?p=CERN-LHCC-2014-001&f=reportnumber&action_search=Search&c=LHCb+Reports
8. L. Collaboration, LHCb PID upgrade technical design report. Technical report. CERN-LHCC-2013-022. LHCB-TDR-014 (2013)
9. K. Föhl et al., TORCH—an innovative high-precision time-of-flight PID detector for the LHCb upgrade, in *Proceedings, 21st Symposium on Room-Temperature Semiconductor X-ray and Gamma-ray Detectors (RTSD 2014): Seattle, WA, USA, November 8–15, 2014* (2016), p. 7431227. https://doi.org/10.1109/NSSMIC.2014.7431227
10. P. Carniti et al., Claro-cmos, an asic for single photon counting with ma-pmts, mcps and sipms. J. Instrum. **8**(01), C01029 (2013)
11. LHCb RICH Upgrade, L. Cassina, LHCb RICH upgrade: an overview of the photon detector and electronic system. JINST **11**(01) C01025 (2016). https://doi.org/10.1088/1748-0221/11/01/C01025, arXiv:1511.09308
12. LHCb, E. Picatoste, *LHCb calorimeter upgrade electronics*, in *Proceedings, International Conference on Calorimetry for the High Energy Frontier (CHEF 2013): Paris, France, April 22–25* (2013), pp. 363–368
13. LHCb Trigger and Online Upgrade Technical Design Report. Technical report. CERN-LHCC-2014-016. LHCB-TDR-016 (2014)
14. F. Alessio, R. Jacobsson, A new readout control system for the lhcb upgrade at cern. J. Instrum. **7**(11), C11010 (2012)
15. LHCb, F. Alessio, The LHCb upgrade, in *Meeting of the APS Division of Particles and Fields (DPF 2013) Santa Cruz, California, USA, August 13–17* (2013), arXiv:1310.0183
16. F. Alessio, Trigger-less readout architecture for the upgrade of the LHCb experiment at CERN. JINST **8**, C12019 (2013). https://doi.org/10.1088/1748-0221/8/12/C12019

Chapter 4
Tracking in LHCb and Stand-Alone Track Reconstruction for the Scintillating Fibre Tracker at the LHCb Upgrade

Track reconstruction in the LHCb experiment is implemented in three distinct stages listed in execution order:

1. Pattern recognition: particles traversing tracking detectors release a small amount of energy in the active volumes of the detector. The energy is converted to an electronic signal and if the deposit is above a given read-out threshold, *hits* are produced. Pattern recognition aims at connecting the *hits*, recognizing the pattern of tracks in the detector. Several pattern recognition algorithms are implemented in the LHCb software and each of them aim at finding different types of tracks. Classification of tracks in LHCb depends on the track path in the detector: the presence or absence of *hits* for a given track in the tracking sub-detectors is used to define the track type.
2. Track fit: pattern recognition algorithms reconstructed tracks are fitted using the Kalman filter fit [1–4]. The Kalman filter fit provides the best possible estimation of the real trajectory of the reconstructed tracks taking into account the magnetic field, material interaction and multiple scattering effects.
3. Track removal and duplicates killer: tracks failing the fit from the Kalman filter are removed from the final output tracks used in physics analysis. Also tracks containing the same or a significant overlap of hit content with other tracks are removed. The presence of duplicated reconstructed tracks comes from the fact that different pattern recognition algorithms can produce the same or a shorter version of the same track.

The first part of this chapter introduces the basics concept of track reconstruction at LHCb, with a special focus on the upgrade, as well as a description of the various pattern recognition algorithms composing the tracking sequence expected for the LHCb upgrade.

In the second part of this chapter, a detailed description of the Scintillating Fibre Tracker (SciFi) working principles and implementation in the LHCb simulation

software is provided (see Sect. 4.2) as well as the description and performance studies for pattern recognition algorithm aiming at performing a stand-alone track reconstruction with the SciFi (see Sect. 4.4).

4.1   Track Types and Tracking Strategies

In LHCb, tracks are classified based on the hit content in the three different tracking sub-detectors (see Fig. 4.1) and they are searched for using dedicated pattern recognition algorithms:

- `Velo` tracks are tracks composed solely by hits in the VELO. They are used for vertexing and as starting point to seed the search of tracks traversing the full spectrometer. The pattern recognition algorithm used for the upgrade is called *PrPixelTracking*.
- `T-tracks` are reconstructed using solely the hits from the tracker placed downstream of the dipole magnet (T-station), i.e. the SciFi for the upgrade. They are called also Seed tracks since they are used to seed the search of both `Long` and `Downstream` tracks. The pattern recognition algorithm used to reconstruct those tracks in the upgrade is called *Hybrid Seeding* algorithm and this algorithm will be extensively described in Sect. 4.4.
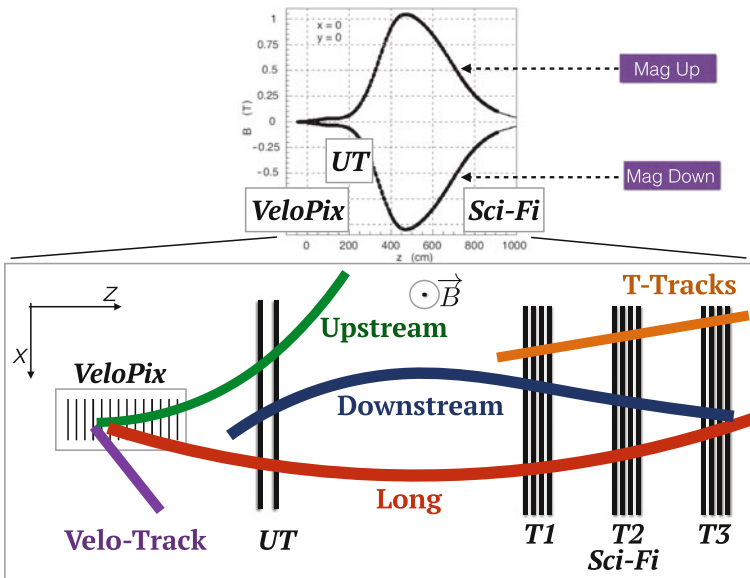
Fig. 4.1   Schematic view of the track types defined in LHCb

- `Upstream` tracks are tracks composed by hits in the VELO and the UT. Those tracks are found matching `Velo` tracks to hits in the tracker upstream the dipole magnet (UT). A pure `Upstream` track (no hits at all in the downstream tracker) is a low p track which is bent out of the acceptance by the dipole magnet before reaching the tracker downstream of the dipole. The pattern recognition algorithm used to reconstruct upstream tracks is called `VeloUT` algorithm.
- `Long` tracks are the most important track types used in LHCb analyses since they are typically associated to decay products of a decaying b or c hadron. These tracks traverse all the LHCb spectrometer leaving measurements in VELO, UT and SciFi. Although these tracks traverse the whole spectrometer, UT hits are not required to define a `Long` track, but they are generally used to achieve a better momentum resolution and to speed-up the event reconstruction. Different pattern recognition algorithms aim at finding them: *PrForwardTracking* (or simply *forward* tracking) uses the `Velo` tracks as input (or `Upstream` ones for timing/trigger purposes) and searches for matching hits in the SciFi; *PrMatchNN* (or simply *matching* algorithm) uses `Velo` tracks and `T-tracks` as input and it builds `Long` track candidates matching them according to quality requirements and employing a fast parametrisation of the magnetic field.
- `Downstream` tracks: long-lived particles such as K_S^0 and Λ^0 fly a significant distance in the VELO, before decaying into charged particles. This can result in tracks that only leave hits in the UT and the SciFi, referred to as `Downstream` tracks. The pattern recognition algorithm aiming at finding those tracks uses as seed the `T-tracks` and it searches for matching hits in the UT. The algorithm used to reconstruct this kind of tracks is called *PrLongLivedTracking*.

All the tracks in LHCb are represented within the LHCb software as a series of vectors called track states. A track state at position z_i is defined by a vector of the form:

$$\overrightarrow{S}_i = (x, y, t_x, t_y, q/p)^T \tag{4.1}$$

consisting of x and y coordinates, slopes in x-z ($t_x = \dfrac{\partial x}{\partial z}$) and y-z ($t_y = \dfrac{\partial y}{\partial z}$) projections and the inverse track momentum times its charge q at $z = z_i$ along the track. The track state's uncertainty is embedded in the corresponding 5×5 covariance matrix. Track states and covariance matrices are used by the Kalman Filter to evaluate the final track quality taking into account multiple scattering, bremsstrahlung, material interaction and the complete magnetic field map effects.

Apart from the Kalman Filter, a fast $\dfrac{q}{p}$ estimation for tracks which is used in several pattern recognition is the so-called $p_T - kick$ method. The same method is also employed to predict tolerances given a momentum requirement. Details can be found in Sect. 4.1.1.

4.1.1   Momentum Estimation Using the p_T-Kick Method

The effect of a magnetic field between two detectors region can be parametrised as an instantaneous kick to the momentum vector in the centre of the magnet. The actual momentum kick, $\Delta \vec{p}$, depends on the integrated magnetic field along the path followed by the track:

$$\Delta \vec{p} = q \cdot \int d\vec{l} \times \vec{B} \tag{4.2}$$

In LHCb B_y and B_z can be neglected in first approximation and the equation (4.2) is simplified as follows:

$$\Delta p_x = p_{x,final(f)} - p_{x,initial(i)} = p \left(\frac{t_{x,f}}{\sqrt{1 + t_{x,f}^2 + t_{y,f}^2}} - \frac{t_{x,i}}{\sqrt{1 + t_{x,i}^2 + t_{y,i}^2}} \right)$$

$$= q \cdot \int \left| d\vec{l} \times \vec{B} \right|_x \tag{4.3}$$

which rearranged properly, is read as:

$$\frac{q}{p} = \frac{1}{\int \left| d\vec{l} \times \vec{B} \right|_x} \cdot \left(\frac{t_{x,f}}{\sqrt{1 + t_{x,f}^2 + t_{y,f}^2}} - \frac{t_{x,i}}{\sqrt{1 + t_{x,i}^2 + t_{y,i}^2}} \right) \tag{4.4}$$

In (4.3) and (4.4) the $t_{x,f}$ and $t_{y,f}$ are the slopes of the track defined at the position z_f being downstream of z_i. In the equations q is determined from the sign of the curvature and the dipole magnet polarity.

The knowledge of the slopes at the z_i and z_f positions and the integrated magnetic field allows to provide a measurement of the track's momentum. Furthermore, in absence of a knowledge for the slopes at z_f (for instance $z_f = z_{T-stations}$), one can define a tolerance in p and calculate the corresponding field of interest search window at various z_f (as it is done in the *forward* tracking described in Sect. 4.1.4). Figure 4.2 shows the situation accounting for the actual LHCb dipole magnet effect on tracks.

4.1.2   VELO Tracking: PrPixelTracking

The magnetic field intensity in the VELO region is almost negligible, therefore pattern recognition using solely hits in the VELO is rather straight forward in the sense that tracks are build searching for straight lines in both the *x-z* and *y-z* plane. The pixel readout is binary, meaning that pixels on a sensor are represented by a 2D array of bits: status 1 of the bit means that the pixel is active and it can be used to perform
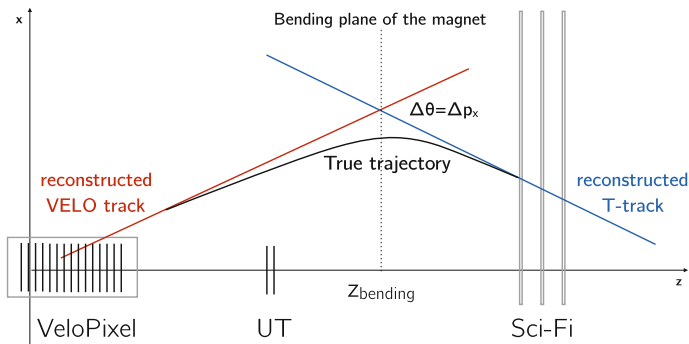
Fig. 4.2 Geometrical interpretation of the p_T-kick method when dealing with `Velo` tracks and `T-tracks`. The same can be applied between VELO and UT, or between `VeloUT` and T-station

tracking. Optimised format of the binary information produced by the detector [5] allows to execute a fast clustering of pixels to produce hits, assign them a Cartesian coordinate (x, y, z) and errors in both x and y coordinates (Δ_x, $\Delta_y = p/\sqrt{12}$, where p is the pixel pitch size) and use them to perform VELO track reconstruction. The *PrPixelTracking* pattern recognition algorithm is rather straight forward:

- A search for pairs of unused hits on neighbouring same-side modules is performed.[1] Pairs are generated if the resulting track slope is less than 400 mrad ($\left|\dfrac{dx}{dz}\right| < 0.4$, $\left|\dfrac{dy}{dz}\right| < 0.4$).
- Pairs are searched starting from the most downstream module position and the seed track is linearly extrapolated in the upstream direction x_p, y_p on the next same side module.
- Hits are collected in upstream modules if compatible with a tolerance accounting for a maximal scattering angle. The hit search in upstream modules for the seed pairs is abandoned if no hits on three consecutive stations have been found. Track candidates with less than three hits are rejected.
- Track candidates with only three hits are required to be composed by unused hits and have a very good χ^2 of a least-square line fit. Track candidates with more than three hits are allowed to be composed of already used hits for a maximal amount equal or less than the 50% of the track hit content. All the hits on candidates passing these requirement are flagged as used.
- All tracks are re-fitted using a simplified Kalman filter where a fixed amount of scattering is employed. This approach allows to achieve at a very early stage a very good primary vertex resolution (using the reconstructed VELO tracks) and track's impact parameter which is closer to the one achievable by a full track fit (which is time expensive and using the whole spectrometer measurements, thus requiring all algorithms to be run).

---

[1]Used hits are hits already used to create a final `Velo` track candidate.

- Track states at the end of the VELO ($z = 770$ mm) and at the z position corresponding to the distance of closest approach of the track to the beam line[2] are stored together with the track candidate for further processing.

The simplified Kalman filter used for the `Velo` track fit is based on the assumption that the track momentum is constant within the VELOPix region leading to a reduction of the 5D track state to two independent two-dimensional vectors defining the track's state at z_i position: $\overrightarrow{x}_i = (x_i, t_{x,i})^T$, $\overrightarrow{y}_i = (y_i, t_{y,i})^T$. Details on the upgraded VELO simulation, track reconstruction and pattern recognition performance can be found in [5, 6].

4.1.3 `VeloUT` *Tracking Algorithm: PrVeloUT*

Tracks found by the VELO tracking pattern recognition are matched to hits in the UT, i.e. UT hits are added to VELO tracks. The algorithm finding `VeloUT` tracks is called *PrVeloUT* algorithm. The integrated small fringe field experienced from tracks travelling from VELO to UT is around $\int B \cdot dl = 0.15$ Tm which allows to measure the track's p with a resolution of $\sim$15–25%. The main purposes of the algorithm is to reconstruct `Upstream` tracks, i.e. low momentum tracks which are bent outside the LHCb acceptance by the dipole magnet and the high p_T ones which can be used to seed the search of segment in the SciFi speeding up the track reconstruction in the trigger system. The current implementation of the algorithm is optimised and used only to find high p and p_T tracks for trigger purpose. For each VELO track, the last `Velo` track available measurement is used as well as the associated track state defined as $\overrightarrow{S}_{VELO} = (x_{VELO}, z_{VELO}, t_x^{VELO}, t_y^{VELO})^T$ and the associated errors. The track state $\overrightarrow{S}_{VELO}$ is defined at the z position corresponding to the most downstream `Velo` track available measurement.

A linear extrapolation to the central z position of the UT tracker is performed for all the `Velo` tracks and hits are pre-selected if they fall within tunable tolerances around the extrapolated position. The pre-selected hits undergo a clustering step aiming at selecting groups of hits in the four different UT layers matching a `Velo` track. The clustering procedure on selected hits has been modified for the LHCb upgrade and back-ported for Run II. The novel clustering procedure first attempts to form hit-doublets within the selected hits using the first and the neighbour UT layers. Doublets are projected to the third and fourth layer and search windows allow to form triplets or quadruplets of UT hits. Quadruplet candidates are used to define a line segment in the UT which is used for further processing. When no quadruplets are found, triplets are selected. Several clusters solution for the same VELO track are then allowed and the best one is kept accounting for a pseudo-χ^2 based on track quality from the VELO and the straight line defined by the matching UT hits. A sketch of the clustering procedure used in the `VeloUT` is shown in Fig. 4.3.

---

[2]The corresponding track state is also called first measurement.
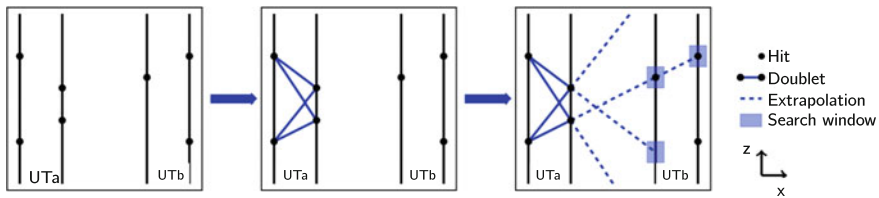
Fig. 4.3 Sketch of the hit-clustering strategy used in the `VeloUT` pattern recognition algorithm. `Velo` tracks are projected to one of the UT layer station. Doublets are formed looking at the neighbour layer and based on the local slopes, hits are collected layers to form triplets or quadruplets candidates

Besides the algorithm implementation, the overall idea of the algorithm is to approximate the magnetic field effect on tracks travelling from the VELO to the UT tracker through an "effective magnet" placed at a focal plane placed at z_{mid}^{Bdl}. The value of z_{mid}^{Bdl} is defined as follows:

$$\int_{z_{VELO}}^{z_{mid}^{Bdl}} \left| \overrightarrow{B} \times d\overrightarrow{l} \right|_x = \frac{1}{2} \int_{z_{VELO}}^{z^{UT}} \left| \overrightarrow{B} \times d\overrightarrow{l} \right|_x \tag{4.5}$$

In other words z_{mid}^{Bdl} is the z position at which the track travelling from z_{VELO} to z^{UT} has experienced half of effects from the magnetic field. The value of z_{mid}^{Bdl} and $\int Bdl$ are evaluated from a look-up table providing as input the track $t_y = t_y^{VELO}$, z_{origin} position and z_{VELO}. z_{origin} is defined as the position at which the `Velo` track segment intersect the z axis. Once z_{mid}^{Bdl} becomes available the VELO segment and the UT hits segments are linearly projected to the $x - y$ reference plane defined at z_{mid}^{Bdl}. The linear projection is performed according to t_x^{VELO} and t_x^{UT} for the VELO segment and the line defined by the triplets or quadruplets in the UT. The value of $t_x^{VELO'}$ is computed joining the $x_{mid}^{Bdl'}$ (projected x position from the UT line to the reference plane) and the VELO track state x position. At this stage two slopes are defined for the `Velo` track segment: one evaluated directly from the last available measurement in the VELO and obtained from the simplified Kalman filter in *PrPixelTracking* (t_x^{VELO}) and the other one obtained joining the x position of the last available measurement in the VELO to $x_{mid}^{Bdl'}$, which is obtained projecting the UT line to z_{mid}^{Bdl}.

As final step the `VeloUT` track candidates are filtered based on a pseudo-χ^2 per degrees of freedom (nDoF) defined as $\chi^2/\text{nDoF} = \dfrac{\chi_{UT}^2 + \chi_{VELO}^2}{\#\text{hits} - 1}$, where:

$$\chi_{VELO}^2 = \left(\frac{t_x^{VELO} - t_x^{VELO'}}{\sigma_{t_x^{VELO}}} \right)^2$$

$$\chi^2_{UT} = \sum_{i=1}^{^{N}\text{UT hits}} \left(\frac{x_i^{fit} - x_i^{hit}}{\sigma_i}\right)^2$$

The "best" `VeloUT` track candidate per `Velo` input track is chosen depending on the amount of fired UT layers and the pseudo-χ^2 value. `VeloUT` track candidates seeded from the same VELO track with larger amount of UT layers are preferred, for same amount of hits, the track having a smaller pseudo-χ^2 is kept. For the best `VeloUT` track candidates, an additional track state is added (the UT one) as well as the estimated momentum, calculated through the p_T−kick method described in Sect. 4.1.1. The $\dfrac{q}{p}$ is therefore estimated as:

$$\frac{q}{p} = -\frac{1}{\sqrt{1 + (t_y^{VELO})^2}} \left(\frac{t_x^{UT}}{\sqrt{1 + \frac{\left(t_x^{UT}\right)^2}{\sqrt{1+(t_y^{VELO})^2}}}} - \frac{t_x^{VELO'}}{\sqrt{1 + \frac{\left(t_{xVELO'}\right)^2}{\sqrt{1+(t_y^{VELO})^2}}}} \right) \cdot \frac{1}{0.3 \cdot \int B \cdot dl} \frac{1}{\text{GeV}}$$

(4.6)

Further details on the `VeloUT` tracking algorithm for the LHCb upgrade can be found in [7].

4.1.4   Forward Tracking Algorithm: PrForwardTracking

The forward tracking algorithm is one of the two main algorithms used to reconstruct `Long` tracks in the HLT. Thanks to the tracking strategy used in the algorithm, it can be tuned to find high momentum tracks, strongly reducing the processing time and making it suitable for the fast trigger decisions. The model behind the algorithm is an optical model: the magnetic field between the VELO (or the UT) and the SciFi can be seen as a lens kicking the flight path of particles from a direction into another at a specific position in space (the "magnet bending" plane). The complication to the simple model comes from the fact that the LHCb magnetic field is a fringe magnetic field. As a consequence, the position of the "magnet bending" plane is not constant and correction factors are accounted for when using the p_T-kick method. The flight path of a track can be fully predicted knowing the shape of the magnetic field, neglecting multiple scattering effects and material interactions.

The main idea of the *forward* tracking for the LHCb upgrade [8] is based on the fact that track segments upstream of the magnet, called "seeds", can be extrapolated to the T-stations layers downstream of the magnet. Knowing the magnetic field in between the regions, a single hit in the T-station allows to predict the value of $\dfrac{q}{p}$ and the expected path of the track in the whole T-station. Therefore, groups of hits sharing the "same" projected position in x on a reference plane allow to determine T-station track segments associated to the input `Velo` track.
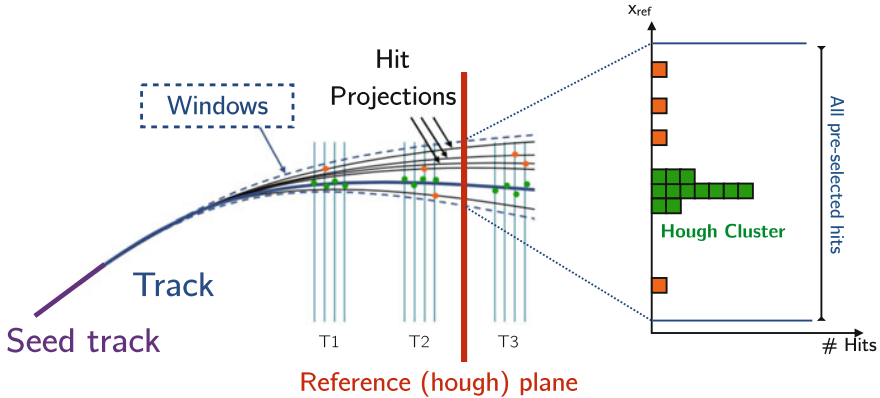
Fig. 4.4 Sketch of the 1D Hough transform used in the Forward Tracking algorithm at LHCb. "Seed" tracks upstream the dipole magnet, according to the momentum requirement, defines search windows in each layer downstream of the magnet where all the hits are collected. The collected hits are projected to a reference plane thanks to the track model accounting for the momentum of the track arising from the "seed" segment and the hit itself

What has been just described is an application of the Hough Transform [9]. In general, the Hough transform is a global method aiming at identifying and recognizing features of objects. It uses a parametric description of an object (track in this case) by a set of parameters and it allows to project all input measurements (hits in this case) into the track parameter space (1D $x_{projected}$ position in this case). With the accumulation of elements in the track parameter space, usually found through peak-finding on binned histograms, one is able to identify a track candidate. A 1D Hough cluster search is employed in the algorithm, thus no graphical strategy is needed. Therefore, it is enough to perform a 1-D loop and select groups of hits being within a given tolerance. This strategy suffers in terms of performance and execution time when the detector occupancy increases. A sketch of the working principle of the *forward* tracking algorithm is shown in Fig. 4.4.

The building blocks of the current *PrForwardTracking* algorithm is based on six main (taking as input a single "seed" track):

1. Hits on *x-layers* from the SciFi are preselected based on minimal track momentum requirement or on previously knowledge of the seed momentum.
2. Within the preselected hits, *x-hit* clusters are searched for through the previously described Hough Transform based approach, requiring in a first iteration five different fired layers and in a second stage, called second loop and executed only in the *best* tracking stage of the upgrade reconstruction sequence (see Sect. 4.1.9) a minimum of four fired layers to recover for detector hit inefficiencies. The forward tracking algorithm in Run II has in fact introduced the two loop approach: 5*x-hit* hough clusters are processed upfront, the hits on the resulting track candidates are flagged as used, and the non-promoted VELO tracks are re-processed requiring a 4*x-hit* and 4 fired *x-layers* as minimum. This approach allows to optimise the algorithm for trigger purposes and to reduce the fake track rate.

3. The resulting candidate's *x-z projection* is fitted for, *u/v-hits* are added on track through a second hough transform dealing with straight lines in the track's *y-z* plane projection.
4. A neural net based track quality parameter is assigned to the resulting track candidates.
5. Fake tracks and clones are removed based on the amount of hits shared among tracks and the Neural Net-based track quality requirements.
6. If UT hits are not already present in the input "seed" tracks, they are added computing the expected position in both x, y plane.

Depending on the minimal p_T requirement, the hit selection window for each "seed" track used for the pre-selection of hits can be reduced, boosting by a large factor the execution time of the algorithm, but this is inefficient at finding lower p_T tracks. Furthermore, if the input "seed" track already contains information on the p_T and on the sign of the charge, tolerances according to the estimated momenta can be defined. The latter scenario is what is used for trigger purpose where only high momentum tracks are required to be found.

The algorithm is used in two different configurations for the upgrade: *PrForwardTrackingFast* and *PrForwardTrackingBest*. The *fast* configuration uses as seed the output of the `VeloUT` algorithm configured to find high p_T and p tracks using the fact that a momentum and charge estimation for the track is already available in the seeds, thus reducing the search windows. This results in a faster hit pre-selection.

The *best* tracking sequence configuration uses as seed all the `Velo` tracks found by the *PrPixelTracking* and search windows are opened aiming at finding all the tracks with almost no minimal momentum requirement applied. Details on how the effective parametrisation of the magnetic field is obtained and the track model used to predict the position of the hits in the Hough Plane can be found in detail in [8, 10, 11].

4.1.5 Seeding Algorithm: PrHybridSeeding

The `Hybrid Seeding` is dedicated to a stand-alone track reconstruction using only hits in the T-stations. The upgrade algorithm implementation at the Technical Design Report (TDR) time [12] is described in [13]. Both algorithms are based on a tracking-in-projection approach, i.e. first $x - z$ plane `T-track` projections are found and lately *u/v-hits* are added on tracks. The new algorithm, which will be extensively described in Sect. 4.4, employs novel tracking strategy techniques, as well as a completely revisited track model accounting for the local magnetic field in T-stations. The implementation of the algorithm aims at first finding high momentum tracks and lately, with the left-over hits, the lower momentum ones. A final track recovery routing has been also introduced aiming at recovering the lower p and p_T tracks. The novel algorithm outperforms the previous implementation in all the performance indicators as it will be described in Sect. 4.5.

Notably, the same performance would have been achieved with the previous tracking strategy implementation and the improved track model description paying up to a factor four in fake track rate and a slow down of the pattern recognition algorithm corresponding to two orders of magnitude, resulting in a critical bottleneck for the trigger strategy. Overall, the main goal of the algorithm is to provide inputs for the matching algorithm (Sect. 4.1.7) for `Long` track reconstruction and for the long lived particle reconstruction (Sect. 4.1.6).

4.1.6 Downstream Tracking Algorithms: PrLongLivedTracking

Charged decay products of long-living particles decaying outside the VELO leave hits only in the UT and SciFi. Furthermore, these long-living particles are produced in the interaction region and they are strongly boosted in the forward direction. This implies that also their daughters (produced after the VELO) are expected to have pointing features to the origin. The pattern recognition algorithm reconstructing such tracks uses as "seed" the outcome of the Seeding algorithm, i.e.`T-tracks`. `T-tracks` track state, defined at the T-station position, is backward propagated to the UT central position assuming the track originates from the origin. It is important therefore, according to the p_T-kick method, to define the centre of the magnet bending the track, such that a track slope from the origin can be defined. Given the presence of a fringe field in between the UT and the SciFi, the centre of the bending plane is parametrized with an empirical formula having six parameters (α_i) fixed from simulation studies:

$$z_{mag} = \quad \alpha_0 + \alpha_1 t_y^2 + \alpha_2 t_x^2 + \alpha_3 \times \frac{1}{p} + \\ + \alpha_4 \cdot |x_{state}| + \alpha_5 \cdot |y_{state}| + \alpha_6 \cdot |t_y|. \quad (4.7)$$

In (4.7), the values of $x_{state}, y_{state}, t_y, t_x$ and p are extracted from the input `T-track` state which is calculated at the z position of the third T-station. With as input a z_{mag} position, a linear extrapolation of the x position at the magnet centre (x_{mag}) is computed, as well as the extrapolated y position (y_{mag}). The y_{mag} is evaluated accounting for small deviations from the x and z components of the magnetic field through the following parametrization :

$$y_{mag} = y_{state} + t_y \cdot (z_{mag} - z_{state}) - \beta_1 t_y \Delta_{slope}^2,$$

where $\Delta_{slope} = |x_{mag}/z_{mag} - t_x|$, i.e. the deviation angle at the magnet centre assuming the `T-track` comes from the origin. Concerning the momentum estimation, it is obtained through the following parametrisation:

$$p = \frac{\gamma_0 + \gamma_1 \cdot t_x^2 + \gamma_2 \cdot t_y^2}{\Delta_{slope}},$$

where $\gamma_{0,1,2}$ are fixed from Monte Carlo simulation.

T-tracks used as input are first filtered through a multivariate (MVA) selection, aiming at removing clear fake tracks, and then they are used to define search windows from the backward projection in the first *x-layer* in the UT. A single measurement in the UT is then sufficient to re-compute the track parameters releasing the constrain for tracks to come from the origin and predict the position in the remaining UT layers. The prediction in the remaining layers should in principle be extracted from a parabolic model accounting for the small magnetic field present within the UT layers, nevertheless the curvature parameter can be fully fixed with the estimation of the momentum available from the p_T-kick method. Hits in the remaining layers are collected and the resulting candidate is fitted with a χ^2 fit using the modified parabolic model (curvature term fixed). Final candidates which are allowed to have 3 or 4 hits in the UT only are selected through a multivariate classifier track quality assignment.

The described algorithm has been introduced to reconstruct downstream tracks in Run II [14] largely improving the execution time and the fake track rejection of its predecessor, called *PatDownstream* [15]. The algorithm has been ported with minimal changes for the upgrade. More details on the Run II implementation of the long-living particle pattern recognition algorithm can be found in Ref. [16].

4.1.7 Matching Algorithm: PrMatchNN

The track matching algorithm is complementary to the *forward* tracking. The algorithm uses as input the Velo tracks found by the *PrPixelTracking* algorithm and the T-tracks found by the *PrHybridSeeding* and it attempts to match them accordingly to p_T-kick method. A preliminary filtering of tracks and important quantities are extracted by the algorithm. Velo tracks flagged as backward are not used by the algorithm as well as the invalid ones. Each of them are projected to $z_0 = 0$ mm and the corresponding track state is evaluated defining $\overrightarrow{S}_V(z_0) = \left(x_V(z_0), y_V(z_0), t_{x,V}, t_{y,V}, q/p\right)^T$. T-tracks are projected to $z_S = 10$ m which is after the T-stations and the corresponding T-track state at z_S position is evaluated: $\overrightarrow{S}_T(z_S) = \left(x_T(z_S), y_T(z_S), t_{x,T}, t_{y,T}, q/p\right)$. Velo and T-tracks are sorted by their estimated value of y position at z_S. For the Velo, a linear extrapolation to z_s is computed: $y_V(z_S) = y_V(z_0) + z_S \cdot t_{y,V}$.

Velo/T-track pairs are formed if the $|y_V(z_S) - y_T(z_S)|$ is smaller than 250 mm search window. For each y-compatible Velo/T-track pair a χ^2_{match} is calculated determining how well the two track segments are matching together. The χ^2_{match} determination is based on the p_T-kick method. The steps aiming at selecting the pairs and producing the final track candidates are the following:

- The magnet bending plane z position (z_{mag}) is found using the VELO and T-track states:

$$z_{mag} = \alpha_0 + \alpha_1 \cdot \left| d_{Slope-x} \right| + \alpha_2 \cdot d^2_{Slope-x} + \alpha_3 \cdot |x_T(z_S)| + \alpha_4 \left(t_{x,V} \right)^2 ,$$

where $d_{Slope-x} = t_{x,V}(z_0) - t_{x,T}(z_S)$. Also $d_{Slope-y} = t_{x,V} - t_{y,T}$ and α_{0-4} are empirical parameters calculated from Monte Carlo simulation.
- The $x(z_{mag})$ position is calculated with a linear extrapolation for both the Velo and T-track states defining the quantities $x_V(z_{mag})$ and $x_T(z_{mag})$. The extrapolated $y_V(z_S)$ is re-computed accounting for the small deviation expected in y direction ($y'_V(z_S)$) for tracks traversing the full spectrometer. The quantities used to define the χ^2_{match} are:

$$
\begin{aligned}
x_V(z_{mag}) &= x_V(z_0) + & z_{mag} \cdot t_{x,V}, \\
x_T(z_{mag}) &= x_T(z_S) + (z_{mag} - z_S) \cdot t_{x,T}, \\
y'_V(z_S) &= y_V(z_0) + & z_S \cdot t_{y,V} & + t_{y,V} \cdot \left(\beta_0 \cdot d^2_{Slope-x} + \beta_1 \cdot d^2_{Slope-y} \right) \\
\text{and} \quad y_T(z_S) &
\end{aligned}
$$

$$(4.8)$$

- Velo/T-track pairs are rejected if the distance in y at z_S, after the correction factor is applied, is greater than 250 mm or if the distance in x at $z = z_{mag}$ is greater than 400 mm.
- The χ^2_{match} is computed as follow:

$$\chi^2_{match} = \frac{(x_T(z_{mag}) - x_V(z_{mag}))^2}{\epsilon_0 + \epsilon_1 \cdot d^2_{Slope-x}} + \frac{(y_T(z = 10\,\text{m}) - y'_V(z = 10\,\text{m}))^2}{\epsilon_2 + \epsilon_3 \cdot (t^2_{V,x} + t^2_{V,y})} + d^2_{Slope-y} \cdot \epsilon_4$$

$$(4.9)$$

where ϵ_{0-4} are empirical parameters evaluated from Monte Carlo simulations.
- A loose selection is applied based on the χ^2_{match} value. A neural-net based track quality (*track-NN*) is calculated using as input variables the χ^2_{match}, $t^2_{V,x} + t^2_{V,y}$, $\left| x_T(z_{mag}) - x_V(z_{mag}) \right|$, $\left| y_T(z_S) - y'_V(z_S) \right|$, $|d_{Slope-x}|$ and $|d_{Slope-y}|$.
- Final track candidates are produced for Velo/T-track pairs having a good *track-NN* and UT hits are added as measurements (no additional track states defined) projecting the track in the UT stations.

The algorithm does not require for a given Velo track a matching to a single T-track, but several combinations are possible according to the quality requirements for the *track-NN*. The previous implementation of the algorithm was based on Kalman Filter Fitted T-tracks and Velo tracks as inputs. In such scenario a too large timing was measured because of the preliminary Kalman Filter Fit step: the algorithm was not able to run on the online-trigger system. The χ^2_{match} defined in a more empirical way in *PrMatchNN* reflects the "original" χ^2_{match} which was formally defined as:

$$\chi^2_{match'} = \left(\vec{S}^K_V(z_{mag}) - \vec{S}^K_T(z_{mag}) \right)^T \cdot \left(C^K_{VELO} + C^K_T \right)^{-1} \cdot \left(\vec{S}^K_V(z_{mag}) - \vec{S}^K_T(z_{mag}) \right)$$

$$(4.10)$$

where $\overrightarrow{S}_{V}^{K}(z_{mag})$ and $\overrightarrow{S}_{T}^{K}(z_{mag})$ are the propagation of the VELO track state and T-track state to z_{mag} using the Kalman formalism (see Sect. 4.1.8), respectively. $C_{V}^{K}(z_{mag})$ and $C_{T}^{K}(z_{mag})$ are instead the covariance matrices obtained propagating through the Kalman formalism the VELO and the T-track, respectively.

More details on the algorithm can be found in Ref. [17] and the implementation of the matching algorithm for the Run I and Run II can be found in Refs. [18, 19].

4.1.8 Track Fit: Kalman Filter

The most accurate estimate of track parameters and the corresponding covariance matrix is the main goal of the Kalman Filter. Precise measurement of the track's parameters are key ingredients to achieve high resolution in reconstructed mass spectrum, to determine the centre of the Cherenkov rings for particle identification purposes and to identify primary and secondary vertices in the event, while the track quality (χ^2_{track}) is used to reject fake tracks, i.e. tracks arising from random combination of hits. Track fitting in LHCb uses the Kalman filter technique introduced in 1960 [1]. Mathematically the Kalman filter is equivalent to a least squares fit, with the advantage that, differently from a global fit method, the addition of a new measurement does not require a total refit, saving time in its execution.

The inputs to the Kalman filter fit are the track states available from the pattern recognition algorithms and the different measurements (hits) used to build such tracks. Typically track states are defined at the same location of measurement planes. The possible operations applicable to track states which are of interest for the Kalman filter are the propagation and projection. A sketch showing the Kalman Filter procedure logic is shown in Fig. 4.5.

Propagation allows to calculate a projected track state ($\overrightarrow{S}_{f}^{i}$) at position z_f given the best estimate of a track state at position z_i, according to:

$$\overrightarrow{S}_{f}^{i} = \left(x_f, y_f, t_{x,f}, t_{y,f}, \left(\frac{q}{p}\right)_f\right) = F_{z_i \to z_f} \overrightarrow{S}_i. \tag{4.11}$$

In the case of LHCb track states, the track propagation function F is a 5×5 matrix which is also used to propagate and evaluate the covariance matrix at z_f as follow:

$$\overrightarrow{S}_{f}^{i} = F_{i \to f} \overrightarrow{S}_i, \tag{4.12}$$

where F is the track propagation matrix from z_i to z_f. The same propagation matrix is used to transport the best estimation of the covariance matrix C_i at z_i as follows:

$$C_{f}^{i} = F_{i \to f} C_i F_{i \to f}^{T} + Q_f , \tag{4.13}$$
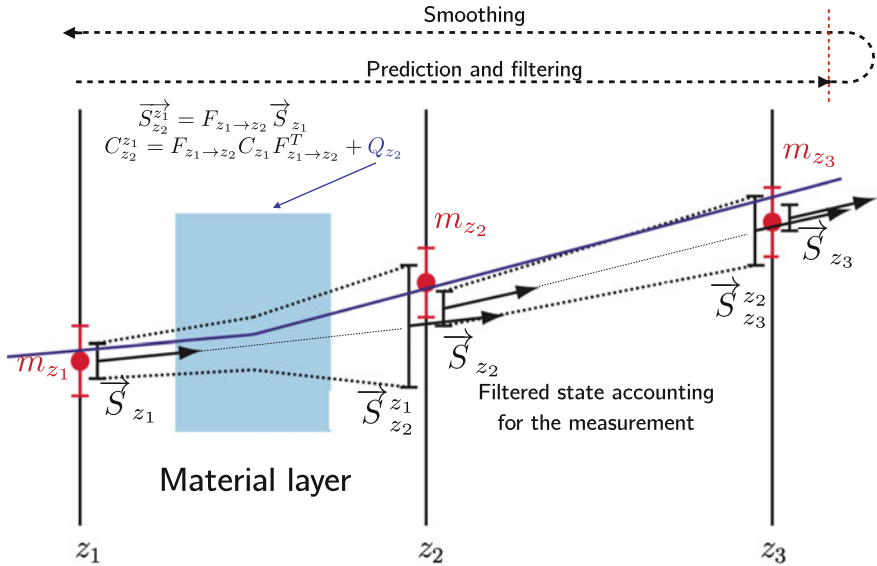
Fig. 4.5 Kalman formalism illustration: $\overrightarrow{S}_{z^i}$ represents the filtered states while $\overrightarrow{S}^i_f$ is the predicted state. The red dots are the actual detector measurements m_k used to perform the filtering. Material interactions are represented as a "wall" adding a "noise" term in the covariance matrix propagation (Q_{z_2} in the picture) and treating the effect as a local kink enlarging the error on the predicted state. The Kalman filter corrects for the change in direction of the trajectory by pulling the filtered state towards the actual measurements in the minimisation of the residual between the predicted state and the actual measurement

where C^i_f represents the increased uncertainty due to the propagation from z_i to z_f, while Q_f represents the system "noise" where material interaction can enter to parametrise the multiple scattering which can occur between z_i and z_f as well as energy losses.

In absence of a magnetic field between z_i and z_f the matrix form of $F_{i\to f}$ is the following:

$$\overrightarrow{S}_f = F_{z_i\to z_f}\overrightarrow{S}_i = \begin{pmatrix} 1 & 0 & z_f - z_i & 0 & 0 \\ 0 & 1 & 0 & z_f - z_i & 0 \\ 0 & 0 & 1 & 0 & 0 \\ 0 & 0 & 0 & 1 & 0 \\ 0 & 0 & 0 & 0 & 1 \end{pmatrix} \begin{pmatrix} x_f \\ y_f \\ t_{x,f} \\ t_{y,f} \\ \left(\dfrac{q}{p}\right)_f \end{pmatrix}. \tag{4.14}$$

The projection step aims at describing the relation between a measurement at a given $z = z_l$ in the detector (m_l) and a propagated state at z_l ($\overrightarrow{S}_l$):

$$m_l = H_l \overrightarrow{S}_l. \tag{4.15}$$

In this case H_l is the projection function at $z = z_l$ and the relation is highly simplified if a measurement m_l directly provides one of the coordinates of the track state. In such simpler case, H_l can be written as a matrix. The projection of track states to measurement is used to perform the so-called filtering of a measurement into the state. The detector measurement m_l and its covariance matrix V_l are, in general, expressed in different coordinate frames with respect to the track state at the same z_l. Therefore the projection function is a matrix which is able to project a track state into the measurement space. The difference between the measurement (m) and the projected state allows to calculate the predicted residual for which also an additional error can be assigned. The predicted residual r_f^i and its predicted error R_f^i is therefore computed as follows:

$$\begin{aligned}
r_f^i &= m_f - H_f \vec{S}_f^{\,i} \\
R_f^i &= V_f + H_f C_f^i H_f^T \ .
\end{aligned} \tag{4.16}$$

In order to calculate the best estimated state $\vec{S}_f$ at position f, the measurement (m_f) and the predicted state ($\vec{S}_f^{\,i}$) and their errors are used to build a χ^2 function. The minimisation of the χ^2 function leads to the following relations:

$$\begin{aligned}
\vec{S}_f &= \vec{S}_f^{\,i} + K_f r_f^i \\
C_f &= (1 - H_f K_f) C_f^i
\end{aligned} \tag{4.17}$$

where the K_f is the gain matrix and corresponds to the weight of the predicted residual (r_f^i) used to correct the predicted state $\vec{S}_f^{\,i}$. The gain matrix is computed as follows:

$$K_f = C_f^i H_f^T \left(V_f + H_f C_f^i H_f^T \right)^{-1} \tag{4.18}$$

Although a very expensive CPU operation would be required to invert the matrix, in LHCb the dimension of the matrix to invert is 1 (for UT and SciFi) and dimension 2 for the VELOPix (x, y measured simultaneously) according to the detector measurement V_f used to compute the residuals. For instance the x position measured in the detector is used for the SciFi as V_f for *x-layers* measurements.

Similarly to (4.16), one can compute a filtered residual (r_f) and error (R_f):

$$\begin{aligned}
r_f &= (1 - H_f K_f) r_f^i \\
R_f &= (1 - H_f K_f) R_f^i \ .
\end{aligned} \tag{4.19}$$

The hits for which the measurement V_f is defined can be accepted or rejected according its contribution to the χ^2, defined as:

$$\chi^2 = \frac{r_k}{R_k}. \tag{4.20}$$

Requirements on this χ^2 also allow to accept or reject hits on a given track as well as sum up the various χ^2 contributions from all the measurements in the track.

The Kalman filter is therefore an iterative procedure composed by the prediction of a track state from another known track states at the measurements position provided by the pattern recognition algorithms. The prediction is compared to the actual measurement provided by the detector and a residual is computed. The minimisation of the resulting χ^2 allows to evaluate an updated best track state which can then be used to iterate the process all over the other available measurements. Prediction and filter procedures propagate information in one dimension including at each iteration a new measurement.

The smoothing procedure is the same as prediction and filtering, but it starts from the last added measurement and it iterates in a reversed order to provide the best estimates of the track states at all measurement positions. Therefore, the outcome of the previous iteration in the forward directions are updated again providing a more accurate track quality assignment. We can summarise the main sub-algorithms used by the Kalman Filter as follows:

1. Seeding: it initialise the fit procedure determining an initial track state and its covariance matrix.
2. Prediction and projection: : the prediction step allows to compute the parameters of a state at a given position z_f given a known track state at the position z_i, using (4.11). The prediction step requires at least one initial track state (and its covariance matrix), which is usually provided by a "rough" fit performed in pattern recognition algorithms. Modifications of the covariance matrices are also provided in this step accounting for the multiple scattering which can occur between z_f and z_i.
3. Projection: it updates the track state with the measurement at the given plane as described above.
4. Smoothing: the fit iteration is reversed from the last added measurement to the first one to achieve the best precision in each node.

The Kalman fit running on LHCb trigger in Run I and Run II and the one currently implemented for the upgrade are executed without a prior knowledge of the *PID* (a π hypothesis is assigned for the multiple scattering corrections), therefore no energy loss for electrons and positrons are considered in the fit. It may be worth for the upgrade to introduce this feature if the timing budget will allow that. In LHCb the Kalman filter fit is run starting from the T-station up to the VELO. The simplified Kalman filter uses a simplified and fully parametric description of the detector allowing for a much faster execution of the fit.

4.1.9 Tracking Sequence Reconstruction for the LHCb Upgrade

The upgrade tracking sequence is designed to take advantage of the real-time detector alignment and calibration trigger strategy adopted for the LHCb Run II allowing to run data analysis directly on the trigger output without the need for reprocessing [20]. The run-by-run calibration and alignment tasks are run on the output of a fast tracking stage (*fast*), while the second track reconstruction stage (*best*) aims at being as efficient as possible. A block diagram of the two main tracking stages is show in Figs. 4.6 and 4.7.

The *fast* stage aims at reconstructing high momentum Long tracks as well as the primary vertices in order to perform efficient trigger selections at 40 MHz input rate. The output of the *fast* stage is used to run the real-time alignment and calibration tasks as it was the case in Run II as well as to perform HLT1-like trigger decisions. The reduced output rate of the *fast* stage allows to perform the full event reconstruction in the *best* stage. Although the primary requirement for the algorithms running in the *best* stage is to be the most efficient as possible, they also have to fit in the expected timing budget of the upgrade. A final strategy and a timing budget to be used as a reference for the *best* stage is not yet available. Nonetheless, the algorithms are still required to be as fast as possible also in the *best* stage to allow extra tasks to be executed and to reduce the cost of the upgrade farm.

Efforts are currently spent in the migration of the current LHCb software framework and all the event reconstruction related algorithms from a sequential structure to a parallel and multi-threaded one in order to optimise the usage of available computing resources. In few words, the current framework (used in Run I and Run II) allows to run one instance of the event reconstruction per CPU, while for the upgrade
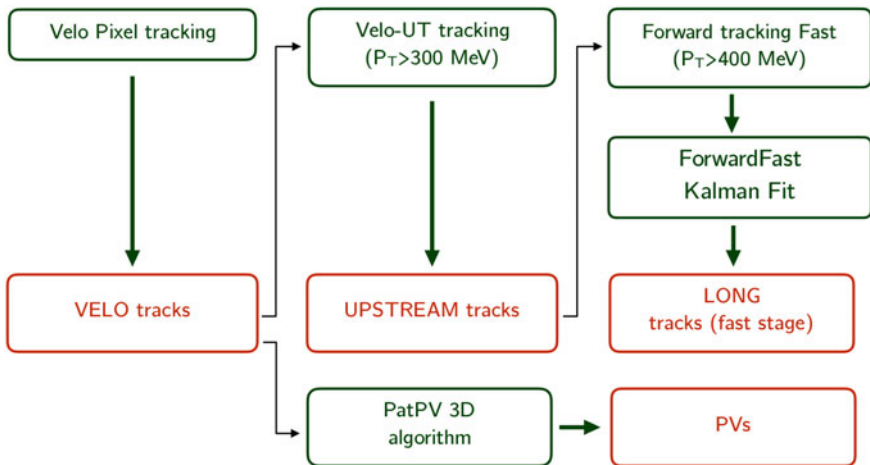
Fig. 4.6 A schematic view of the *fast* tracking stage
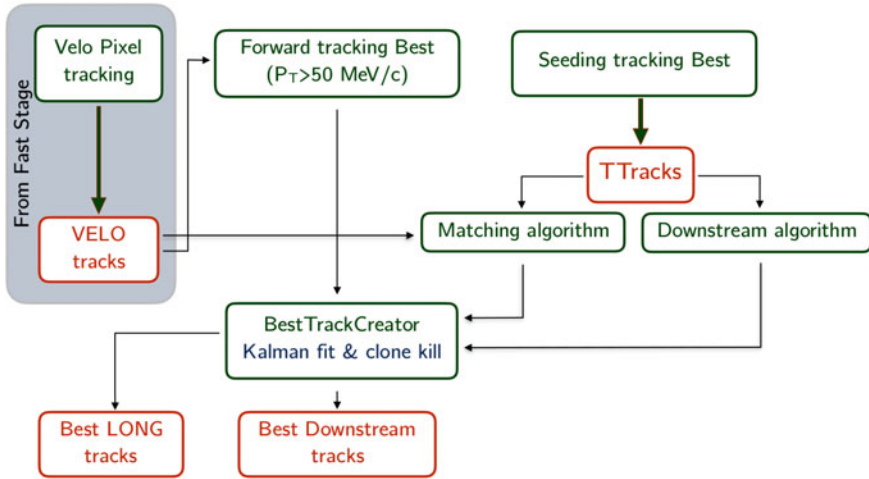
Fig. 4.7 A schematic view of the *best* tracking stage

the framework will be able to execute different pieces of the reconstruction sequence in different CPUs, maximising the usage of the available resources. The last step can be achieved only with a fully scheduled reconstruction sequence and an "a priori" knowledge of data object dependencies among algorithms. Furthermore, the data objects stored in the Transient Event Store (TES) which are needed for the event reconstruction (for example the detector hits, or the produced LHCb tracks) must be constant and algorithms are not allowed to modify their internal status otherwise race-conditions would appear and one cannot trust the outcome of the event reconstruction and reproduce the results in Monte Carlo simulations.

The pattern recognition algorithms used in the *fast* stage are, in sequential order:

1. Full VELO track reconstruction is performed finding all the VELO tracks, thanks to the *PrPixelTracking* algorithm (see Sect. 4.1.2).
2. `Upstream` tracks are reconstructed using the *PrVeloUT* reconstruction algorithm (see Sect. 4.1.3) tuned to find high p and p_T tracks. Only tracks with a p_T larger than 300 MeV/c are kept and for them the charge and the momentum are estimated.
3. `Long` tracks are reconstructed with the *PrForwardTracking* algorithm configured to find high p and p_T tracks. The input tracks used to seed the search of hits in the SciFi are the `Upstream` tracks found by the *PrVeloUT* algorithm. The forward tracking p_T threshold at this stage is 400 MeV/c. The reconstructed `Long` tracks serve as input to the calibration and alignment tasks as well as inputs for the trigger decisions.
4. `Long` tracks are fitted with a simplified Kalman Filter (simplified geometry description) and those tracks serve as input for the real-time alignment and calibration.

5. Once `Velo` tracks are reconstructed, PVs and SVs are reconstructed using the *PatPV3D* algorithm. The PV and SVs reconstruction can be run at any stage after the *PrPixelTracking*. Details on the PV reconstruction algorithm can be found in Ref. [21].

The *fast* stage is similar to the sequence described in the trigger TDR [22]. The *best* track reconstruction sequence is expected to run after the real-time alignment and calibration tasks are performed and trigger selections based on the presence of PV and SVs of physics interests is made. The sequence is composed by the following steps:

1. `Long` tracks are reconstructed again using as input all the VELO tracks reconstructed in the *fast* reconstruction sequence and the *PrForwardTracking* algorithm is run in a configuration aiming at finding all the lower momentum tracks.
2. `T-tracks` are reconstructed by the *Hybrid Seeding* algorithm.
3. `T-tracks` and `Velo` tracks are matched through the *PrMatchNN* algorithm producing a second set of `Long` tracks.
4. `Downstream` tracks are reconstructed by the *PrLongLivedTracking* algorithm aiming at matching `T-tracks` to hits in the UT.

`Long` tracks, `Downstream` tracks and `T-tracks` are fitted by the Kalman Filter algorithm which in LHCb is called *TrackBestTrackCreator* and replication of tracks or shorter versions of the same track is removed through a clone killing algorithm.

4.1.10   Performance Indicators

The performance of a tracking algorithm can be determined from simulation studies, comparing the number of tracks the algorithm is able to find (*reconstructed* tracks) with the maximum number of tracks that it could possibly find (*reconstructable* tracks).

It is also useful to define the tracking performances depending on the track type (`Long`, `Downstream`, `Upstream`, `Velo`, `T-Track`). Therefore, also subdetector *reconstructibility* criteria are defined in LHCb. Concerning the SciFi, a Monte Carlo simulated particle is said to be *reconstructable* in the SciFi if it has at least one *x-layer* and one *stereo* hit in each station. Therefore the minimum number of hits for a track to be *reconstructable* in the SciFi is 6. The various sub-detectors reconstructibility criteria are:

1. A Monte Carlo simulated particle is *reconstructible* in the VELOPix if it fires at least three modules, i.e. if there are clusters (produced out of the pixels) associated to the particle in three or more modules.
2. A particle is *reconstructible* in the SciFi if there are at least one *x-layer* and one *stereo* hit in each of the three tracking stations.
3. A particle is *reconstructible* in the UT if there is one *x-layer* and one *stereo* hit associated to the particle out of the four detection layers.

Therefore, the definition of reconstructibility criteria depending on the track type are the following:

1. A particle is *reconstructible* as a `Velo` tracks if it satisfies the VELOPix reconstructibility criteria.
2. A particle is *reconstructible* as a `Upstream` track if it satisfies the VELOPix and UT reconstructibility criteria.
3. A particle is *reconstructible* as a `Long` track if it satisfies the VELOPix and SciFi reconstructibility criteria.
4. A particle is *reconstructible* as a `Downstream` track if it satisfies the SciFi and UT reconstructibility criteria.

In order to associate the *reconstructed* tracks to the *reconstructable* ones a cross-check of the content of hits in both of them is performed. A *reconstructed* track is said to be *matched* to a simulated particle if they share at least 70% of the hits. Based on these definitions, one can evaluate the following performances indicators.

- The **tracking efficiency** ($\epsilon_{Tracking}$) is defined as the ratio between the amount of *reconstructed* and *matched* tracks with respect to the total amount of *reconstructable* tracks:

$$\epsilon_{Tracking} = \frac{reconstructed \ \& \ matched}{reconstructible}$$

- The **ghost rate** is the amount of *reconstructed* tracks not associated to a Monte Carlo particle (i.e. having less than 70% of hits matching) with respect to the total amount of tracks found by the pattern recognition algorithm:

$$ghost \ rate = \frac{reconstructed \ not \ matched}{reconstructed}$$

These tracks arise when hits, mostly coming from different particles or from noise, are randomly combined, producing candidates which pass the quality cuts of the pattern recognition algorithm. Higher track multiplicity events tend to produce more fake tracks than lower ones, so it is also useful to estimate the event-averaged *ghost rate*.

- The **hit purity** of a *reconstructed* track *matched* to a simulated particle, is the fraction of hits of the *reconstructed* track in common with the *matched* track:

$$hit \ purity = \frac{hits \ shared \ between \ the \ matched \ and \ the \ reconstructed \ track}{hits \ of \ the \ reconstructed \ track}$$

- The **hit efficiency** expresses the efficiency of the pattern recognition algorithm to pick up hits on *reconstructed* tracks which are expected to belong to the associated particle:

$$hit \ efficiency = \frac{hits \ shared \ between \ the \ matched \ and \ the \ reconstructed \ track}{hits \ of \ the \ matched \ particle}$$

The described performance indicators have been used to determine the stand-alone tracking algorithm for the SciFi (see Sect. 4.5).

In the new fully software based trigger system, the track reconstruction will play a crucial role: all the tracking algorithms must be able to run on the online farm [22]. The more complete are the information available to perform trigger decisions at early stages in the event reconstruction sequence, the higher are the physics capabilities of the detector. The real challenge is therefore the development of reconstruction software algorithms optimised in terms of performance and timing.

The tracking system, together with the knowledge of the magnetic field of the LHCb dipole [23] are the fundamental ingredients to reconstruct the charged tracks produced in the collisions and to provide a measurement of their momentum. The momentum is correlated to the "kick" that charged particles receive from the magnetic field when they travel from the UT to the SciFi. The SciFi is a fundamental component of the tracking, as it allows the reconstruction of charged particles both originating close to the interaction point or coming from other long-lived decaying particles. The latter would not leave any hits in the VELO but only in the UT and the SciFi.

4.2   The Scintillating Fibre Tracker Detector: Principles and Simulation

The SciFi is composed by three tracking stations, *T1*, *T2*, *T3* as shown in Fig. 4.8 and a front view of one detection layer is shown in Fig. 4.9.

Each station is composed by four layers of stacked scintillating fibers, separated by air-filled gap of 50 mm, oriented in the so called *stereo* configuration (*x-u-v-x*).

The elementary components of a detection layer are (see Fig. 4.9):

- Modules: a total of 12 modules in the detection layers placed at the *T2* and *T3* z positions. 10 modules will be used in *T1*.
- Fibre mats: each module is separated at $y = 0$ by a mirror which is used to increase the light yield of the scintillating fibres. A total of 4×2 fibre mats compose a module.
- Scintillating fibres: a fibre mat is composed by six stacked layers of 2.5 m long scintillating fibres for a total depth in z of 1.6 mm which are used as active material. A total of 11,000 Km of fibres will be used for the entire detector.
- Silicon PhotoMultipliers (*SiPM*): fibre mats (width = 540 mm) are read-out by four *SiPM*. Each *SiPM* has 128 read-out channels (channel pitch of 250 μm) aiming at collecting the light produced and transported in the fibers.
- Read-Out system: the *SiPM* are connected to the Front-End electronics where dedicated algorithms (implemented in FPGA) are used to process the *SiPM* output producing clusters. Clusters are sent to the online into a packed form matching the bandwidth requirements and are used to perform track reconstruction.

The fibers mats in the first and fourth *x-layer* (within the same station) are vertically oriented, i.e. the fiber mats are parallel to the y axis of the laboratory frame. Therefore, the read-out of a *x-layer* provides the direct measurement of the $x^{track}(z_{layer})$ position. The second (*u*) and the third (*v*) layers are identical to the *x-layer*, but their fiber
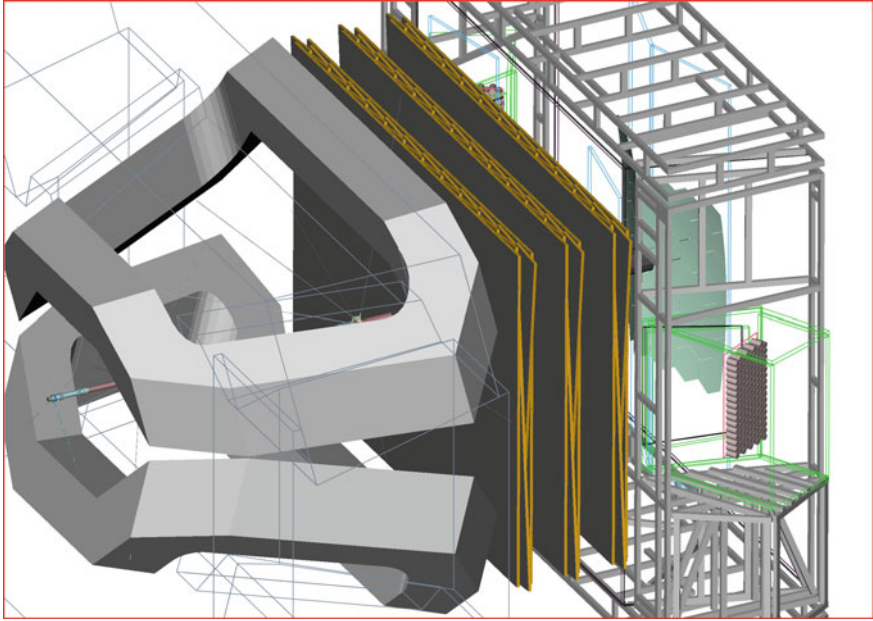
Fig. 4.8 Sketch of the three SciFi stations placed downstream the magnet. Each station is composed by four layers of stacked 2.5 m long scintillating fibres (diameter $\Phi = 250\,\mu$m) used as active material, following an *x-u-v-x stereo* configuration
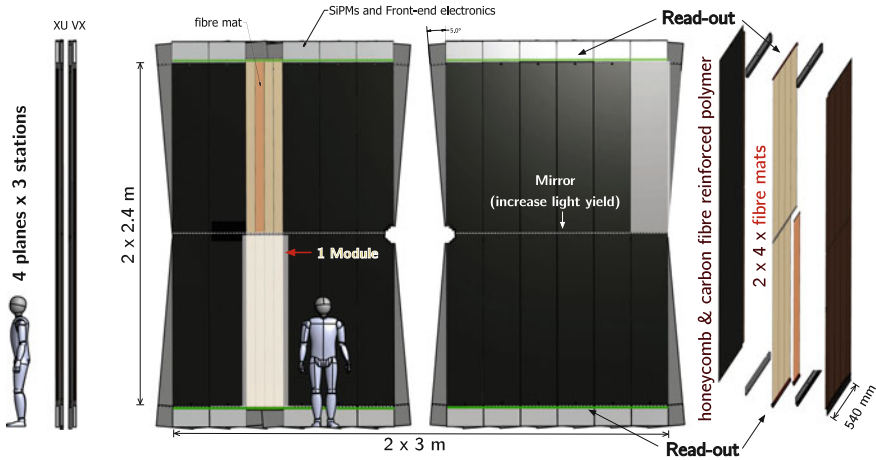
Fig. 4.9 Front view of one SciFi station. Scintillating fibers (diameter $\Phi = 250$ mm) run vertically and they are stacked into six layers of fibre to form the fibre mat. Fibers are mirrored at one end (at $y = 0$) to increase the light yield and the light produced by the interacting particle is collected by *SiPM* outside the LHCb acceptance. Fibre mats are placed in each layer in between honeycomb and carbon fibre reinforced polymers to ensure mechanical stability. The *SiPM* are directly coupled to the front-end electronics boards. Figure taken from [24]
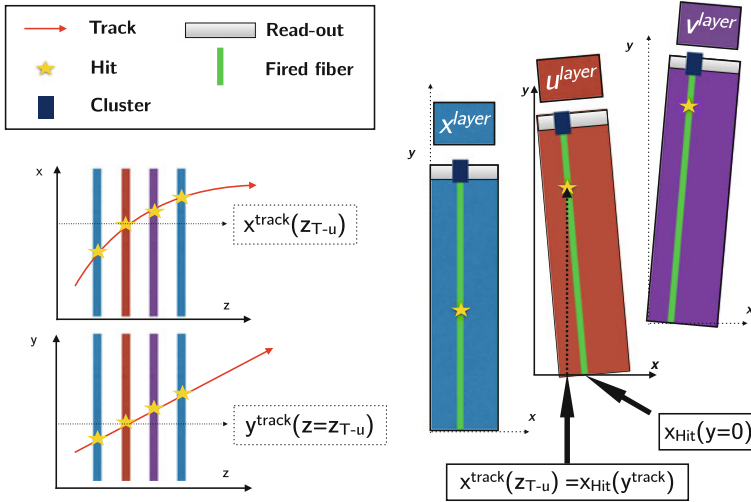
Fig. 4.10 From the *x-layers* measurements, the *x* position in *u/v-layers* can be predicted. Information on the *y-z* plane motion of the particle can be found combining measurements from the *u/v-layers* hits

mats are tilted with respect to the *x-layer* by $+5°$ and $-5°$ respectively. The readout of the *u/v-layers* provides the *u* and *v* stereo coordinates, which are used to extract the information on the *y-z* plane motion of the particles. The main geometrical information used in pattern recognition algorithms when dealing with *u/v-layers* are sketched in Fig. 4.10. In the following a description of the SciFi elementary components is provided as well as the flow of information to produce an actual hit, the elementary object used for pattern recognition.

4.2.1 Scintillating Fibres

The active detector material of the SciFi tracker are scintillating plastic fibres of type SCSF-78MJ produced by Kuraray [25]. The length of the fibers used for the SciFi is 2.5 m and they have a cylindrical shape made of a core surrounded by two claddings as shown in Fig. 4.11.

The core of the fibres is made of polystyrene used as scintillating material doped with two organic dyes. The traversing particle interacts with the fibre core and the few eV energy is deposited exciting the polystyrene. The first doping organic dye is made of p-terphenyl (TP) and the second doping dye is made of tetraphenyl butadiene (TPB). The TP dye absorbs the excitation energy from polystyrene via nonradiative dipole-dipole interactions, process called Förster Transfer [26]. The excited electron of the dye, when returning to its initial quantum state, emits photons. The re-absorption of the photon inside the fibre itself is avoided using a second doping
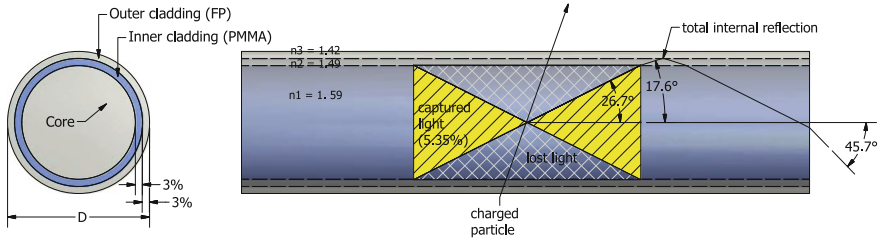
Fig. 4.11 A schematic view of the scintillating fibre with two claddings. Traversing particles produce light in the core of the fibre and the light produced inside the trapping angle is able to travel via total reflection to both ends of the fibres. Figure taken from [24]

dye which is employed as a wavelength shifter. TP is used because of its high quantum efficiency ($>95\%$) and fast decay time ($<$ few ns) and the TPD because of its success as wavelength shifter in previous experiments [12].

The fibre diameter is $250\,\mu$m and the size accounts for the double-cladding structure ($6\% + 6\%$ of the total diameter). The light produced inside the fibres is propagated via total reflections and the claddings are arranged by decreasing indices of refraction material to increase the amount of trapped light. Around 300 photons are produced isotropically per MIP interacting particle and the total trapping efficiency of the fibre is 10.7%, leading to 30 photons fully captured and propagated via total reflection in the fibers which can be detected by the *SiPM*.

Several effects lead to an attenuation of the trapped light in the fibre: photons with $\lambda < 450$ nm are re-absorbed by the wavelength shifter dye; for $\lambda > 450$ nm molecular vibrations, Rayleigh scattering, electronic transitions and effects due to quality of the fibers boundaries become the dominant source of attenuation. The nominal expected attenuation length for brand-new fibers is 3.5 m. It has been estimated that a 40% loss in transmission properties for the most irradiated region of the detector will be reached after $50\,\text{fb}^{-1}$ of data taking due to the ionising radiation absorbed by the fibres during data taking.[3] This effect is implemented in the simulation through an attenuation field map taking into account both ageing of the detector after $50\,\text{fb}^{-1}$ data taking period as well as the path length of direct and reflected light reaching the *SiPM*. The simulated dose distribution in Gy at *T1* for $50\,\text{fb}^{-1}$ is shown in Fig. 4.12. The dose peaks at about 30 kGy close to the beampipe and decreases steeper than exponential to the outer region.

---

[3]Ionising radiation implies the creation of absorption and scattering centres inside the fibres, leading to further attenuation of the light in the fibres.

Fig. 4.12 Simulated dose distribution in Gy (z-axis) as a function of the x-y plane after 50 fb^{-1} of data taking at the first T-station z location. The higher loss in transmission properties will affect the region close to the beampipe because of the highest radiation dose. Figure taken from [12]
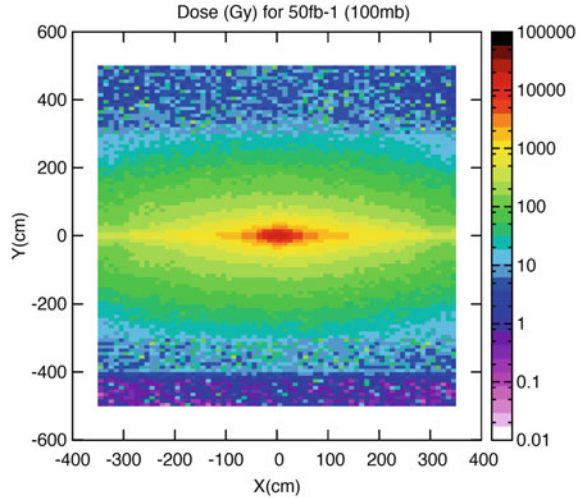
4.2.2 Silicon Photomultipliers (*SiPM*)

The light escaping the fibre end is detected by *SiPM* made of custom 128-channel arrays with single channel pitch of 250 μm. The main characteristics behind the choice of such technology are the high gain, low operational voltage, small granularity, fast response, insensitivity to magnetic fields and the single photon counting properties. A schematic view of the 128-channel array composing the *SiPM* is shown in Fig. 4.13. Missing fibres-*SiPM* coupling arise from the separation between the two dies with 64 channels mounted on one mechanical unit made of 128 channels as well as from the distance separating two consecutive *SiPM*. Also this effect is simulated as it will be explained later.

The single read-out channel composing the *SiPM* is made of a rectangular matrix (250 μm ×1.6 mm) of pixels operating as avalanche photodiodes in Geiger-mode. The *SiPM* are designed as a matrix of small pixels (see Fig. 4.13). Each photon having an energy above the bandgap induce an electron-hole pair creation. Each pixel is basically a $p − n$ junction operating at reverse voltage. When the electron-hole pair is created by the incoming photon, an avalanche is generated (with a given probability), and the avalanche is stopped with the help of a quench resistor serially connected to the diode. The current produced by each pixel is independent of the number of entering photons in each pixel, and it only depends of the applied voltage. Therefore a matrix of pixels with very small granularity (smaller than the fibre diameter), allows to perform single photon counting and the amount of fired pixels represents the number of collected photons defining what is called the light yield.

The amounts of fired pixels for a small amount of entering light is proportional to the number of photons and it saturates when the amount of photons is much higher than the number of pixels. A fundamental parameter is the photo detection efficiency
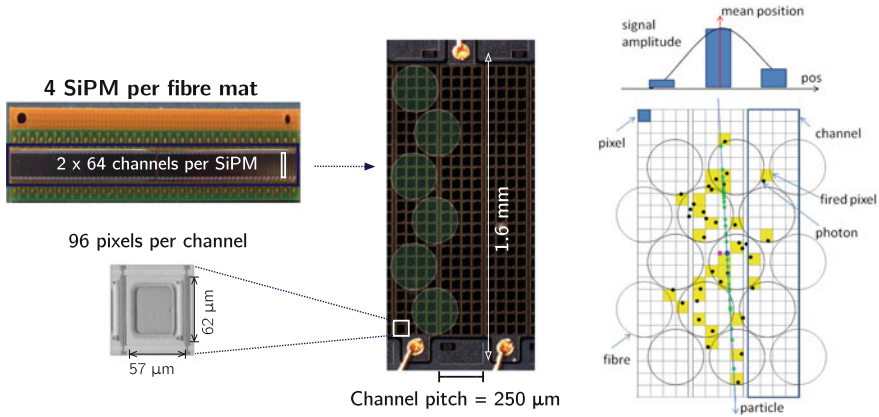
Fig. 4.13 Each fibre mat is composed of 4 *SiPM* and each *SiPM* has a total of 128 read-out channels. Each read-out channel is coupled to the six layers of stacked fibres. A single read-out channel is composed of a rectangular matrix of pixels aiming at performing photon counting. On the right a sketch showing the cluster formation: the average position of the track is computed once the charge from each pixel within a read-out channel is collected. Figure taken from [24]

(PDE) which accounts for the combined probabilities that a single electron-hole is produced from a photon with a given wavelength (λ) and that the electron-hole pair is able to generate the avalanche. The PDE also accounts for the fraction of active surface in the pixel with respect to the total surface of the pixel. The PDE for the *SiPM* that will be used for the SciFi is shown in Fig. 4.14.

Signal from the *SiPM* can be generated also without light from the fibers and this defines what is called noise:

- Thermal noise: random avalanches from thermal agitation can generate the same signal than real photons. Thermal noise becomes very important after irradiation since the entering particles modifies the structure of the silicon devices raising the probability of thermal noise. Indeed, the SciFi will operate the *SiPM* at $-40\,°C$ to reduce such noise effect. The thermal noise rate is expected to be reduced of a factor 2 every 8–$10\,°C$ [27]. The cooling technology is briefly described in Sect. 4.2.3.
- After pulse: there is a non-null probability that after a pixel has fired it can fire again. This contribution is relatively small compared to the other ones for the *SiPM* which will be used for the SciFi.
- Pixel-to-Pixel cross-talk: the avalanche in one pixel can lead to the emittance of an additional photon which triggers an avalanche in the close-by pixel. Cross-talk depends on the over voltage as the PDE and the final device must satisfy specific requirements on both the parameters.

Laboratory measurements are used to set the parameters describing the *SiPM* noise effects for the SciFi simulation.
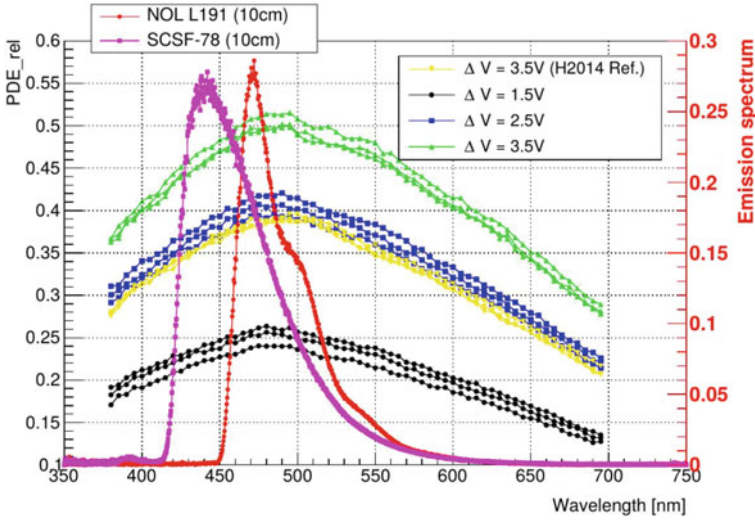
Fig. 4.14 Photon detection efficiency (PDE) measured on three *SiPM* channels (Hamamatsu devices available in 2015) at different reversed-bias overvoltage (ΔV) as a function of the wavelength of the photon triggering the electron-hole pair creation: $\Delta V = 1.5$ V (black), 2.5 V (blue), 3.5 V (green). The PDE of the Hamamatsu *SiPM* available in 2014 are also shown in yellow for $\Delta V = 3.5$ V. The emission spectra of Kuraray fibre is also plotted in red (NOL L191) as well as the emission spectra of another type of fibres emitting on green wavelength (in magenta, named SCSF-78 L191). A matching between PDE and fibre emission spectra is mandatory to maximise the light yield. Figure taken from [24]

4.2.3   Read-Out Electronics

The SciFi electronics can be grouped into two categories: front-end (FE) electronics and back-end (BE) electronics. The former is mounted directly in the SciFi modules and is surrounded by the cooling box, the latter is placed outside the LHCb cavern in the counting house. The FE electronics is responsible for the digitisation and clustering of the *SiPM* signal output and the BE is responsible of processing the transmitted data.

A custom designed mixed-signal ASIC connected without interface to the *SiPM* arrays, called PACIFIC, is responsible of the amplification, shaping and charge integration within a 25 ns time window of the *SiPM* output current. The PACIFIC convert the analogic value to a digital value through a non-linear 2-bit ADC, comparing the analog signal to three individual adjustable thresholds. Concerning the time integration of the signal, although PACIFIC uses two interleaved gated integrators to avoid dead time in order to count all the photons produced by one particle hit, the output of the integrator strongly depends on the arrival time of the light from the fibres.

The "quantized" 2-bit charge information from the *SiPM* channels is sent to a clustering FPGA which serves as zero suppression of the signal and as reducer of the
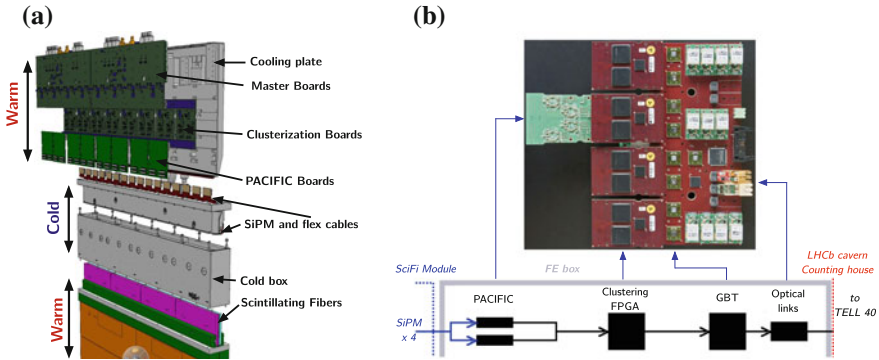
Fig. 4.15 **a** shows the structure of the read-out box and the implementation of the cooling system for the *SiPM*. **b** shows the Front-End electronics used for the SciFi. The *SiPM* signals are converted to a digital signal by the PACIFIC chip and its output is processed by clustering FPGA devices. The output is sent to the Back-End electronics and processed by the trigger farm

output bandwidth. Indeed, several channels are merged into a single measurement, called cluster. The four different steps of the clustering algorithm are:

- If a signal in one channel exceeds the *highest* threshold (3.5 photoelectrons) corresponding to a value unlikely to be generated from noise, a cluster is directly produced with a cluster size equal to one (i.e. one read-out channel contributes to the cluster). The produced cluster is identified by the unique identifier of the read-out channel.
- If the highest threshold is not reached, channels exceeding the *seed* threshold are considered and a search of neighbouring channels is performed.
- The neighbour read-out channels (relative to the one exceeding the seed threshold) are added to the cluster formation process if they exceed the *neighbour* threshold.
- A cluster is produced if the sum of the charges exceeds the *sum* threshold. The charge-weighted channel position is evaluated and the cluster is stored with the unique identifier of the channel corresponding to the mean position.

The produced clusters are sent to the BE electronics with the help of a GigaBit Transreceiver (GBT) able to handle the high bandwidth. Before pattern recognition algorithms are executed, the clusters are decoded: the unique identifier stored in binary format from the clustering algorithm is converted into a x position (placed in the middle of the channel where the weighted charge mean is computed) identifying the hit to be used for track reconstruction.

A sketch showing the read-out board, FE electronics layout and cooling system for the *SiPM* is shown in Fig. 4.15.

4.2.4   SciFi Simulation

The SciFi simulation and the simulation used to produce the samples used to develop and test the `Hybrid Seeding` algorithm described in Sect. 4.4 consists of three different steps:

1. The collisions are simulated and the particles from a specific decay chain are generated. The particles decays and their interactions with the detector are simulated. Therefore, each simulated particle generates a list of energy deposits in the various sub-detectors.
2. The read-out electronics chain is simulated producing the corresponding *hits*. *Hits* in the SciFi are the result of the clustering procedure described in Sect. 4.2.3 aiming at combining the electronic signals arising from the converted energy deposits in the various read-out channels. The single cluster contains compressed information in binary format concerning the position of the cluster and extra information which are useful for pattern recognition. The cluster (i.e. the packed version of the hits) is encoded in simulation as it is expected to be in real data taking. This step is called digitization.
3. The hit is decoded producing the actual hit which is used to perform track reconstruction.

The most critical SciFi detector simulation aspect which has an important effect for pattern recognition is the digitization step. The relevant information stored in the energy deposit are the following:

- Entry, middle and exit position of the particle interacting in the active material volume.
- The amount of energy deposited and the time stamp of the interaction with respect to a common reference. The energy deposited depends on the path length of the track in the active material.
- The reference true particle producing the energy deposit, which is used in the simulation to keep track of the relation between detector hits and interacting true simulated particles.

The digitization step aims at reproducing the expected read-out output for real data. Its simulation is performed in sequential order by different steps:

1. The scintillation light is produced in the fibres proportionally to the amount of deposited energy.
2. The amount of light produced in the fibres is converted into a number of photons which are able to reach the read-out chip (placed outside the LHCb acceptance at around $y = 2.5$ m). In this step different effects are simulated:

    - Light attenuation in the fibres due to the path length traversed by the photons before reaching the corresponding read-out channel. Different timings are assigned to the light going directly to the read-out channels and the light reflected by the mirror placed at $y = 0$.

- Additional light attenuation is simulated accounting for the fibers opacity arising from the expected radiation damages after $50\,\mathrm{fb}^{-1}$ of data-taking. All the samples used in this document account for the ageing of the SciFi detector after around 10 years of data taking.
- The amount of light produced by the fibre mat (stacked layers of fibres) in a single read-out channel ($250\,\mu\mathrm{m}$ pitch size) is converted to *deposits* having a proper time distribution, the charge deposit information and the location of the corresponding read-out channel.

3. The read-out noise effects (dark counts, thermal noise, after-pulses and crosstalk) and time response are also simulated adding charge deposits to the read-out channels.
4. Dead-regions of the read-out channels are also simulated removing the energy deposits corresponding to the missing couplings between fibres and read-out channels.
5. The charge deposit is quantized producing the so called *digits*. *Digits* have a one-to-one correspondence with single read-out channels and they are combined together via a clustering algorithm.
6. The clustering algorithm uses the quantized charge in each read-out channel to compute a weighted mean position of the resulting cluster. A sketch of the working principle of the clustering algorithm is shown in Fig. 4.13.
7. The produced cluster stores among various information, the cluster size corresponding to the amount of channels from which the cluster has been generated as well as the unique identifier (ID, in binary format) of the read-out channel where the mean position has been computed.

Thresholds, clustering algorithm implementation, amount of noise, size of dead regions, detector acceptance, fibres thickness, *SiPM* characteristics as well as spillover contributions (hits from previous/next bunch crossing) are simulated and measurements in laboratory and test-beam are used to tune the various effects to have the best description of the detector.

In the simulation, for each cluster a linker to the list of particles contributing to its is also stored to evaluate tracking efficiencies. The detector characteristics having an impact on the track reconstruction and its performance are:

- the **detector occupancy** which is the amount of hits in the detector. For instance, higher read-out noise, lower thresholds in the clustering algorithm, larger time integration window, shorter bunch spacing, higher track multiplicity, higher acceptance in the central region imply an increasing of detector occupancy. For the SciFi, a single *SiPM* array contains a total of 128 read-out channels, thus the occupancy is measured in terms of number of hits per *SiPM* array.
- the **hit conversion probability**, i.e. the probability that an energy deposit in the active material is converted into a hit for pattern recognition;
- the **acceptance of the detector**, depending on the detector geometry.

A comparison plot of the actual hit density in the SciFi and how the detector is seen by the pattern recognition algorithms after digitization is shown in Fig. 4.16.
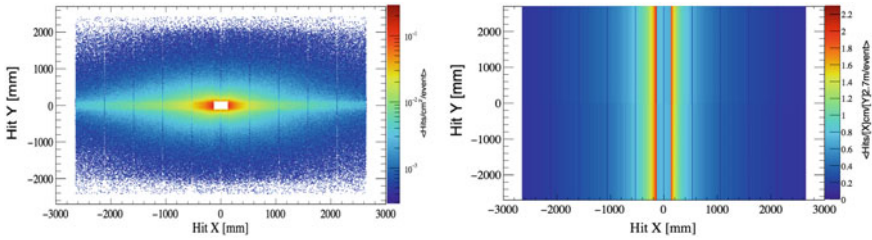
Fig. 4.16 On the left the spatial-density of energy deposits from traversing particles in the transverse plane across the first station of the SciFi. On the right the detector hit density after loosing the *y* information due to the 2.5 m fibers length. Pattern recognition algorithms using the SciFi "see" the detector stations (on average) as shown on the plot on the right. The 2.5 m length of the scintillating fibers makes impossible to extract simultaneously the *x* and *y* information. In the plot it is also possible to visualize the geometrical gaps between the SciFi modules

The detector occupancy for the simulated samples is on average 4.5 clusters per *SiPM* per event in the largest hit density detector region. This means that one would expect to find on average in the largest hit density part of the detector one cluster every 7 mm, assuming the clusters to be uncorrelated (i.e. not generated from the same hit). The average number of hits per layer in the SciFi for a typical event is around 500–700 at the upgrade conditions.[4]

We will refer in this document to three samples differing one from another not only in detector description, but also in event topology. *Sample 1* uses the detector geometry and same digitization used for the SciFi Technical Design Report (TDR) [28] (no spill-over and detector noise simulated), while *Sample 2* implements a more realistic detector description including spill-over and noise but still the same digitization as in the TDR. *Sample 3* uses an improved detector description and an updated digitization of the detector, compatible with the test beam results performed in 2015 and 2016. The conventions and the amount of simulated events used are shown in Table 4.1b and the simulated upgrade running conditions for each sample are shown in Table 4.1a. For each sample, the occupancies in different SciFi regions are shown in Fig. 4.17.

All the samples have been produced at the upgrade conditions (Table 4.1a) but with different geometries and digitization implementations. The main differences are summarized in Table 4.1c. The details of how the samples have been digitized for *Sample 1* and *Sample 2* can be found in Ref. [28] and the description of the simulated geometry of the detector for *Sample 1* can be found in Ref. [29].

Different beam-pipe hole geometries lead to different acceptances for the tracks, while the *SiPM* gaps, i.e. the distance between consecutive *SiPM* arrays and the gaps between the 2×64 channels inside the same read-out channel lead to digitization inefficiencies. It can be observed in Fig. 4.17 that *Sample 1* does not contain hits

---

[4]Both the occupancy (and track multiplicity) in the detector and the amount of hits in the whole SciFi are directly correlated to the amount of primary vertices per event, the noise of the read-out and the spill-over.

Table 4.1 Simulated samples summary tables

$\sqrt{s}$	Bunch spacing	$\mathscr{L}$	ν
14 TeV	25 ns	20×10^{32} cm^{-2}s^{-1}	7.6

a Simulated running conditions for all the samples. ν is the mean number of primary vertices per bunch crossing.

Sample	Nb. Events	Decay mode	Geometry version
Sample 1	10,000	$B_s^0 \to \phi(K^+K^-\phi)K^+K^-$	V2
Sample 2	10,000	$D^{*-} \to D^0(K_S^0\pi^+\pi^{-0})\pi^-$	V5
Sample 3	10,750	$B_s^0 \to \phi(K^+K^-\phi)K^+K^-$	V6

b Different decay modes used for the simulated samples.

Sample	$\epsilon_{Acceptance}$ *long from B* tracks	$\epsilon_{conversion}$	$\epsilon_{effective}$	Noise simulated	Spill-over	Updated digitization
Sample 1	100%	$(96.6 \pm 0.2)\%$	$(95.6\pm 0.2)\%$	✗	✗	✗
Sample 2	99.08%	$(99.0\pm 0.2)\%$	$(97.5\pm 0.2)\%$	✓	✓	✗
Sample 3	99.07%	$(97.7 \pm 0.2)\%$	$(96.2\pm 0.2)\%$	✓	✓	✓

c Intrinsic properties of the samples used in this thesis. The $\epsilon_{Acceptance}$ for *Sample 2* and *Sample 3* is evaluated taking as reference the *Sample 1*
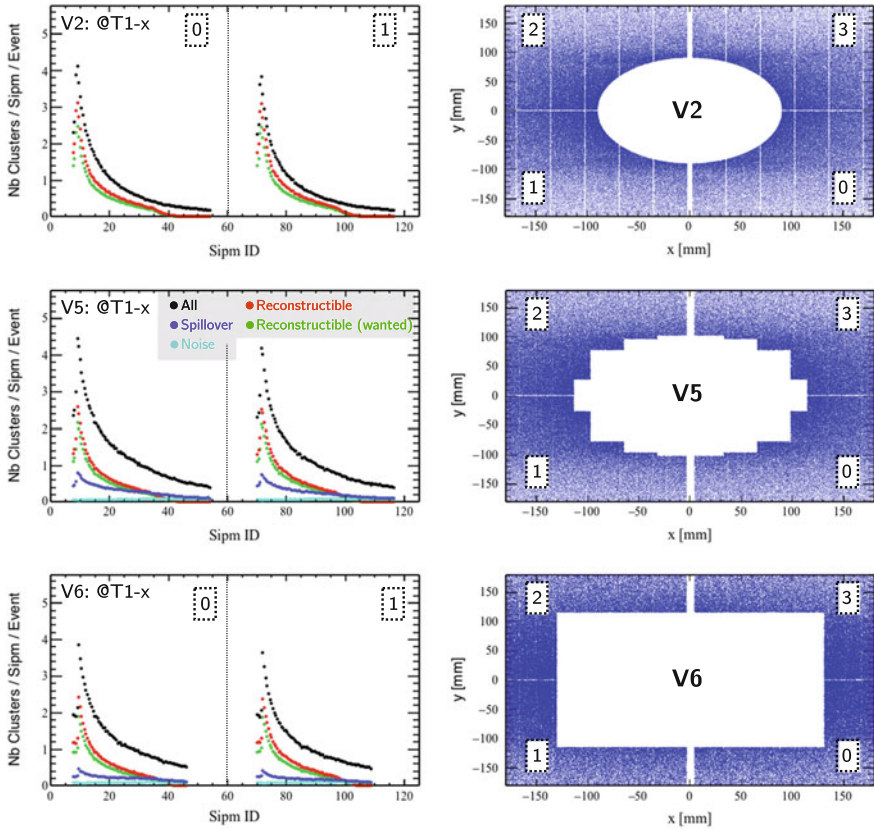
Fig. 4.17 On the left, the occupancy distributions of the three samples in the first *x-layer* SciFi tracking station. The contributions of the different sources are presented, as well as the difference for the case of *reconstructable* tracks and *reconstructable* tracks not originating from material interaction. The numbers inside the dotted rectangles refer to the layer quarters defined on the right plot (quarters 2 and 3 are not shown, they are basically equal to quarters 0 and 1). On the right, the energy deposits from particles going through the first *x-layer* SciFi tracking station which are producing useful hits for pattern recognition are shown as well as the naming of the various geometry versions for the different used samples. It can also be noted that V6 geometry has 1 module less than V2 and V5 from the cut-off in the Sipm ID distribution

arising from spill-over and detector noise, but it covers a larger acceptance (smaller beam-pipe hole size). Nevertheless, the gaps between *SiPM* are larger than the other two cases, causing a higher rate of missing conversion of energy deposits into useful hits for pattern recognition. In addition, *Sample 3* has two modules (16 *SiPM* arrays) less in *T1* stations corresponding to large $|x|$ values with respect to *Sample 2* and *Sample 1*.[5]

---

[5]Note the sharp cut in the *SiPM* ID distribution for the occupancy in Fig. 4.17.

The detector geometry and its digitization (noise, time response, thresholds, cluster cuts and clusterization algorithm) play a fundamental role in the determination of the minimal requirements to determine if a track is considered *reconstructable*, since this definition requires a minimal number of fired layers (from digitized clusters). Furthermore, they are also crucial in the determination of the minimal number of hits per track to be required for in the pattern recognition algorithm and it sets an upper limit on achievable performance according to the requirements. Acceptance ratios between the different geometries have also been evaluated. We quote in Table 4.1c the ratio ($\epsilon_{Acceptance}$) of long tracks from decaying *b* hadrons (*long from B*) being in the SciFi geometrical acceptance with respect to the geometrical acceptance defined in *Sample 1*.

Another important aspect for which the samples are differing among each other is the amount of active material simulated. *Sample 1* is simulated with five layers of packed fibers per tracking layer for a total depth in *z* direction of 1.2 mm, while both *Sample 2* and *Sample 3* have a total depth in *z* direction of 1.3 mm leading to a better light yield but larger budget material. In order to disentangle the impact of geometry and digitization inefficiencies, we introduce the following parameters:

- *hit conversion probability* ($\epsilon_{conversion}$) defined as the probability to find a cluster after digitization given the existence of an energy deposit in the simulated detector. This value depends on several factors we simulate: light attenuation in the fibers, time response of the *SiPM*, noise, clustering thresholds, radiation damage in the *SiPM* and fibers and the presence of read-out dead regions.[6]
- *effective hit probability* ($\epsilon_{effective}$) arises from the product of acceptance and digitization effects. This value is basically the value one would get fitting the probability distribution of number of fired layer for a given track given the 12 available layers (see Fig. 4.18) as follows:

$$Prob(n_{track}^{layers}|12) = \binom{12}{n_{track}^{layers}} \cdot (1 - \epsilon_{effective})^{12-n_{track}^{layers}} \cdot \left(\epsilon_{effective}\right)^{n_{track}^{layers}}$$

where n_{track}^{layers} is the number of layers containing at least one hit for a given track and $\epsilon_{effective}$ is the *effective hit probability* which is extracted from the fit.

The knowledge of the $\epsilon_{effective}$ parameter, for a given detector geometry and digitization, plays an important role:

1. it allows to know the theoretical upper limit for *tracking efficiencies* when a minimal requirement on the number of hits on track is applied;
2. if very high tracking efficiencies are desired (>98%), it allows to evaluate what is minimal amount of hits to be required to reconstruct tracks.

---

[6]For example, *Sample 1* has larger gaps between one *SiPM* and the next one with respect to the other *Samples*.
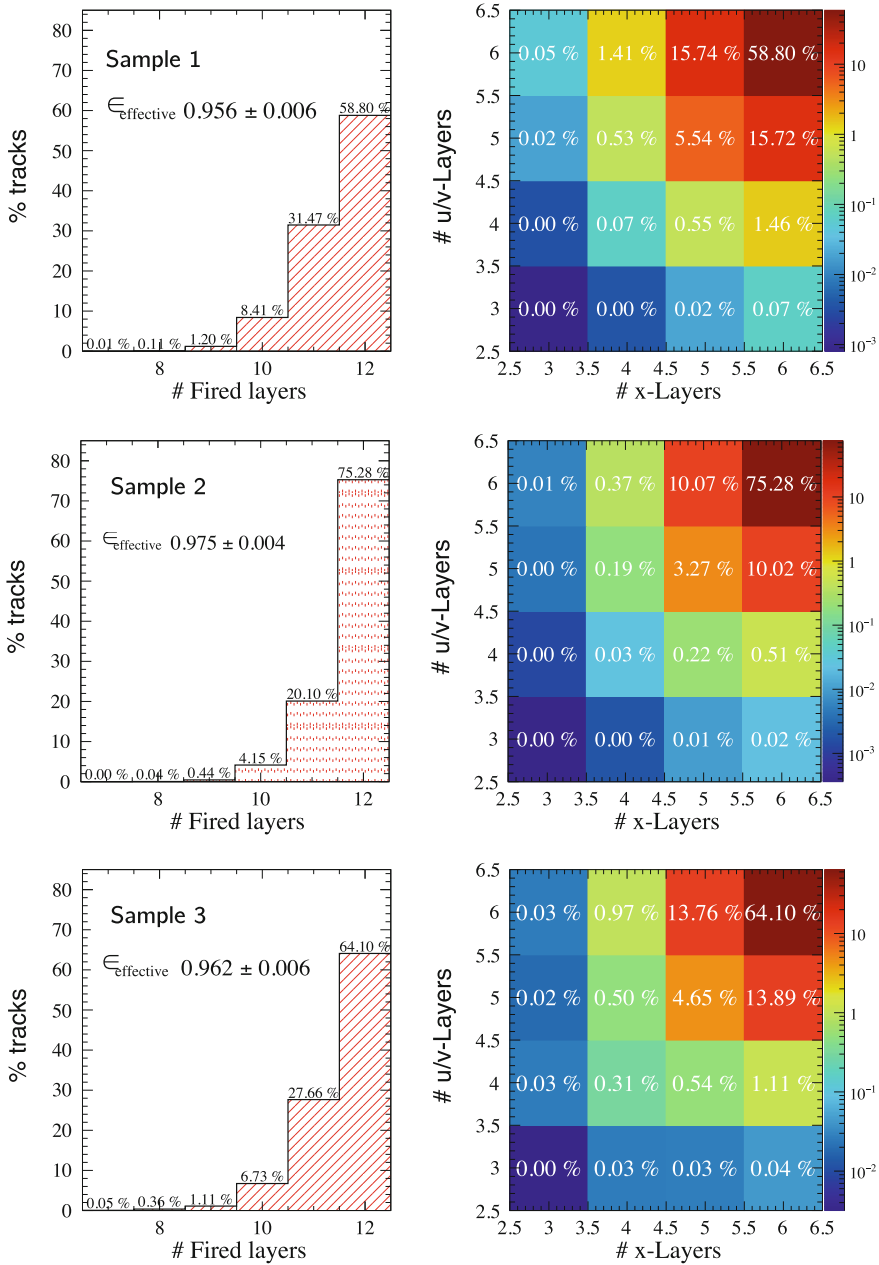
Fig. 4.18 On the left, the distributions of *reconstructable* tracks of physics interest. The x-axis shows the number of layers with at least one hit for the tracks considered. On the right, the same distribution but as a function of the number of fired *x-layers* and *u/v-layers*. These plots allows to determine the upper limit of *tracking efficiency* achievable corresponding to a minimal requirement of *x-layer* and *u/v-layer*

Testing the algorithm against different geometries and hit conversion probability scenarios allows also to estimate the robustness of the algorithm in different running conditions.

The impact of the simulated radiation damage is stronger in the central region leading to higher *hit conversion probability* inefficiencies for central tracks. Therefore, due to the radiation damages and the light attenuation in the fibers, it will be more likely to have tracks with a lower number of hits in the central region of the detector rather than in the external one.

4.3   Dedicated Track Fit in SciFi Region

The analytical parameterization of a track is a crucial ingredient for any pattern recognition algorithm, since it has a direct impact on its performance. The model described in Sect. 4.3.1 is the one adopted by the stad-alone track reconstruction algorithm using only information from the SciFi which is called `Hybrid Seeding` (see Sect. 4.4). The model takes into account the detector configuration, in particular the simulation of the magnetic field in T-stations positions. The track model has a significant impact on the track fit procedure as well as in track parameter estimation used by the other pattern recognition algorithms.

4.3.1   Track Model

The equation of motion of a charged particle of momentum $\overrightarrow{p}$, charge q and velocity $\overrightarrow{v}$ in a magnetic $\overrightarrow{B}$ field is:

$$\frac{\mathrm{d}\overrightarrow{p}}{\mathrm{d}t} = q\,\overrightarrow{v} \times \overrightarrow{B}$$

leading to the following equations for the different momentum components p_x, p_y, p_z:

$$\frac{\mathrm{d}p_x}{\mathrm{d}z} = q(t_y B_z - B_y); \quad \frac{\mathrm{d}p_y}{\mathrm{d}z} = q(B_x - t_x B_z); \quad \frac{\mathrm{d}p_z}{\mathrm{d}z} = q(t_x B_y - t_y B_x) \quad (4.21)$$

where $t_x = p_x/p_z = \mathrm{d}x/\mathrm{d}z$ and $t_y = p_y/p_z = \mathrm{d}y/\mathrm{d}z$ are the track slopes. The differential equation for the track slope in the *x-z* plane is:

$$\frac{\mathrm{d}t_x}{\mathrm{d}z} = \frac{q}{p}\sqrt{1 + t_x^2 + t_y^2}\left(t_x t_y B_x - (1 + t_x^2)B_y + t_y B_z\right) \quad (4.22)$$

and for the *y-z* plane:

$$\frac{\mathrm{d}t_y}{\mathrm{d}z} = \frac{q}{p}\sqrt{1 + t_x^2 + t_y^2}\left((1 + t_y^2)B_x - t_x t_y B_y - t_x B_z\right) \tag{4.23}$$

Within the volume covered by the three SciFi stations *T1*, *T2*, *T3*, we want to define a track model accounting for the local magnetic field $\vec{B}$, in the approximation of small $|t_x|$ and $|t_y|$, as the particles are highly boosted along the z axis. In addition, most of the tracks are in the central region, where the dominant component of the field is B_y. So, keeping only the first order terms, the equations of the trajectory Eqs. 4.22 and 4.23 are simplified into:

$$\frac{\mathrm{d}^2 x}{\mathrm{d}z^2} = \frac{\mathrm{d}t_x}{\mathrm{d}z} \simeq -\frac{q}{p}B_y \quad ; \quad \frac{\mathrm{d}^2 y}{\mathrm{d}z^2} = \frac{\mathrm{d}t_y}{\mathrm{d}z} \simeq 0 \tag{4.24}$$

The second equation results in a simple linear model for the y-z track projection:

$$y(z) = y_0 + t_y(z - z_0) \tag{4.25}$$

where y_0 is the y coordinate at the reference position z_0.

For the first equation, concerning the x-z track projection, we want also to account for the dependence of B_y on z at first order as:

$$B_y(z) \simeq B_0 + B_1(z - z_0) \tag{4.26}$$

so that, solving the Eq. 4.24 we get:

$$\begin{aligned}
x(z) &= x_0 + t_x(z - z_0) + \frac{q}{p}\left(\frac{B_0}{2}(z - z_0)^2 + \frac{B_1}{6}(z - z_0)^3\right) \\
&= x_0 + t_x(z - z_0) + \frac{q}{2p}B_0(z - z_0)^2\left(1 + \mathtt{dRatio}(z - z_0)\right)
\end{aligned} \tag{4.27}$$

where x_0 is the coordinate at the reference position z_0. The quantity $\mathtt{dRatio} = B_1/3B_0$ is roughly constant in the central region, while at large distance from the z axis, we will need to introduce a correction depending on x and y. We will refer to it as the parameter of the *cubic correction* and it will not be a free parameter: it will be evaluated from the track position at $z = z_0$.

In summary, when fitting a trajectory, the model depends linearly on five adjustable parameters: two (y_0 and t_y) related to the y-z projection, and three (x_0, t_x and $B_0 q/p$) concerning the x-z projection. Defining $a_x = x_0$, $a_y = y_0$, $c_x = \frac{q}{2p}B_0$ and $dz = z - z_0$, we can finally write the track model as:

$$\begin{aligned}
x_{track}(z) &= a_x + t_x \cdot dz + c_x \cdot dz^2 \cdot (1 + \mathtt{dRatio} \cdot dz) \\
y_{track}(z) &= a_y + t_y \cdot dz
\end{aligned} \tag{4.28}$$

where the z_0 value is fixed to 8520.0 mm, corresponding roughly to the position of the first layer of the second SciFi station *T2*.

4.3.2 `dRatio` *Parameterization*

In order to parameterize the value of `dRatio` for the track model, only *reconstructable* `long` and `downstream` tracks have been selected from the simulated samples. Tracks associated to electrons and positrons have been removed to perform this study, because they can emit photons via Bremsstrahlung. Therefore, to evaluate the `dRatio` properly for $e^{\pm}$, one should include Bremsstrahlung corrections.

The selected tracks have been fitted using as input the true hits before digitization and the following model, where a cubic term for the *x-z projection* is included as a free parameter:

$$x(z) = a_x + t_x \cdot (z - z_0) + c_x \cdot (z - z_0)^2 + d_x \cdot (z - z_0)^3$$
$$y(z) = a_y + t_y \cdot (z - z_0)$$

Knowing the track parameters, one can directly determine the value of `dRatio` computing the ratio $\dfrac{d_x}{c_x}$. The distribution of the values obtained for `dRatio` is shown in Fig. 4.19.

One can notice that `dRatio` is constant to a good approximation, except for low values of the track momenta, corresponding to large distances from the z axis. This dependence from z can be factorized out. Assuming that B_1 and B_0 have the same z dependence:

$$B_1 = B_1(x, y, z) \simeq F(x, y)g(z)$$
$$B_0 = B_0(x, y, z) \simeq F'(x, y)g(z) \tag{4.29}$$
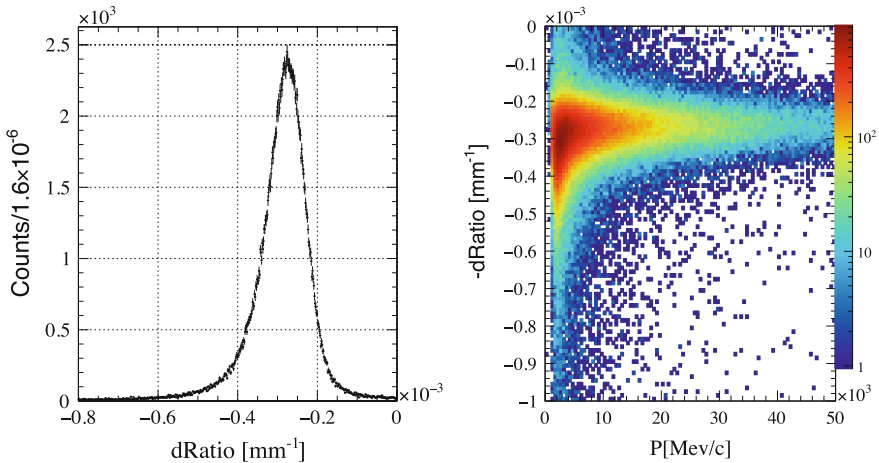
Fig. 4.19 On the left hand side, the `dRatio` distribution. As expected its value is negative, i.e. the magnetic field is decreasing with z (B_1 term). On the right hand side, the `dRatio` value versus the track momentum. The lower is the momentum, the less accurate is the assumption $\dfrac{B_1}{B_0} = Const$, since tracks at lower momentum are highly bent and do not experience the same effect from the magnetic field
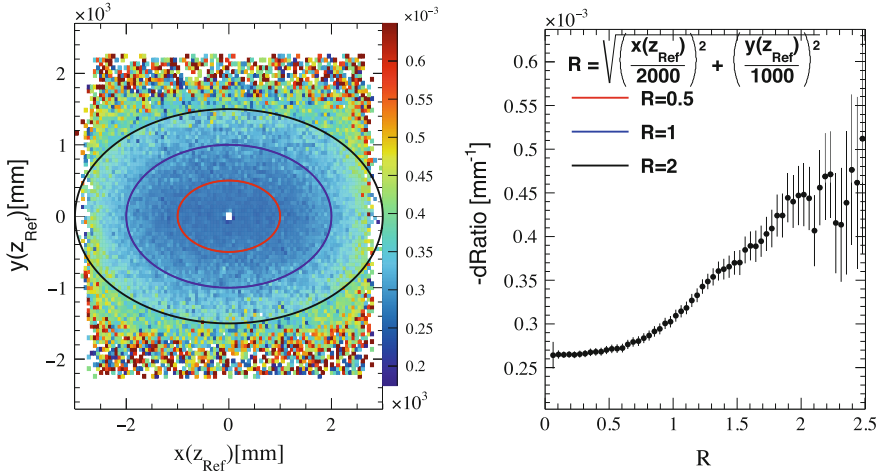
Fig. 4.20 On the left hand side, the dRatio value is shown on the z axis as function of the $x_{track}(z_0)$ and $y_{track}(z_0)$. The value of dRatio is changed in sign in this plot. On the right hand side, the dRatio value (y axis) as function of the parametrized radius R given by the combination of ($x_{track}(z_0)$, $y_{track}(z_0)$)

one can redefine dRatio as:

$$\texttt{dRatio} = \frac{B_1}{3B_0} = \frac{1}{3}\frac{F(x,y)}{F'(x,y)} \tag{4.30}$$

and correct it using the information of the track position ($x_{track}(z_0)$, $y_{track}(z_0)$) at the reference $z_{ref} = z_0$, as shown in Fig. 4.20.

The following parametrization has been found for dRatio :

$$\texttt{dRatio} = -\left(2.633 \times 10^{-4} - 3.59957 \times 10^{-6} \cdot R + 4.7312 \times 10^{-5} \cdot R^2\right) [\text{mm}^{-1}]$$

where R is defined as:

$$R = \sqrt{\left(\frac{x_{track}(z_0)[\text{mm}]}{2000}\right)^2 + \left(\frac{y_{track}(z_0)[\text{mm}]}{1000}\right)^2}$$

Note that this parametrization can be applied in the algorithm at the fit level only when the knowledge of ($x_{track}(z_0)$, $y_{track}(z_0)$) becomes available, i.e. when tracks are fitted with the *simultaneous fit* which will be defined in Sect. 4.3.3. Regarding the *x-z projection fit*, which will be discussed later in this section as well, the value used for dRatio is fixed to $\texttt{dRatio}_{R=0} = -2.633 \times 10^{-4} \text{mm}^{-1}$ (see Fig. 4.20).

4.3.3   Track Fit Implementation

The track fit is implemented in the algorithm by solving a linear system of equations, arising from the minimization of the χ^2 defined as:

$$\chi^2 = \sum_{i=1}^{nHits} \left(\frac{x_i - x_{track}(z_i)}{\sigma_i} \right)^2 \tag{4.31}$$

where σ_i is the error assigned to the ith hit of the track and $x_{track}(z_i)$ is the position of the reconstructed track at the z_i position of the ith hit. Here, the value of x_i (the x position of the ith hit of the track in the laboratory reference frame) is computed as:

$$x_i = x_i(y = 0) + \alpha_i \cdot y_{track}(z_i)$$

being α_i the stereo angle of the layer to which the ith hit of the track belongs (it is zero in case of *x-layers*). Using the track model defined in (4.28) and defining the vector of track parameters as:

$$\overrightarrow{p} = \left(a_x, t_x, c_x, a_y, b_y \right)^T$$

the fitted parameters can be extracted solving the linear system arising from:

$$\overrightarrow{\nabla} \chi^2 = \frac{\partial \chi^2}{\partial p_i} = 0$$

which in a matricial form is $M_{ij} p_j = r_i$, written explicitly as follows:

$$M \cdot p = \left(\begin{array}{ccc|cc}
<1> & <dz> & <d\eta> & <-\zeta> & <-\zeta \cdot dz> \\
<dz> & <dz^2> & <d\eta \cdot dz> & <-\zeta \cdot dz> & <-\zeta \cdot dz^2> \\
<d\eta> & <d\eta \cdot dz> & <d\eta^2> & <-\zeta \cdot d\eta> & <-\zeta \cdot d\eta \cdot dz> \\
\hline
<-\zeta> & <-\zeta \cdot dz> & <-\zeta \cdot d\eta> & <\zeta^2> & <\zeta^2 \cdot dz> \\
<-\zeta \cdot dz> & <-\zeta \cdot dz^2> & <-\zeta \cdot d\eta \cdot dz> & <\zeta^2 \cdot dz> & <\zeta^2 \cdot dz^2>
\end{array}\right) \left(\begin{array}{c} a_x \\ b_x \\ c_x \\ a_y \\ b_y \end{array}\right) = \left(\begin{array}{c} <\Delta x> \\ <dz \cdot \Delta x> \\ <d\eta \cdot \Delta x> \\ <-\zeta \cdot \Delta x> \\ <-dz \cdot \zeta \cdot \Delta x> \end{array}\right) = r$$

$$\tag{4.32}$$

where the following notation are adopted:

$$\begin{aligned}
d\eta_i &= (dz_i)^2 \cdot (1 + \texttt{dRatio} \cdot dz_i) \\
\zeta_i &= \alpha_i \\
\Delta x_i &= x_i - x_{track}(z_i)
\end{aligned} \tag{4.33}$$

and the following convention is used for some hit-based quantity q:

$$< q > = \sum_{i=1}^{nHits} \frac{1}{\sigma_i} q_i$$

In Sect. 4.4, we will refer to the fitting for the tracks in three different ways:

Table 4.2 Errors assigned to the hits depending on the cluster size

$Size_{Cluster}$	1	2	3	4
σ_x	0.080 mm	0.110 mm	0.140 mm	0.170 mm

- **x-z projection fit**: the fit is applied only to the *x-z* plane track projection. It is performed solving for a_x, t_x and c_x in (4.32) the linear system arising from the 3×3 matrix. In the algorithm the fit is applied using only hits from *x-layers*. The value of `dRatio` used for the *x-z projection fit* is kept constant and it has been evaluated from the simulation studies described earlier in the section.
- **y-z projection fit**: the fit is applied only to the *y-z* plane track projection. It is obtained by solving for a_y and b_y in (4.32) the linear system arising from the 2×2 matrix. In the algorithm the fit is applied through the knowledge of the track *x-z projection* using solely the *u/v-layers* hits. Also in this case the value of `dRatio` is kept constant.
- **simultaneous fit**: the fit is applied in both *x-z* and *y-z* planes simultaneously, using both *x-layers* and *u/v-layers* information. It is obtained solving for all the track parameters in (4.32) the linear system arising from the 5×5 matrix. In this case the value of `dRatio` is dependent on $\left(x^{track}(z_0), y^{track}(z_0) \right)$ and the dependence is extracted from simulation studies described earlier in the section.

Once the parameters are fitted, the χ^2 of the tracks can be computed using the formula in (4.31). The errors on the hits are assigned independently from the algorithm, taking into account the properties of the digitized clusters from which the hits are generated [28]:

$$\sigma_i = \texttt{XerrOffset} + \texttt{coeffClusterSize} \cdot Size_{Cluster}$$

where by default `XerrOffset` is equal to 0.05 mm and `coeffClusterSize` is 0.03 mm. The values of the $Size_{Cluster}$ in the samples used for this document (see Sect. 4.2.4) range between 1 and 4 in the digitization, leading to the errors shown in Table 4.2.

4.4   The Hybrid Seeding Algorithm: A Stand-Alone Track Reconstruction Algorithm for the Scintillating Fibre Tracker

A novel stand-alone algorithm, the `Hybrid Seeding`, conceived to reconstruct tracks using solely the information that will be provided by the Scintillating Fibre Tracker during the LHCb upgrade, has been developed and will be described in this section. The algorithm leads to significant improvements with respect to its first implementation used for the Technical Design Report (TDR) [13], in all the performance indicators: *tracking efficiency*, *ghost rate* and *timing*. The algorithm takes advantage of an improved track model description in the T-station region, described in

Sect. 4.3. The improved track model is used to fit the tracks internally to the algorithm providing precise track parameter estimation as well as a more accurate track quality estimation, especially for low p and p_T tracks. The design of the algorithm and the various internal steps are described in Sect. 4.4.1. Section 4.5 provides an overview of the `Hybrid Seeding` performances and a set of suggestions for future improvements. A summary of the algorithm is provided in Sect. 4.5.4 together with the overall impact to the LHCb track reconstruction performance is also provided.

In order to develop the algorithm *true* tracks from the simulation are used: electrons have not been used to tune the search windows (to neglect multiple-scattering effects) and only tracks interesting for physics have been selected. A track is defined to be interesting for physics if it is *reconstructable* in the SciFi and if it belongs to a decay chain of a $b-$ or $c-$hadron as well as if it belongs to the decay chain of a of long-lived particles.

4.4.1 `Hybrid Seeding` *Algorithm Overview*

The `Hybrid Seeding` is an evolution of the seeding algorithm used in the TDR [30], called `TDR Seeding` [13]. The algorithm is designed to reach a good compromise between tracking efficiencies, ghost rate and timing. The main idea behind the `Hybrid Seeding` is to progressively clean the tracking environment: first finding the tracks which are easier to reconstruct, and then looking for the harder ones using the left-over hits. The design of the algorithm is shown in Fig. 4.21. An overview of its implementation is illustrated here.

1. **Cases**. The algorithm is divided in different steps, called `Cases`, where tracks covering different momentum ranges are searched for. The algorithm supports and execute a total of three `Cases` by default and it can be configured to execute only one or two of them through the configurable option named `NCases`. The momentum ranges covered depending on the `Case` are shown in Table 4.3. Each `Case` depend on the execution of the previous one, since it considers the left-over hits from the previous track search iteration. This behavior can be changed by the `FlagHits` and `RemoveFlagged` options, which are taking care of flagging the hits at the end of each `Case` and to not allow to re-use the flagged hits.[7]
2. **Upper/lower division**. For each `Case`, the tracks are searched first in the $y > 0$ part of the detector and then in the $y < 0$ part. We use this approach because the fraction of tracks migrating from the upper to the lower part of the detector is negligible (less than 0.01%). Even for tracks originated from long lived particles, the fraction is still low (0.15%).
3. **Find *x-z* projections**. For each `Case`, all the *x-z* track projections are searched for using solely the hits from *x-layers*. The track search in each `Case` is designed in a projective approach, i.e. the tracks are looked for starting from a *two-hit*

---

[7]For example, the `Case` 2 is looking for tracks using the unused hits of tracks found in `Case` 1, if the `RemoveFlagged` and `FlagHits` options are enabled.

combination from two different *x-layers* which are the farthest possible (one hit in *T1* and a second one in *T3*). A third hit is searched in *T2* for each *two-hit* combination and from the resulting parabola other hits in the three remaining *x-layers* are searched for. The strategy used to find *x-z projection* candidates is illustrated in Fig. 4.22.

4. **Remove clones X**. An intermediate clone removal step is applied to the *x-z* track projections. This is achieved by counting the number of hits shared between the projections found in the same `Case` and selecting the best one based on the value of the track χ^2 and the number of fired *x-layers*.

5. **Add stereo hits**. All stereo hits compatible with a *x-z projection* surviving the intermediate clone killing step are collected. A Hough-like transformation on the stereo hits is used to identify potential line candidates as *y-z* projections associated to the *x-z projection* of the track. Additional preliminary criteria are applied to select the potential line candidates for a given *x-z projection*. For each line candidate, the full track (*x-z projection* plus line candidate) undergoes the *simultaneous fit* procedure, eventually removing outlier hits. The final χ^2 is checked to be within the tolerances and a track candidate is generated. The best track candidate among those sharing the same *x-z projection* is selected on the basis of its χ^2 and the number of hits involving different layers.

6. **Flag hits**. The hits used by the track candidates found by the first two `Cases` are flagged (if `FlagHits` option is enabled) and they become unavailable for the track search in the following `Case` (if `RemoveFlagged` option is enabled).

7. **Global clone removal**. Once all the `Cases` have been processed, a global clone removal step is applied based on the fraction of shared hits between the tracks and their $\chi^2/ndof$.

8. **Track recovering routine**. All the *x-z projections* from all the `Cases` which are not promoted to full tracks when looking at matching *u/v-hits* are recovered requiring for them to be composed of hits which are not used by any of the already found full track candidates. For the recovered *x-z projections* stereo layer hits are added using a set of dedicated parameters. Details of its implementation are described in Sect. 4.4.7.

9. **Convert tracks to LHCb objects**. All the track candidates found by the algorithm are converted into standard LHCb objects, which can be used by other algorithms and handled by the *Kalman filter*.

Few points need to be underlined. First of all, the search windows, tolerances and track quality cuts have been chosen to be `Case` dependent. This allows the algorithm to be fully flexible and able to cope with different data taking scenarios. The `Case` separation helps also in recovering the *hit conversion* inefficiencies, allowing to explore different combinatorics (Sect. 4.4.2.2). Finally, an important improvement of the `Hybrid Seeding` is the updated *track model* (Sect. 4.3.1). This provides a more appropriate χ^2 of the tracks and determination of the track parameters, compared to the `TDR Seeding`, without introducing additional degrees of freedom in the fit. A more detailed description of the four main steps performed by each case in
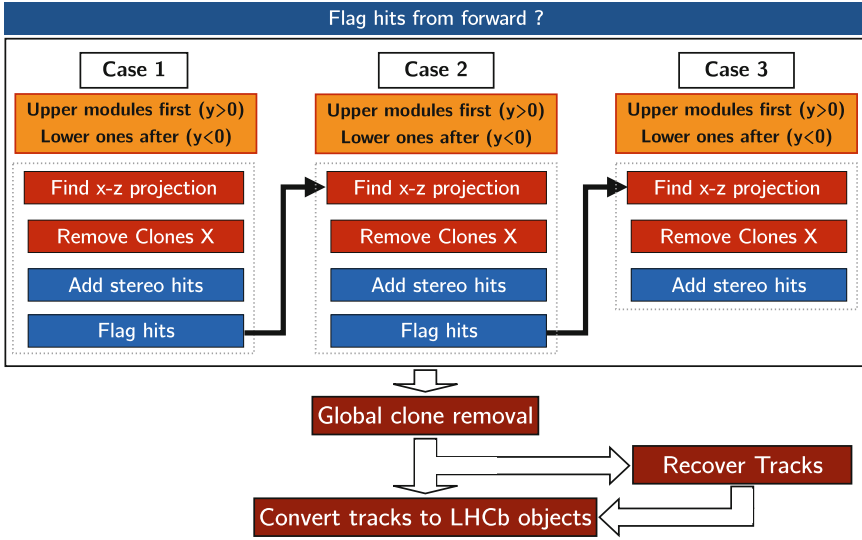
Fig. 4.21 Main structure of the algorithm. If the algorithm is run after the forward tracking, it is possible to remove all the hits of the tracks found by the forward tracking algorithm. T-station segments are extracted by the forward tracking output and they are directly stored as final candidates. The algorithm is then divided in three `Cases`, and each `Case` is executed separately in the upper and lower modules. Each `Case` is composed by four main steps (three for the `Case 3`): the search for *x-z* plane tracks projections, an intermediate clone killing step, the addition of *u/v-hits* at each *x-z* projection and finally the tracking environment cleaning through the hit flagging routine. Once all the `Cases` track search is performed, a global clone killing is applied. By default the algorithm performs a track recovering step before converting all the found candidates from a simple collection of hits into LHCb objects, which can be handled by the *Kalman filter*, the *matching* and the *downstream* algorithms

Table 4.3 Momentum ranges covered by the algorithm depending on the `Case`

Case 1	Case 2	Case 3
$p > 5\,\text{GeV/c}$	$p > 2\,\text{GeV/c}$	$p > 1.5\,\text{GeV/c}$

the `Hybrid Seeding` is given in the following sections, together with the list of the tunable parameters and their default values for each `Case`.

4.4.2 Find x-z Projections

Track projections in the bending plane, i.e. the *x-z plane* projections of the tracks, are looked for at first, using the *tracking in projection* approach. The goal of this step is to find track candidates projections as a set of hits in different *x-layers*. This part of the algorithm is structured as follows.

- **Two-hit combination**. *Two-hit* combinations are generated using one hit from the *x-layer* of *T1* and one hit from the *x-layer* in *T3*. Different starting combinations of layers in *T1* and *T3* are explored depending on the `Case`. The main momentum selection comes from the *two-hit* combination, since the `Cases` cover different momentum ranges.
- **Three-hit combination**. A third hit is searched for in both the *x-layers* of *T2*, defining the `ParabolaSeedHits` for a given *two-hit* combination. The tolerances given at this step are crucial because they are linked to the allowed sagitta for the tracks, i.e. to the track momentum(p) and the transverse momentum(p_T).

- **Complete and fit the** *x-z projections*. For each of the *three-hit* combinations a fast computation of the track parameters is done,[8] allowing a look-up procedure in the remaining *x-layers*: for each of them, the hit closest to the predicted positions is picked up. The *x-z projections* undergo a preliminary filtering based on the number of hits found. Finally, the track-fit procedure is applied using the *x-z projection fit* and tracks are selected based on their χ^2.
- *x-z projections* **clone killing**. Tracks are compared among them in order to get rid of those sharing the same hits.

Each one of the items listed above are described in detail below and a graphical interpretation of the various steps can be found in Fig. 4.22.

4.4.2.1   Hit Caching

Hits in single tracker detection layer are stored in a container which is sorted by increasing $x-$values. Initially, the algorithm was taking advantage of the sorted property of the data objects using binary search operations from the standard libraries, namely the `std::upper_bound` and `std::lower_bound` operations to find the boundaries defining the search windows and to determine the list of hits to process. The timing of such operation is proportional to $log_2(N) + 1$, where N is the amount of hits in the range provided to perform the search. Given the processing order of hits in the first station (from small x to higher x) and the implementation logic of the *x-z projections* search, it is clear that the highest frequency of such "search of boundaries" operation happens more frequently when processing hits in the central detector region where higher occupancy is expected. Therefore, for the most frequent calls the timing will be roughly proportional to $log_2(\frac{N}{2}) + 1$, which for large N can be slower than a linear operation moving forward or backward the boundaries of a couple of hits. A speed-up is then possible caching in memory the previous processed iterators to the hits defining the boundaries and simply searching for the new boundaries around the already cached one (moving back or forward of

---

[8]The track parameters for the *x-z projection* are three: a_x, t_x, c_x. Therefore, three hits are enough to solve the linear system. If one would allow `dRatio` to be not fixed, moving to a full cubic track model, four hits would be needed.
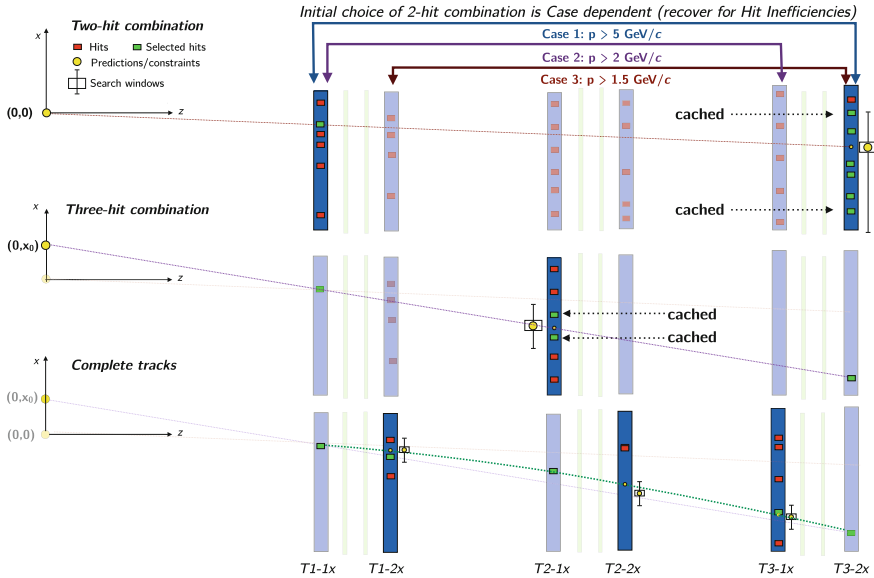
Fig. 4.22 Logic implementation of the three main steps in the *x-z projections* track finding. Actual hits in the detector are shown in red while the green ones picked in the track building are in green. Hits (actually iterators) at the border of tolerances are cached to speed up the look-up sequence given the order of hit processing. Two hit combinations are build considering combinations of hits in T1 and T3 forcing the track origin at $(x, z) = (0, 0)$. The three hit combination is built

Table 4.4 *Two-hit combinations depending on the case*

Case	T1 station *x-layer*	T3 station *x-layer*
0	T1-1 x	T3-2 x
1	T1-2 x	T3-1 x
2	T1-1 x	T3-1 x

few hits). Given the implementation logic of the *x-z projection* track search, the hit caching approach allows to achieve a speed up of 16%.

4.4.2.2 *Two-Hit* Combination

For each of the hits found in the first station, hits in the last one are looked for. Depending on the Case, different layers are selected to create the *two-hit* combination, as listed in Table 4.4 (the names of the layers are shown in Fig. 4.22). The choice of changing the layers considered for the *two-hit* combination depending on the Case is taken to be able to recover for hit inefficiencies in the detector. Indeed, if a given track is inefficient in one of the two layers considered to start the track search, that track would never be found by the corresponding Case.

All the hits in the first station *x-layer* (*T1-X*) are read and for each one the infinite momentum assumption is applied, together with the assumption that the track comes from $z = 0$ mm. This infinite track momentum assumption is used to find the highest momentum track first. For these tracks, at this stage, the kick due to the magnet when migrating from the VELO to the SciFi can be neglected.

In such hypothesis, one can safely assume that the tracks are almost straight line in the bending plane since the track deviation is proportional to $\dfrac{p_x}{p_z}$. On top of that, if one also assumes that the tracks are produced at $z = 0$ mm, the x position of the hit in the first station already contains the information needed to predict the x position in all the other layers. Under these two assumptions we can compute $x_{T3}^{predicted}$, i.e. the expected value of the x position in the last T station *x-layer*, as follows:

$$\text{with } t_x^{\infty} = \frac{x_{T1}}{z_{T1}}$$

$$x_{T3}^{predicted} = x_{T1} + t_x^{\infty} \cdot [(z_{T3} - z_{T1}) + \texttt{L0\_AlphaCorr[Case]}]$$

Then, all the hits in the last layer satisfying the following condition are collected:

$$\left| x_{T3} - x_{T3}^{predicted} \right| < \texttt{L0\_tolHp[Case]}$$

This condition is based on the two parameters `L0_AlphaCorr` and `L0_tolHp`. The `L0_AlphaCorr` parameter depends explicitly on the choice of the first and last *x-layers* for each `Case`, while the `L0_tolHp` depends on the momentum range covered by the `Case`. `L0_ AlphaCorr` allows to take into account the fact that it is more likely for positive charged tracks to reach the first T-station in one side (left or right) of the tracker, while for negative ones the opposite one. This parameter is magnet polarity independent.

The default values of these parameters for this first selection are shown in Table 4.9. They have been determined from simulation studies looking at the *true two-hit* combinations, as shown in Fig. 4.23a, b, as function of the `Case` and the track p (Fig. 4.24a) and p_T (Fig. 4.24b).

Figure 4.23a and b show how much the search windows can be reduced when looking at a given momentum range. Indeed, smaller search windows imply a faster execution time. Figure 4.24a and b show the search window size as a function of the track p and p_T: from such plot one can define the value for the search window (`tolHp[Case]`) depending on the track p_T and p.

It is also important to underline that the larger `L0_tolHp`, the higher the number of fake combinations. This is also one good reason to divide the search in three subsequent different cases, removing the hits of the good combinations found when moving from one `Case` to the next one, making the lower p and p_T track search faster.

(a) All p.

(b) $p > 5$ GeV/c, $p > 2$ GeV/c, $p > 1.5$ GeV/c respectively for `Case 1,2 and 3`.

Fig. 4.23 From the left to the right, the *Two-hit* combination for true tracks given by the first and the last layer selected, for `Case 1,2` and 3. On the horizontal axis, the value of $t_x^\infty = \dfrac{x_{First}}{z_{First}}$ is shown, where *First* stands for the *T1-1x , T1-2x, T1-1x* for `Case 1` , 2 and 3 respectively. On the vertical, the value of $\Delta = x_{Last} - t_x^\infty \cdot (z_{Last} - z_{First})$ is shown for Fig. 4.23a, while the value of Δ is subtracted by `L0_AlphaCorr[Case]`$\cdot t_x^\infty$ for Fig. 4.23b. The name *Last* stands for *T3-2x, T3-1x, T3-1x* for `Case 1`, 2 and 3 respectively. The values of `L0_tolHp[Case]` have been obtained by looking at the y-axis and selecting different momentum ranges: p greater than 5 GeV/c for `Case 1` , 2 GeV/c for `Case 2`, 1.5 GeV/c for `Case 3`

4.4.2.3 *Three-Hit* Combination

At this stage of the algorithm a *two-hit* combination is available. The first step to look for a third hit in the *x-layers* in *T2* is to compute the slope in the bending plane defined by the *two-hit* combination (t_x^{picked}) and the extrapolation of the line joining the two hits to $z = 0$ (x_0), i.e.:

$$t_x^{picked} = \frac{x_{Last} - x_{First}}{z_{Last} - z_{First}}$$
$$x_0 = x_{First} - z_{First} \cdot t_x^{picked}.$$

In such a way, one can look at the third hit of *T2* assuming the magnet field inside the T-Stations is negligible. This linear predicted position in the second station, $x_{T2}^{predicted}$, is given by:

$$x_{T2}^{predicted} = x_{First} + t_x^{picked} \cdot (z_{T2} - z_{First})$$

where *T2* identifies both the *x-layers* in the second T-station (i.e. *T2-1 x* and *T2-2 x*). Hits around the predicted position are collected according to tolerances. A correction

(a) All p, tracks p versus $\Delta - t_x^\infty \cdot$ LO_alphaCorr [Case] for Case 1 (left), Case 2 (center), Case 3(right).

(b) All p, tracks p_T versus $\Delta - t_x^\infty \cdot$ LO_alphaCorr [Case] for Case 1 (left), Case 2 (center), Case 3(right).
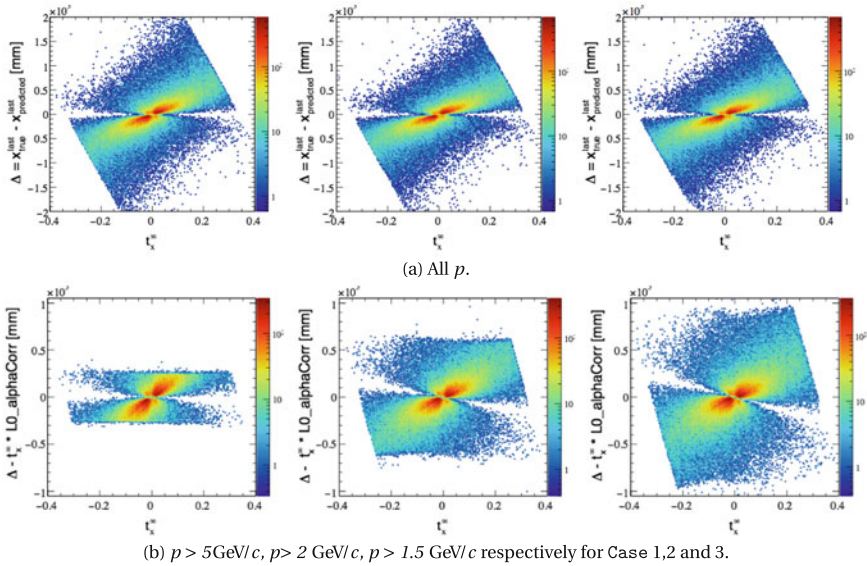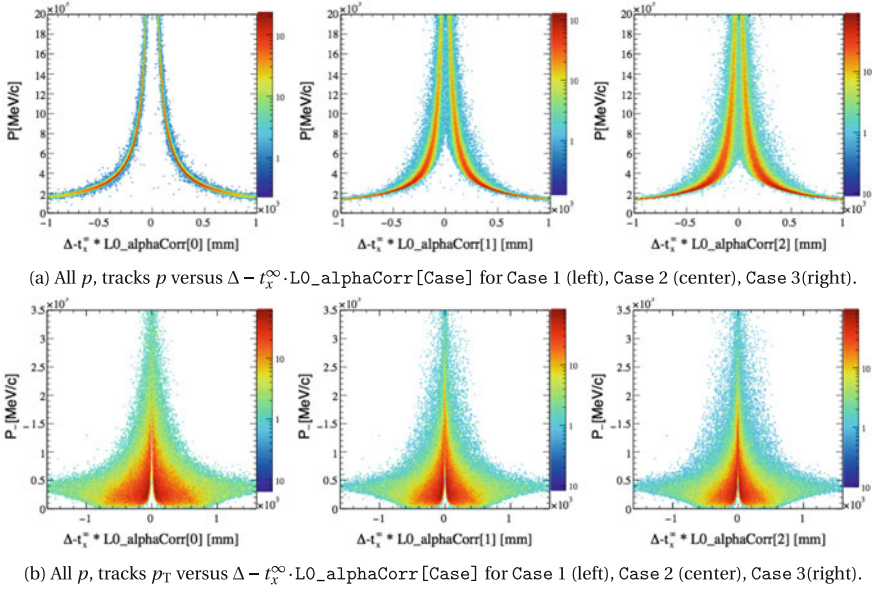
Fig. 4.24 From the left to the right, the *Two-hit* combination for true tracks given by the first and the last layer selected, for Case 1,2 and 3 versus the tracks momentum and transverse momentum. On the horizontal axis, the value of $\Delta - t_x^\infty \cdot$ LO_AlphaCorr [Case] is shown, where $t_x^\infty = \dfrac{x_{First}}{z_{First}}$ and $\Delta = x_{First} + (z_{Last} - z_{First}) \cdot t_x^\infty$. Here, *First* stands for the *T1-1x, T1-2x, T1-1x* while *Last* stands for *T3-2x, T3-1x, T3-1x* for Case 1, 2 and 3 respectively. The values of LO_tolHp[Case] have been obtained by looking at the x-axis and selecting different momentum ranges: p greater than 5 GeV/c for Case 1 , 2 GeV/c for Case 2, 1.5 GeV/c for Case 3

is applied to the predicted position which is taken from Monte-Carlo studies. So, the value of $x_{T2}^{predicted}$ is first corrected as follows:

$$x_{T2}^{predicted;corrected} = x_{T2}^{predicted} + x_0 \cdot \text{x0Corr[Case]}$$

Then, in order to provide the tolerances used for the hit selection, two different slopes are computed:

$$S_1 = \frac{\text{TolAtX0Cut[Case]} - \text{ToleranceX0Up[Case]}}{\text{x0Cut[Case]} - \text{X0SlopeChange[Case]}}$$

$$S_2 = \frac{\text{TolAtX0CutOpp[Case]} - \text{ToleranceX0Down[Case]}}{\text{x0Cut[Case]} - \text{X0SlopeChangeDown[Case]}}$$

(4.34)

In (4.34), TolAtX0Cut[Case], ToleranceX0Up[Case], Tolerance X0Down[Case], x0Cut[Case], X0SlopeChange[Case] and X0SlopeChangeDown[Case] are used to parametrise the selection of hit in the *T2x-layers* according to Fig. 4.25.
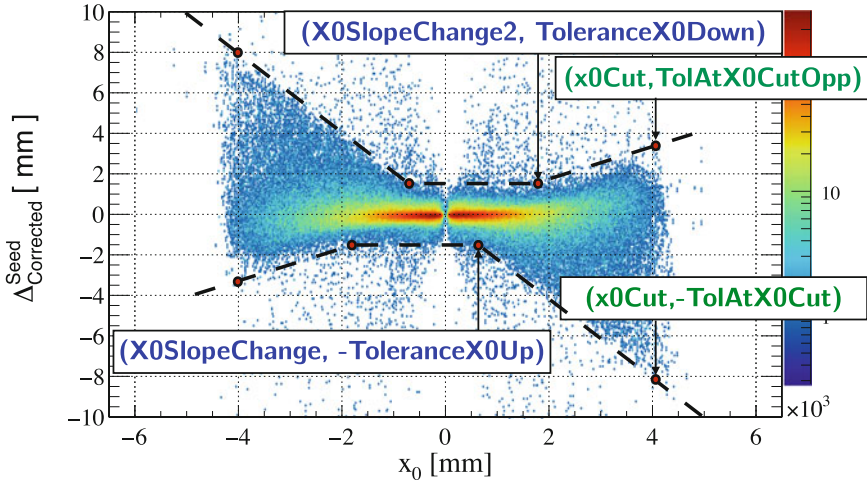
Fig. 4.25 Graphical interpretation of the tolerances for the *three-hit* combination. In this picture the tracks have been selected to have a momentum greater than 2 GeV/c (Case 2). Tolerances to collect hits are defined by the dashed black lines which are obtained defining the fixed points (red bullets) in the 2-D space defined by x_0 and $\Delta_{Corrected}^{Seed}$

The hits in *T2x-layers* satisfying the following condition are collected:

$$B_L < x_{T2} - x_{T2}^{predicted;corrected} < B_H$$

Here, the definition of B_L and B_H depends on the sign of x_0:

$$x_0 > 0 : \begin{cases} x_0 > \text{X0SlopeChange[Case]} : B_L = -S_1 \cdot (x_0 - \text{X0SlopeChange[Case]}) \\ x_0 < \text{X0SlopeChange[Case]} : B_L = -\text{ToleranceX0Up[Case]} \\ x_0 > \text{X0SlopeChange2[Case]} : B_H = S_2 \cdot (x_0 - \text{X0SlopeChangeDown[Case]}) \\ x_0 < \text{X0SlopeChange2[Case]} : B_H = \text{ToleranceX0Down[Case]} \end{cases}$$

$$(4.35)$$

$$x_0 < 0 : \begin{cases} x_0 < -\text{X0SlopeChange[Case]} : B_H = -S_1 \cdot (x_0 + \text{X0SlopeChange[Case]}) \\ x_0 > -\text{X0SlopeChange[Case]} : B_H = +\text{ToleranceX0Up[Case]} \\ x_0 < -\text{X0SlopeChange2[Case]} : B_L = S_2(x_0 + \text{X0SlopeChangeDown[Case]}) \\ x_0 > -\text{X0SlopeChange2[Case]} : B_L = -\text{ToleranceX0Down[Case]} \end{cases}$$

$$(4.36)$$

The previous formula appears quite complicated, but a graphical interpretation of the parameters is possible looking at the value of $\Delta_{Corrected}^{Seed} = x_{T2} - x_{T2}^{projected;corrected}$ for true tracks as a function of x_0 (See Fig. 4.25). The various distributions for the different momentum ranges covered by each Case are shown in Fig. 4.26a (Case 1), b (Case 2) and c (Case 3).

At this stage, for each of the *two-hit* combinations, a list of hits in both the *x-layers* of the second T-station (*T2-1 x* and *T2-2 x*), called in the algorithm `ParabolaSeedHits`, is collected according to the tolerances given in Table 4.9. Note that these tolerances are magnet-polarity independent. Finally, the hits in *T2* are

(a) `Case 1`, $p > 5\,\text{GeV}/c$ tracks selected. Note the logarithmic scale.

(b) `Case 2`, $p > 2\,\text{GeV}/c$ tracks selected. Note the logarithmic scale.

(c) `Case 3`, $p > 1.5\,\text{GeV}/c$ tracks selected. Note the logarithmic scale.
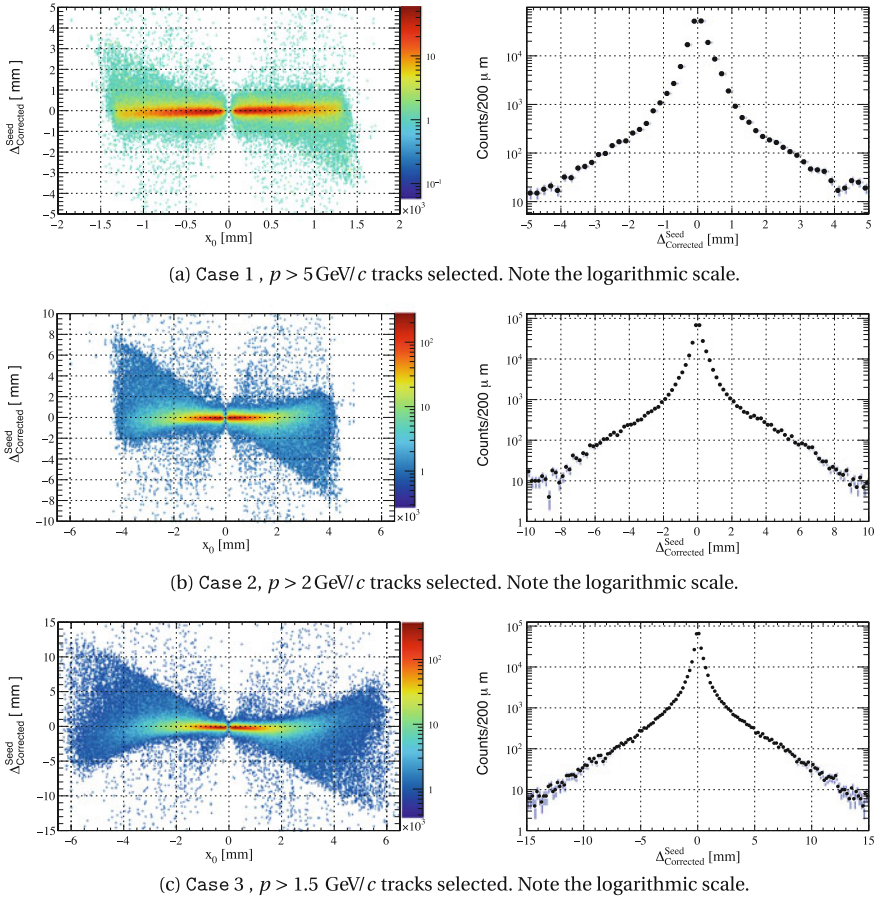
Fig. 4.26 Search windows for the *three-hit* combinations (`Case` dependent). For each `Case`, the plot has been obtained looking at a specific momentum range and looking at the distance of the true hit from the linear prediction ($x_{T2}^{predicted;corrected}$) given by the two hit combination

sorted by increasing value of $\left| x_{hit} - x_{T2}^{projected;corrected} \right|$ and they are processed one by one, generating the *three-hit* combinations. The number of `ParabolaSeedHits` to process is set at maximum equal to the value of the `maxParabolaSeedHits` parameter. This parameter is common to all the cases and its value is 12 by default. As a result of the sorting, *three-hit* combinations with a smaller value $\left| x_{hit} - x_{T2}^{projected;corrected} \right|$ are preferred.
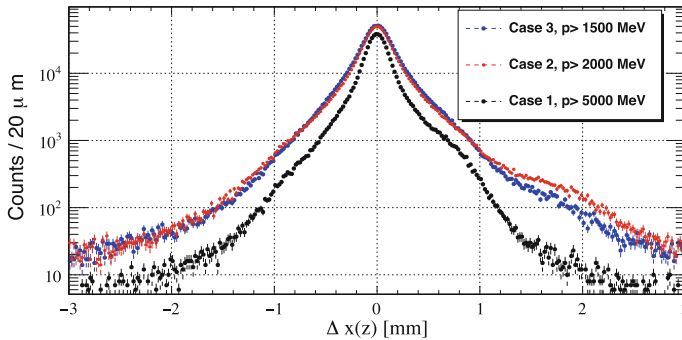
Fig. 4.27 The distance between the true position of tracks of physics interest and the $x_{expected}$ ($\Delta x(z)$) is shown in the three different Cases

4.4.2.4 Complete the Track and Fit of the *x-z projection*

Given the *three-hit* combination (one hit in *T1*, one in *T2* and one in *T3*), the track parameters are estimated solving for a_x, t_x, c_x the linear system of equations arising from

$$x_i = a_x + t_x \cdot (z_i - z_0) + c_x \cdot (z_i - z_0)^2 \cdot (1 + \texttt{dRatio} \cdot (z_i - z_0))$$

where x_i and z_i are the coordinates of the *three-hit* combination. Once the values of a_x, t_x, c_x are computed, it becomes possible to evaluate the value of the expected position $x^{expected}(z)$ in all the remaining layers:

$$x^{expected}(z) = a_x + t_x \cdot dz + c_x \cdot dz^2 \cdot (1 + \texttt{dRatio} \cdot dz)$$

where $dz = z_{Layer} - z_0$, and z_{Layer} is the z position of the layer where the remaining hits have to be collected. All the hits for which $\left| x_{hit} - x_{expected} \right| <$ `TolXRemaining[Case]` are collected and for each layer only the hit having the smallest distance from $x_{expected}$ is considered. Therefore, the resulting track will be composed by a single hit per *x-layer*. The values of `TolXRemaining` are listed in Table 4.9 and the distributions of the residuals $\Delta x(z) = x_{hit}^{true} - x^{expected}(z)$ for the three different cases are shown in Fig. 4.27.

From this stage onwards, only collections of five or more hits in five different *x-layers* are further processed. This threshold was chosen because even in the worst simulated scenario (96% *effective hit probability conversion*) the number of tracks expected to have four or fewer hits on the *x-planes* is quite low ($\sim$1%).

A preliminary check is performed to remove the clones generated starting from the same *two-hit* combination: in fact, different `ParabolaSeedHits` attached to the same *two-hit* combination could lead to the same five- or six-hit combination. `ParabolaSeedHits` are processed one by one building for each *three-hit* candidate the final *x-z projection* candidate. The choice of processing single hits in *T2* and not considering only one of the two available *x-layers* is because we want to be independent from the *hit conversion probability* inefficiencies in *T2*. Indeed, if a
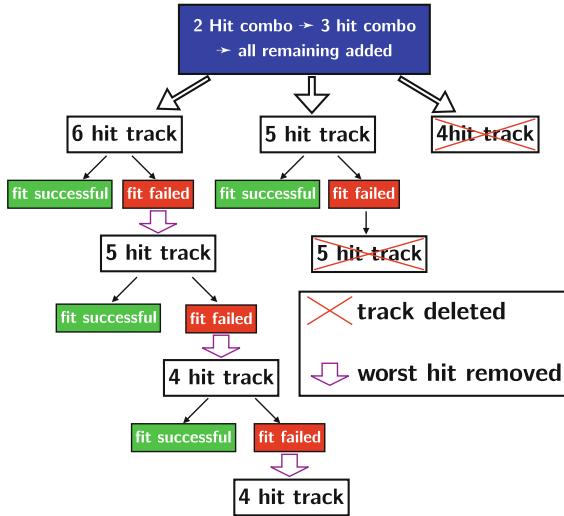
Fig. 4.28 Once the track is created based on the hit selection criteria (two hit combination plus the *three-hit* combination and the look up for the remaining layers), it enters the fitting procedure only if it is composed by five or six hits. If the fit does not converge or the track does not satisfy the requirements for `maxChi2HitsX`, the worst hit is removed and the resulting track is re-fitted. Only tracks initially found with six hits can undergo the full removal and re-fitting procedure, until a minimal number of hits equal to `MinXPlanes` is reached

track is expected to have a missing hit in one of the two layers in *T2*, the algorithm ensures that an independent check is performed in the other *x-layer* in *T2*.

The next step is to fit the track using the *x-z projection fit* of Sect. 4.3.3. The fitting procedure (*x-z projection fit*) is iteratively repeated for a maximum of three times in order to let the fit converge to a more accurate value for the track *x-z* plane parameters. This is achieved updating the track-hit distance appearing on the right hand side of (4.32) with the values fitted at the previous iteration. The fit is recognized as failed if the matrix is singular or if the fitted parameters assume non-physical values. Once the fit for the parameters is done, the maximal contribution to the χ^2 from a single hit on track is evaluated. If the value is larger than `maxChi2HitsX[Case]` the fit status is recognized as well as failed. The default values for `maxChi2HitsX[Case]` are shown in Table 4.9. For all the tracks having six hits for which the fit failed, the hit contributing the most to the χ^2 is removed and the track is then re-fitted until the number of hits on track reaches the `MinXPlanes` value, which is set to 4 by default and shared by all the three `Cases`. The road-map of a track entering the fitting procedure is shown in Fig. 4.28.

All tracks with a converged fit are stored in the container of *x-z candidates* if their $\chi^2/ndof$ is smaller than `maxChi2DoFX`, where for the track *x-z projection* the $ndof$ is equal to the number of hits on the track minus three. The default values for the *x-z projection* candidates selection are listed in Table 4.9. The selected *x-z projections* are finally sent to the following step, aiming at removing the clones and suppressing ghosts.

4.4.3 x-z Projection Clone Killing

All the *x-z projections* found in the previous step undergo the step of the clone killing, which is also important in reducing the ghost rate. For this purpose a one by one comparison between tracks is performed. To allow fast track comparison, the algorithm first check that the two tracks undergoing the comparison are at least at a distance less than 5 mm in at least one of the three T-stations. This approach allows to not investigate the hit contents for tracks which are distant one to another (therefore unlikely to share hits). The previous implementation was performing the comparison regardless of how far the two track were passing through wasting CPU resources and being slower.

Since the *x-z* track construction in the previous step is done selecting one single hit per layer, the comparison involves only tracks having $\texttt{minXPlanes} \leq n_{hits} \leq 6$. The clone killing procedure is based on the assumption that a track containing six hits is a well constrained track and more likely to be a good one, while tracks with a lower number of hits are more likely to be a ghost. For each compared track pair, the number of hits they share (*nCommon*) is evaluated. If *nCommon* is greater or equal to $\texttt{minCommon}$, only the track with the larger number of hits is retained, if they have the same amount of hits, the one with the smaller $\chi^2/ndof$ is kept.

The value of $\texttt{minCommon}$ is crucial for the clone removal and the ghost suppression. The lower the value of $\texttt{minCommon}$ is, the lower the *ghost rate* will be. When $\texttt{minCommon}$ is set to 1, the algorithm always ends-up in a configuration which highly suppresses the *ghost rate*, from 60% (no clone removal at all) to 20%. The side effect of setting the value of $\texttt{minCommon}$ to 1 is a reduction from 98 to 80%. Note that the *ghost rate* and the tracking efficiencies mentioned here consider only the *x-z projection* reconstruction step: no stereo hits have been added, meaning that no additional selection on them has been performed yet.

A good compromise between efficiency and ghost rejection for the clone removal procedure has been found, and it is shown in Table 4.5. This allows to have high tracking efficiency, suppress completely the clone rate and have a reasonable ghost rate of about 50%, which can be handled and further suppressed by including information from the *u/v-layers*.

Table 4.5 $\texttt{minCommon}$ values for two tracks comparison, based on their n_{hits}

n_{hits}^{track1}	n_{hits}^{track2}		
	6	5	4
6	3	3	2
5	3	2	1
4	2	1	1
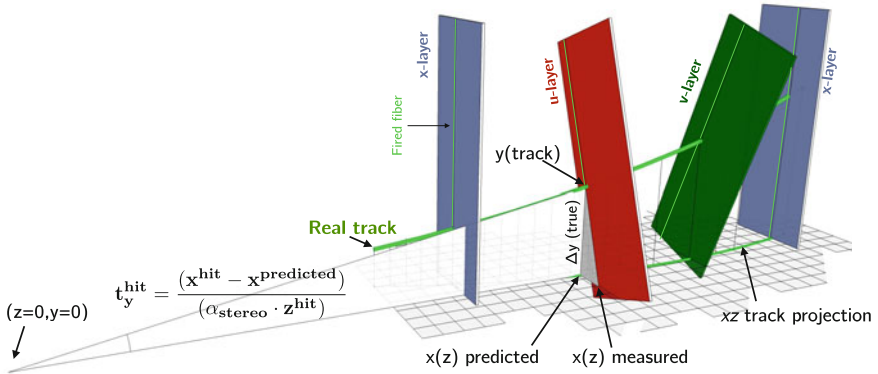
Fig. 4.29 Sketch showing the logic and geometrical interpretation of compatible hits based on *x-z projections*

4.4.4 Addition of the Stereo Hits

The selected *x-z projection* track candidates contain only hits from *x-layers* and have an estimation of the *x-z* plane parameters (a_x, t_x, c_x). The *y-z* plane track motion is extracted from the *u/v-layers* since their local frame is obtained from a rotation of the *x-y* plane around the *z* direction by $+5°$ and $-5°$. Therefore, it is possible to add the information of the track motion in the *y-z* plane looking at the *u/v-layer* hits which are compatible with the *x-z* plane track projection.

Thus *x-z projection* candidates are used as "seed" for such task. The magnetic field effect on the *y-z* plane is negligible compared to the *x-z* plane bending plane for tracks in the central region, so a straight line trajectory is already a very good approximation for the track model (see Sect. 4.3.1). The addition of stereo hits can be summarized as follows:

- **Collect compatible** *u/v-hits*: for each *x-z projection*, the predicted *x* position at the *z* position of *u/v-layers* is evaluated. The distance between the *u/v-layers* measurements and the predicted *x* position allows to identify for each *u/v-hits* a *y* measurement. Therefore all the hits compatible in *y* with respect to the "seed" *x-z projection* are collected and stored in a container (called `MyStereo`). A sketch showing the usage of SciFi detector geometry (one T-Station) and the *x-z projection* information to extract hits according to the *y* tolerance is shown in Fig. 4.29.
- `Hough-like Cluster` **search**: the pre-selected *u/v-hits* for each track are assumed to originate at $y(z = 0) = 0$. Therefore, a group of hits sharing the "same" value of $t_y^{hit} = \left| \dfrac{y_{hit}}{z_{hit}} \right|$ defines a potential line candidate to be attached to the *x-z projection*. Several improvements and a new strategy have been implemented to speed-up the selection of such group of hits defining the `Hough-like Cluster` and guarantee high efficiencies in this step when performing the 1D `Hough-like Cluster` search.

- **Hough-like Cluster to line candidate conversion**: the `Hough-like Clusters`, which is simply a group of *u/v-hits* compatible by construction with the *x-z projection* "seed" and compatible among themselves in the *y-z* plane undergoes a selection procedure aiming at generating a list of straight lines candidates made of single-*u/v-hit* per layer (thus, a maximum of 6 hits is admitted). A fast *y-z projection fit* procedure is performed for the lines candidates. Selection criteria are applied to the lines: tighter ones are applied for the candidates found to have few hits, and looser ones for the candidates having more hits.
- **Full Track fit** : the *x-z projection* and the line candidates found are merged to produce a set of final track candidates. The *simultaneous fit* of the full track is performed and outliers are removed similarly to the procedure described in Sect. 4.4.2.4. Additional selection criteria are applied realizing an *in-situ y-segmentation* of the detector. Tracks are selected depending on *y* position of the track at $z = 0$ and $z = z_0$. This is done to further suppress the *ghost rate* arising from the large amount of fake tracks found in the central detector region combined with the high occupancy expected in central *u/v-layers* region.
- **Tracks from same "seed"** *x-z projection* **selection**: among all the candidates produced from the same "seed" *x-z projection*, only the best one is promoted as final track candidate. Meanwhile candidates are found by the previous steps for the same "seed" *x-z projection*, selection criteria for the minimal number of *u/v-hits* within the available `Hough-like Cluster` are updated according to the already found candidates. Indeed, a preliminary storage and sorting by quality of all the `Hough-like Clusters` found for a given *x-z projection* are performed to guarantee that the first `Hough-like Cluster` are the ones more likely to be associated to the real set of *u/v-hits* for the "seed" *x-z projection*. This is the key aspect leading to a huge speed-up for the algorithm.

A detailed description of each step is provided in the following sections.

4.4.4.1 Collect Compatible *u/v-hits*

For each one of the *x-z projection* candidates, hits from the six *u/v-layers* are collected according to a set of tolerances. Given a *x-z* plane track projection, one can compute the $x^{track}_{predicted}(z_{u/v\text{-}layer})$ extrapolating the expected *x* position in the *u/v-layer* where hits are expected to be found.

Due to the tilted orientation of the *u/v-layers* ($\alpha_{u/v}$, called stereo angle), the predicted x'_{hit} position in the local frame of *u/v-layers* corresponds to:

$$x'_{hit}(y^{true}_{track}) = x'_{hit}(y = 0) + y^{true}_{track} \cdot \tan(\alpha) \tag{4.37}$$

where $x'_{hit}(y = 0)$ is the actual available measurement for *u/v-layers* and $x'_{hit}(y^{true}_{track})$ is the actual *x* position which can be predicted from the "seed" *x-z projection*. Thus, a tolerance in *y* is essentially translated into a tolerance in $x'(y = 0)$ for stereo layers.

Table 4.6 Different
configurations for the *u/v* hit
collection

Track type	$y > 0$ *u/v* modules	$y < 0$ *u/v* modules
UpTrack	Up-Up	Up-Down
DownTrack	Down-Up	Down-Down

The compatibility of the *u/v-hits* for a given *x-z projection* "seed" candidate can be defined looking at the y_{hit} quantity which is based on the value of $x^{track}_{predicted}$ evaluated from the *x-z projection*:

$$y_{hit} = \frac{x^{track}_{predicted}(z = z_{hit}) - x_{hit}(y = 0)}{\sin \alpha_{u/vlayer}};$$

The hits are preselected according to:

$$Min < y_{hit} < Max$$

where Min and Max are defined in such a way to cover the y range between 0 and 2.5 m (mirror to fibre end) for tracks travelling in the upper detector region and between −2.5 and 0 m for those travelling in the lower detector region.

Depending on whether the *x-z projection* was found using the *x-layers* in the upper half of the detector or the lower one, the values of Min and Max change their signs, thus the selection is symmetric for the upper and lower detector region. This leads to two cases: tracks which are found from *x-layers* in the upper region ($y > 0$) (UpperTrack) and tracks found from *x-layers* looking at the lower region ($y < 0$) (DownTrack). In order to efficiently collect all compatible *u/v-hits*, some specific aspects of the detector must be taken into account. The most relevant for the search of compatible *u/v-hits* is the so called TriangleFixing.

Fibers in the upper (lower) half of the *u/v-layers*, depending on their position in the module, cover a fraction of the *u/v-layers* modules at $y < 0$ ($y > 0$) detector acceptance and do not cover a portion of the $y > 0$ ($y < 0$). In order to be fully efficient in collecting the *u/v-hits* for tracks travelling in $y > 0$ detector region, the missing parts of the upper modules is recovered looking at the lower ones and removing the hits in the upper module corresponding to $y < 0$ position. Four different configurations are possible also taking into account if the "seed" *x-z projection* has been reconstructed from upper modules ($y > 0$, UpTrack) or lower ones ($y < 0$, DownTrack) as described in Table 4.6.

For all the configurations listed in Table 4.6, all the hits for which:

$$Min < y^{hit}_{measured} < Max$$

are collected, where Min and Max are initialized to the values of yMin and yMax (default values in Table 4.9), when falling in the Up-Up and Down-Down situation respectively, and:

$$y^{hit}_{measured} = \frac{x^{track}_{predicted} - x_{hit}(y = 0)}{\alpha}.$$

Table 4.7 Hit searching tolerances in *u/v-layers* as a function of the different configurations for the `TriangleFixing`

Configuration	*Min*	*Max*
Up-Up	yMin	yMax
Up-Down	yMin_TrFix	yMax_TrFix
Down-Down	-yMax	-yMin
Down-Up	-yMax_TrFix	-yMin_TrFix

In the two remaining cases, the values of *Min* and *Max* are instead initialized with the yMin_TrFix and yMax_TrFix tolerances (see Table 4.9) respectively. The values assigned to *Min* and *Max* depend on whether we are looking for tracks once applying the triangle fix are summarized in Table 4.7. For example, the Up-Down case refers to search of compatible *u/v-hits* in the lower modules while processing *x-z projection* candidates obtained searching in *y > 0 x-layers*.

Furthermore, if the option `TriangleFix2ndOrder` is set to `True` (which is the case by default), then an additional selection is applied, taking into account the resulting triangular shapes of the modules when cutting them at $y = 0$. This is achieved using the information of the minimal (or maximal) *y* position that the fiber can reach, available for each hit. We will refer to these values as Hit_{yMin} and Hit_{yMax}. An additional refinement of *Max* and *Min* comes from the various combinations arising from the first `TriangleFix` operation, given by the tolerances in Table 4.7. All the four possible combinations are shown in Fig. 4.30. With the help of Fig. 4.30 the tolerances for the *u/v-hits* collection are updated (if `TriangleFix2ndOrder` is `True`) as follows: $Min^{2nd} < y_{Hit} < Max^{2nd}$ The tolerances are given in Table 4.8. An additional hit selection in the central modules is performed to take into account the shape of the beam-pipe hole. This behavior is activated if `RemoveHole` option is set to `True` (default value). This hit selection is obtained looking at the value of $r = \sqrt{x^2_{Predicted} + y^2_{Hit}}$, i.e. the distance from the centre of the layer of the track-*stereo hit* combination in the *x-y* plane. The hits are rejected if *r* is less than `Radius` (by default `Radius = 87.0 mm`). At the end, the *u/v-hits* satisfying all the selection criteria described before are stored in the `MyStereo` container. For each of them the track-based quantity t_y^{hit} is assigned[9]:

$$t_y^{hit} = \left| \frac{y_{hit}}{z_{hit}} \right|.$$

Once the container has been filled, its elements are sorted by increasing values of t_y^{hit}. The sorting step is the basic ingredient for the `Hough-like Cluster` search.

---

[9]When the computed value of y_{hit} belongs to the side opposite to where it is expected to be (let's say $y < 0$ for `UpperTrack`), the t_y^{hit} value is changed in sign. In such a way a completely symmetric upper and lower modules search can be achieved, scanning through the `MyStereo` from smaller to larger values of t_y^{hit}.
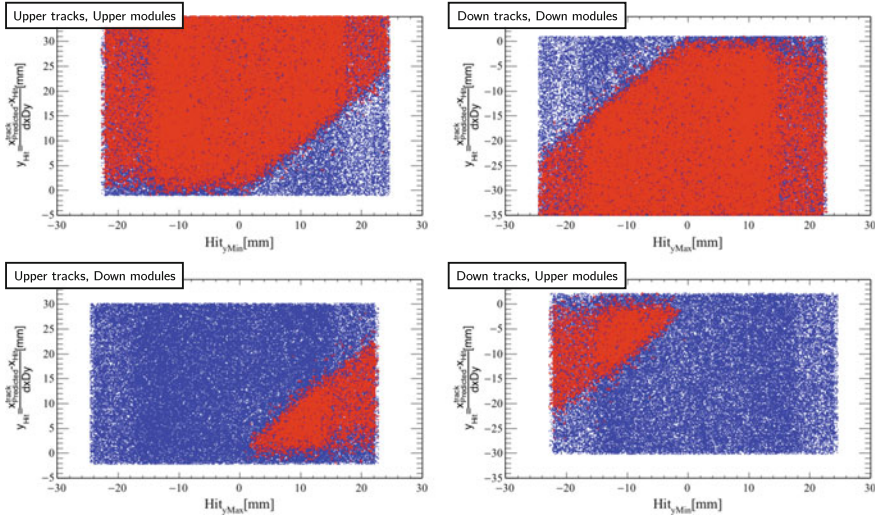
Fig. 4.30 Second order triangle fixing: it aims at removing the hits associated to a non-existing region of the detector. This is achieved thanks to the track-based quantity y_{Hit} and the hit information regarding the maximal (Hit_{yMax}) and minimal (Hit_{yMin}) y position that the fiber can reach. In the picture, the two dimensional distributions for hits matched (from upper and lower *u/v-layers* modules) to the various configurations of track type (going at $y > 0$ or $y < 0$) are shown. In red, the true hits the algorithm is expected to collect. In blue the wrong hits surviving the selections defined by the initialization of *Min* and *Max*. It is therefore possible to remove hits from the preselected container simply applying a cut aiming at removing the non overlapping region

Table 4.8 Triangle fixing for the stereo layers hit collection

Track	Modules	Module region	Min^{2nd}	Max^{2nd}
Up tracks	*UpperModule*	$\text{Hit}_{yMin} <$ mm	yMin(−2.0 mm)	yMax(2500.0 mm)
		$\text{Hit}_{yMin} >$ mm	$(-2.0 + \text{Hit}_{yMin})$ mm	yMax(2500.0 mm)
	DownModule	$\text{Hit}_{yMax} <$ mm	skip	skip
		$\text{Hit}_{yMax} >$ mm	−1.0 mm	$(+2.0 + \text{Hit}_{yMax})$ mm
Down Tracks	*UpperModule*	$\text{Hit}_{yMin} <$ mm	$(-2.0 + \text{Hit}_{yMin})$ mm	+1.0 mm
		$\text{Hit}_{yMin} >$ mm	skip	skip
	DownModule	$\text{Hit}_{yMax} <$ mm	−yMax(−2500.0 mm)	$(+2.0 + \text{Hit}_{yMax})$ mm
		$\text{Hit}_{yMax} >$ mm	−yMax(−2500.0 mm)	−yMin(+2.0 mm)

4.4.4.2 Storing the Hough Cluster

Once all the compatible hits are collected inside the $\texttt{MyStereo}$ container and sorted by increasing value of t_y^{hit}, the algorithm inspects the container and picks up the *u/v-hits* defining a line candidate well fitting the parabolic *x-z projection* and satisfying a minimal number of layers requirements.

Instead of processing all the possible `Hough-like Clusters` in an iterative way (looping through all the stereo hits in the container), the algorithm pre-stores the first three best 4-hit, 5-hit and 6-hit `Hough-like Clusters` for a given *x-z projection*, provided that the `Hough-like Cluster` spread $\Delta_{Cluster} = t^{hit}_{y,max} - t^{hit}_{y,min}$ is smaller than a given tolerance `TolTy`. Therefore, in one single pass-over, the best clusters (containing 4, 5 or 6 hits) with the smallest spreads are found.

The reason why the smallest spread clusters are preferred to larger spread ones is because almost all the physic-interesting tracks in LHCb are pointing to $y(z = 0) = 0$ close to the interaction point. Given the track model, it is easy to understand why smallest spread clusters are preferred: a collection of hits fully compatible with the "seed" *x-z projection* and to a straight-line in *y-z* plane pointing to $y(z = 0) = 0$, would arise from a group of hits placed in the `MyStereo` container in close-by position. In the perfect limit case, all the hits would share the exact same t^{hit}_y value. This is a good assumption for most of the tracks. The reason why the algorithm stores the first three best clusters and not just picks up the best one can be explained as follows:

1. Not all the tracks actually point to $y(z = 0) = 0$. There are also tracks slightly affected by the component of the magnetic field in the *x-z* plane. This implies the necessity of a larger value of $\Delta_{Cluster}$.
2. `Downstream` tracks have softer p and p_t spectrum with respect to `Long` tracks and they do not point to the origin. Furthermore, they experience some effect from the $B_{x,z}$ magnetic field component. This implies a larger value of $\Delta_{Cluster}$. These tracks are mainly searched for in `Case 2`, `Case 3` and in the track recovering routine when the value of `TolTy` is enlarged.
3. Higher occupancy and also the presence of noisy clusters can introduce in a given list of subsequent elements (*u/v-hits*) in `MyStereo` some "contamination" in the `Hough-like Cluster`.
4. The track parameters for the *x-z projection* are not taking into account the *y-z* plane track motion, resulting in a systematic error for the evaluation of t^{hit}_y, potentially enlarging the value of $\Delta_{Cluster}$.
5. Due to hit inefficiencies, the algorithm needs to take into account that not all the *x-z projections* will be matched by a group of six hits, but the requirement on the number of *u/v-hits* needs to go down to four. Therefore, looking only to six consecutive elements defining a `Hough-like Cluster` is a sub-optimal choice. It is for this reason that the matrix is defined as a 3×3 matrix.

All the previous effects are attempted to be recovered by progressively enlarging the threshold value for $\Delta_{Cluster}$, i.e. defining bigger `TolTy` when moving from one `Case` to the next one. This is not a dangerous approach in terms of *ghost rate* increase, provided that the occupancy in the detector remains at a reasonable level ($<10\%$). In any case, the smallest-spread criteria is valid for a large fraction of tracks which are interesting for physics, also considering `downstream` tracks.[10]

---

[10]`Downstream` track originates from long-lived particles decaying downstream the VELO and upstream the UT. `Downstream` tracks are strongly boosted in the forward detector region as their

Given the sorted shape of the `MyStereo` container and the definition of t_y^{hit}, the tolerance can be interpreted as a maximal angle variation between hits in the container, assuming the track originates at $y = 0$. The group of hits satisfying the tolerance are promoted to a `Hough Cluster`. In order to store the "best spread" clusters, the algorithm scans through the full `MyStereo` container only once per *x-z projection* candidate. The calculation of the "best spread" is achieved in an intuitive way. Starting from one hit (*i*th), the algorithm searches inside the sorted `MyStereo` container for the k_jth hit, where $j = 4, 5, 6$ and $k_j = i + j$, e.g. given a hit in the *i*th position, the algorithm looks for the hit placed in the sixth, fifth and fourth position afterwards and it computes the 4/5/6 hit group `Hough-like Cluster` candidate spread associated to the *i*th hit (having the lower value of t_y^{hit}):

$$\Delta_{Cluster}^{i,j} = t_y^{(i+j)^{th}-hit} - t_y^{i^{th}-hit}$$

where $j = 4, 5, 6$. The algorithm first looks at the value of $\Delta_{Cluster}^{i,6}$ and it checks if it satisfies:

$$\Delta_{Cluster}^{i,6} < \texttt{TolTy} \qquad (4.38)$$

where

$$\texttt{TolTy} = \texttt{TolTyOffset[Case]} + \texttt{TolTySlope[Case]}\, t_y^{i^{th}-hit}. \qquad (4.39)$$

Thanks to the `TolTySlope[Case]`, the tolerance for the cluster increases linearly with the value of the t_y^{hit}, so that larger tolerances are used for tracks expected to go at larger y in the clusters selection. This is justified, since lower momentum tracks and `downstream` tracks are more likely to pass through the external detector region.

If $\Delta^{i,6}$ is within the tolerance, the six hits defining the cluster are stored in the 3×3 matrix checking if its spread is better than the one already found. The pre-storing of `Hough-like Clusters` composed by the same amount of hits (4, 5, 6 for the algorithm) is performed in such a way that the clusters are ordered by spread value from smaller to higher value.

If $\Delta_{Cluster}^{i,6}$ does not satisfy the tolerance or it is worse than the ones already found, the same procedure is applied looking at $\Delta_{Cluster}^{i,5}$. If also in this case the tolerance is not satisfied, the algorithm checks for $\Delta_{Cluster}^{i,4}$. Thus the ordering quality of the clusters is obtained by construction: the first three best clusters contain six hits and they are ordered by $\Delta^{i,6}$. The second best set of clusters contains five hits and they are ordered by increasing values of $\Delta^{i,5}$. The third best set of clusters contains four hits and they are ordered by increasing values of $\Delta^{i,4}$.

---

ancestors, thus the criteria requiring the track to point to the origin remains valid also for them. Low momentum `Downstream` tracks are more likely kicked away from the detector acceptance by the magnet even before arriving to the SciFi.

4.4.4.3 `Hough-like Cluster` Selection

Once the clusters have been stored, the algorithm investigates them starting from the first row of the matrix, which is filled by $(i, 6)_{Clusters}$, and going from lower to larger $\Delta_{Cluster}$ values. The first attempt is to try to extend the cluster looking at the next element on the right hand side. At any "extend the cluster" iteration, it checks if $\Delta_{Cluster}^{i,last+1}$ is within `TolTy`. If this is the case, it updates the last element (*u/v-hit*) in the `Hough-like Cluster`, shifting it in the forward direction by one unit:

$$(i, last)_{Cluster} \rightarrow (i, last + 1)_{Cluster}.$$

The "extending cluster" procedure is applied as soon as the cluster contains six different layers. If all the elements in the first row are processed (or if they are empty), the algorithm looks at the second row $(i, 5)_{Clusters}$ and the "extending cluster" procedure is applied as well. Basically, if the algorithm fails to find any good candidate from $(i, 6)_{Clusters}$, it looks at smaller number of hits in the stored `Hough-like Clusters`. The "extended" cluster is checked to ensure that it contains at least `minUV-J[Case]` different fired layers, where `J` stands for the amount of hits in the initial *x-z projection*. Thanks to that it is possible to recover hit-detector inefficiencies weighting in the same way the amount of *x-layers* and *stereo* ones.

If the condition is not satisfied, the next best cluster is processed repeating the previous steps. The default values of `minUV-J[Case]` and `TolTy` can be found in Table 4.9. If the processed `Hough-like Cluster` satisfies also the requirement on the minimal number of different layers, the algorithm checks if it can potentially lead to a track candidate having a number of different fired layers greater or equal to a previously found final track candidate based on the same *x-z projection*.[11] Due to the 3×3 matrix structure, the maximal number of `Hough-like Clusters` that can reach this step is nine. In order to suppress the ghosts and also to reduce the timing of the algorithm, a tunable parameter `maxNbestCluster[Case]` has been introduced. If the amount of `Hough-like Clusters` reaching this step is larger than `maxNbestCluster[Case]`, the addition of stereo hits is interrupted. As a consequence, if no `Hough-like Cluster` has been able to reach the end and to produce a track candidate, the initial *x-z projection* is not promoted to a track candidate.[12] The default values for `maxNbestCluster[Case]` are shown in Table 4.9.

When all the previous conditions are satisfied, the `Hough-like Cluster` is promoted to a line candidate after undergoing the *y-z projection fit*. At this stage, if more than one hit per layer is present in the cluster the single-hit per layer combination leading to the best χ^2 from the *y-z projection fit* is kept. In other words, the algorithm converts the `Hough-like Cluster` to a line candidate forcing outliers removal of hits within the same cluster being in the same layer and with a worse contribution

---

[11]This is done because the "best" track selection is based on the amount of different fired layers.

[12]This is actually the underneath *ghost rate* suppression power of a tracking in projection algorithm, e.g., it does not find compatible hits while searching for them.

to the track $\chi 2$. Therefore, by construction, final track candidates will never have an amount of hits greater than the available number of layers in the SciFi.

The line candidate is accepted if the *y-z projection fit* is considered successful (see Sect. 4.4.4.4). If the fit is not successful, the next best `Hough-like Cluster` is investigated.

4.4.4.4   `Hough-like Cluster` to Line Candidate Conversion

For the simulation used, 10% of the tracks of physics interest produce multiple hits in the same layer. This results from the fact that tracks entering at a large angle are able to produce more than one cluster (after clusterization) in the same detection layer. This effect is also enhanced by the cut-off in the clustering algorithm for the maximal cluster size leading to a splitting of the true cluster into two neighbouring ones.

For these tracks, the true number of hits in the `Hough-like Cluster` will not correspond to the number of fired layers in the `Hough-like Cluster`. In addition to that, having multiple hits per layer from the same track leads to a wrong evaluation of the final track χ^2, since the hits in the same layer are correlated. In order to avoid these complications, the full cluster with more than one hit per layer is fitted, and outliers are remove until the cluster is composed of a single hit per layer. The line candidate arising from the `Hough-like Cluster` is further processed depending on the value of $\chi^2_{Line+x/z}$ where:

$$\chi^2_{Line+x/z} = \frac{\chi^2}{ndof} \, (x\text{-}z \text{ projection}) + \frac{\chi^2}{ndof} \, (y\text{-}Line).$$

The value of $\dfrac{\chi^2}{ndof}$ (*y-Line*) is the one obtained from the *y-z projection fit* procedure. Depending on the total number of hits given by the *x-z projection* and the *u/v-hits* line candidate, the *y-z projection fit* for the line candidate is recognised as successful if:

$$\chi^2_{Line+x-z} < \texttt{MinChi2} \,,$$

where the value of `MinChi2` is associated to two different tunable values, which depend on the total number of different layers provided by the *x-z projection* and the line candidate.

The default values and the dependence on the number of different fired layers `MinChi2` are shown in Table 4.9. The line candidates passing this step are attached to the initial *x-z projection*. For completeness, the structure of the stored clusters matrix and the history of the `Hough-like Clusters` up to this step are sketched in Fig. 4.31 where details about the storing of the `Hough-like Cluster`, the `Hough-like Cluster` selection and the `Hough-like Cluster` to line candidate conversion step is shown.
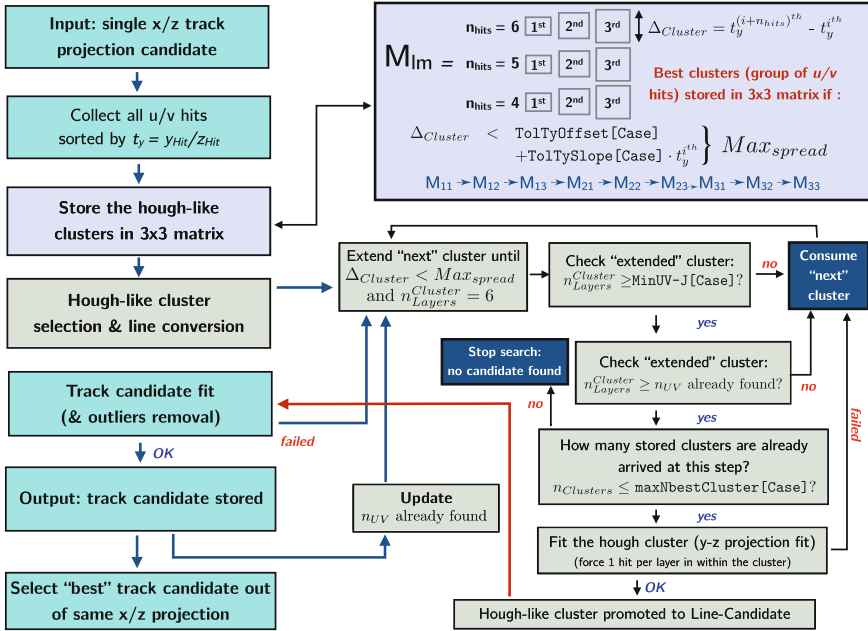
Fig. 4.31 Sketch of the logic used to produce the full track candidates looking at stereo hits layers for a given *x-z projection* candidate. Logic details of the `Hough-like Clusters` storage and processing are also included

4.4.4.5 Track Fit and Track Selection

At this stage of the algorithm a full track candidate (*x-layers* plus *u/v-hits*) is generated merging the *x-z projection* and the line candidate. A 5-dimensional fit is then performed with all the hits of the track. For the simultaneous fit, at each iteration of the χ^2 minimization, the y_i and z_i positions of the hit are corrected to take into account the fact that each layer has also a slope the in *z*-direction [31] (see Fig. 4.32).

The fitting status of the track is then analyzed, depending on whether the track has more than 11 hits or not. Tighter criteria are applied to tracks with $n_{hits} < 11$ with respect to the $n_{hits} > 10$ ones, and all the tracks with $n_{hits} < 11$ going at large *y* and not pointing back to $y = 0$ are killed. This is done because, making the assumption that the algorithm is 100% efficient in collecting the hits, tracks affected by *hit probability conversion* inefficiency are expected to be found only in the central region of the detector, where the radiation damages and the light attenuation have the largest impact. Therefore, the algorithm allows to integrate ghosts from tracks affected by detector inefficiencies only in the central region.

Tighter selection criteria are also applied for $n_{hits} < 11$ tracks: the condition for the outliers removal (maximal contribution to the χ^2 from single hit: Max χ^2_{hit} <`MaxChi2Hit`) is tighter when $n_{hits} < 11$, as shown in Table 4.9. When the

$$\Delta_z = y^{new} \cdot \gamma,$$
$$y^{new} - y^{old} = \beta \cdot \Delta_z,$$
$$y^{new} = \frac{y^{old}}{1. - \beta \cdot \gamma},$$
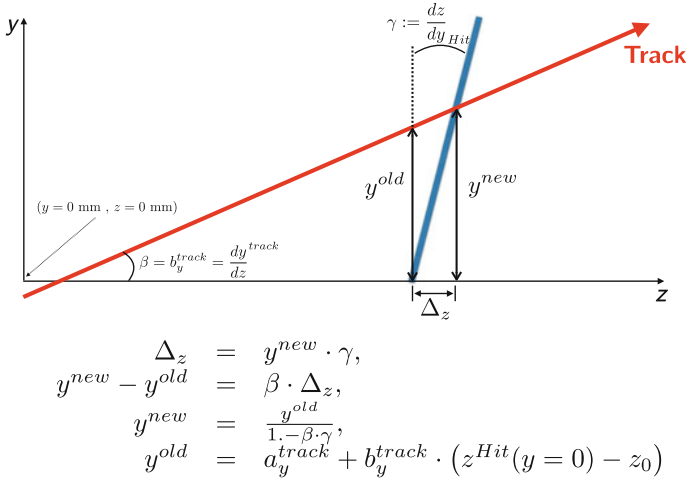$$y^{old} = a_y^{track} + b_y^{track} \cdot \left(z^{Hit}(y=0) - z_0 \right)$$

Fig. 4.32 Geometrical interpretation of the $y_{Hit_i}^{corr}$ computation (y^{new})

track is found to have the $\mathtt{Max\chi_{hit}^2}$ >MaxChi2Hit, the worst hit is removed and the *simultaneous fit* is performed again.[13] For tracks with less than eleven hits, an additional selection is applied looking simultaneously at the value of $|y(0)|$ and the value of $|y(z_0)|$: the latter is almost equivalent to define a detector which would be segmented in y, when searching for tracks expected to have not fired all the available 12 layers. The former, instead, requires for the hit-inefficient track to be *long* ones not experiencing a large variation in y. The tracks experiencing a large variation in y are likely to be low momentum ones which should have been kicked away from the magnet even before reaching the SciFi.

In absence of a hardware *y-segmentation*, which would be able, by construction, to tell if a track is in the internal or external y region of the detector, the track y information can be accessed once the track fit results become available.[14] The selections for $n_{hits} < 11$ tracks are applied as follows:

$$|y(0)| < \mathtt{maxYatZeroLow\ [Case]}$$
$$|y(z_0)| < \mathtt{maxYatzRefLow\ [Case]}$$

where the default values of the geometrical parameters are listed in Table 4.9.

Once the outliers are removed, the final track is accepted and stored as a candidate if $\dfrac{\chi^2}{ndof}$ <maxChi2PerDoF and if it contains at least $\mathtt{minTot}$ hits, where the default values are given in Table 4.9. The track candidates are then stored, and the

---

[13]The fit is performed each time the track has at least 4 fired *x-layers* and 4 fired *u/v-layers*.

[14]In case of a hardware *y-segmentation*, it would be possible to assign to each hit the corresponding *y* region, leading as well to a reduction of the detector occupancy. Using the *in-situ y-segmentation* the knowledge becomes available a posteriori, once all the job has been already done. This is important for *timing* as well.

minimal number of *u/v-layers* to find given a *x-z projection* in the next `Hough-like Cluster` search is updated based on the initial number of *x-z projection* hits and on the final number of hits on the found track candidate.

Once all the `Hough-like Clusters` are processed, the best track candidate is selected among the ones produced by the same *x-z projection*, where, again, "best" stands for "higher number of fired layers", and "lower $\chi^2/ndof$" if they have the same amount of hits.

4.4.5 Flag Hits on Track

The flagging of the hits on a track is enabled by default. The tracks are flagged only if they have been found by `Case 1` and `Case 2`. Only tracks containing $n_{hits} \geq 11$, i.e. either 6 *u/v-layers* or 6 *x-layers*, are used to flag the hits. The minimal number of hits required on track candidates for the flagging can be changed to 12 through the `SizeToFlag[Case]` parameter. By default all the hits on track candidates with $n_{hits} = 12$ are flagged. Hits on tracks having $n_{hits} = 11$ are flagged depending on how well they point back to $x(z = 0) = 0$ and on their $\chi^2/ndof$. The $|x(z = 0)|$ is required to be smaller than `Flag_MaxX0_11Hits[Case]` and the $\chi^2/ndof$ has to be smaller than `Flag_MaxChi2DoF_11Hits[Case]`. The default values used by the algorithm are shown in Table 4.9.

The `Flag_MaxX0_11Hits` parameter is related to what we call "backward projection". The "backward projection" value for a given track allows to have a rough estimate of how likely a track originates at the origin in the *x-z* plane. The "backward projection" takes advantage of the known track parameters (a_x, t_x, c_x) estimated only considering the $\vec{B}$ field in the SciFi volume. Since c_x encodes the value of $\frac{q}{p}$, it is therefore possible to extract the expected x position of the tracks at $z = 0$ accounting for the effect of the integrated magnetic field. What we try to solve is the general form of (4.24), leaving the $B_y(z)$ dependence unknown and trying to estimate the average impact (p_T-kick) of the magnetic field in between the VELO and the SciFi. In particular we try to make a link between the track parameters we have in the SciFi (slope and x position) providing a very rough estimation of where the track is pointing to at $z = 0$ mm.

As for the track model parameterization (see Sect. 4.3.1), we also assume $|t_{x,y}| <<$ 1, $B_{x,z} << B_y$, and $\frac{p_x}{p_z}$ and $\frac{q}{p}$ roughly constant when the track migrates from 0 to z_0. In such a way it is possible to solve the equation and to define the "backward projection" as follows:

$$X_0^{back} = a_x - t_x \cdot z_0 + c_x \cdot C_{Const} \tag{4.40}$$

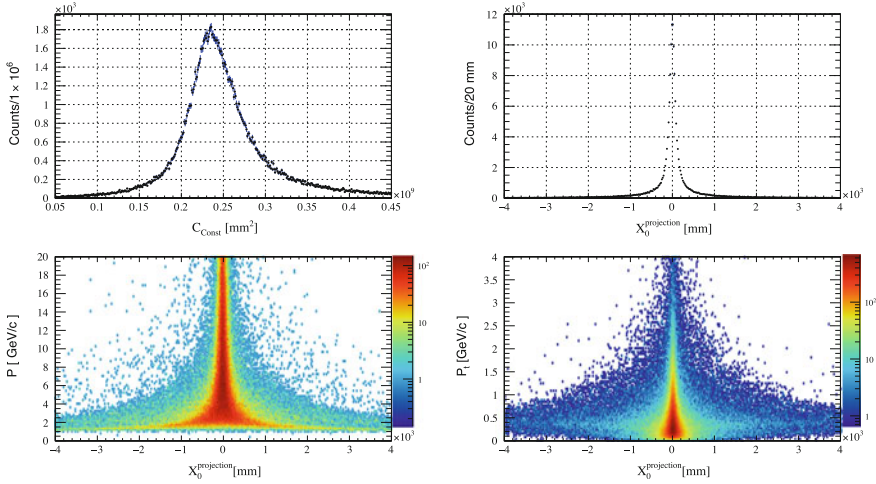recognizing c_x being proportional to $\frac{q}{p}$ and defining:

Fig. 4.33 On the top left, the distribution of C_{Const} found from Monte-Carlo studies. On the top-right, the 1-D distribution of the value of X_0^{back} for all the reconstructible tracks imposing $C_{Const} = 245.8 \cdot 10^6$. On the bottom left and bottom right, the estimated X_0^{back} as a function of the true p and p_T of tracks, respectively (note the logarithmic scale in the z axis)

$$C_{Const} = \int_0^{z_0} \frac{q}{p} dz' \cdot \int_0^{z'} B_y(z'') dz''. \tag{4.41}$$

The value of C_{Const} has been found from Monte Carlo studies, by imposing for all the "fitted" true reconstructible particles $X^{back} = 0$. The distribution for C_{Const} is shown in Fig. 4.33. The most probable value for C_{Const} has been found to be equal to $245.8 \cdot 10^6 \text{mm}^2$. For all track candidates, the fixed value of C_{Const} is used to evaluate X_0^{back}. The distributions for reconstructible tracks of X_0^{back} are shown in Fig. 4.33, where also the dependence with p and p_T is provided. The value of C_{Const} is stored in the configurable called CConst, assuming by default the value provided before.

4.4.6   Global Clone Removal Step

The tracks found after running all the NCases are stored in a container sorted from lower to higher number of hits and from higher to lower $\chi^2/ndof$. The number of shared hits between tracks is counted and if the value exceeds FracCommon times the number of hits on track with less hits, the track with lower number of hits is killed, while if the two tracks have the same amount of hits, the one with higher $\chi^2/ndof$ is removed. All the tracks surviving the global clone removal step are stored as standard LHCb objects, so that they can be handled by other algorithms and by the *Kalman filter*.

4.4.7 Track Recovery

Due to the momentum selection of the `Cases` and the different requirements for the stereo hit search for all the *x-z projection*, tracks having low momentum, low transverse momentum and not pointing to $y(0) = 0$ are penalized: some of them will not be reconstructed even if the actual *x-z projection* was found. In order to recover them, without dramatically increasing the *ghost rate* and timing, a track recovering routine has been designed. This routine can be switched off thanks to the `Recover` tunable parameter. A more accurate track model description and a dedicated track search is required for these tracks and one possible way to find them would rely into enlarging the tolerances of the hit search (in particular for the *two-hit* and *three-hit* combination), increasing the `Hough-like Cluster` spread tolerance and relaxing the track quality requirements. Doing so directly modifying the three `Cases` settings, it is in fact possible to bring a 3–4% tracking efficiency gain but the *ghost rate* increases dramatically to 30–40%, more than a factor 3–4 with respect to the baseline performance (without the track recovery executed).

The main reason why we observe for this behaviour is because of the tracking in projection approach employed by the algorithm: the most powerful way to get rid of fakes is to not find matching hits in the track building sequence. This approach goes in the opposite direction of enlarging tolerances and lowering the hit requirements, especially if the initial track container to process (in this case of *x-z projection* candidates) in the stereo search routine is highly polluted by fake tracks.

A turn-around method to have the same gain without paying a too high price in *ghost rate* is to get rid of the combinatorics by requiring a very limited amount of hits to be shared between tracks,[15] as it has been already discussed in Sect. 4.4.3. Therefore, the track recovering is two main steps:

1. **Selection of** *x-z projections* **to recover**, aiming at filtering all the *x-z projection* candidates which did not find a matching set of *u/v-hits* while executing the 3 `Cases` as follows:

   - All the *x-z projections* found by each one of the `Cases` which do not manage to get a line attached (due to hough-cluster tolerance, track quality requirements, etc.) are temporary stored.
   - Once the algorithm ends the three `Cases` track search and the global clone removal is applied, all the hits on the final selected tracks are flagged as used.
   - All tracks in the temporary container are then required to have a limited amount of used hits. This allows to suppress the large combinatorial component of the *x-z projections* in a reasonable timing and reduce the effective occupancy in stereo layers. Thus, the *x-z projection* candidates are filtered requiring to be "almost unique" tracks, i.e. being composed of hits which have not been used by any of the already found tracks.

---

[15]The candidate is recognized to be almost unique in hit content with respect to all the other candidates already found.
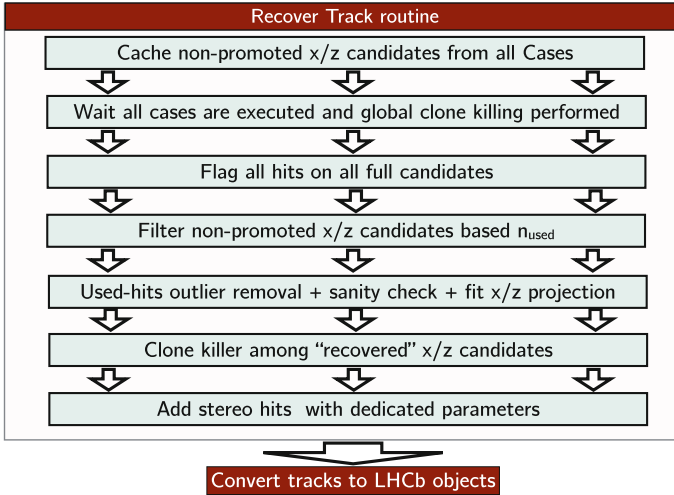
Fig. 4.34 Implemented logic of the track recovering routine. *x-z projections* candidates which are not promoted to full tracks are temporary stored and selected afterwards. The selection is based on how unique the *x-z projection* candidates are. The "unique" criteria relies on counting the number of hits a track candidate has which already used by all the other candidates. A stereo hit search in the cleanest as possible environment is then performed for the selected and recovered *x-z projection* candidates

2. **Dedicated add stereo hit search**, aiming at completing the *x-z projection* filtered candidates adding *u/v-hits*:

   - The resulting recovered *x-z projections* are re-processed through the "add stereo hits" routine with a set of dedicated parameters.
   - The *x-z projections* passing all the "add stereo hits" step are finally added to the final track container.

A sketch of the working flow for the track recovering routine is shown in Fig. 4.34. The two main steps are described in the following subsections.

4.4.7.1 Selection of *x-z projections* to Recover

Each *x-z projection* entering in the stereo hit addition step can get or not a line attached depending on the applied tolerances and track requirements. All the hits on the tracks found by the standard three `Cases` algorithm are marked as used and each one of the *x-z projections* populating the temporary recovering container is required to have an amount of used hits smaller than `nUsedThreshold[0,1,2]` (tunable parameter) where the `nUsedThreshold[0]` is the value used for *x-z projections*

having six hits, `nUsedThreshold[1]` for five hits and `nUsedThreshold[2]` for four hits.[16] This strategy allows to save time in the hit sharing counting.

All the used hits on the *x-z projection* passing the `nUsedThreshold[0,1,2]` selection are removed from the track and only those candidates having at least four fired *x-layers* and at least one hit per T-station are propagated further. Those tracks passing the selection are then fitted again with the *x-z projection fit* in order to better estimate the track parameters before searching for stereo hits and among the recovered *x-z projections* a clone killing routine is performed removing those candidates sharing the 70% of hits with other recovered candidates.

The tracks passing the steps described here are used to perform an additional stereo hit search with dedicated parameters.

4.4.7.2   Dedicated Stereo Hit Search for Recovered *x-z projections*

The same logic described in Sect. 4.4.4 is used to look for *u/v-hits* to attach to the recovered *x-z projections*. The same χ^2 requirements for lines and final $\chi^2/ndof$ as in `Case 3` are applied, but no *in-situ y-segmentation* is used. Also, the minimal number of stereo hits to attach to the *x-z projections* is defined thanks to the `Recover_minUV[0,1,2]` tunable parameter, where `Recover_minUV[0]`, `Recover_minUV[1]` and `Recover_minUV[2]` are the minimal number of *u/v-hits* to find for *x-z projections* having six, five and four hits, respectively.

Furthermore, the `Hough-like Cluster` spread for the stereo hit search is defined through the tunable `Recover_tolTy` parameter, and also the full final track is stored if the total number of fired layers is greater or equal to `Recover_minTotHits` and the selection $|y(z = 0)| <$ `Recover_maxY0` is applied. The values used by default are summarized in Table 4.9.

4.4.8   Summary of the Changes with Respect to the `TDR` `Seeding`

Using as a starting point the `TDR Seeding`, the `Hybrid Seeding` implements new efficient strategies, summarized in the following:

- The tracking in projection design has been optimized defining new parametrizations for the search windows;
- A progressive cleaning of the tracking environment is used, while recovering for hit inefficiencies and relaxing search windows for lower momentum tracks;
- Hits in the stereo layers are not simply used to confirm a *x-z projection* found: they are actively used to apply stringent requirements on candidates, leading to a large reduction of the *ghost rate*, while keeping high level of efficiencies;

---

[16]Due to the *x-z projection* track search logic, the number of hits corresponds to the number of fired layers.

- The hit requirements are applied in such a way to have a compensation between *x-z* search and *u-v* hit search.
- An *in-situ y-segmentation* is applied, so that the algorithm allows to integrate ghosts only where detector inefficiencies are expected (i.e. in the detector region close to the beam-pipe);
- Different processing of the `Hough-like Clusters`: not all clusters within a given tolerance are processed, but only those with smaller spreads, which are more likely defining the true line to attach at a *x-z projection* candidate. In the `TDR Seeding` all clusters were processed without any external supervision and self-checking. The different stereo-layers processing is responsible of almost a factor two in speed-up of the algorithm, without any tracking performances loss.
- The track recovering routine: it allows to guarantee high performance also for lower *p* tracks and improve the robustness of the algorithm.

4.4.9 Parameters Summary

4.5 `Hybrid Seeding` **Performances**

The final part of this chapter is dedicated to the evaluation of the performances of the `Hybrid Seeding`, and additionally provides a direct comparison with the `TDR Seeding` (Sect. 4.5.1). Suggestions for future improvements of the `Hybrid Seeding` are also discussed in Sect. 4.5.2. Tracking performances have been evaluated including also $e^{\pm}$.

4.5.1 Results and Comparison with the `TDR Seeding`

The performances of the `Hybrid Seeding` have been evaluated on three different samples described in Sect. 4.2.4. *Tracking efficiencies* are quoted for various track type categories (*hasT*, *long*, *fromB*, etc..). Details of the naming scheme is given in Table 4.10. The summary table of performances (Tables 4.12, 4.13 and 4.14) shows that the `Hybrid Seeding` performs significantly better than the first implementation of the algorithm (`TDR Seeding`). A significant improvement is achieved in all the fields (Tables 4.11 and 4.12):

- The *ghost rate* is reduced by a factor 2 with respect to the old seeding version, and the efficiencies are significantly higher.
- The *tracking efficiencies* get a significant improvement for all the track categories, especially for lower *p* and p_t tracks (20 %) while for higher *p* a gain of 4–6% is achieved.

Table 4.9   Table of tunable parameters used in `Hybrid Seeding`, and their default values

Name	Default Value
General Parameters	
TimingMeasurement	False
InputName	""
DecodeData	False
NCases	3
Clone Removal (Sec. 4.4.3 and Sec. 4.4.6)	
RemoveClonesX	True
RemoveClones	True
FracCommon	0.71
Track model (Sec. 4.3.1)	
dRatio[mm^{-1}]	$-2.62 \cdot 10^{-4}$
x-z projection: 2-hit combination (Sec. 4.4.2.2)	
L0_AlphaCorr[mm]	[120.64 , 510.64 , 730.64]
L0_tolHp[mm]	[280.0 , 540.0 , 1080.0]
x-z projection: 3-hit combination (Sec. 4.4.2.3)	
x0Corr[mm]	[2.152 , 1.534 , 1.834]·10^{-3}
X0SlopeChange[mm]	[400. , 500. , 500.]
x0Cut[mm]	[1500.0 , 4000. , 6000.]
TolAtX0Cut[mm]	[4.5 , 8.0 , 14.0]
ToleranceX0Up	[0.75, 0.75 , 0.75]
X0SlopeChangeDown[mm]	[2000.0 , 2000.0 , 2000.0]
TolAtX0CutOpp[mm]	[0.75 , 2.0 , 7.0]
ToleranceX0Down[mm]	[0.75 , 0.75 , 0.75]
maxParabolaSeedHits	12
x-z projection: Collect remaining and fit (Sec. 4.4.2.4)	
TolXRemaining	[1.0 , 1.0 , 1.0]
maxChi2HitsX	[5.5 , 5.5 , 5.5]
MinXPlanes	4
maxChi2DoFX	[4.0 , 5.0 , 6.0]
Recover track routine (Sec. 4.4.7)	
Recover	True
nUsedThreshold	[2,1,1]
Recover_tolTy[rad]	[0.010]
Recover_MaxNCluster	3
Recover_maxY0[mm]	1800
Recover_minTotHits	9
Recover_minUV	[4,5,5]

Name	Default Value
Add stereo: Collect compatible u/v-hits (Sec. 4.4.4.1)	
TriangleFix	True
TriangleFix2ndOrder	True
yMin[mm]	-1.0
yMax[mm]	2700.0
yMin_TrFix[mm]	-2.0
yMax_TrFix[mm]	30.0
RemoveHole	True
RadiusHole[mm]	87.0
Add stereo: store, select and clusters to line conversion (Sec. 4.4.4.2, 4.4.4.3 and 4.4.4.4)	
TolTyOffset[rad]	[0.0017 , 0.0025 , 0.0035]
TolTySlope	[0.0 , 0.025 , 0.035]
maxNbestCluster	[2 , 4 , 4]
minUV6	[4 , 4 , 4]
minUV5	[5 , 5 , 4]
minUV4	[6 , 5 , 5]
Chi2LowLine	[5.0 , 6.5 , 7.5]
Chi2HighLine	[30.0 , 50.0 , 80.0]
Add stereo: - in-situ y-segmentation and simultaneous fit (Sec. 4.4.4.5)	
maxChi2Hits_less11Hit	[2.5 , 2.5 , 2.5]
maxYatZeroLow[mm]	[50.0 , 60.0 , 70.0]
maxYatzRefLow[mm]	[400.0 , 550.0 ,700.0]
maxChi2PerDoF	[4.0 , 6.0 , 7.0]
maxChi2Hits_11and12Hit	[5.5 , 5.5 , 5.5]
minTot	[9 , 9 , 9]
Flag Hits (Sec. 4.4.5)	
RemoveFlagged	True
FlagHits	True
CConst[mm^2]	245.8×10^6
SizeToFlag	[12 , 11 , 10]
Flag_MaxChi2DoF_11Hits	[0.5 , 1.0 , 1.0]
Flag_MaxX0_11Hits	[100. , 8000. , 200.]

Table 4.10   Sub-selections used by the performances indicators

Name	Property
hasT	*reconstructable* in SciFi
UT + SciFi	*reconstructable* in SciFi and UT
noVelo	not *reconstructable* in the VELO
long	*reconstructable* in VELO and SciFi
strange	daughter of a strange particle (K_S^0, Λ^0,..)
from B	belongs to the decay chain of a *b* hadron
from D	belongs to the decay chain of a *c* hadron

Table 4.11 Average, maximum and minimum timing of the algorithms for the different used samples. Timing performance are also quoted with respect to the *forward* tracking used for the upgrade in the *best* tracking sequence

Machine speed $n \cdot 2.8$ GHz Xenon	Sample	Algorithm	Avg. time $[\frac{ms}{evt.}]$	Min. time $[\frac{ms}{evt.}]$	Max. time $[\frac{ms}{evt.}]$
2.76	1	Forward Tracking Best	29.95	0.11	612.1
		TDR Seeding	72.75	0.15	1770.0
		Hybrid Seeding	23.53	0.24	589.4
2.79	2	Forward Tracking Best	48.62	0.30	1271.4
		TDR Seeding	150.95	1.86	6069.0
		Hybrid Seeding	46.80	0.70	1239.1
2.99	3	Forward Tracking Best	30.16	0.20	1013.4
		TDR Seeding	79.44	0.91	2042.9
		Hybrid Seeding	22.30	0.37	662.7

- The *clone* killing is more efficient than in the previous algorithm version. This is achieved thanks to a more accurate track comparison and thanks to the internal sorting of the hits, which allows a better track-to-track comparison.
- Also the *timing* of the `Hybrid Seeding` is significantly improved compared to the `TDR Seeding`. On average almost a factor 3–4 is gained, depending on the detector occupancy level, as shown in Table 4.11. Furthermore, the maximal timing leakage observed for very busy events in the `TDR Seeding` is corrected for. This is evident looking at the significant drop (almost a factor 5) for the maximal time per event in Table 4.11. In other words, `Hybrid Seeding` is more robust against busy events compared to the `TDR Seeding`. Timing comparisons have been achieved running both algorithms on the same machine (a standard lxplus machine SLC6 in 64-bit mode) and we also quote the timing of the *forward tracking* algorithm (as a reference value) in the *best* tracking sequence stage, i.e., the configuration aiming at finding all *long* tracks in the event.

The performance improvements are well understood and they are mainly driven by the following aspects:

Table 4.12 Tracking performances comparison between the `TDR Seeding` and the `Hybrid Seeding` algorithms for *Sample 1*. The event average *ghost* rate is evaluated averaging the rates of fake tracks in each events

Track type	Sample 1	
	`TDR Seeding` ϵ (*clone rate*) (%)	`Hybrid Seeding` ϵ (*clone rate*) (%)
hasT	(50.9 ± 0.1) (2.4)	(65.7 ± 0.1) (0.0)
long	(75.3 ± 0.1) (2.3)	(90.3 ± 0.1) (0.0)
long $P > 5$ GeV/c	(85.0 ± 0.1) (1.4)	(93.1 ± 0.1) (0.0)
long from B	(81.8 ± 0.2) (1.7)	(92.1 ± 0.1) (0.0)
long from B $P > 5$ GeV/c	(87.0 ± 0.2) (1.3)	(93.6 ± 0.1) (0.0)
long from B or D	(80.6 ± 0.2) (1.8)	(91.8 ± 0.1) (0.0)
long from B or D $P > 5$ GeV/c	(86.6 ± 0.1) (1.3)	(93.4 ± 0.1) (0.0)
UT +SciFi *strange*	(71.6 ± 0.1) (2.5)	(89.7 ± 0.1) (0.0)
UT +SciFi *strange* $P > 5$ GeV/c	(85.4 ± 0.2) (1.4)	(93.3 ± 0.1) (0.0)
noVELO +UT +SciFi *strange*	(72.2 ± 0.2) (2.4)	(89.1 ± 0.1) (0.0)
noVELO +UT +SciFi *strange* $P > 5$ GeV/c	(85.3 ± 0.2) (1.4)	(93.1 ± 0.2) (0.0)
ghost rate	(23.1 ± 0.1)	(9.4 ± 0.1)
ghost rate (evt.avg)	12.0	4.9
hit purity	99.0	99.6
hit efficiency	96.0	97.82

- A better description of the tracks behavior in the SciFi, achieved by the new track model. The simple parabolic track model was not describing properly the overall effect of the magnetic field on tracks, as discussed in Sect. 4.3.1.
- Processing all the tracks in a single step (especially for the *u/v-hits* search), as done in the `TDR Seeding`, was a suboptimal choice, leading to worse performances in both *ghost rate* and *tracking efficiencies*. When *x-z projections* are found, there is almost a 2.5 m indetermination of where the track goes in the *y-z* plane. Therefore, *u/v-hits* cannot be only used to validate a *x-z projection*. Since the only regions of the detector where inefficiencies can arise are the ones closer to the beam-pipe hole,[17] there is no need to require fewer hits on track in the external region, which is also the region where the `Hough-like Clusters` need to be set to a larger value.
- The *clone rate* is basically zero in the `Hybrid Seeding`. In the `TDR Seeding` the counting of the common hits between tracks was also done looking at the identifier of the hits, but the hits on the compared tracks were not sorted according to the identifier, resulting into a sub-optimal implementation of the clone removal step.

---

[17]Light attenuation and fiber opacity due to radiation.

Table 4.13 Tracking performances comparison between the `TDR Seeding` and the `Hybrid Seeding` algorithms for *Sample 2*. The event average *ghost* rate is evaluated averaging the rates of fake tracks in each events

Track type	Sample 2	
	`TDR Seeding` ϵ (*clone rate*) (%)	`Hybrid Seeding` ϵ (*clone rate*) (%)
hasT	$(53.5 \pm 0.1)(3.5)$	$(66.6 \pm 0.1)(0.0)$
long	$(78.4 \pm 0.1)(3.3)$	$(92.1 \pm 0.1)(0.0)$
long P > 5 GeV/c	$(87.5 \pm 0.1)(2.6)$	$(95.4 \pm 0.4)(0.0)$
long from B	$(80.4 \pm 0.6)(2.7)$	$(93.0 \pm 0.3)(0.0)$
long from B P > 5 GeV/c	$(88.5 \pm 0.5)(2.3)$	$(95.9 \pm 0.1)(0.0)$
long from B or D	$(80.7 \pm 0.2)(2.7)$	$(93.3 \pm 0.1)(0.0)$
long from B or D P > 5 GeV/c	$(89.3 \pm 0.2)(2.3)$	$(95.9 \pm 0.1)(0.0)$
UT +SciFi *strange*	$(76.3 \pm 0.1)(3.3)$	$(91.8 \pm 0.1)(0.0)$
UT +SciFi *strange* P > 5 GeV/c	$(88.8 \pm 0.1)(2.5)$	$(95.7 \pm 0.1)(0.0)$
noVELO +UT +SciFi *strange*	$(76.8 \pm 0.2)(3.3)$	$(91.3 \pm 0.1)(0.0)$
noVELO +UT +SciFi *strange* P > 5 GeV/c	$(88.7 \pm 0.2)(2.7)$	$(95.6 \pm 0.1)(0.0)$
ghost rate	(37.3 ± 0.1)	(19.4 ± 0.1)
ghost rate (evt.avg)	21.6	11.2
hit purity	98.9	99.6
hit efficiency	93.6	95.4

- The *hit probability conversion* inefficiencies are recovered limiting the *ghost rate* thanks to the progressive cleaning of the tracking environment. In particular, detector hit inefficiencies are recovered exploring different *two-hit* initial combinations in the *x-z projection* track search but also in the stereo hits search, when we define the minimal number of different *u/v-layers* required (`MinUV-J[Case]`) on track candidates. The *ghost rate* can be kept under control thanks to the *in-situ y-segmentation*, the tighter selections applied for candidates which are found to have $n_{hits}^{track} < 11$, and the maximal number of stored clusters to process.

The *ghost rate* comparison between the `Hybrid Seeding` and the `TDR Seeding` for the *Sample 1* is shown in Fig. 4.35, while the *tracking efficiencies* comparison for *long from B or D* tracks in *Sample 3* is shown in Fig. 4.37.

The same *tracking efficiencies* distributions are shown for the *Sample 2* in Fig. 4.36, but looking at the tracks potentially originated from the daughters of K_S^0 and Λ^0. We also define ϕ as the ratio between the y component of the momentum and the x one, i.e., $\phi = \dfrac{p_y}{p_x}$. $\phi \in [-\pi/2, \pi/2]$ is used for $p_x > 0$ and $\phi \in [-\pi, -\pi/2] \cup [\pi/2, \pi]$ for $p_x < 0$. Another interesting variable is the number of expected hits, defined as the total amount of clusters expected to be reconstructed

Table 4.14 Tracking performances comparison between the TDR Seeding and the Hybrid Seeding algorithms for *Sample 3*

Track type	Sample 3	
	TDR Seeding ϵ (*clone rate*) (%)	Hybrid Seeding ϵ (*clone rate*) (%)
hasT	$(53.4 \pm 0.1)(2.8)$	$(67.2 \pm 0.1)(0.0)$
long	$(77.1 \pm 0.1)(2.6)$	$(90.6 \pm 0.1)(0.0)$
long P > 5 GeV/c	$(88.2 \pm 0.1)(1.8)$	$(94.8 \pm 0.1)(0.0)$
long from B	$(84.4 \pm 0.1)(2.0)$	$(93.4 \pm 0.1)(0.0)$
long from B P > 5 GeV/c	$(90.0 \pm 0.1)(1.6)$	$(95.4 \pm 0.1)(0.0)$
long from B or D	$(83.3 \pm 0.1)(2.2)$	$(92.9 \pm 0.1)(0.0)$
long from B or D P > 5 GeV/c	$(89.8 \pm 0.1)(1.6)$	$(95.3 \pm 0.1)(0.0)$
UT +SciFi *strange*	$(73.6 \pm 0.1)(3.0)$	$(89.7 \pm 0.1)(0.0)$
UT +SciFi *strange* *P* > 5 GeV/c	$(88.7 \pm 0.2)(1.8)$	$(95.2 \pm 0.1)(0.0)$
noVELO +UT +SciFi *strange*	$(74.2 \pm 0.2)(2.8)$	$(89.4 \pm 0.1)(0.0)$
noVELO +UT +SciFi *strange* *P* > 5 GeV/c	$(88.6 \pm 0.4)(1.7)$	$(95.0 \pm 0.1)(0.0)$
ghost rate	(21.3 ± 0.1)	(7.9 ± 0.1)
ghost rate (evt.avg)	10.9	4.5
hit purity	99.1	99.7
hit efficiency	94.9	96.8

for a given track. It gives us an idea of whether the clustering algorithm is producing more than one hit per layer for a given track. At the same time it allows to check how well the algorithm is able to handle hit inefficiencies (Fig. 4.37).

4.5.2 Suggestions for Future Improvements

The reason why the Hybrid Seeding is outperforming the TDR Seeding has been extensively demonstrated and described. We now would like to underline some aspects of the algorithm which can be further improved in the future.

1. Tracks entering at a large angle in the detector generate signals in many different channels, leading to multiple clusters per layer. In order to be partially independent from correlations between hits within the same layer, arising if the cluster gets split, the current algorithm reconstructs tracks forcing them to contain a single hit per layer. An alternative solution would be to re-weight the hits for the fit if they are found to be in the same layer in such a way to take properly into account the hit correlations or a revisit of the clustering algorithm to suppress the cluster splitting.
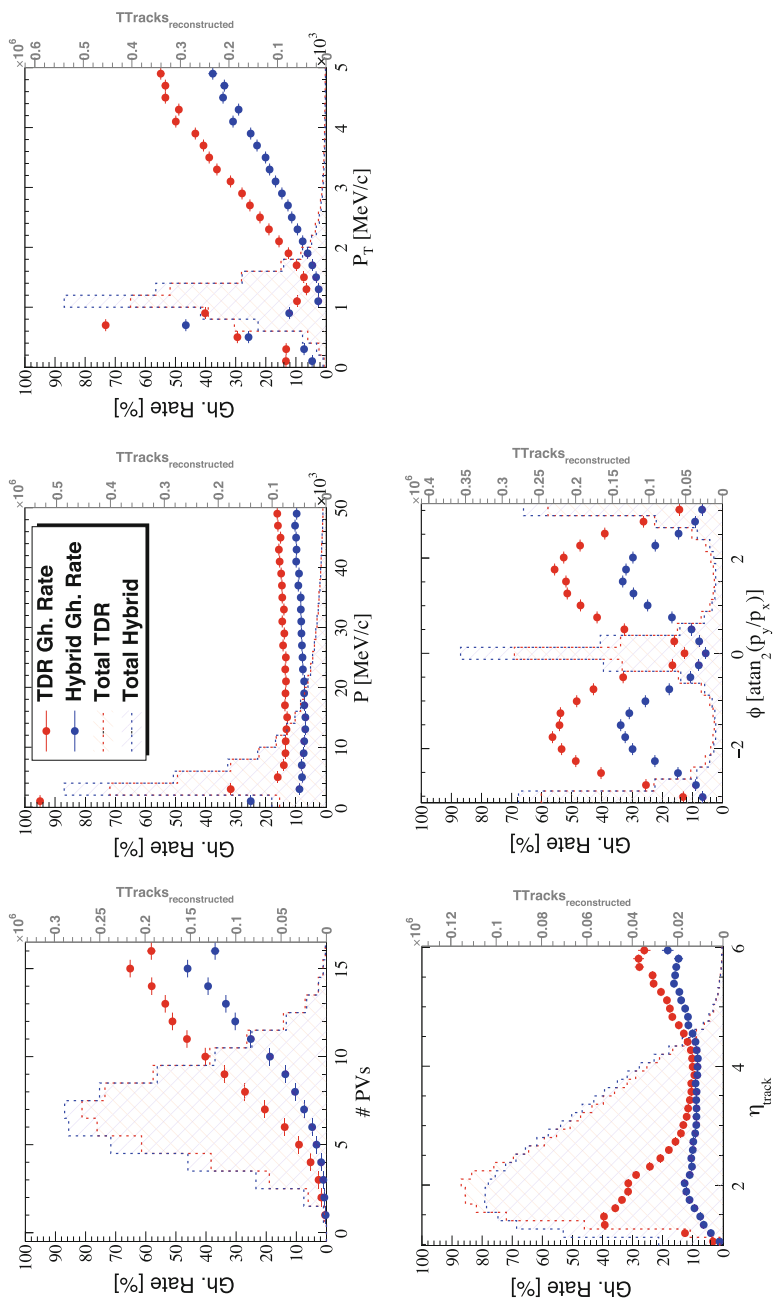
Fig. 4.35 *Sample 1: ghost rate* comparison between the Hybrid Seeding (in blue) and the TDR Seeding (in red). The plots show also the reconstructed track distributions from the two versions of the algorithm. Note that the p, p_T, η_{track} and ϕ distributions are determined using solely the SciFi segment information
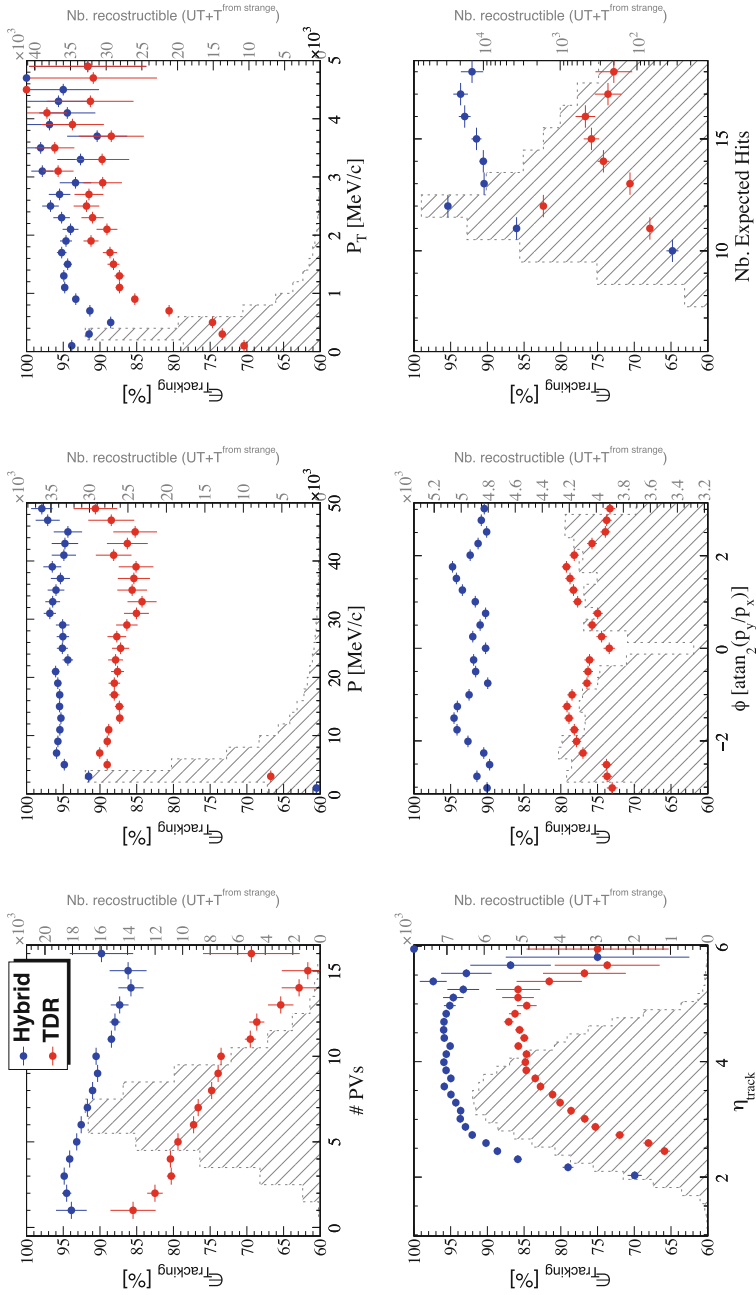
Fig. 4.36 *Tracking efficiencies* distributions for the *Sample 2* selecting tracks having hits in the UT and the SciFi and being daughters of long-lived strange particles, such as K_S^0 or Λ^0. The efficiencies obtained with the Hybrid Seeding (blue) algorithm are on average 12% better than the ones from the TDR Seeding
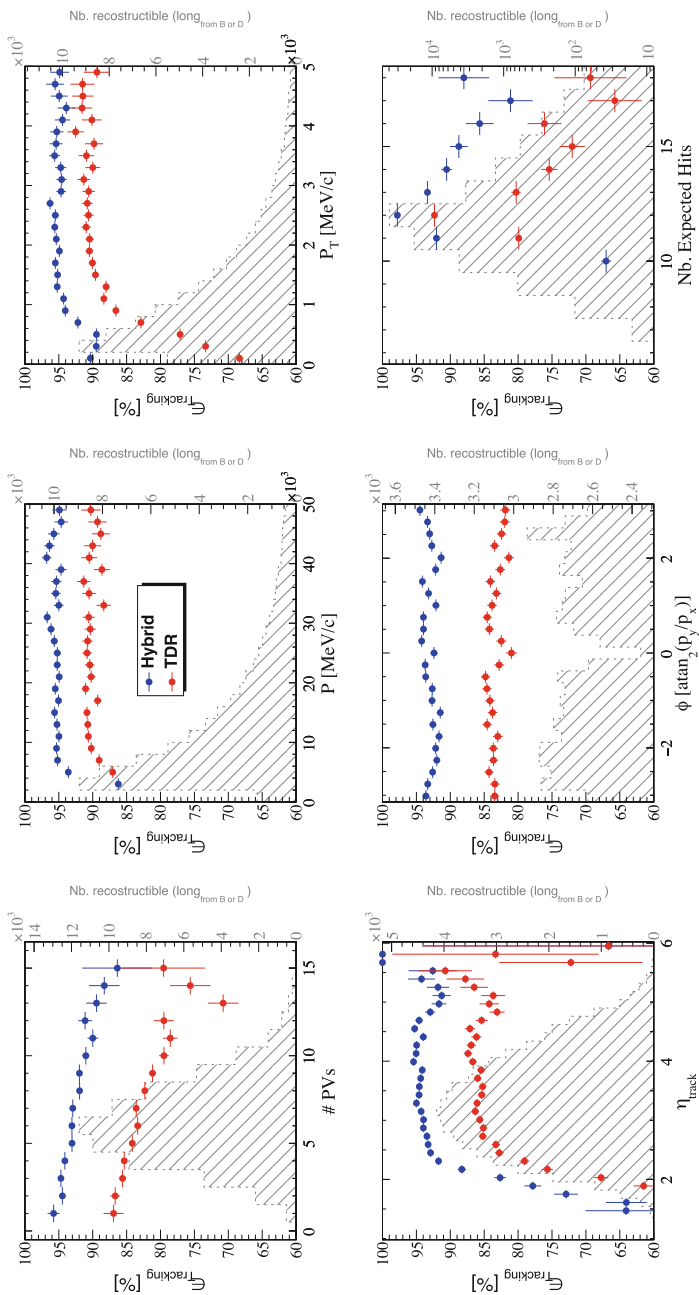
Fig. 4.37 *Sample 3: tracking efficiencies* plot distributions for *long* tracks. The plots shows the *tracking efficiencies* comparison between the `Hybrid Seeding` (in blue) and the `TDR Seeding` (in red). A large gain is achieved especially at low p_T. Low p_T long tracks constitute the larger fraction of tracks as it can be seen from their distributions (dashed distributions). A significant gain is also achieved at larger p and p_T

2. Tracks with low momenta require larger tolerances for the `Hough-like Clusters` selection. Low p and p_T tracks are searched for in the track recovering routine, in `Case 3` and partially in `Case 2`. Therefore, if a low momentum track is not firing the *two-hit* combination of `Case3` and `Case 2`, then the track would not be found in any of the other `Cases`, since `Case 1` is only looking at higher momentum *two-hit* combinations. A possible improvement could be achieved through a partial re-design of the algorithm. The re-design would consist in a search for *x-z projections* in all the `Cases`, splitting the *x-z projection* candidates found in different containers depending on the track quality. In a second step, *u/v-hits* are looked for the best quality *x-z projection*, hits on candidates are flagged and *u/v-hits* are searched for the lower quality *x-z projections* after cleaning-up the container imposing a limited number of used hits with the better quality candidates found previously. In such proposed approach, instead of a tracking environment cleaning, we would realize a progressive clean-up of the *x-z projections* candidates. This kind of approach could lead to a reduced *ghost rate* and *timing* improvements.

3. Tracks going to large $|y(z_0)|$ and having a large $|y_0|$ (which are also the ones with low momenta and being potentially long-lived particle daughters) can be found requiring larger tolerances for the `Hough-like Cluster` selection (up to `TolTy` $\simeq 15$ mrad), which at the moment is not reached by anyone of the `Cases` in the algorithm, except for the recover track routine. The track recovering routine is attempting to find them, but out of the potential 5% tracking efficiency gain achievable, only 3–4% is accomplished.

4. A better track quality parametrization needs to be further investigated in order to improve the clone killing removal step. In the current implementation, each time that tracks are compared to each other, the ones with a higher number of hits are always preferred. Instead, one could define some track quality parameter, for instance dependent on both the $\chi^2/ndof$ and the number of hits. In such a way, a track found containing only five hits but with a very good $\chi^2/ndof$ could be preferred to a track with six hits and a large $\chi^2/ndof$, in case they share some of their hits. This could also improve the *ghost rate* and *tracking efficiency*, reducing the minimal number of shared hits to do the track comparison.

4.5.3   Break-Up of Algorithm Steps

In order to fully understand the performance of the algorithms and eventually tune it to maximise the timing, the performances have been estimated in 8 different steps ordered in sequential execution order as defined in Table 4.15. Figure 4.38 shows the evolution of performances as a function of the tracking steps defined before and Fig. 4.39 shows the evolution of the total amount of tracks classified by type as a function of the tracking steps using the *Sample 3*.

Table 4.15 Different steps defined in the algorithm used to break-up the performance evolution of the `Hybrid Seeding`.

Step 0	exit of `Case 1` *x-z projection* search (after performing the removal of clones)
Step 1	exit of `Case 1` stereo hit search for the *x-z projections* found in `Case 1`
Step 2	exit of `Case 2` *x-z projection* search (after performing the removal of clones)
Step 3	exit of `Case 2` stereo hit search for the *x-z projections* found in `Case 2`
Step 4	exit of `Case 3` *x-z projection* search (after performing the removal of clones)
Step 5	exit of `Case 3` stereo hit search for the *x-z projections* found in `Case 3`
Step 6	at the step in the track recovery routine in which the recovered *x-z projections* are selected (just before adding the stereo hits with dedicated parameters)
Step 7	at the exit of the `Hybrid Seeding`, where all track candidates have been found

Fig. 4.38 Evolution of *tracking efficiency*, *ghost rate* (red) and clone tracks rate (for *hasT* track categories in yellow) for the `Hybrid Seeding` algorithm. *Tracking efficiency* is shown for all `Long` track from *b*-hadrons in the event (green) and selecting only those having $p > 5\,\text{GeV/c}$ (blue). The various `Hybrid Seeding` step are defined in Table 4.15
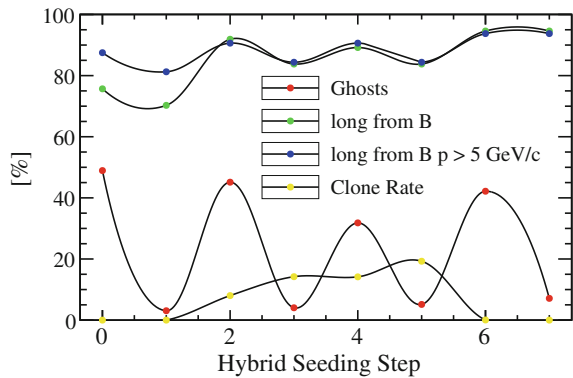

Fig. 4.39 Evolution of the `Hybrid Seeding` algorithm amount of tracks found (and handled) depending on the algorithm steps. In red the total track container, in yellow the fraction of real tracks found by the algorithm, in green the fake ones and in blue the clones. The number of tracks in the *y* axis is provided in arbitrary scale. The various `Hybrid Seeding` step are defined in Table 4.15
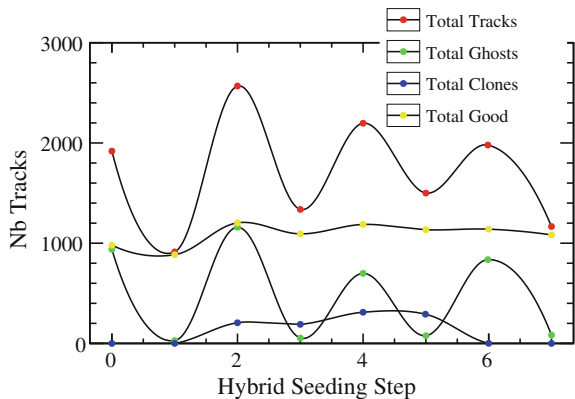
This study allows to better understand the impact of a tracking in projection approach when dealing with a detector such as the SciFi. The *x-z projections* contamination from fakes is huge, and the missing matching of hits from the *u/v-layers* to the *x-z projection* is the key ingredient to kill fake tracks. Nonetheless, the price
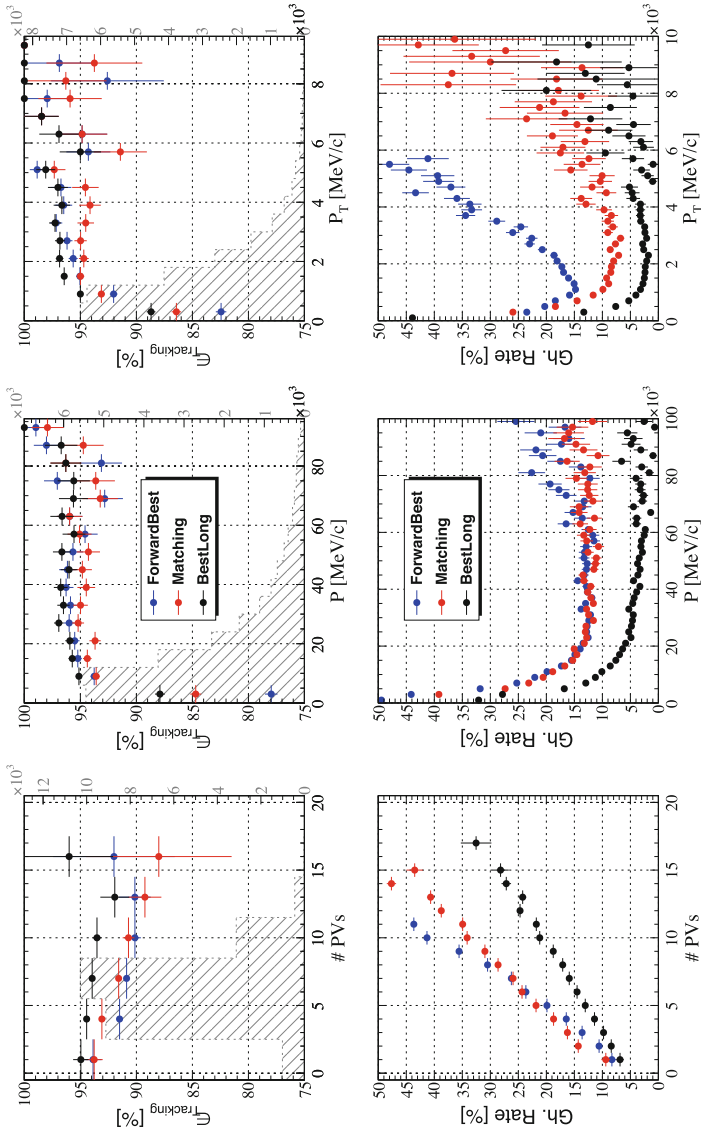
Fig. 4.40 Comparison of Long track reconstruction performances in the *best* tracking stage between the *matching* (red), *forward* (blue) and the output of the combined containers after the Kalman Filter Fit (black) using *Sample 3*. The Hybrid Seeding serving as input for the *matching* significantly helps at improving the lower p and p_T track reconstruction as well as reconstruction efficiencies at higher momentum

to pay to suppress the *ghost rate* from around 50% to well below 10% in the *u/v-hits* search is a small loss in *tracking efficiency*. As expected, lower p tracks are found mainly thanks to `Case 2` and `Case 3`, as well as the track recovery routine. In terms of timing, one could spot from this study that a lot of useless tracks are found in the *x-z projection* search (clones and fakes), and any kind of a priori suppression of those before adding the *u/v-hits* to them would lead to a large speed-up of the algorithm.

4.5.4   Summary

A new pattern recognition algorithm for the LHCb upgrade, the `Hybrid Seeding` has been described. The algorithm is a stand-alone track reconstruction algorithm using only the available hits in the SciFi detector which is foreseen for the LHCb upgrade. The algorithm is based on new, improved and faster reconstruction strategies with respect to the `TDR Seeding`. All the performances indicators are significantly improved. Tracking efficiencies are significantly higher, for both *long* and *downstream* tracks, mainly thanks to a novel track parametrization; the ghost rate is decreased by a factor three, thanks to the *in-situ y-segmentation*, the progressive cleaning of the tracking environment and the active usage of the information from the stereo hits to select tracks. The timing is decreased by almost a factor 4, thanks to the new processing of stereo hits logic and the progressive tracking environment cleaning.

The `Hybrid Seeding` output is used to reconstruct `Long` tracks through the *matching* algorithm (see Sect. 4.1.7) which adopts a different strategy from the *forward* algorithm (see Sect. 4.1.4). From Fig. 4.40 it can be seen that the `Hybrid Seeding` impact in the final `Long` track reconstruction helps to find additional tracks which cannot be found from the *forward* algorithm, especially at low p_T and p at a reduced *ghost rate* (compared to the *forward*). Furthermore, the amount of fake tracks in the *matching* algorithm is much lower than the one obtained in the *forward* algorithm. Also a similar timing is measured when considering the time spent by the `Hybrid Seeding` and *matching* with respect to the *forward* in the *best* sequence.

These good performances are expected to further improve in the future, thanks to the additional ideas discussed in Sect. 4.5.2.

References

1. R.E. Kalman, A new approach to linear filtering and prediction problems. Trans. ASME-J. Basic Eng. **82D**, 35 (1960)
2. P. Billoir, Track fitting with multiple scattering: a new method. Nucl. Instrum. Meth. **A225**, 352 (1984). https://doi.org/10.1016/0167-5087(84)90274-6
3. R. Fruhwirth, Application of Kalman filtering to track and vertex fitting. Nucl. Instrum. Meth. **A262**, 444 (1987). https://doi.org/10.1016/0168-9002(87)90887-4

4. G. Gracia, M. Merk, W. Rückstuhl, R. Van der Eijk, Track reconstruction for LHCb. Technnical report. LHCb-98-045, CERN, Geneva (1998)
5. T. Bird et al., VP simulation and track reconstruction. Technical report. LHCb-PUB-2013-018. CERN-LHCb-PUB-2013-018, CERN, Geneva (2013)
6. L. Collaboration, LHCb VELO upgrade technical design report. Technical report. CERN-LHCC-2013-021. LHCB-TDR-013 (2013)
7. E. Bowen, B. Storaci, VeloUT tracking for the LHCb upgrade. Technical report. LHCb-PUB-2013-023. CERN-LHCb-PUB-2013-023. LHCb-INT-2013-056, CERN, Geneva (2014)
8. Y. Amhis, O. Callot, M. De Cian, T. Nikodem, Description and performance studies of the Forward Tracking for a scintilating fibre detector at LHCb. Technical report. LHCb-PUB-2014-001. CERN-LHCb-PUB-2014-001, CERN, Geneva (2014)
9. P.V.C. Hough, *Method and Means for Recognizing Complex Patterns* (1962), http://www.freepatentsonline.com/3069654.html
10. O. Callot, S. Hansmann-Menzemer, The forward tracking: algorithm and performance studies. Technical report. LHCb-2007-015. CERN-LHCb-2007-015, CERN, Geneva (2007)
11. M. Benayoun and O. Callot, The forward tracking, an optical model method, Technical report. LHCb-2002-008, CERN, Geneva, Feb, 2002. revised version number 1 submitted on 2002-02-22 17:19:02
12. L. Collaboration, LHCb tracker upgrade technical design report. Technical report. CERN-LHCC-2014-001. LHCB-TDR-015 (2014)
13. Y. Amhis et al., The Seeding tracking algorithm for a scintillating detector at LHCb, Technical report. LHCb-PUB-2014-002. CERN-LHCb-PUB-2014-002, CERN, Geneva (2014)
14. A. Davis, M. De Cian, A.M. Dendek, T. Szumlak, PatLongLivedTracking: a tracking algorithm for the reconstruction of the daughters of long-lived particles in LHCb. Technical report. LHCb-PUB-2017-001. CERN-LHCb-PUB-2017-001, CERN, Geneva (2017)
15. O. Callot, Downstream pattern recognition. Technical report. LHCb-2007-026. CERN-LHCb-2007-026, CERN, Geneva, Mar, 2007
16. M. De Cian, U. Straumann, O. Steinkamp, N. Serra, Track reconstruction efficiency and analysis of $B^0 \rightarrow K^{*0}\mu^+\mu^-$ at the LHCb Experiment. Ph.D thesis, Zurich U., 2013
17. S. Esen, M. De Cian, A track matching algorithm for the LHCb upgrade. Technical report. LHCb-PUB-2016-027. CERN-LHCb-PUB-2016-027, CERN, Geneva (2016)
18. M. Needham, Performance of the track matching. Technical report. LHCb-2007-129. CERN-LHCb-2007-129, CERN, Geneva (2007)
19. M. Needham, J. Van Tilburg, Performance of the track matching. Technical report. LHCb-2007-020. CERN-LHCb-2007-020, CERN, Geneva (2007)
20. R. Aaij et al., Tesla: an application for real-time data analysis in high energy physics. Comput. Phys. Commun. **208**, 35 (2016). https://doi.org/10.1016/j.cpc.2016.07.022, arXiv:1604.05596
21. A. Dziurda, J. Wanczyk, Primary vertex reconstruction for upgrade at LHCb. Technical report. LHCb-PUB-2017-002. CERN-LHCb-PUB-2017-002, CERN, Geneva (2017)
22. LHCb Trigger and Online Upgrade Technical Design Report, Technical report. CERN-LHCC-2014-016. LHCB-TDR-016 (2014)
23. LHCb collaboration, LHCb magnet: technical design report. CERN-LHCC-2000-007.LHCb-TDR-001, http://cdsweb.cern.ch/search?p=CERN-LHCC-2000-007&f=reportnumber&action_search=Search&c=LHCb+Reports
24. R. Quagliani, *SciFi - A Large Scintillating Fibre Tracker for LHCb* (2016), https://cds.cern.ch/record/2207956
25. Kuraray Co., Kuraray Home Webpage, http://kuraraypsf.jp/psf/index.html. Accessed 20 Feb 2017
26. T. Förster, Zwischenmolekulare energiewanderung und fluoreszenz. Annalen der Physik **437**(1–2), 55 (1948). https://doi.org/10.1002/andp.19484370105
27. M. Deckenhoff, B. Spaan, Scintillating fibre and silicon photomultiplier studies for the LHCb upgrade (2015), http://cds.cern.ch/record/2140068. Presented 23 Feb 2016
28. E. Cogneras, M. Martinelli, J. van Tilburg, J. de Vries, The digitisation of the scintillating fibre detector. Technical report. LHCb-PUB-2014-003. CERN-LHCb-PUB-2014-003, CERN, Geneva (2014)

29. L. del Buono, O. Gruenberg, D. Milanes, Geometry of the Scintillating Fiber detector, Technical report. LHCb-PUB-2014-005. CERN-LHCb-PUB-2014-005, CERN, Geneva (2014)
30. LHCb Collaboration, LHCb tracker upgrade technical design report, CERN-LHCC-2014-001. LHCB-TDR-015, http://cdsweb.cern.ch/search?p=CERN-LHCC-2014-001&f=reportnumber&action_search=Search&c=LHCb+Reports
31. R. Lindner, Definition of the coordinate system. Technical report (2003)

Chapter 5
The $B \rightarrow DDK$ Phenomenology

The CKM matrix (V_{CKM}) encodes the complex amplitudes of flavour changing processes between quarks (see Sect. 1.6.1).

The experimental absolute values of V_{CKM} elements ($|V_{ij}|$) are [1]:

$$V_{CKM} = \begin{pmatrix} & d & s & b \\ u & 0.97417 \pm 0.00021 & 0.2248 \pm 0.0006 & 0.00409 \pm 0.00039 \\ c & 0.220 \pm 0.005 & 0.995 \pm 0.016 & 0.0405 \pm 0.0015 \\ t & 0.0082 \pm 0.0006 & 0.0400 \pm 0.0027 & 1.009 \pm 0.031 \end{pmatrix}$$

Therefore, the majority of b ($\bar{b}$) quarks decay weakly into a c ($\bar{c}$) quark and a tiny fraction decays into u ($\bar{u}$).

For long time, the number of charmed particles produced in B meson decays and the semileptonic B meson decay branching fraction has been difficult to be explained simultaneously. The proposed solution was that the $b \rightarrow c\bar{c}s$ decays hadronize in more final states than foreseen [2]. Until 1995, it was thought that the transition $b \rightarrow c\bar{c}s$ was principally due to B decay modes such as $\bar{B} \rightarrow X D_s^{(*)}$. The hypothesis that in $b \rightarrow c\bar{c}s$ transition, quarks could also hadronize as $B \rightarrow D^{(*)}\overline{D}^{(*)}K^{(*)}$ was proposed [3]. The typical leading tree level Feynman diagram contributing to the process is shown in the Fig. 5.1. The existence of $B \rightarrow D^{(*)}\overline{D}^{(*)}K^{(*)}$ decay modes has been proven by ALEPH first and CLEO. BaBar [4], ALEPH [5] and Belle experiments measured all the inclusive and exclusive branching ratio of $B \rightarrow D^{(*)}D^{(*)}K$ decays with non-excited K meson as final state. Due to lack of statistics neither Belle or BaBar have been able to observe and measure the exclusive decay mode $B^0 \rightarrow D^0\overline{D}^0K^{*0}$.

Nowadays, the interest in these channels is related to the production of exotic particles decaying into a pair of $D^{(*)}$ mesons (XYZ exotic states), the spectroscopy study related to the D_s^* and the study of non-factorizable contributions in the flavour changing neutral current processes $b \rightarrow s((c\bar{c}) \rightarrow l^+l^-)$, also called charm loops. In particular, the observed anomalies in the angular analysis of $B^0 \rightarrow K^{*0}\mu^+\mu^-$ [6]

Fig. 5.1 Example of
$B \to D^{(*)}D^{(*)}K^{(*)}$ decay
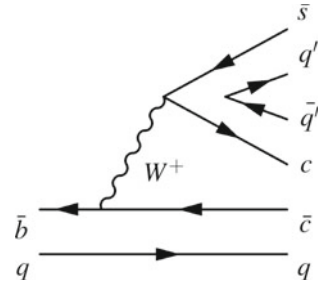
points towards NP, or that our current models describing the non-factorizable contributions to such process from the $b \to s((c\bar{c}) \to l^+; ^-)$ have to be re-evaluated. This chapter summarises the motivation for studying $B \to D^{(*)}\overline{D}^{(*)}K^{(*)}$ decay modes. In the following $D^{(*)}$ is meant to represent the four possibilities D^+, D^0, D^{*+}, D^{*0} and their charge conjugates, while $K^{(*)}$ represents K^+, K^0, K^{*+}, K^{*0} and their charge conjugates.

The neutral B^0 decay modes to D and K ground states are $B^0 \to D^+D^-K^0$, $B^0 \to D^0\overline{D}^0K^0$ and $B^0 \to D^-D^0K^+$. The corresponding charged $B^{\pm}$ decay modes to D and K ground states are $B^+ \to D^+\overline{D}^0K^0$, $B^+ \to D^+D^-K^+$ and $B^+ \to D^0\overline{D}^0K^+$. Thus, a total of 6 decay modes describes the $B \to D\overline{D}K$. Accounting for the 8 different families of decays with excited final states, namely $B \to D\overline{D}K^*$, $B \to D\overline{D}^*K$, $B \to D\overline{D}^*K^*$, $B \to D^*\overline{D}K$, $B \to D^*\overline{D}K^*$, $B \to D^*\overline{D}^*K$ and $B \to D^*\overline{D}^*K^*$, the full sum of exclusive decay modes having as final states two D mesons and a K are 48 (24 for the neutral B^0 and 24 for the charged $B^{\pm}$). The decay modes with an excited K have never been observed and the number of exclusive modes for which the branching ratio has been measured is 24.

5.1   *B* Mesons Decay Modes

The b quark is the heaviest quark in the SM which is able to hadronize and its bare mass is $m_b \simeq 4.18\,\text{GeV/c}^2$ [1]. The tree-level decay modes of b hadrons are described via the $b \to c$ or $b \to u$ (suppressed by the V_{ub}) transitions where a virtual W^- is emitted. Also the flavour changing neutral currents described by the $b \to s$ transition are possible but they do not occur at tree level and they are suppressed. The Cabibbo favoured $b \to c$ transition can lead to different final states:

- hadronic final states for the Cabibbo favoured $b \to c(W^- \to \bar{c}s)$ and $b \to c(W^- \to \bar{u}d)$ and Cabibbo suppressed $b \to c(W^- \to \bar{c}d)$ and $b \to c(W^- \to \bar{u}s)$;
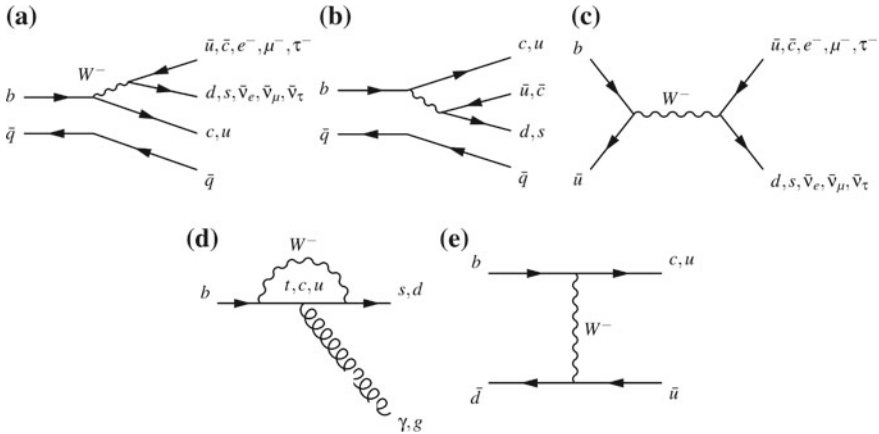- leptonic final states for $b \to c(W^- \to l^-\nu_l)$.

Fig. 5.2 The different *B* mesons decay topologies. **a** External *W* emission (colour-favoured). **b** Internal *W* emission (colour-suppressed). **c** Annihilation. **d** Penguin diagram (flavour changing neutral current $b \rightarrow s, d$). **e** *W* exchange

Concerning the double-charmed decay mode where a $K^{(*)}$ is produced as final state, the $b \rightarrow c(W^- \rightarrow \bar{c}s)$ transition encodes the dominant amplitude.

A *B* meson can decay in many different ways and Fig. 5.2 shows the different topologies of *B* meson decays. The decay modes containing two $D^{(*)}$ mesons as final state are produced in majority through internal and external *W* emission modes. Internal *W* emission decay modes correspond to color-suppressed decay amplitudes while external *W* emission corresponds to color-favoured decay amplitudes. Doubly charmed *B* decay modes can occur through only internal, only external or both of them and details are provided in Sect. 5.2.

5.2 Quark Diagrams of $B \rightarrow D^{(*)}\overline{D}^{(*)}K^{(*)}$

The decays of interest in this thesis are:

- $B^0 \rightarrow D^0\overline{D}^0K^{*0} + c.c.$
- $B^0 \rightarrow D^0(D^{*-} \rightarrow \overline{D}^0\pi^-)K^+ + c.c.$,   used   as   reference   mode
  $(\mathcal{B}(B^0 \rightarrow D^{*-}D^0K^+) = (2.47 \pm 0.10 \pm 0.18) \times 10^-)$,

where *c.c* stands for the charge conjugate mode and it will be implied in the rest of the document. At the quark level, they are described through the $\bar{b} \rightarrow \bar{c}(W^+ \rightarrow c\bar{s})$ transition. This kind of transition occurs via internal *W* emission, external *W* emission or both of them.

Colour suppression in the internal *W* emission is explained considering the colour state of the quark from the *W* which has to arrange together with the spectator quark from the *B* meson (*u* for B^+ or *d* for B^0) to form a color-singlet final state. External *W* emission does not have this limitation and is described by colour-favoured
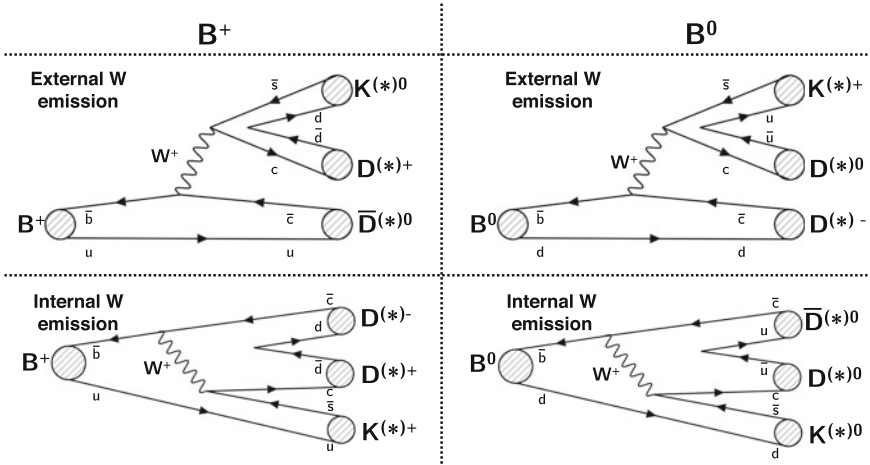
Fig. 5.3 Leading quark diagrams for (only) internal and external W emission decays for charged and neutral B mesons. The signal mode $B^0 \to D^0 \overline{D}^0 K^{*0}$ is shown in the bottom right and it is given by an internal W emission decay amplitude. The reference channel decay mode $B^0 \to D^{*-} D^0 K^+$ is shown in the top right quadrant and it is given by an external W emission decay
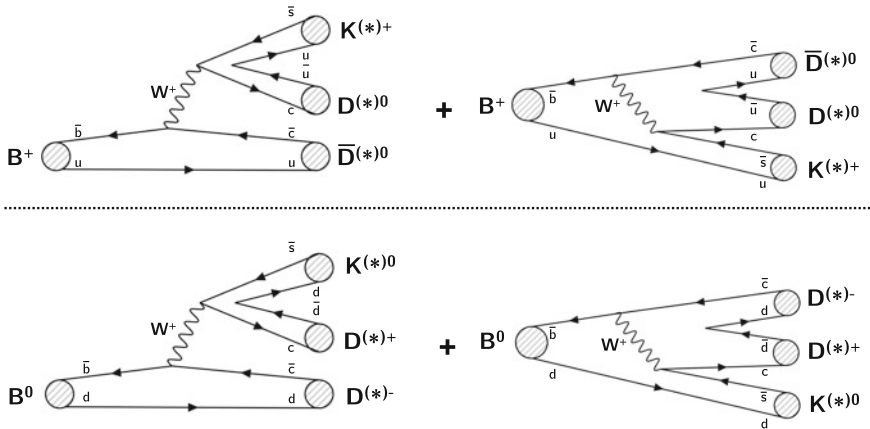

Fig. 5.4 Leading quark diagrams for internal plus external W emission decay modes for charged (top) and neutral (bottom) B meson

transition amplitude. Naively one expects around a $\frac{1}{3}$ ratio between internal and external branching ratios. The leading quark diagrams for charged and neutral B decays in doubly charmed decay modes are shown in Figs. 5.3 and 5.4.

Although $B \to \overline{D}^{(*)} D^{(*)} K^{(*)}$ decay modes can also results from gluonic penguin transitions $\bar{b} \to g\bar{s}$ (as shown in Fig. 5.5c–f), the corresponding amplitude is heavily suppressed with respect to the external and internal W emission amplitudes. $B \to \overline{D}^{(*)} D^{(*)} K^{(*)}$ can also proceed via the $\bar{b} \to \bar{u} W^+ \to \bar{u} u \bar{s}$ transition, where an
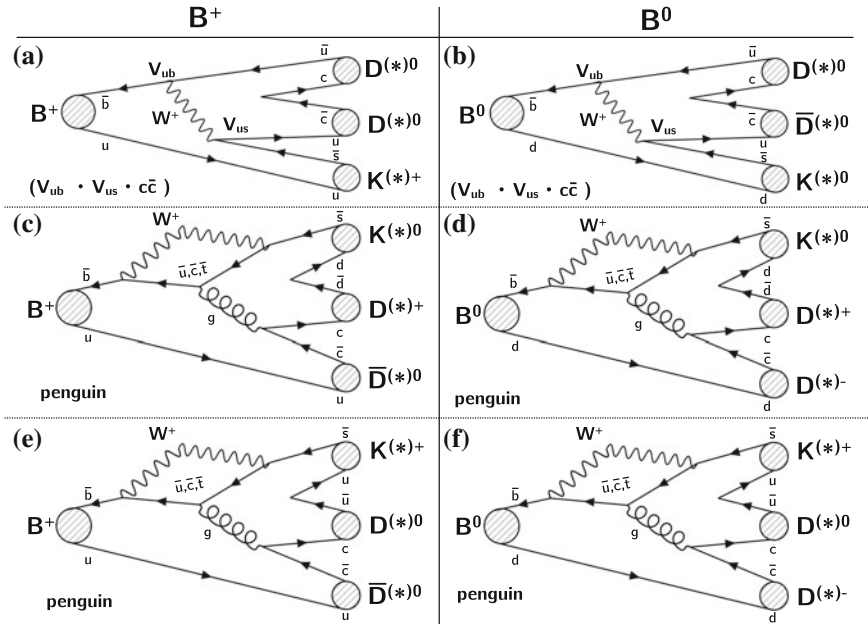
Fig. 5.5 Suppressed modes in $B \to D^{(*)}D^{(*)}K^{(*)}$ mode. In **a** and **b** the suppression is given by $V_{ub} \cdot V_{us} \cdot (c\bar{c})$ while in **c–f** the suppression is given by the penguin insertion. These contributions are negligible when compared to the tree level transitions for the $B^0 \to D^{*-}D^0K^+$ and $B^0 \to D^0\overline{D}^0K^{*0}$

additional $c\bar{c}$ pair is required to be created from the QCD vacuum (Fig. 5.5a, b). This transition involves two CKM-unfavoured weak vertices: $b \to \bar{u}W$ and $W \to u\bar{s}$ as well as a large suppression factor from the $c\bar{c}$ pair creation from the non-trivial QCD vacuum. Such modes are suppressed (at least) with respect to the internal or external W emission by a factor

$$\left(\frac{|V_{ub}V_{us}|}{|V_{cb}V_{cs}|}\right)^2 \simeq 4 \times 10^{-4}$$

without taking into account the suppression factor due to the $c\bar{c}$ pair creation.

The list of the possible $B \to \overline{D}^{(*)}D^{(*)}K^{(*)}$ decays are summarized in the Table 5.1 and they are classified according to the underlying $W-$emission.

5.3   Isospin Relations

Although isospin is not conserved in weak interactions, the $b \to c\bar{c}s$ transition is an isospin conserving process. B mesons can be arranged into an iso-doublet $I = 1/2$ representation of the $SU(2)$ isospin group: $\begin{pmatrix} B^+ \\ B^0 \end{pmatrix}, \begin{pmatrix} \overline{B}^0 \\ B^- \end{pmatrix}$. The third component of

Table 5.1 The 48 different three-body double-charmed decays of B^+ and B^0 decays with two D mesons and an extra K (or K^*) classified by decay topology

External W emission	
$B^+ \to \overline{D}^0 D^+ K^0$	$B^0 \to D^0 D^- K^+$
$B^+ \to \overline{D}^0 D^+ K^{*0}$	$B^0 \to D^0 D^- K^{*+}$
$B^+ \to \overline{D}^0 D^{*+} K^0$	$B^0 \to D^0 D^{*-} K^+$
$B^+ \to \overline{D}^0 D^{*+} K^{*0}$	$B^0 \to D^0 D^{*-} K^{*+}$
$B^+ \to \overline{D}^{*0} D^+ K^0$	$B^0 \to D^{*0} D^- K^+$
$B^+ \to \overline{D}^{*0} D^+ K^{*0}$	$B^0 \to D^{*0} D^- K^{*+}$
$B^+ \to \overline{D}^{*0} D^{*+} K^0$	$B^0 \to D^{*0} D^{*-} K^+$
$B^+ \to \overline{D}^{*0} D^{*+} K^{*0}$	$B^0 \to D^{*0} D^{*-} K^{*+}$
Internal W emission	
$B^+ \to D^- D^+ K^+$	$B^0 \to \overline{D}^0 D^0 K^0$
$B^+ \to D^- D^+ K^{*+}$	$B^0 \to \overline{D}^0 D^0 K^{*0}$
$B^+ \to D^- D^{*+} K^+$	$B^0 \to \overline{D}^0 D^{*0} K^0$
$B^+ \to D^- D^{*+} K^{*+}$	$B^0 \to \overline{D}^0 D^{*0} K^{*0}$
$B^+ \to D^{*-} D^+ K^+$	$B^0 \to \overline{D}^{*0} D^0 K^0$
$B^+ \to D^{*-} D^+ K^{*+}$	$B^0 \to \overline{D}^{*0} D^0 K^{*0}$
$B^+ \to D^{*-} D^{*+} K^+$	$B^0 \to \overline{D}^{*0} D^{*0} K^0$
$B^+ \to D^{*-} D^{*+} K^{*+}$	$B^0 \to \overline{D}^{*0} D^{*0} K^{*0}$
External + Internal W emission	
$B^+ \to \overline{D}^0 D^0 K^+$	$B^0 \to D^- D^+ K^0$
$B^+ \to \overline{D}^0 D^0 K^{*+}$	$B^0 \to D^- D^+ K^{*0}$
$B^+ \to \overline{D}^0 D^{*0} K^+$	$B^0 \to D^- D^{*+} K^0$
$B^+ \to \overline{D}^0 D^{*0} K^{*+}$	$B^0 \to D^- D^{*+} K^{*0}$
$B^+ \to \overline{D}^{*0} D^0 K^+$	$B^0 \to D^{*-} D^+ K^0$
$B^+ \to \overline{D}^{*0} D^0 K^{*+}$	$B^0 \to D^{*-} D^+ K^{*0}$
$B^+ \to \overline{D}^{*0} D^{*0} K^+$	$B^0 \to D^{*-} D^{*+} K^0$
$B^+ \to \overline{D}^{*0} D^{*0} K^{*+}$	$B^0 \to D^{*-} D^{*+} K^{*0}$

the isospin I_3 of the corresponding B meson is determined by the light quark content of the meson $I = +1/2$ for u and $\overline{d}$ and $I = -1/2$ for d and $\overline{u}$.

Assuming that the spectator quark (which is the one determining the isospin state of the B) does not play a role in B meson decay, the following relation holds for the partial decay rates:

$$\Gamma\left(B^+ \to f\left(\overline{c}c\overline{s}\right)\right) = \Gamma\left(B^0 \to \tilde{f}\left(\overline{c}c\overline{s}\right)\right). \tag{5.1}$$

In (5.1), $\tilde{f}\left(\overline{c}c\overline{s}\right)$ is obtained via a $180°$ rotation in the Isospin space of the $f\left(\overline{c}c\overline{s}\right)$ final states. It is also said that $\tilde{f}\left(\overline{c}c\overline{s}\right)$ is the isospin mirror of $f\left(\overline{c}c\overline{s}\right)$. These relations were firstly noted by *Lipkin* and *Sanda* [7].

From (5.1) one can derive for example that

$$\frac{\mathscr{B}\left(B^+ \to \overline{D}^0 D^+ K^0\right)}{\tau_{B^+}} = \frac{\mathscr{B}\left(B^0 \to D^- D^0 K^+\right)}{\tau_{B^0}}$$

$$\frac{\mathscr{B}\left(B^+ \to \overline{D}^- D^+ K^+\right)}{\tau_{B^+}} = \frac{\mathscr{B}\left(B^0 \to \overline{D}^0 D^0 K^0\right)}{\tau_{B^0}},$$

where τ_{B^+} and τ_{B^0} are the B^+ and B^0 lifetimes. Such simple relation can be used to assert and estimate branching fractions of decay modes without actually measuring them, assuming, as said, that the spectator quark does not play a role in the decay mechanism.

Final states of $B \to D^{(*)} \overline{D}^{(*)} K^{(*)}$ can be decomposed into states of a definite isospin. Choosing as a base of the decomposition the $D^{(*)} K^{(*)}$ subsystem (where the $D^{(*)}$ considered is the one coming from the $b \to cW$ transition), the decay amplitude can be expressed as a linear combination of amplitudes where the $D^{(*)} K^{(*)}$ is in state $I = 0 \,(\mathscr{A}_0)$ or $I = 1 \,(\mathscr{A}_1)$ as shown in Table 5.2 for the $B \to DDK$ decay modes family. Considering the quark diagrams describing the decay one can notice that the final states in $B \to \overline{D}^{(*)} D^{(*)} K^{(*)}$ can be decomposed into states of a definite isospin. Each family of $B \to \overline{D}^{(*)} D^{(*)} K^{(*)}$ modes, i.e. $B \to \overline{D}DK$, $B \to \overline{D}DK^*$, $B \to \overline{D}D^*K$, $B \to \overline{D}^* DK$, $B \to \overline{D}^* D^*K$, $B \to \overline{D}^* DK^*$ and $B \to \overline{D}^* D^* K^*$ have different values of $\mathscr{A}_1$ and $\mathscr{A}_0$, but within the same family the amplitudes can be used to relate different decay modes and the relations can be expressed in the form of triangle relations (here for the $B \to \overline{D}DK$ family):

$$-\mathscr{A}(B^0 \to D^- D^0 K^+) = \mathscr{A}(B^0 \to D^- D^+ K^0) + \mathscr{A}(B^0 \to \overline{D}^0 D^0 K^0) \quad (5.2)$$
$$-\mathscr{A}(B^+ \to \overline{D}^0 D^+ K^0) = \mathscr{A}(B^+ \to \overline{D}^0 D^0 K^+) + \mathscr{A}(B^+ \to D^- D^+ K^+). \quad (5.3)$$

Table 5.2 Decay amplitude decomposition for different decay modes of the $B \to D\overline{D}K$ family

Channel	Decay amplitude
$B^0 \to \overline{D}DK$	$\mathscr{A}\left(B^0 \to D^- D^0 K^+\right) = \dfrac{1}{\sqrt{6}}\mathscr{A}_1 - \dfrac{1}{\sqrt{2}}\mathscr{A}_0$
	$\mathscr{A}\left(B^0 \to D^- D^+ K^0\right) = \dfrac{1}{\sqrt{6}}\mathscr{A}_1 + \dfrac{1}{\sqrt{2}}\mathscr{A}_0$
	$\mathscr{A}\left(B^0 \to \overline{D}^0 D^0 K^0\right) = -\sqrt{\dfrac{2}{3}}\mathscr{A}_1$
$B^+ \to \overline{D}DK$	$\mathscr{A}\left(B^+ \to \overline{D}^0 D^+ K^0\right) = \dfrac{1}{\sqrt{6}}\mathscr{A}_1 - \dfrac{1}{\sqrt{2}}\mathscr{A}_0$
	$\mathscr{A}\left(B^+ \to \overline{D}^0 D^0 K^+\right) = \dfrac{1}{\sqrt{6}}\mathscr{A}_1 + \dfrac{1}{\sqrt{2}}\mathscr{A}_0$
	$\mathscr{A}\left(B^+ \to D^+ D^- K^+\right) = -\sqrt{\dfrac{2}{3}}\mathscr{A}_1$

Isospin amplitudes decomposition is valid not only for the total decay amplitude but also for individual helicity amplitudes also when they are expressed as a function of the Dalitz plane coordinates. The latter is true for non-resonant components of the amplitudes. Therefore, the measurement of the branching ratio related to $\mathscr{A}_0$ and $\mathscr{A}_1$ in a given $B \to \overline{D}^{(*)} D^{(*)} K^{(*)}$ decay family and the relative phase in decay modes where both external and internal W emission are possible, $\delta = arg(\mathscr{A}_1 \mathscr{A}_0^*)$, allow to provide insight concerning the decay mechanism and the goodness of the tools used to deal with the QCD corrections to the process. Assuming isospin relations are valid, the measurement of a limited set of branching fractions in a given $B \to D^{(*)} \overline{D}^{(*)} K^{(*)}$, allows to access the remaining ones without measuring them. The most recent precise isospin analysis using the $B \to \overline{D}^{(*)} D^{(*)} K$ decays can be found in Ref. [8].

5.4   Hadronic Effects in B Decays

The Feynman diagrams shown in Figs. 5.3, 5.4 and 5.5 express the free-quark diagrams and they represent a gross simplification of the double charm B meson exclusive decays. Indeed, b quarks are bound inside the B meson via strong interactions. The nature of the strong interaction is non-perturbative and the theoretical description of the decay is more complicated. Furthermore, strong interactions between initial or final quarks (final state interaction) can change the colour structure of the quarks and affect the decay amplitudes since the final state quarks have to combine to form colour-singlet hadrons.

The phenomenology of double charm decays (and in general B mesons decay) is described by a complex interplay between weak and strong interactions. Tools to control and describe such phenomenology have been developed and they rely on concepts of heavy-quark symmetry, heavy-quark expansion and chiral symmetry. Such concepts and their implications will be reviewed briefly in the following subsections.

5.4.1   Heavy Quark Symmetry

Heavy quark symmetry is modelled considering atomic physics concepts. The B meson (the same is true for the c hadrons) is described as a bound state of an heavy quark Q and a light anti-quark $\overline{q}$. A quark is considered heavy when $m_Q \gg \Lambda_{QCD}$, where $\Lambda_{QCD} = 200$ MeV is the energy scale separating the asymptotic freedom and confinement regime of strong interactions. As m_Q increases, the velocity of the Q in the $Q\overline{q}$ meson rest frame decreases. The hadronic radius of the B meson is of the order of $1/\Lambda_{QCD}$ (few fm) and it is much larger than the heavy-quark Compton wavelength ($\sim 1/m_Q$). Such ingredients allows to draw parallels between the $Q\overline{q}$ bound state and the hydrogen atom: Q plays the role of the proton and q plays the role of the electron.

The heavy quark can therefore be considered in the B meson as a static colour source of chromoelectric field for $m_Q \to \infty$ and relativistic effects such as chromomagnetic interactions, related to gluon-exchange, vanishes as $m_Q \to \infty$. Considering both c and b quarks as heavy quarks, we can conclude that decay amplitudes and form factors of b and c hadrons are closely related each others and this is the basic concept known as *heavy-quark flavour symmetry*. The spin of the heavy quark $\overrightarrow{s}_Q$ enters in the interaction between Q and q through relativistic effects (such as the spin-orbit relativistic corrections for the hydrogen atom) and $\overrightarrow{s}_Q$ corrections are proportional to the chromomagnetic moment of the heavy quark system which is proportional to $1/m_Q$. Thus, for $m_Q \to \infty$, the $\overrightarrow{s}_Q$ is a good quantum number to describe the system and it is conserved in the interaction. This concept is also known as *heavy-quark spin symmetry*. The consequence of the *heavy-quark spin symmetry* is that the spin quantum number of the light quark $\overrightarrow{s}_{\bar{q}}$ and the one for the heavy one ($\overrightarrow{s}_Q$) are separately conserved. Both of them are therefore good quantum numbers to use to describe the $Q\bar{q}$ system.

The total angular momentum of the light quark is $\overrightarrow{j}_q = \overrightarrow{L_{Q\bar{q}}} + \overrightarrow{s}_{\bar{q}}$, where $\overrightarrow{L}_{Q\bar{q}}$ is the orbital momentum of the $Q\bar{q}$, where Q is treated as a quasi-static chromoelectric field source. Thus, the total angular momentum of the meson is $\overrightarrow{J} = \overrightarrow{j}_{\bar{q}} + \overrightarrow{s}_Q$. The chromomagnetic interaction term is proportional to $\overrightarrow{s}_{\bar{q}} \cdot \overrightarrow{S}_Q$ and its macroscopic effect is the hyperfine splitting of the heavy-light meson spectrum, i.e. the mass-splitting between the different B or D mesons (B/B^* or D/D^*).

Leptonic decays of b (and c) mesons are easier to describe since the leptonic final states do not interact strongly with the quarks. Non-leptonic B decays are described by a low-energy effective theory called *Heavy Quark Effective Theory* [9, 10] (*HQET*) and the main idea behind this effective theory will be briefly described in the following. The *HQET* interaction Lagrangian is obtained by integrating out the effects of the heavy quark degrees of freedom in the hadronic system resulting in a non-local effective Lagrangian. The non-locality is related to the fact that in the full theory the heavy quark can appear in virtual processes and propagate over a short but finite distance $\Delta x \sim 1/m_Q$. The non-local effective action ($S = \int \mathcal{L} dt$) is therefore rewritten in an infinite series of local terms in an Operator Product Expansion (OPE), which, roughly speaking, corresponds to an expansion in powers of $1/m_Q$. In this step, short and long-distance physics effects are disentangled. Long-distance physics corresponds to interactions at low energies and they are written in the same way as in the full theory, i.e. long-distance terms of *HQET* and SM are exactly the same and the soft gluon infrared divergences are resolved through renormalization group techniques. Short distance physics arises from quantum corrections involving large virtual momenta ($\sim m_Q$) and they are integrated out. Those short distance terms are added in the theory in a perturbative way using renormalization group techniques. The short distance effects leads to a renormalization of the coefficients of the local operators in the effective Lagrangian. For instance, the effective Lagrangian for non-leptonic weak decays where radiative corrections from hard gluons with virtual momenta between m_W and some renormalization scale $\mu \sim 1\,\text{GeV}$ leads to the Wilson coefficients aiming at renormalizing the local four-fermion interactions.
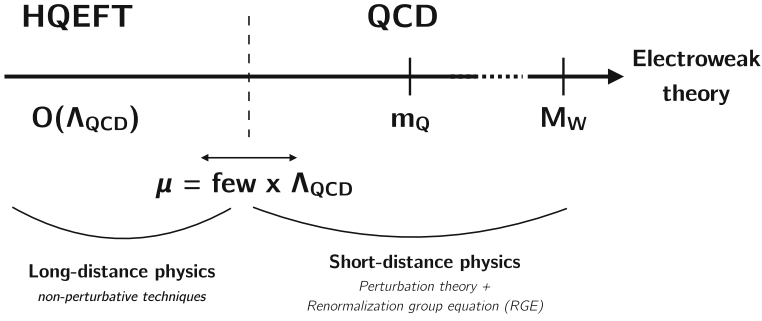
Fig. 5.6 Philosophy of the heavy-quark effective theory showing the energy scales separating the long and short distance physics effects

HQET is therefore constructed to provide a simplified description of processes where the heavy quark interacts with the light quark degrees of freedom through exchange of soft gluons. In this picture m_Q is the high-energy scale and Λ_{QCD} is the scale of the hadronic physics effects. The philosophy behind the heavy-quark effective theory is sketched in Fig. 5.6. The OPE expansion for the *HQET*, also called Heavy Quark Expansion (HQE) is obtained rewriting the Lagrangian as a series of powers of $1/m_Q$. The expansion allows to separate short-distance and long-distance physics phenomena. A separation scale μ is introduced to separate the long and short distance physics such that $\Lambda_{QCD} \ll \mu \ll m_Q$.

The *HQET* is constructed to be identical to QCD in the long-distance region (i.e. for scales below μ) while for the short distance region, the effective theory is incomplete since the high momentum modes are integrated out from the full theory. However, since the physics is independent of the arbitrary scale μ, one can derive the corresponding renormalization group equation which can be used to deal with the short distance effects in an efficient way. The starting point to build the low-energy effective theory is that the heavy quark inside the heavy meson moves more or less with the same meson velocity v and it is almost on shell.

The renormalized effective Hamiltonian for the $\bar{b} \to \bar{c}c\bar{s}$ tree level transition becomes [11]:

$$H_{eff} \sim G_F V_{cb} V_{cs}^* \{ \; C_1(\mu) \left[(s\gamma^\mu (1 - \gamma_5)\bar{c})(c\gamma_\mu (1 - \gamma_5)\bar{b}) \right] + \atop C_2(\mu) \left[(c\gamma^\mu (1 - \gamma_5)\bar{c})(s\gamma_\mu (1 - \gamma_5)\bar{b}) \right] \; \} \tag{5.4}$$

where $C_1(\mu)$ and $C_2(\mu)$ are the Wilson coefficients and μ is the re-normalization scale. At the relevant scale of B decays (i.e. $\mu \simeq m_b$) their values correspond to $C_1 = 1.13$ and $C_2 = -0.3$. The term with C_1 corresponds to a color-allowed transition, whereas the term with C_2 to a colour-suppressed one.

Behind this brief sketch given about the *HQET*, the fundamental assumption is the factorization of amplitudes. Other important aspects in the treatment of non perturbative effects of QCD are the colour suppression and the chiral symmetry.

5.4.2 Factorization

HQET allows to calculate the total amplitudes describing a weak hadronic decay. The assumption made is the local hadron-parton duality hypothesis, according to which hadronization effects are unimportant in calculation of decay amplitudes. Under this assumption, one can factorize the total amplitude with a product between the terms describing the short-distance effects to the process (large q^2) and the terms describing the subsequent hadronization taking place with a probability equal to 1.

The calculation of decay amplitudes through the naive factorization model (the most common model used) relies on replacing the hadronic matrix elements of four quark operators by products of current matrix elements. Those matrix elements encode decay constants of the mesons considered and their form factors which are either provided by experimental measurements or evaluated from first principles through lattice QCD computations. Those phenomenological coefficients are denoted as a_i. These factors intrinsically depend on the colour and Dirac structure of the operators describing the strong-interaction effects and they are postulated to be universal constants (reason why they can be extracted from independent measurements).

There is no rigorous proof of the factorization, although arguments for its validity do exist thanks to large N_{color} expansion approach [12]. One of the predictions of the factorization approach is the colour transparency phenomenon [13] which occurs in large energy release decays of B mesons. It will be briefly explained here. The quarks in the final state of a weak decay ($\overline{b} \to \overline{c}c\overline{s}$ for example) travel in a medium composed of gluons and light $q\overline{q}$ pairs with which they interact strongly. If one considers the $c\overline{s}$ pair having a small invariant mass, then these quarks remain close together while moving through the medium. If the c and $\overline{s}$ quarks are in a colour singlet, the interaction of the pair with the medium is not described as a sum of single quark interaction but as an interaction between the medium and a colour dipole. It is therefore possible that the $c\overline{s}$ pair leaves the coloured environment before the dipole moment becomes large enough for the corresponding dipole interaction to become significant. In such case the $c\overline{s}$ pair is expected to hadronize as a $D_s^{(*)}$. On the other hand, if the $c\overline{s}$ pair has a large invariant mass, the quarks interact strongly with the medium and it becomes unlikely for them to hadronize into a $D_s^{(*)}$.

The W decay products in external and internal B meson decays travel fast enough to leave the interaction region without influencing the other decay products. The interactions with the remaining decay products occurs through soft gluon interactions and these effects are proportional to $1/m_Q$, thus suppressed. Since $m_b \gg m_c$, the factorization hypothesis for B meson decays is expected to work better than the case of D meson.

The factorized amplitude for $B \to \overline{D}^{(*)} D_s^{(*)}$, according to the model described is therefore expressed as the product of two independent hadronic currents:

$$\mathscr{A} \sim G_F \cdot V_{cb} \cdot V_{cs}^* \quad \langle D_s^{(*)}|(s\gamma^u(1-\gamma_5)\overline{c})|0\rangle \quad \times \quad \langle D^{(*)}|(c\gamma_\mu(1-\gamma_5)\overline{b})|B\rangle,$$
$$(5.5)$$

where the first hadron current, which leads to the creation of the $D_s^{(*)}$ from the vacuum, is related to the $D_s^{(*)}$ decay constant $f_{D_s^{(*)}}$ as follows:

$$
\begin{aligned}
\langle D_s(p_{D_s})|(s\gamma^\mu(1-\gamma^5)\overline{c})|0\rangle &= if_{D_s}p_{D_s}^\mu \\
\langle D_s^*(p_{D_s^*}, \epsilon_{D_s^*})|(s\gamma^\mu(1-\gamma^5)\overline{c})0\rangle &= if_{D_s^*}p_{D_s^*}^\mu\epsilon_{D_s^*}.
\end{aligned}
\tag{5.6}
$$

In (5.6), the term $p_{D^{(*)}}$ represents the momentum of the $D_s^{(*)}$ and $\epsilon_{D_s^*}$ is the polarization vector of the D_s^*.

The second hadron current in (5.5) is used to describe the $\overline{D}^{(*)}$ meson formation which contains the B meson spectator quark. Such current can be experimentally determined from semileptonic decay, i.e. $B \to D^{(*)}l^+\nu_l$.

5.4.3   Color Suppression

The exchange and emission of gluons in B meson decay leads to a change of the color state of quarks. Therefore, the transition amplitude of the decay is affected from this. Quarks have three colors ($N_c = 3$) and the suppression of the decay rate in color suppressed modes corresponds to a factor 1/3. To take into account the rearrangement of the color structure in the expression of the transition amplitudes, the effective Hamiltonian from the naive factorization approach (5.4) is rewritten in terms of a factorizable part and a non-factorizable correction as follows:

$$
H_{eff} \sim G_F V_{cb} V_{cs}^* \left(s\gamma^\mu(1-\gamma_5)\overline{c}\right)\left(c\gamma_\mu(1-\gamma_5)\overline{b}\right)\left[\left(C_1 + \frac{C_2}{N_c}\right)(1+\epsilon_1) + 2C_2\epsilon_8\right],
\tag{5.7}
$$

where the $a_1 = (C_1 + C_2/N_c)$ is the coefficient of factorizable term as in (5.4). The ϵ_1 coefficient describes the deviation of the color-singlet amplitude from the naively factorized form of the amplitude. The term ϵ_8 describes the corrections arising from the color-octet operator $O^{(8)}$. The color-octet operator prohibits the generation of any $c\overline{s}$ state and therefore requires the presence of at least one extra gluon in the transition. The 'wrong' colour structure amplitudes are usually assumed to be intrinsically small. Thus, both ϵ_1 and ϵ_8 are expected to be small (in (5.5) they are set to zero). All non-factorizable contributions are suppressed by $1/N_c^2$ [14].

The amplitude is said to be colour-allowed for $(C_1 + C_2/N_c) \ll 2C_2$, while for the opposite the amplitude is classified as to colour-suppressed. The effective Hamiltonian for B decays dominated by the color suppressed mode is written as follows:

$$
H_{eff} \sim G_F V_{cb} V_{cs}^* \left(c\gamma^\mu(1-\gamma_5)\overline{c}\right)\left(s\gamma_\mu(1-\gamma_5)\overline{b}\right)\left[\left(C_2 + \frac{C_1}{N_{color}}\right)(1+\tilde{\epsilon}_1) + 2C_1\tilde{\epsilon}_8\right],
\tag{5.8}
$$

where $\tilde{\epsilon}_1$ and $\tilde{\epsilon}_8$, analogously to (5.7), describe the corrections to the factorized form. Since the coefficient $2C_1 \cdot \tilde{\epsilon}_8$ is much larger than the product of $a_1 = (C_2 + C_1/N_c)$ and than the factorizable part, the factorization in colour-suppressed decays is not

very reliable and the presence of large non-factorizable color-octet contributions in such processes is probable.

Factorization can be violated by final-state interactions (FSI) between the decay products. Extra phases between hadronic amplitudes are introduced by the FSI as well as the possibility of rescattering into other decay channels. FSI, additionally, can also affect the decay rates through interferences. Large phase differences make indeed CP-violation studies especially interesting in such decay modes.

5.4.4 Chiral Symmetry

Complementary to the $m_Q \to \infty$ leading to the *HQET* theory, the limit for which $m_q \to 0$ which can be applied for $m_{d,u,s}$ is used to introduce the chiral symmetry. As the masses of light quarks tend to zero, no interaction between quarks of left and right helicities is predicted and they decouple from each other. The resulting Lagrangian in the limit of $m_q \to 0$ becomes invariant under rotation among (u_L, d_L, s_L) and (u_R, d_R, s_R) where the subscript $L(R)$ is used for the left-(right-)handed component of the quark spinor. This corresponds to the $SU(3)_L \times SU(3)_R$ chiral flavour symmetry. The direct consequence of such a symmetry is the parity doubling in the u, d, s spectrum, where the parity doubling is the occurrence of opposite-parity states of equal spin value. Such symmetry, due to the non-trivial QCD vacuum, is spontaneously broken through the quark condensate for which the expectation value in the vacuum is different from zero: $\langle q_i \overline{q}_j \rangle \neq 0$.

The spontaneous symmetry breaking leads to eight "almost massless" Goldston pseudoscalar bosons in the light meson spectrum: $\pi^{\pm,0}$, η, η', $K^{\pm,0}$ and in the mass degeneration of opposite parity $q\overline{q}$ states. The chiral symmetry breaking energy scale is $\Lambda_\chi \simeq 1$ GeV which is related to the expectation value of the quark condensate $< q_i \overline{q}_j > \neq 0$. Therefore, it becomes possible to construct an effective Lagrangian to describe the low energy interactions of particles with light masses and small momenta by introducing systematic expansions of interaction terms in powers of m_q/Λ_χ and p/Λ_χ with $m_q, p \ll \Lambda_\chi$. Such an expansion is the basis for the Chiral Perturbation Theory (ChPT) in the u, d, s, sector.

Although the heavy-flavour hadrons have large masses, ChPT can be applied as well to $Q\overline{q}$ systems together with the heavy-quark symmetry. The role of chiral-symmetry breaking becomes less important in heavy-light quark systems due to the large energy scale, i.e. m_Q, thus chiral symmetry is effectively restored. Such effect has important consequences in $Q\overline{q}$ mesons spectroscopy, which can be studied in $B \to D^{(*)}D^{(*)}K^{(*)}$, looking at the $D^{(*)}K$ resonant structures.

ChPT is commonly used for non-leptonic B decays to evaluate the decay amplitudes in the low momentum phase space regions of particles. For instance, it has been employed in the calculation of the $B^0 \to \overline{D}^* D^* K^0$ [15] branching fraction.

5.5 Spectroscopy of $c\bar{s}$ and $c\bar{c}$ States

Decays of B mesons offer a very clean environment for spectroscopic studies. The symmetries described before define the dynamic behaviour of the quarks in decays while static approaches are related to spectroscopic observables. The approach used to compute properties of bound states are several: *non relativistic potential models*, lattice QCD and *effective theories*.

- The *non relativistic potential models* free parameters are fitted to reproduce the observed states and to reproduce the asymptotic behaviours of QCD. Masses and widths of bound states are obtained solving Schrödinger-like equations.
- Lattice QCD (LQCD) is a more fundamental approach which use the Lagrangian of the Standard Model as input. In lattice QCD, observables are calculated using numerical methods to evaluate the QCD path integral on a four-dimensional space-time lattice.
- *Effective field theories* use the symmetries of QCD and the hierarchies of scales of different processes providing effective Lagrangians that describe QCD at a given energy regime. These Lagrangians are obtained by "integrating out" the effects of the others energy regimes.

In order to understand the charmonium spectrum the *Non-Relativistic Potential* model can be used (called *Cornell-Potential*). First of all, the potential has to repro-duce the asymptotic behaviours of QCD:

$$V(r) \to \frac{\alpha_s(r)}{r} \quad \text{for } r \to 0, \tag{5.9}$$

reproducing the *asymptotic freedom* for large energy scales (small distances) and

$$V(r) \to kr \quad \text{for } r \to \infty, \tag{5.10}$$

reproducing the QCD confinement regime. In addition to these asymptotic behaviours also a *spin-orbit* term, a *spin-spin* term and a *tensorial* term are added. Such terms lead to scalar and vectorial potentials V_S and V_V. The *Coulomb-like* part of the poten-tial corresponds to one-gluon exchange and only the vectorial part of the potential contributes to it, while the linear confining potential is due to the scalar part of the potential.

The great success of this simple potential is given by the prediction in the char-monium spectrum below the open charm threshold ($<2m_D$). The decay process $B \to DDK$ can be used to investigate the properties of the states with a mass greater than the open charm threshold decaying into DD or D^*D or D^*D^*. The charmo-nium spectrum prediction and the observed states are sketched in Fig. 5.7 and it can be clearly seen that below the *open-charm threshold* the models works very well while above threshold there are several discrepancies. The $B \to D^{(*)}\overline{D}^{(*)}K^{(*)}$ decay modes can provide useful inputs in such topic.
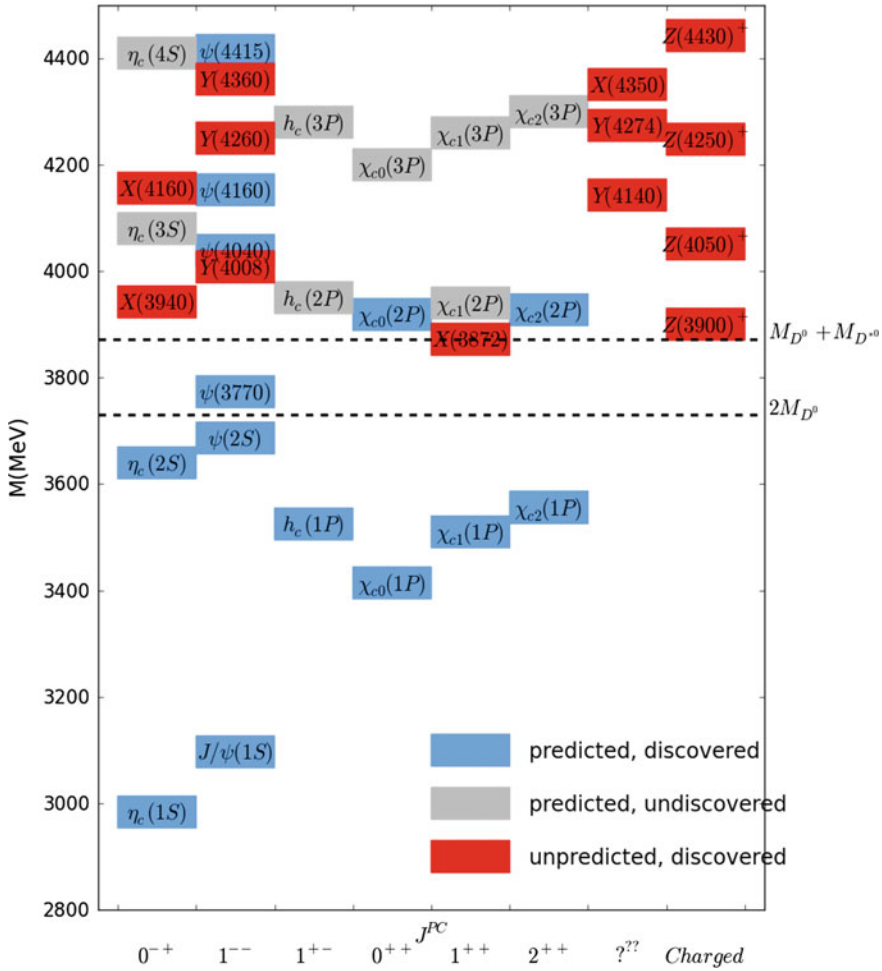
Fig. 5.7 Experimental situation about charmonium spectrum below and above open charm threshold. In blue the charmonium predicted and experimentally discovered states, in gray the charmonium predicted but experimentally not found states, in red the exotic states which for static and dynamic behaviours does not match with standard $c\bar{c}$ state. Charged states Z are not $c\bar{c}$ conventional states due to the electric charge

The $B \to D\overline{D}K^*$ transition is described in terms of spin-parity (J^P) of the particles by the relation $0^- \to 0^-0^-1^-$. Thus, the existence of at least an extra contribution in final states to the total angular momentum, either from a resonance or a relative angular momentum between the particles, is required in such decay to preserve angular momentum. Indeed, the fixed spin of the parent B meson and the angular momentum conservation considerably constrains possible quantum numbers of the decay particles and of possible resonant structures.

Many analyses of three-body B decays performed so far indicate that these decays proceed predominantly via quasi-two-body processes, with rather small non-resonant components and LHCb with the huge statistics of B mesons produced can play a central role in this field. The production of resonances in B meson decays is abundant and exotic mesons can be studied with great precision. The $D^{(*)}\overline{D}^{(*)}K^{(*)}$ three-body final states are promising for spectroscopic studies of $c\bar{c}$ states lying above the open charm threshold ($>2M_D$) as well as $c\bar{s}$ states.

The $c\bar{s}$ states can hadronize from externally-emitted W that couples predominantly to 1^+, 1^- and 0^- states. Potential models of heavy-light quark systems, based on heavy-quark symmetry, predict two doublets of P-wave $c\bar{s}$ excitations, carrying the light-quark angular momentum $\frac{1}{2}$ or $\frac{3}{2}$. The $J_q = \frac{3}{2}$ doublet comprises 1^+ and 2^+ narrow states. They are identified with $D_{s1}(2536)$ and $D_{sJ}(2573)$ mesons, which predominantly decay to D^*K and DK, respectively. However, $HQET$ predicts that the production of members of the $J_{\bar{q}} = \frac{3}{2}$ doublet is suppressed in B decays in comparison to the $J_q = \frac{1}{2}$ state [16].

Many questions are open in this sector and the dynamics of the decays $B \to \overline{D}^{(*)}D^{(*)}K^{(*)}$ can provide inputs for the models aiming at describing the nature of the observed states as well as describing their production in B decays and fine tune the models to match the observed states. The same arguments are valid concerning the $D_s^{(*)}$ mesons spectroscopy studies.

About the exotic mesons, the year 2013 marks the 10th anniversary of the observation of the $X(3872)$ [17, 18] charmonium-like state that put an end to the era where heavy quarkonium was considered as a well established system of bound heavy quark and anti-quark. Since 2003, every year has been bringing discoveries of new particles with unexpected properties, not fitting a simple $q\bar{q}$ classification scheme. The wealth of new results in the last 10 years is mainly from B- and charm factories (the Belle, BaBar and BES experiment), where data samples with unprecedented statistics became available. The discussion about exotic mesons and the possibility to find such resonances in the decay goes beyond the work presented in this thesis and more details can be found in Ref. [19].

Exotic mesons spectroscopy is a very active field in recent years at LHCb. Indeed, the four-quark state $Z(4430)^-$ has been confirmed in 2014 [20] and its quantum numbers have been unambiguously established. Furthermore, LHCb discovered the five-quark bound state P_c^+ [21]. In both cases, the amplitude analysis of the B decay in which these states are observed have been used to establish the quantum numbers, and to perform a model-independent measurement of the complex lineshapes which showed the expected characteristics of a resonance.

The analysis subject of this thesis consists on the first observation of the $B^0 \to D^0\overline{D}^0K^{*0}$ decay without any invariant mass selection for the K^{*0}. Thus, the actual decay mode studied is $B^0 \to D^0\overline{D}^0K^+\pi^-$ and the study of resonant structures in the $D^0\overline{D}^0K^+$ or $D^0\overline{D}^0\pi^-$ mass spectrum could add useful information to the exotic nature of the charged four quark bound states observed so far.

5.6 $B^0 \to D^0 \overline{D}^0 K^{*0}$ Role in the Charm Counting Puzzle

The problem of charm counting is an old problem which nowadays is basically solved. It consists in the observed discrepancy between the number of charmed states produced in B decays and the semileptonic branching fraction of B hadrons. The possibility that a significant fraction of $\overline{b} \to \overline{c}c\overline{s}$ decays can hadronize into $\overline{D}^{(*)} D^{(*)} K^{(*)}$ was first suggested in the context of the charm counting problem [3]. The number of charmed hadrons per B decay ($\mathcal{N}_c$) can be related to the semileptonic branching fraction of B hadrons. $\mathcal{N}_c$ is the average number of quarks c or $\overline{c}$ produced in the weak decay of a b quark. In principle, it corresponds to the average number of charmed mesons or baryons produced in B meson decays. The charmonium states $c\overline{c}$, like the J/ψ, are exceptions in the counting because they have to be counted twice [22]. So,

$$\mathcal{N}_c = \frac{\text{number of charmed states in } B \text{ decays}}{\text{number of } B \text{ decays}} \tag{5.11}$$

The parameters $\mathcal{N}_c^+$ and $\mathcal{N}_c^0$ are defined analogously, for charm counting using only B^+ and B^0, respectively.

The semileptonic branching ratio $\mathcal{B}_{sl}$ is defined in this context as the average number of electrons produced directly in the decay of a b quark:

$$\mathcal{B}_{sl} = \mathcal{B}(B \to Xev_e) = \frac{\Gamma_{sl}}{\Gamma_{tot}}. \tag{5.12}$$

To extract the relation between $\mathcal{N}_c$ and $\mathcal{B}_{sl}$, the following assumption is made:

$$\frac{\mathcal{B}(B \to Xev_e)}{\mathcal{B}(B \to X\mu v_\mu)} = 1. \tag{5.13}$$

The semitaunic branching fraction, where the τ mass cannot be neglected [23] because of the reduction of the available phase space for the decay, is related to $\mathcal{B}_{sl}$ via the followings:

$$\frac{\mathcal{B}(B \to X\tau v_\tau)}{\mathcal{B}(B \to X\mu e_e)} = 0.25. \tag{5.14}$$

The partial width of the B in semi-leptonic decays is then:

$$\Gamma(B \to Xlv_l) = \Gamma_{sl} + \Gamma_{sl} + 0.25\Gamma_{sl} = 2.25\Gamma_{sl} \tag{5.15}$$

while the hadronic partial width is given by the sum of three terms:

- $\Gamma_{\overline{u}d}$ is sum of the partial widths from the Cabibbo favoured $b \to c\overline{u}d$ and the Cabibbo suppressed $b \to c\overline{u}s$ transitions,

- $\Gamma_{\bar{c}s}$ is sum of the partial widths from the Cabibbo favoured $b \to c\bar{c}s$ and the Cabibbo suppressed $b \to c\bar{c}d$,
- Γ_{rare}: for the charmless decays.

i.e.

$$\Gamma_{had} = \Gamma_{\bar{u}d} + \Gamma_{\bar{c}s} + \Gamma_{rare}. \tag{5.16}$$

The $b \to u\bar{c}s$ and $b \to u\bar{c}d$ transitions give a small contribution because the V_{ub} *CKM* matrix element is small and they are neglected. It is therefore possible to express the total B decay width as:

$$\Gamma_{tot} = 2.25 \cdot \Gamma_{sl} + \Gamma_{had} \tag{5.17}$$

If we denote r_x as the ratio of the partial width:

$$r_x = \frac{\Gamma_x}{\Gamma_{sl}}, \tag{5.18}$$

then:

$$\mathscr{B}_{sl} = \frac{\Gamma_{sl}}{2.25\Gamma_{sl} + \Gamma_{had}} = \frac{1}{2.25 + r_{had}} \tag{5.19}$$

where

$$r_{had} = r_{\bar{u}d} + r_{\bar{c}s} + r_{rare} \tag{5.20}$$

The process $b \to c\bar{u}d'$[1] gives a charm quark in the decay, the $b \to c\bar{c}s'$[2] contribute with two charm quarks while the rare decays contributes with zero charm quarks.

Therefore, the final expression of $\mathscr{N}_c$ is written as

$$\begin{aligned}
\mathscr{N}_c &= \frac{(\Gamma_{\bar{u}d} + 2\Gamma_{\bar{c}s} + 2.25\Gamma_{sl})}{\Gamma_{tot}} \\
&= \frac{(\Gamma_{tot} + \Gamma_{\bar{c}s} - \Gamma_{rare})}{\Gamma_{tot}} \\
&= 1 + \frac{\Gamma_{\bar{c}s}}{\Gamma_{tot}} - \frac{\Gamma_{rare}}{\Gamma_{tot}} \\
&= 1 + \mathscr{B}_{sl} \times r_{\bar{c}s} - \mathscr{B}_{sl} \times r_{rare} \\
&= 1 + \frac{r_{\bar{c}s} - r_{rare}}{2.25 + r_{had}},
\end{aligned} \tag{5.21}$$

---

[1] $d' = \cos\theta_c d + \sin\theta_c s$, where θ_c is the *Cabibbo* angle.
[2] $s' = \cos\theta_c s + \sin\theta_c d$, where θ_c is the *Cabibbo* angle.

Table 5.3 Multiplicity of charmed hadrons in B^+ decays. Values are taken from the 2016 version of the PDG [1]. Correct (wrong) sign indicates the presence of a charmed final having a charm quantum number compatible with $b \to cX$ ($b \to \overline{c}X$)

B^+ decay $\dfrac{\Gamma_i}{\Gamma_{tot}}$	Value
$\overline{c}X$ (correct sign)	$0.968 \pm 0.019^{+0.041}_{-0.039}$
cX (wrong sign)	$0.234 \pm 0.012^{+0.018}_{-0.014}$
$c\overline{c}X$ (it's $\mathcal{N}_c^+$)	$1.202 \pm 0.023^{+0.053}_{-0.049}$
$e^+\nu_e X$ (it's Γ_{sl})	$10.99 \pm 0.28\%$
$e^+\nu_e X_c$	$(10.79 \pm 0.25 \pm 0.27)\%$

Table 5.4 Multiplicity of charmed hadrons in B^0 decays. Values are taken from the 2016 version of the PDG [1]. Correct (wrong) sign indicates the presence of a charmed final having a charm quantum number compatible with $b \to cX$ ($b \to \overline{c}X$)

B^0 decay $\dfrac{\Gamma_i}{\Gamma_{tot}}$	Value
$\overline{c}X$ (correct sign)	$0.947 \pm 0.030^{+0.045}_{-0.040}$
cX (wrong sign)	$0.246 \pm 0.024^{+0.021}_{-0.017}$
$c\overline{c}X$ (it's $\mathcal{N}_c^0$)	$1.193 \pm 0.030^{+0.053}_{-0.049}$
$e^+\nu_e X$ (it's Γ_{sl})	$10.33 \pm 0.28\%$
$e^+\nu_e X_c$	$(10.08 \pm 0.30 \pm 0.22)\%$

The term $r_{\overline{c}s}$ is the term which has the largest theoretical uncertainty. It can be removed from the expression using the relations (5.19) and (5.20) leading to

$$\mathcal{N}_c = 2 - (2.25 + r_{\overline{u}d} + 2r_{rare})\,\mathcal{B}_{sl}, \tag{5.22}$$

which can be expressed as

$$\mathcal{N}_c = 2 - (6.75 \pm 0.40)\,\mathcal{B}(B \to X_c e^+\nu), \tag{5.23}$$

where ± 0.40 is the theoretical uncertainty on the value of $(2.25 + r_{\overline{u}d} + 2r_{rare})$ and it is taken from Ref. [3]. The theoretical value predicted for $\mathcal{N}_c$ is affected by the uncertainty in the quark masses (m_b and m_c) and the mass scale μ. In the past, there was a discrepancy between the theoretical and observed values for $\mathcal{N}_c$. This discrepancy has been resolved by better taking into account the contribution from $b \to c\overline{c}s$. Nowadays the experimental values of charm counting and semileptonic branching fraction agree with the predictions but some exclusive modes have never been observed and measured. The most important experimental values for this kind of study are summarized in the Tables 5.3 and 5.4.

From Table 5.3, using (5.23) we have:

$$\mathcal{N}_{exp}^{+} = 1.202 \pm 0.023_{-0.049}^{+0.053}$$

$$\mathcal{N}_{th}^{+} = \quad 1.272 \pm 0.081$$

$$\mathcal{N}_{exp}^{0} = 1.193 \pm 0.030_{-0.049}^{+0.053}$$ (5.24)

$$\mathcal{N}_{th}^{0} = \quad 1.320 \pm 0.090$$

In (5.24), the value of $\mathcal{N}_{exp}$ is extracted from Tables 5.3 and 5.4, and the value of $\mathcal{N}_{th}$ is computed using (5.23) and the value of $\mathcal{B}(e^{+}\nu_{e}X_{c})$ is taken from Tables 5.3 and 5.4.

In 2010, BaBar reported the measurement of 22 exclusive branching ratios (10 for the neutral and 12 for the charged B meson) for the decay $B \to \overline{D}^{(*)}D^{(*)}K$ [24] fixing the results for the sum of all $B \to \overline{D}^{(*)}D^{(*)}K$ decay to:

$$\mathcal{B}(B^{0} \to \overline{D}^{(*)}D^{(*)}K) = (4.05 \pm 0.11 \pm 0.28)\%$$
$$\mathcal{B}(B^{+} \to \overline{D}^{(*)}D^{(*)}K) = (3.68 \pm 0.10 \pm 0.24)\%$$ (5.25)

where the first error is statistical and the second one systematic. These decays do not saturate the wrong-sign D production which can be computed subtracting from the inclusive $B \to cX$ (wrong sign) the contributions from the wrong sign D_s and Λ_c. The branching ratios quoted in (5.25) account to roughly one third of the wrong sign D production in B decays. This points towards the fact that decays of the type $B \to \overline{D}^{(*)}D^{(*)}K^{*}$ or $B \to \overline{D}^{(*)}D^{**}K$[3] have a non-negligible contribution to the hadronization of the $b \to c\overline{c}s$ transition.

The measurements of the exclusive branching ratio of the decay $B^{0} \to D^{0}\overline{D}^{0}K^{*0}$ has never been measured so far as well as all the decay modes $B \to \overline{D}^{(*)}D^{(*)}K^{*}$. Such modes will allow to complete the puzzle, allowing to match and check the consistency of inclusive measurements for wrong charm sign with the sum of exclusive modes for which the measurement of the branching ratio is not available. The currently measured exclusive branching ratio for double charm B decays (values taken from [8]) are summarised in Table 5.5.

---

[3] D^{**} stands for any excited D meson other than D^{*0} and D^{*+}.

Table 5.5 Branching ratios ($\mathscr{B} = \dfrac{\Gamma_{channel}}{\Gamma_{tot}}$) for each $B \to \bar{D}^{(*)}D^{(*)}K$ mode. The second column shows the experimental results. The first error on the experimental branching fraction is the statistical uncertainty and the second is the systematic one. The experimental results for the modes $B^0 \to D^{*-}D^{*+}K^0$ and $B^+ \to \bar{D}^0D^0K^+$ are a combination between the *BaBar* and *Belle* measurements [8]

B decay mode	$\mathscr{B}$(experimental) (10^{-4})
B^0 decays through external W-emission amplitudes	
$B^0 \to D^-D^0K^+$	$10.7 \pm 0.7 \pm 0.9$
$B^0 \to D^-D^{*0}K^+$	$34.6 \pm 1.8 \pm 3.7$
$B^0 \to D^{*-}D^0K^+$	$24.7 \pm 1.0 \pm 1.8$
$B^0 \to D^{*-}D^{*0}K^+$	$106.0 \pm 3.3 \pm 8.6$
B^0 decays through external + internal W-emission amplitudes	
$B^0 \to D^-D^+K^0$	$7.5 \pm 1.2 \pm 1.2$
$B^0 \to D^{*-}D^+K^0 + D^-D^{*+}K^0$	$64.1 \pm 3.6 \pm 3.9$
$B^0 \to D^{*-}D^{*+}K^0$	$79.3 \pm 3.8 \pm 6.7$
B^0 decays through internal W-emission amplitudes	
$B^0 \to \bar{D}^0D^0K^0$	$2.7 \pm 1.0 \pm 0.5$
$B^0 \to \bar{D}^0D^{*0}K^0 + \bar{D}^{*0}D^0K^0$	$10.8 \pm 3.2 \pm 3.6$
$B^0 \to \bar{D}^{*0}D^{*0}K^0$	$24 \pm 5.5 \pm 6.7$
B^+ decays through external W-emission amplitudes	
$B^+ \to \bar{D}^0D^+K^0$	$15.5 \pm 1.7 \pm 1.3$
$B^+ \to \bar{D}^0D^{*+}K^0$	$38.1 \pm 3.1 \pm 2.3$
$B^+ \to \bar{D}^{*0}D^+K^0$	$20.6 \pm 3.8 \pm 3.0$
$B^+ \to \bar{D}^{*0}D^{*+}K^0$	$91.7 \pm 8.3 \pm 9.0$
B^+ decays through external + internal W-emission amplitudes	
$B^+ \to \bar{D}^0D^0K^+$	$14.0 \pm 0.7 \pm 1.2$
$B^+ \to \bar{D}^0D^{*0}K^+$	$63.2 \pm 1.9 \pm 4.5$
$B^+ \to \bar{D}^{*0}D^0K^+$	$22.6 \pm 1.6 \pm 1.7$
$B^+ \to \bar{D}^{*0}D^{*0}K^+$	$112.3 \pm 3.6 \pm 12.6$
B^+ decays through internal W-emission amplitudes	
$B^+ \to D^-D^+K^+$	$2.2 \pm 0.5 \pm 0.5$
$B^+ \to D^-D^{*+}K^+$	$6.3 \pm 0.9 \pm 0.6$
$B^+ \to D^{*-}D^+K^+$	$6.0 \pm 1.0 \pm 0.8$
$B^+ \to D^{*-}D^{*+}K^+$	$13.2 \pm 1.3 \pm 1.2$

5.7 Non Resonant Components in $D^{(*)}D^{(*)}K^*$ as Input to $b \to sll$ Angular Analysis

The penguin induced flavour-changing neutral current (FCNC) transitions $b \to s$ and $b \to d$ are exceptional probes of flavour physics validity and they are very sensitive to NP contributions as well as to the impact of short-distance QCD corrections. The sensitivity is of particular interest when looking at differential branching ratios

and other quantities. A complete review of possible measurements can be found in Ref. [25].

The first experimental observation of $b \rightarrow s$ transition has been obtained studying $B \rightarrow K^* \gamma$ at CLEO in 1993 [26]. Such decay mode allows to perform branching ratio, CP and Isospin asymmetry and time dependent CP asymmetry measurements. Multibody decays, such as $b \rightarrow sl^+l^-$, provide a wider range of NP-sensitive observables, such as differential decay rate, as a function of the leptons invariant mass for instance, as well as forward-backward asymmetries (A_{FB}). In particular, the analysis of $B \rightarrow K^*l^+l^-$ decays is of particular as it allows the access to a multitude of observables [27] sensitive in different ways to NP. This kind of measurement has been performed by BaBar, Belle, CDF, ATLAS and CMS [28–32]. The most precise and complete results have been obtained by the LHCb experiment, in a variety of $b \rightarrow sl^+l^-$ decay modes. LHCb has found several interesting hints of New Physics [33, 34] in these modes, for example in the angular distribution of $B^0 \rightarrow K^{*0}l^+l^-$. The interpretation of these results has been controversial. On one hand, the result can be interpreted as a hint of NP. On the other hand, it might be that QCD corrections to the matrix elements of $B \rightarrow K^*l^+l^-$ transition are under estimated. Such corrections arise from long-distance and from penguin short-distance perturbative effects.

Matrix elements corrections have an important interplay with the double charm B decays due to $b \rightarrow (c\bar{c} \rightarrow \gamma^* \rightarrow l^+l^-)s$ transition. The formation of an intermediate virtual resonance such as the J/ψ is possible in the charm loop. Its factorization from the rest of the decay, classified as a long-distance effect, leads to terms which could mimic the observed discrepancies.

The short-distance perturbative effects are described by Wilson coefficients in the relevant effective Hamiltonian while long-distance perturbative effects are described, largely but not completely, by form factors.

The extraction of physics and conclusions regarding the observation of NP effects rely on the validity of QCD factorization. In this respect, we will briefly review the Effective Hamiltonian for the $B \rightarrow K^*\mu^+\mu^-$ decay and we will highlight the role of $b \rightarrow c\bar{c}s$ corrections in the theoretical models in Sect. 5.7.1. Indeed, the study of doubly charmed decay modes could play an important role to solve the controversy. Indeed, the role of non-resonant $B \rightarrow D^{(*)}\overline{D}^{(*)}K^*$ components could have been underestimated in all the current studies. Such components can be extracted from a full amplitude analysis.

5.7.1 Effective Hamiltonian for $b \rightarrow s\mu^+\mu^-$ and Charm Loops

The evaluation of the decay amplitude for $B \rightarrow K^*\mu^+\mu^-$ (Feynman diagram in Fig. 5.8) is obtained in three different steps:
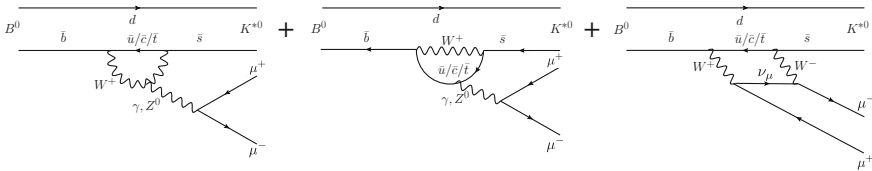
Fig. 5.8 Dominant Feynman diagrams contributing to the $B^0 \rightarrow K^{*0}\mu^+\mu^-$ decay

- short-distance (QCD, weak interaction and new physics) effects are separated from long-distance QCD effects in an effective Hamiltonian $\mathscr{H}_{\text{eff}}$;
- matrix elements of local quark bilinear operators J of type $\langle K^*|J|B \rangle$ (form factors) are calculated;
- the 4-quark operators in $\mathscr{H}_{\text{eff}}$ are calculated using QCD factorization.

For a full review of the calculations, see Ref. [35]. The relevant step in which the non-resonant $B \rightarrow D\overline{D}K^*$ components can play an important role leading to a potential mis-interpretation of the deviations observed as a source of NP concerns the first step. Thus, we will only highlight the main steps to derive $\mathscr{H}_{\text{eff}}$ for $B \rightarrow K^*l^+l^-$ and the relevant terms which are affected by the $b \rightarrow c\overline{c}s$ transitions.

According to [36, 37], the effective Hamiltonian for $b \rightarrow s\mu^+\mu^-$ transitions is

$$\mathscr{H}_{\text{eff}} = -\frac{4\,G_F}{\sqrt{2}} \left(\lambda_t \mathscr{H}_{\text{eff}}^{(t)} + \lambda_u \mathscr{H}_{\text{eff}}^{(u)} \right) \tag{5.26}$$

with the CKM combination $\lambda_i = V_{ib}V_{is}^*$ and

$$\mathscr{H}_{\text{eff}}^{(t)} = C_1\mathscr{O}_1^c + C_2\mathscr{O}_2^c + \sum_{i=3}^{6} C_i\mathscr{O}_i + \sum_{i=7,8,9,10,P,S} (C_i\mathscr{O}_i + C_i'\mathscr{O}_i')\,,$$

$$\mathscr{H}_{\text{eff}}^{(u)} = C_1(\mathscr{O}_1^c - \mathscr{O}_1^u) + C_2(\mathscr{O}_2^c - \mathscr{O}_2^u)\,.$$

Although $\mathscr{H}_{\text{eff}}^{(u)}$ represents the contribution to the effective Hamiltonian from the doubly Cabibbo-suppressed transitions ($\mathscr{H}_{\text{eff}}^{(t)}$ is the Cabibbo-favoured one), it is relevant contribution for certain observables sensitive to complex phases of decay amplitudes.

The operators $\mathscr{O}_{i \leq 6}$ are identical to the P_i operators given in Ref. [36], while the remaining ones are given by

$$\mathscr{O}_7 = \frac{e}{g^2}m_b(\bar{s}\sigma_{\mu\nu}P_R b)F^{\mu\nu}, \qquad \mathscr{O}_7' = \frac{e}{g^2}m_b(\bar{s}\sigma_{\mu\nu}P_L b)F^{\mu\nu}, \tag{5.27}$$

$$\mathscr{O}_8 = \frac{1}{g}m_b(\bar{s}\sigma_{\mu\nu}T^a P_R b)G^{\mu\nu a}, \qquad \mathscr{O}_8' = \frac{1}{g}m_b(\bar{s}\sigma_{\mu\nu}T^a P_L b)G^{\mu\nu a}, \tag{5.28}$$

$$\mathscr{O}_9 = \frac{e^2}{g^2}(\bar{s}\gamma_\mu P_L b)(\bar{\mu}\gamma^\mu\mu), \qquad \mathscr{O}_9' = \frac{e^2}{g^2}(\bar{s}\gamma_\mu P_R b)(\bar{\mu}\gamma^\mu\mu), \tag{5.29}$$

$$\mathscr{O}_{10} = \frac{e^2}{g^2}(\bar{s}\gamma_\mu P_L b)(\bar{\mu}\gamma^\mu \gamma_5 \mu), \qquad \mathscr{O}'_{10} = \frac{e^2}{g^2}(\bar{s}\gamma_\mu P_R b)(\bar{\mu}\gamma^\mu \gamma_5 \mu), \qquad (5.30)$$

$$\mathscr{O}_S = \frac{e^2}{16\pi^2}m_b(\bar{s}P_R b)(\bar{\mu}\mu), \qquad \mathscr{O}'_S = \frac{e^2}{16\pi^2}m_b(\bar{s}P_L b)(\bar{\mu}\mu), \qquad (5.31)$$

$$\mathscr{O}_P = \frac{e^2}{16\pi^2}m_b(\bar{s}P_R b)(\bar{\mu}\gamma_5\mu), \qquad \mathscr{O}'_P = \frac{e^2}{16\pi^2}m_b(\bar{s}P_L b)(\bar{\mu}\gamma_5\mu), \qquad (5.32)$$

where g is the strong coupling constant $\left(\alpha_s(q^2) = \frac{g^2(q^2)}{4\pi}\right)$ and $P_{L,R} = (1 \mp \gamma_5)/2$ are the left and right projectors of spinors. m_b denotes the running b quark mass. The unprimed operators and $\mathscr{O}_{S,P}$ are highly suppressed in the SM; the primed operators are linked by opposite chirality to the unprimed operators. The contributions of $\mathscr{O}'_i$ for $1 \leq i \leq 6$ are usually neglected and the most interesting ones for the "charm" loops contribution are O_9 and O'_9. They are associated to vector currents which can also arise from $b \to s((c\bar{c}) \to \gamma* \to l^+ l^-)$.

C_i are the Wilson coefficients of (5.26) and they encode short-distance physics, including possible NP effects. They are calculated at the matching scale $\mu = m_W$, in a perturbative expansion in powers of $\alpha_s(m_W)$, and are then evolved down to scales $\mu \sim m_b$ according to the solution of the renormalization group equations. Any NP contributions enter through $C_i(m_W)$, while the evolution to lower scales is determined by the SM.

All C_i are expanded as:

$$C_i = C_i^{(0)} + \frac{\alpha_s}{4\pi}C_i^{(1)} + \left(\frac{\alpha_s}{4\pi}\right)^2 C_i^{(2)} + O(\alpha_s^3), \qquad (5.33)$$

where $C_i^{(0)}$ is the tree-level contribution, which vanishes for all operators but $\mathscr{O}_2$. In the normalization of the operator scheme used, $C_9^{(0)}$ is different from zero. $C_i^{(n)}$ denotes an n-loop contribution. $\mathscr{O}_9$ is given by conserved currents, but mixes with $\mathscr{O}_{1,...,6}$, via diagrams with a virtual photon decaying into $\mu^+\mu^-$. Additional scale dependence in C_9 comes from the factor $1/g^2$.

The decay mode $B \to K^*(\to K\pi)\mu^+\mu^-$ does not allow access to all the coefficients separately. For example the combinations $C_S - C'_S$ and $C_P - C'_P$ enter the decay amplitude. The $C_{7,9,10}$ are accessible in angular observables. The actual decay being observed in experiment is not $B^0 \to K^{*0}\mu^+\mu^-$, but $B^0 \to K^{*0}(\to K^+\pi^-)\mu^+\mu^-$. According to Ref. [27], the additional information provided by the angle between K^+ and π^- gives sensitivity to the polarization of the K^{*0}. The K^{*0} polarization provides an additional probe of the effective Hamiltonian and it allows the access to various parameters appearing in the effective Hamiltonian which can be affected by NP.

The matrix element of the effective Hamiltonian (5.4) for the decay $B \to K^*(\to K\pi)\mu^+\mu^-$ can be written as a function of the dimuon invariant mass squared (q^2), in naive factorization, as

$$\mathcal{M} = \frac{G_F \alpha}{\sqrt{2}\pi} V_{tb} V_{ts}^* \left\{ \left[\langle K\pi | \bar{s}\gamma^\mu (C_9^{\text{eff}} P_L + C_9'^{\text{eff}} P_R) b | \bar{B} \rangle \right. \right.$$

$$\left. - \frac{2m_b}{q^2} \langle K\pi | \bar{s} i \sigma^{\mu\nu} q_\nu (C_7^{\text{eff}} P_R + C_7'^{\text{eff}} P_L) b | \bar{B} \rangle \right] (\bar{\mu}\gamma_\mu \mu)$$

$$+ \langle K\pi | \bar{s}\gamma^\mu (C_{10}^{\text{eff}} P_L + C_{10}'^{\text{eff}} P_R) b | \bar{B} \rangle (\bar{\mu}\gamma_\mu\gamma_5\mu)$$

$$\left. + \langle K\pi | \bar{s} (C_S P_R + C_S' P_L) b | \bar{B} \rangle (\bar{\mu}\mu) + \langle K\pi | \bar{s} (C_P P_R + C_P' P_L) b | \bar{B} \rangle (\bar{\mu}\gamma_5\mu) \right\},$$

$$(5.34)$$

where α is the electromagnetic coupling constant.

In (5.34), $C_{7,9,10}$ are re-defined since they always appear in a particular combination with other C_i due to renormalization. In this respect the "effective" coefficients are defined as follows:

$$C_7^{\text{eff}} = \frac{4\pi}{\alpha_s} C_7 - \frac{1}{3} C_3 - \frac{4}{9} C_4 - \frac{20}{3} C_5 - \frac{80}{9} C_6,$$

$$C_8^{\text{eff}} = \frac{4\pi}{\alpha_s} C_8 + C_3 - \frac{1}{6} C_4 + 20 C_5 - \frac{10}{3} C_6,$$

$$C_9^{\text{eff}} = \frac{4\pi}{\alpha_s} C_9 + Y(q^2),$$

$$C_{10}^{\text{eff}} = \frac{4\pi}{\alpha_s} C_{10}, \qquad C_{7,8,9,10}'^{,\text{eff}} = \frac{4\pi}{\alpha_s} C_{7,8,9,10}', \qquad (5.35)$$

with $\quad Y(q^2) = h(q^2, m_c) \left(\frac{4}{3} C_1 + C_2 + 6 C_3 + 60 C_5 \right)$

$$- \frac{1}{2} h(q^2, m_b) \left(7 C_3 + \frac{4}{3} C_4 + 76 C_5 + \frac{64}{3} C_6 \right)$$

$$- \frac{1}{2} h(q^2, 0) \left(C_3 + \frac{4}{3} C_4 + 16 C_5 + \frac{64}{3} C_6 \right)$$

$$+ \frac{4}{3} C_3 + \frac{64}{9} C_5 + \frac{64}{27} C_6. \qquad (5.36)$$

The function used in theoretical calculation to evaluate C_9^{eff} is

$$h(q^2, m_q) = -\frac{4}{9} \left(\ln \frac{m_q^2}{\mu^2} - \frac{2}{3} - z \right) - \frac{4}{9} (2 + z)\sqrt{|z - 1|} \times \begin{cases} \arctan \dfrac{1}{\sqrt{z-1}} & z > 1 \\ \ln \dfrac{1 + \sqrt{1-z}}{\sqrt{z}} - \dfrac{i\pi}{2} & z \leq 1 \end{cases}$$

$$(5.37)$$

where $z = 4m_q^2/q^2$, is related to the basic fermion loop. The $Y(q^2)$ function drives the corrections to the C_9 coefficient. It encodes contributions from diagrams where quark loops are generated decaying into a virtual photon which produces the lepton pairs. Thus, corrections from QCD are expected to enter, as well as the tails of the virtual resonant structures (such as J/psi for the $c\bar{c}$) one could produce in the loops decaying into $\mu^+\mu^-$ final states.

Experimentally, the fit to the data [38] is performed with the following parametrisation for the final differential decay rate:

$$C_9^{eff} = C_9 + Y(q^2) = C_9 + \sum_j \eta_j e^{i\delta_j} A_j^{res}(q^2) \qquad (5.38)$$

where η_j is the magnitude of amplitude of the vector meson resonance j which can contribute in the loops and δ_j its phase relative to C_9. The resonances included are, for instance, ω^0, ρ^0, ϕ, $\psi(2S)$, $\psi(3770)$, $\psi(4440)$, $\psi(4160)$ and $\psi(4415)$. All of them are included as relativistic Breit–Wigner lineshapes with running width $\Gamma_j(q^2)$. In principle all resonances from $q\bar{q}$ should be included in $Y(q^2)$. No contributions from broad resonances and hadronic continuum is included in the interpretation of the experimental data and this is the exact point where the non-resonant structure in $b \to c\bar{c}s$ could play a role affecting C_9^{eff}.

Thus, large non-resonant and resonant amplitudes from the $c\bar{c}$ loop must be taken into account properly from both theoretical calculation and experimental fits. Indeed, in the angular analysis performed by LHCb [33, 34] only the resonant $c\bar{c}$ states listed before were used, completely neglecting the non-resonant component (assumed to be small). If the non-resonant component is instead large, the $c\bar{c}$ spectrum used so far would be wrong and the "true" amplitudes from such processes can interfere with the other amplitudes and mimic the NP effects observed in $B \to K^*\mu^+\mu^-$.

The best strategy to tackle this problem would be to perform a full amplitude analysis in the 48 exclusive decay modes $B \to D^{(*)}D^{(*)}K^*$ to have full access to all the resonant and non-resonant $c\bar{c}$ spectrum above the open-charm threshold. This would allow to have a control of the virtual contribution of non-resonant components whose tails could affect the C_9^{eff} parameter. Further information on the "charm-loops" potential problem can be found in Ref. [39].

5.8 Summary Concerning $B^0 \to D^0 \overline{D}^0 K^{*0}$

We describe the theoretical motivation for the study of B decays to a pair of $\overline{D}^{(*)}$ and $D^{(*)}$ with an extra $K^{(*)}$. The interest in this typology of channel is mainly due to the following:

- Test isospin relations [8] and improve our understanding about B decays dynamics.
- Study of resonant structures ($R_{c\bar{c}}$) above the open charm threshold decaying into $D^{(*)}\overline{D}^{(*)}$ as well as study of $c\bar{s}$ resonant structures ($R_{c\bar{s}}$) using the $R_{(c\bar{s})} \to D^{(*)}K^{(*)}$ decay mode.
- Understand the impact of $b \to s((c\bar{c}) \to ll)$ diagram in the interpretation of the flavour changing neutral current decays.

References

1. Particle Data Group, C. Patrignani et al., Review of particle physics. Chin. Phys. C **40**(10), 100001 (2016). https://doi.org/10.1088/1674-1137/40/10/100001
2. T.E. Browder, Hadronic decays and lifetimes of B and D mesons, arXiv:hep-ph/9611373
3. G. Buchalla, I. Dunietz, H. Yamamoto, Hadronization of $b \to c\bar{c}s$. Phys. Lett. B **364**, 188 (1995). https://doi.org/10.1016/0370-2693(95)01296-6, arXiv:hep-ph/9507437
4. BaBar, B. Aubert et al., Measurement of the branching fractions for the exclusive decays of B^0 and B^+ to $\bar{D}^{(*)}D^{(*)}K$. Phys. Rev. D **68**, 092001 (2003). https://doi.org/10.1103/PhysRevD.68.092001, arXiv:hep-ex/0305003
5. Barate et al., Observation of doubly-charmed B decays at LEP. Eur. Phys. J. C **4**(3), 387 (1998). https://doi.org/10.1007/s100520050216
6. LHCb, R. Aaij et al., Angular analysis of the $B^0 \to K^{*0}\mu^+\mu^-$ decay using 3 fb^{-1} of integrated luminosity. JHEP **02**, 104 (2016). https://doi.org/10.1007/JHEP02(2016)104, arXiv:1512.04442
7. H.J. Lipkin, A.I. Sanda, Isospin invariance, CP violation and B anti-B mixing. Phys. Lett. B **201**, 541 (1988). https://doi.org/10.1016/0370-2693(88)90615-6
8. V. Poireau, M. Zito, A precise isospin analysis of $B \to \overline{D}^*D^*K$ decays. Phys. Lett. B **704**, 559 (2011). https://doi.org/10.1016/j.physletb.2011.09.097, arXiv:1107.1438
9. A.F. Falk, Introduction to hadronic B physics, arXiv:hep-ph/9812217
10. M. Neubert, Introduction to B physics, arXiv:hep-ph/0001334
11. H.R. Quinn, P.F. Harrison, *The BaBar Physics Book: Physics at an Asymmetric B Factory* (SLAC, Stanford, 1998)
12. A.J. Buras, J.-M. Gérard, R. Rückl, $\frac{1}{N}$ expansion for exclusive and inclusive charm decays. Nucl. Phys. B **268**(1), 16 (1986). https://doi.org/10.1016/0550-3213(86)90200_2
13. J.D. Bjorken, Topics in b-physics. Nucl. Phys. B Proc. Suppl. **11**(0), 325 (1989). https://doi.org/10.1016/0920-5632(89)90019_4
14. C.W. Bauer, B. Grinstein, D. Pirjol, I.W. Stewart, Testing factorization in $B \to D^{(*)}X$ decays. Phys. Rev. D **67**, 014010 (2003). https://doi.org/10.1103/PhysRevD.67.014010
15. T.E. Browder, A. Datta, P.J. O'Donnell, S. Pakvasa, Measuring β in $B \to D^{(*)+}D^{(*)-}K_s$. Phys. Rev. D **61**, 054009 (2000). https://doi.org/10.1103/PhysRevD.61.054009
16. A.F. Falk, M.E. Luke, Strong decays of excited heavy mesons in chiral perturbation theory. Phys. Lett. B **292**, 119 (1992). https://doi.org/10.1016/0370-2693(92)90618_E, arXiv:hep-ph/9206241
17. Belle, S.K. Choi et al., Observation of a narrow charmonium - like state in exclusive $B^{\pm} \to K^{\pm}\pi^+\pi^-J/\psi$ decays. Phys. Rev. Lett. **91**, 262001 (2003). https://doi.org/10.1103/PhysRevLett.91.262001, arXiv:hep-ex/0309032
18. LHCb Collaboration, L. Collaboration, Determination of the $X(3872)$ meson quantum numbers. Phys. Rev. Lett. **110**, 222001 (2013). https://doi.org/10.1103/PhysRevLett.110.222001
19. N. Brambilla et al., QCD and strongly coupled gauge theories: challenges and perspectives, arXiv:1404.3723
20. LHCb Collaboration, R. Aaij et al., Observation of the resonant character of the $Z(4430)^-$ state. Phys. Rev. Lett. **112**, 222002 (2014). https://doi.org/10.1103/PhysRevLett.112.222002, arXiv:1404.1903
21. LHCb Collaboration, L. Collaboration, Observation of $J/\psi p$ resonances consistent with pentaquark states in $\Lambda_b^0 \to J/\psi K^- p$ decays. Phys. Rev. Lett. **115**, 072001 (2015). https://doi.org/10.1103/PhysRevLett.115.072001
22. H. Yamamoto, Charm counting and B semileptonic branching fraction. PoS **hf8**, hf8/015 (1999), arXiv:hep-ph/9912308
23. A.F. Falk, Z. Ligeti, M. Neubert, Y. Nir, Heavy quark expansion for the inclusive decay $B \to \tau\bar{\nu}X$. Phys. Lett. B **326**, 145 (1994). https://doi.org/10.1016/0370-2693(94)91206_8

24. BaBar, P. del Amo Sanchez et al., Measurement of the $B \to \overline{D}^{(*)} D^{(*)} K$ branching fractions. Phys. Rev. D **83**, 032004 (2011). https://doi.org/10.1103/PhysRevD.83.032004, arXiv:1011.3929

25. T. Hurth, Status of SM calculations of $b \to s$ transitions. Int. J. Mod. Phys. A **22**, 1781 (2007). https://doi.org/10.1142/S0217751X07036476, arXiv:hep-ph/0703226

26. Cleo, R. Ammar et al., Evidence for penguins: first observation of $B \to K^* (892)$ gamma. Phys. Rev. Lett. **71**, 674 (1993). https://doi.org/10.1103/PhysRevLett.71.674

27. F. Kruger, L.M. Sehgal, N. Sinha, R. Sinha, Angular distribution and CP asymmetries in the decays $\bar{B} \to K^- \pi^+ e^- e^+$ and $\bar{B} \to \pi^- \pi^+ e^- e^+$. Phys. Rev. D **61**, 114028 (2000). https://doi.org/10.1103/PhysRevD.61.114028, https://doi.org/10.1103/PhysRevD.63.019901, arXiv:hep-ph/9907386. [Erratum: Phys. Rev. D **63**, 019901 (2001)]

28. BaBar, B. Aubert et al., Measurements of branching fractions, rate asymmetries, and angular distributions in the rare decays $B \to K \ell^+ \ell^-$ and $B \to K^* \ell^+ \ell^-$. Phys. Rev. D **73**, 092001 (2006). https://doi.org/10.1103/PhysRevD.73.092001, arXiv:hep-ex/0604007

29. J.-T. Belle, Wei et al., Measurement of the differential branching fraction and forward-backword asymmetry for $B \to K^{(*)} \ell^+ \ell^-$. Phys. Rev. Lett. **103**, 171801 (2009). https://doi.org/10.1103/PhysRevLett.103.171801, arXiv:0904.0770

30. CDF, T. Aaltonen et al., Measurements of the angular distributions in the decays $B \to K^{(*)} \mu^+ \mu^-$ at CDF. Phys. Rev. Lett. **108**, 081807 (2012). https://doi.org/10.1103/PhysRevLett.108.081807, arXiv:1108.0695

31. ATLAS Collaboration, Angular analysis of $B_d^0 \to K^* \mu^+ \mu^-$ decays in pp collisions at $\sqrt{s} = 8$ TeV with the ATLAS detector. Technical report, ATLAS-CONF-2017-023, CERN, Geneva, April 2017

32. CMS Collaboration, Measurement of the P_1 and P_5' angular parameters of the decay $B^0 \to K^{*0} \mu^+ \mu^-$ in proton-proton collisions at $\sqrt{s} = 8$ TeV. Technical report, CMS-PAS-BPH-15-008, CERN, Geneva, 2017

33. G. Ciezarek et al., A challenge to lepton universality in b-meson decays. Nature **546**, 227 (2017)

34. F. Archilli, M.-O. Bettler, P. Owen, K.A. Petridis, Flavour-changing neutral currents making and breaking the standard model. Nature **546**, 221 (2017)

35. W. Altmannshofer et al., Symmetries and asymmetries of $B \to K^* \mu^+ \mu^-$ decays in the standard model and beyond. JHEP **01**, 019 (2009). https://doi.org/10.1088/1126-6708/2009/01/019, arXiv:0811.1214

36. C. Bobeth, M. Misiak, J. Urban, Photonic penguins at two loops and m_t dependence of $BR[B \to X_s l^+ l^-]$. Nucl. Phys. B **574**, 291 (2000). https://doi.org/10.1016/S0550-3213(00)00007_9, arXiv:hep-ph/9910220

37. C. Bobeth, A.J. Buras, F. Kruger, J. Urban, QCD corrections to $\bar{B} \to X_{d,s} \nu \bar{\nu}$, $\bar{B}_{d,s} \to \ell^+ \ell^-$, $K \to \pi \nu \bar{\nu}$ and $K_L \to \mu^+ \mu^-$ in the MSSM. Nucl. Phys. B **630**, 87 (2002). https://doi.org/10.1016/S0550-3213(02)00141_4, arXiv:hep-ph/0112305

38. LHCb, R. Aaij et al., Measurement of the phase difference between short- and long-distance amplitudes in the $B^+ \to K^+ \mu^+ \mu^-$ decay. Eur. Phys. J. C **77**(3), 161 (2017). https://doi.org/10.1140/epjc/s10052-017-4703_2, arXiv:1612.06764

39. J. Lyon, R. Zwicky, Resonances gone topsy turvy - the charm of QCD or new physics in $b \to s \ell^+ \ell^-$?, arXiv:1406.0566

Chapter 6
Measurement of the $B^0 \to D^0\overline{D}^0 K^{*0}$ Branching Ratio

This chapter describes the measurement of the $B^0 \to D^0\overline{D}^0 K^{*0}$ branching ratio using as reference decay mode $B^0 \to D^{*-} D^0 K^+$.

6.1 Analysis Strategy

The following naming for particles and decay modes used for the analysis are the following:

- Signal mode: $B^0 \to (\overline{D}^0 \to K^+_{\overline{D}^0}\pi^-_{\overline{D}^0})(D^0 \to K^-_{D^0}\pi^+_{D^0})(K^{*0} \to K^+_{K^{*0}}\pi^-_{K^{*0}})$
- Reference mode: $B^0 \to (D^*(2010)^- \to (\overline{D}^0 \to K^+_{\overline{D}^0}\pi^-_{\overline{D}^0})\pi^-_{K^{*0}})(D^0 \to K^-_{D^0}\pi^+_{D^0})$ $K^+_{K^{*0}}$

Concerning the signal mode, a K^{*0} candidate is reconstructed without applying any invariant mass selection. Thus, the final branching ratio is measured for considering as signal the $B^0 \to (\overline{D}^0 \to K^+_{\overline{D}^0}\pi^-_{\overline{D}^0})(D^0 \to K^-_{D^0}\pi^+_{D^0})K^+_{K^{*0}}\pi^-_{K^{*0}}$ decay mode.

The experimental value of the $B^0 \to D^{*-} D^0 K^+$ branching fraction has been measured by BaBar [1]:

$$\mathcal{B}(B^0 \to D^{*-} D^0 K^+) = (0.247 \pm 0.010 \pm 0.018)\%$$

with the observation of $\mathcal{N}_S = 1300 \pm 54$ signal events and a significance of 11.4σ.

In this analysis $B^0 \to D^{*-} D^0 K^+$ is reconstructed in the same exact way than $B^0 \to D^0\overline{D}^0 K^{*0}$. Indeed, the two modes have the same topology as it can be seen in Fig. 6.1. Such approach largely simplifies the analysis. The same final states are expected to be observed in the two modes, i.e. three kaons and three pions. The B^0 decay tree is built with a bottom-up approach. Pions and Kaons are combined to form D^0 and $\overline{D}^0$ candidates as well as K^{*0} ones. The resulting D^0, $\overline{D}^0$ and K^{*0} are combined to form the final B^0 candidate. Such approach works well for

Fig. 6.1 Sketch showing the event topology of the $B^0 \to D^0\overline{D}^0 K^{*0}$ and $B^0 \to D^{*-}D^0 K^+$. As it can be observed, at the position of the decay vertex of the B^0, $B^0 \to D^0\overline{D}^0 K^{*0}$ and $B^0 \to D^{*-}D^0 K^+$ share the same topology. A simple cut on the $\overline{D}^0\pi^-$ invariant mass allows to separate the two modes
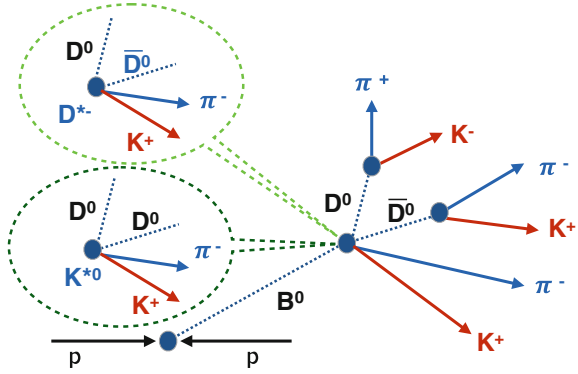
$B^0 \to D^{*-}D^0 K^+$ as well, if no K^{*0} invariant mass selection is applied and this is the case for the analysis. According to the event topology, the reconstructed sample contains both the decay modes and the only discriminating property between the two modes is the narrow $D^{*\pm}$ invariant mass. It is therefore possible to disentangle the $B^0 \to D^{*-}D^0 K^+$ from the $B^0 \to D^0\overline{D}^0 K^{*0}$ in $B^0 \to D^0\overline{D}^0 K^+\pi^-$ (no K^{*0} mass selection) simply imposing the constraint on the $D^{*\pm}$ invariant mass. Such simple selection strongly reduces the background contamination in $B^0 \to D^{*-}D^0 K^+$, while in the $B^0 \to D^0\overline{D}^0 K^{*0}$ case, a very large background to fight against is expected since any $K_{K^{*0}}$ and $\pi_{K^{*0}}$ are free to be combined defining the decay position of the B^0 candidate as well as the origin vertex of the D^0 and $\overline{D}^0$. In $B^0 \to D^{*-}D^0 K^+$ the same argument holds, but the $\pi^-_{K^{*0}}$ kinematic has to match with the $\overline{D}^0$ one to peak at the D^{*-} mass value.

D^0 and $\overline{D}^0$ are reconstructed through the Cabibbo favoured transition $c \to s(W^- \to \overline{u}d)$ (for the D^0), i.e. $D^0 \to K^-\pi^+$ ($\overline{D}^0 \to K^+\pi^-$). Therefore, the flavour of the D^0 can be assigned according to the K electric charge, neglecting the Cabibbo suppressed $D^0 \to K^+\pi^-$ ($\overline{D}^0 \to K^-\pi^+$) decay mode. The branching fraction of $D^0 \to K^-\pi^+$ is known from Ref. [2] and it is equal to:

$$\mathscr{B}(D^0 \to K^-\pi^+) = (3.93 \pm 0.03)\% \qquad (6.1)$$

The K^{*0} is reconstructed through the strong decay $K^{*0} \to K^+\pi^-$ whose branching ratio is assumed to be 2/3.

The separation of the $B^0 \to D^{*-}D^0 K^+$ and $B^0 \to D^0\overline{D}^0 K^{*0}$ decays is performed simply applying a cut to $\Delta M = |m(\overline{D}^0\pi^-_{K^{*0}}) - m(\overline{D}^0) - \overline{\mu}|$ at $\pm 4\sigma$, where σ and $\overline{\mu}$ are extracted from a Gaussian fit to the $m(\overline{D}^0\pi^-_{K^{*0}}) - m(\overline{D}^0)$ spectrum using the $B^0 \to D^{*-}D^0 K^+$ simulation sample. The fitted value of $\overline{\mu}$ is 145.52 MeV/c^2, which is consistent with $m(D^{*-}) - m(D^0)$ from Ref. [2] and $\sigma = 0.72$ MeV/c^2. Events inside the 4σ window are classified as $B^0 \to D^{*-}D^0 K^+$, while the events outside are classified as $B^0 \to D^0\overline{D}^0 K^{*0}$.

Indeed, looking at the invariant mass spectrum of the $K_{K^{*0}}\pi_{K^{*0}}$ system in $B^0 \to D^0\overline{D}^0 K^{*0}$, $B^0 \to D^{*-}D^0 K^+$ and $B^0 \to D^0\overline{D}^0 K^+\pi^-$ in Fig. 6.2, one can

Fig. 6.2 Invariant mass spectrum of the resulting K^{*0} in the $B^0 \to D^0\overline{D}^0 K^{*0}$ (red), $B^0 \to D^{*-}D^0 K^+$ (violet), and $B^0 \to D^0\overline{D}^0 K^+\pi^-$ (blue) decay modes. Events are obtained from generator level (phase space model) requiring the final states particles to be in the LHCb acceptance
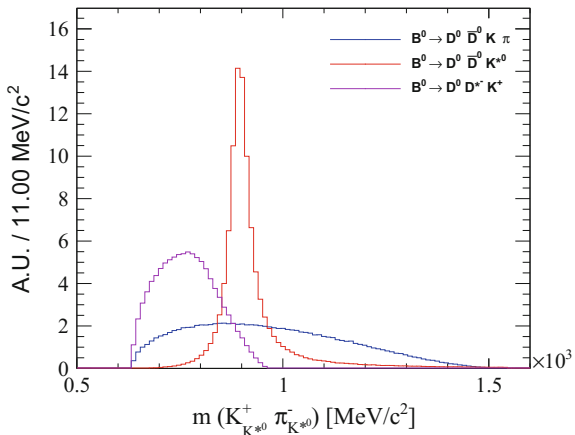
observe that the requirement $m(K^{*0}) > m_K + m_\pi$ and $m(K^{*0}) < m_{B^0} - 2 \cdot m_D^0$ is enough to look inclusively at all the possibilities. We will present in the following the description of the dataset used for the analysis (Sect. 6.2), the selection of the events (Sect. 6.3), the fit to the data (Sect. 6.4), efficiency estimation and the preliminary results (Sect. 6.5). Systematics uncertainties are expected to be added in future works and we will briefly summarise the source of systematics that will be evaluated in the Sect. 6.6.

6.2 Datasets

The entire LHCb 2011 ($\sqrt{s} = 7$ TeV) and 2012 ($\sqrt{s} = 8$ TeV) data taken during the LHC Run I have been used for this analysis. The corresponding integrated luminosity is 3 fb^{-1} [3], which is divided by years and magnet polarity as summarised in Table 6.1. The analysis is performed using all the samples all together, i.e., we do not split the analysis by data taking period and magnet polarity.

Table 6.1 Integrated luminosity used for the analysis splitted by year of data taking and magnet polarity. A total of 3 fb^{-1} has been used for this analysis. The error is a systematic error and it cancels between $B^0 \to D^{*-}D^0 K^+$ and $B^0 \to D^0\overline{D}^0 K^{*0}$ since the same data sample is used for both the decay modes

Type	$\int \mathscr{L}\ [pb^{-1}]$
2012-MagDown ($\sqrt{s} = 8$ TeV)	1015.9 ± 35.6
2012-MagUp ($\sqrt{s} = 8$ TeV)	1033.6 ± 36.2
2011-MagDown ($\sqrt{s} = 7$ TeV)	569.2 ± 19.9
2011-MagUp ($\sqrt{s} = 7$ TeV)	415.2 ± 14.5

6.3   Selection

The event selection is divided in different steps ordered as follow:

- Stripping: after the LHCb HLT processing the data are not directly available for analysis. They undergo a central offline selection process called stripping. Details are provided in Sect. 6.3.1.
- Pre-selection: further selections are applied to reduce the background. Details are provided in Sect. 6.3.2.
- Multivariate selection: multivariate analysis techniques are employed to efficiently select the data. Details are provided in Sect. 6.3.5.
- Trigger selection: trigger requirements are applied to the data as it will be described in Sect. 6.3.11. The resulting dataset is divided in different trigger categories for the extraction of signal yields.

The outcome of the selection is used for the fit to the data aiming at extracting $\mathscr{B}(B^0 \rightarrow D^0\overline{D}^0 K^{*0})$ with respect to the reference $B^0 \rightarrow D^{*-}D^0 K^+$. The fit to the data is performed for different trigger categories in $B^0 \rightarrow D^{*-}D^0 K^+$ and $B^0 \rightarrow D^0\overline{D}^0 K^{*0}$ and efficiencies ratio evaluated for them (see Sects. 6.4 and 6.5).

6.3.1   Stripping

The central offline selection of data is performed aiming at selecting $B^0 \rightarrow D^0\overline{D}^0 K^{*0}$ without K^{*0} invariant mass selections. The procedure to provide reconstructed B^0 candidates is a bottom-up approach, i.e., intermediate particles are reconstructed first and are used in a second step to reconstruct the decay chain. A first selection is applied to ensure a good track quality for the final states $(\pi \& K)_{D^0, \overline{D}^0, K^{*0}}$ and a significant displacement of the tracks from the primary vertex. This is ensured applying the selections listed in Table 6.2, where

- χ^2_{track} is the Kalman Fit χ^2 per degrees of freedom of the corresponding `long` track associated to the particle.[1]
- $IP\chi^2_{Primary}$ is the impact parameter significance with respect to the primary vertex. It is calculated computing the variation in χ^2 for the PV with and without the track under consideration. The larger is the value and the more probable is that the track is not originating from the pp interaction point (also called prompt track).
- $Ghost_{track}$ is a parameter assigned after the Kalman Fit to the track which encodes the probability for the track to be a fake one. The value is assigned based on a neural-net based classifier using as training variables kinematic variables, tracking quality parameters from the various pattern recognition algorithms and the Kalman Fit and number of hits in the various sub detectors used by the track.

---

[1] In this analysis we use only `long` track. In principle, `upstream` tracks could be added to maximise the yields in $B^0 \rightarrow D^{*-}D^0 K^+$ because of the softer momentum spectrum of $\pi_{K^{*0}}$.

Table 6.2 Stripping selections applied to reconstruct $B^0 \to D^0\overline{D}^0 K^{*0}$ (actually $B^0 \to D^0\overline{D}^0 K^+\pi^-$) for the particles used to reconstruct D^0, $\overline{D}^0$ and K^{*0} and the final B^0 candidate

Particle	Cut
$\pi/K_{D^0,\overline{D}^0,K^{*0}}$	$\chi^2_{track} < 3.0$
$\pi/K_{D^0,\overline{D}^0,K^{*0}}$	$p_T > 100\,\text{MeV/c}$
$\pi/K_{D^0,\overline{D}^0}(\pi/K_{K^{*0}})$	$p > 1000\,(2000)\,\text{MeV/c}$
$\pi/K_{D^0,\overline{D}^0,K^{*0}}$	$IP\chi^2_{Primary} > 4$
$\pi/K_{D^0,\overline{D}^0,K^{*0}}$	$Ghost_{Track} < 0.4$
$\pi_{D^0,\overline{D}^0}(\pi_{K^{*0}})$	$PIDK < 20$ (none)
$K_{D^0,\overline{D}^0}(K_{K^{*0}})$	$PIDK > -10$ (none)
At least 1 D^0/K^{*0} daughter	$\chi^2_{track} < 2.5$
At least 1 D^0/K^{*0} daughter	$p_T > 500\,\text{MeV/c}$, $p > 5000\,\text{MeV/c}$
At least 1 final state	$p_T > 1.7\,\text{GeV/c}$, $p > 10\,\text{GeV/c}$
At least 1 final state	$IP_{PV} > 0.1\,\text{mm}$

Table 6.3 Stripping selections applied to reconstruct $B^0 \to D^0\overline{D}^0 K^{*0}$ (actually $B^0 \to D^0\overline{D}^0 K^+\pi^-$) for the intermediate particles (D^0, $\overline{D}^0$, K^{*0}) and the final B^0 candidate

Particle	Cut
D^0, $\overline{D}^0(K^{*0})$	$p_T > 1800(1000)\,\text{MeV/c}$
D^0, $\overline{D}^0(K^{*0})$	$M \in [1764.84, 1964.84]\,\text{MeV/c}^2$ (None)
D^0, $\overline{D}^0$, K^{*0}	$doca_{K\pi} < 0.5\,\text{mm}$
D^0, $\overline{D}^0(K^{*0})$	$\chi^2/ndof$ Vertex $< 10(16)$
D^0, $\overline{D}^0(K^{*0})$	χ^2 Vertex =- PV distance $> 36(16)$
D^0, $\overline{D}^0(K^{*0})$	DIRA PV > 0 (none)
B^0	$M \in [4750, 6000]\,\text{MeV/c}^2$
B^0	$p_T > 5000\,\text{MeV/c}$, $\chi^2/ndof$ Vertex < 10
B^0	$\tau_{PV} > 0.2\,\text{ps}$, $IP\chi^2_{Primary} < 25$
Event	$n_{long}Tracks < 5000$

- $PIDK$ is $\Delta LL = \ln \mathscr{L}(K) - \ln \mathscr{L}(\pi)$ which has been defined in Sect. 2.4.4. It encodes the probability for a given track of being associated to a K hypothesis, using the RICH1 and RICH2 informations.
- IP_{PV} is the value of the impact parameter with respect to the primary vertex.

The final state particles selected according to the Table 6.2 are combined among each other to produce D^0, $\overline{D}^0$ and K^{*0} candidates according to the selections defined in Table 6.3. Finally, D^0, $\overline{D}^0$ and K^{*0} are combined to form B^0 candidates according to the selections defined in Table 6.3, where:

- M is the invariant mass obtained combining the K and the π tracks for D^0, $\overline{D}^0$ and K^{*0}.
- *doca* is the distance of closest approach of the tracks combined to form the intermediate D^0, $\overline{D}^0$ and K^{*0}. This is calculated propagating the bachelor tracks according to their track state at the z of their first measurement in the VELO.
- $\chi^2/ndof$ Vertex encodes the quality of the fitted reconstructed decay vertex of the intermediate D^0, $\overline{D}^0$, K^{*0} particles.
- χ^2 Vertex – PV distance is the χ^2 distance of the reconstructed decay vertex of D^0, $\overline{D}^0$, K^{*0} from the related PV. The larger is the value the more probable is that the decay vertex is displaced from the PV.
- τ_{PV} is the lifetime of the resulting B^0 candidates computed with respect to the PV.
- DIRA PV is the cosine of the angle between the momentum of the particle and the direction vector from the PV to the reconstructed decay vertex of the particle.
- $n_{long}Tracks$ is the number of reconstructed `long` track in the event.

6.3.2   Pre-selection

An additional selection step is applied to the data from stripping. A loose selection is applied on the *PID* for the $\pi_{K^{*0}}$ and $K_{K^{*0}}$, since such selection is not present in the stripping. Further background suppression is achieved selecting the D^0 and $\overline{D}^0$ having a reconstructed invariant mass within a 30 MeV/c^2 mass window around the nominal mass. We also require for both D^0 and $\overline{D}^0$ to fly in the forward region with respect to the decay vertex of the reconstructed B. This allow to suppress at a reasonable level the contamination in $B^0 \rightarrow D^0\overline{D}^0 K^{*0}$ of charmless background as well as the presence of D_s and $D^\pm$ in the decay chain. The list of additional preselections applied to the data for both $B^0 \rightarrow D^0\overline{D}^0 K^{*0}$ and $B^0 \rightarrow D^{*-} D^0 K^+$ are summarised in Table 6.4.

A final selection is applied to disentangle in the $B^0 \rightarrow D^0\overline{D}^0 K^+\pi^-$ selected sample, the $B^0 \rightarrow D^0\overline{D}^0 K^{*0}$ and $B^0 \rightarrow D^{*-} D^0 K^+$:

- $B^0 \rightarrow D^{*-} D^0 K^+$ includes as additional pre-selection the following:

Table 6.4 Additional selections applied after stripping to $B^0 \rightarrow D^{*-} D^0 K^+$ and $B^0 \rightarrow D^0\overline{D}^0 K^{*0}$

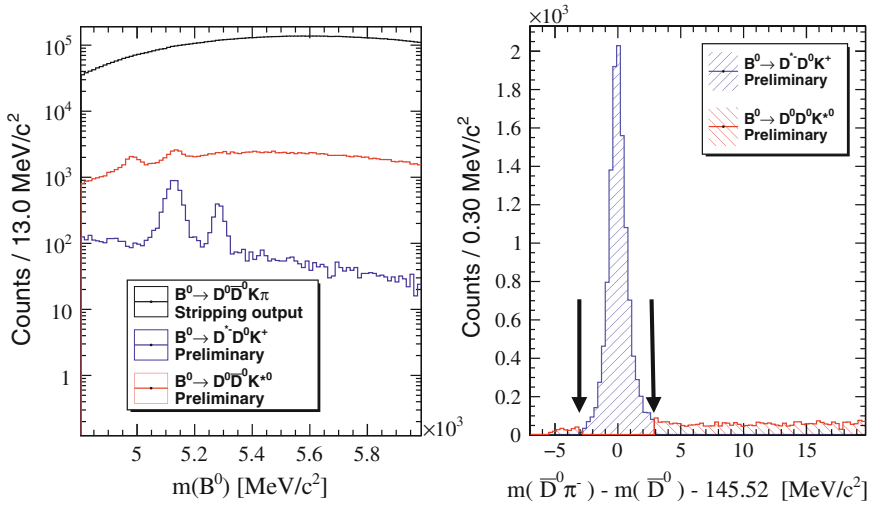| Preliminary selections (both $B^0 \rightarrow D^0\overline{D}^0 K^{*0}$, $B^0 \rightarrow D^{*-} D^0 K^+$) |
| --- |
| DectayTreeFitter fit (with K^{*0} vertex constrain) converged |
| $m(K^{*0}) < 1600$ MeV/c^2 $[m(B^0) - 2m(D^0) + 50$ MeV/c$^2]$ |
| D^0, $\overline{D}^0$ $\dfrac{\text{DecayLength}_{signed}}{\sigma \, \text{DecayLength}} > 0$ |
| $|m(D^0) - m_{PDG}(D^0)| < 30$ MeV/c^2 |
| $|m(\overline{D}^0) - m_{PDG}(\overline{D}^0)| < 30$ MeV/c^2 |
| $\pi_{K^{*0}} \, PIDK < 10$; $K_{K^{*0}} \, PIDK > -10$ |

Fig. 6.3 On the left the B^0 invariant mass distribution after the stripping selections (black), after the pre-selections in $B^0 \to D^0\overline{D}^0 K^{*0}$ (red) and the pre-selections in $B^0 \to D^{*-}D^0K^+$ (blue). On the right, the invariant mass distribution of $\overline{D}^0\pi^-_{K^{*0}}$ after pre-selections in $B^0 \to D^0\overline{D}^0 K^{*0}$ (red) and $B^0 \to D^{*-}D^0K^+$ (blue)

Table 6.5 Stripping and pre-selections efficiencies in $B^0 \to D^{*-}D^0K^+$ and $B^0 \to D^0\overline{D}^0 K^{*0}$

Mode	$\varepsilon_{Stripping|Acceptance}$ (%)	$\varepsilon_{Preliminary|Stripping}$ (%)
$B^0 \to D^0\overline{D}^0 K^{*0}$	(1.026 ± 0.006)	78.08 ± 0.23
$B^0 \to D^{*-}D^0K^+$	(0.62 ± 0.01)	76.60 ± 0.70

$$- \ |m(\overline{D}^0\pi^-) - m(\overline{D}^0) - (m_{PDG}(D^{*-}) - m_{PDG}(D^0))| < (4 \times 0.724) \text{ MeV/c}^2$$

- $B^0 \to D^0\overline{D}^0 K^{*0}$ includes as additional pre-selection the following:

$$- \ |m(\overline{D}^0\pi^-) - m(\overline{D}^0) - (m_{PDG}(D^{*-}) - m_{PDG}(D^0))| > (4 \times 0.724) \text{ MeV/c}^2$$

The resulting invariant mass spectrum of the B^0 candidates with preliminary cuts applied is shown in Fig. 6.3. The pre-selection and stripping efficiencies are evaluated from signal Monte Carlo samples available for the two modes. Their measured value ($\varepsilon_{Stripping|Acceptance}$ for stripping selections and $\varepsilon_{Preliminary|Stripping}$ for pre-selections) are summarized in Table 6.5. Details on their evaluation are provided in Sect. 6.5.

The stripping selection efficiency ($\varepsilon_{Stripping|Acceptance}$) includes also tracking efficiency and partial trigger selections (which are anyhow applied a posteriori as described in Sect. 6.3.11) efficiency. Thus, we find convenient to determine the stripping efficiencies as the ratio of signal events out of stripping with respect to the amount of signal events produced in the LHCb acceptance.
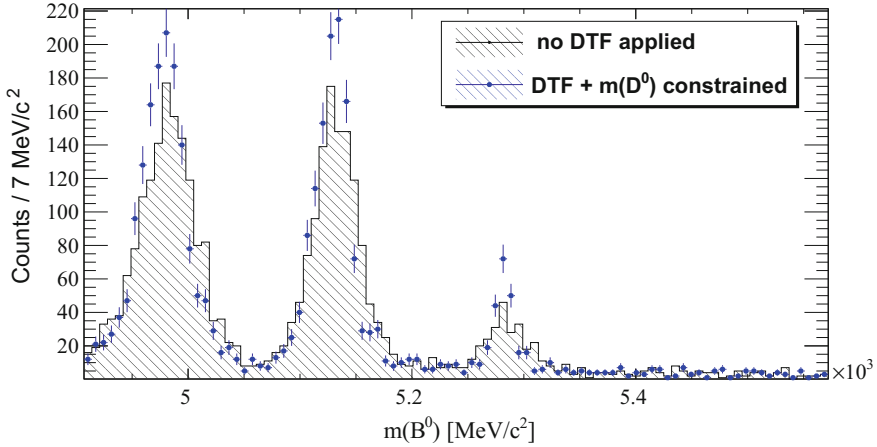
Fig. 6.4 Invariant mass spectrum of B^0 candidates in $B^0 \rightarrow D^0\overline{D}^0 K^{*0}$ selected events for the case where no DTF is applied (black distribution) and the case where the DTF is applied constraining the K^{*0} vertex as well as the invariant masses of both D^0 and $\overline{D}^0$

6.3.3   Decay Tree Fitter

The mass resolution of the final B candidates can be improved using the DecayTreeFitter (DTF) tool available in LHCb [4]. The B candidates in LHCb are found combining final states and their four momentum. In some sense this is similar to the filtering and prediction step in the Kalman Filter, i.e. candidates are reconstructed using a bottom-up approach. It is possible to apply a smoothing of the decay tree applying constraints to masses of intermediate particles and applying a constraint to the decay vertices of the particles. This step allows to find the best fit value for the four momentum of final states and the overall effect on the final B meson candidate is an improvement of the mass resolution as it can be seen in Fig. 6.4 for selected $B^0 \rightarrow D^0\overline{D}^0 K^{*0}$ events comparing the spectrum of B^0 candidates with and without the DTF applied with D masses constrained.

6.3.4   PID Response Resampling Using `Meerkat`

Particle identification at LHCb is not well modelled in Monte Carlo simulation. Particle identification variables are often excluded from multivariate selection in LHCb and data driven methods are used to evaluate the corresponding selection efficiencies. This analysis avoids the data driven method and it employs the `Meerkat` package [5] to reproduce in Monte Carlo simulation a correct description of the particle identification variables for the various final states in the signal and reference decay mode.

The `Meerkat` package [5] is used in this analysis to re-sample the neural net *PID* variables (*ProbNN*). Such re-sampling method is based on kernel density estimation with corrections to account for boundary effects. The *PID* variables are assumed to depend only on the kinematics (p_{T}, η) and detector occupancy (which is proportional to the number of tracks in the event N_{tr}).[2] Thus, the *PID* response can be expressed as a function of those variables.

Calibration data samples are used to evaluate the probability distribution function of the *PID* variable as a function of the kinematics and detector occupancy. Once the PDF (g) is known $g(PID) = f(p_{\mathrm{T}}, \eta, N_{tr})$, it is possible to randomly generate the *PID* response in simulated samples given the values of p_{T}, η and N_{tr}. This approach allows to have correct *PID* responses in Monte Carlo and be able to use such variables as input for multivariate selections as well as to evaluate the efficiencies. Thus, the basic ingredient is the knowledge of the *PID* variable x for a given particle species as a function of the particle p_{T}, η and the event variable N_{tr}: $p(x|p_{\mathrm{T}}, \eta, N_{tr})$.

The comparison in $B^0 \to D^{*-} D^0 K^+$ between selected signal events and the signal Monte Carlo simulation of the re-sampled *PID* responses used in this analysis are shown in Fig. 6.5.

6.3.5 Multivariate Selection

Classification of signal events against background events can be performed in different ways. The most trivial one is based on rectangular cuts on variables which are able to separate background to signal. Such approach is inefficient when the discriminating variables are correlated one to another. Thus, multivariate analysis techniques (MVA) are generally used and they are much more powerful to solve classification problems than the cut based methods [6]. In order to further suppress the background and purify the data sample of the $B^0 \to D^0 \overline{D}^0 K^{*0}$, MultiVariate Analysis (MVA) techniques have been used. The selection is based on a two-stage Boosted Decision Tree decision, one aiming at selecting D mesons from B hadron decays and the second stage aiming at selecting $B^0 \to D^0 \overline{D}^0 K^{*0}$ and $B^0 \to D^{*-} D^0 K^+$.

From a practical point of view MVA techniques allows to squash a large set of discriminating variables for the searched signal into a single variable, called MVA classifier. In this analysis, only Boosted Decision Trees (BDT) have been employed as MVA technique and the first BDT aiming at selecting the D mesons is called D_{fromB}. Several cases have been tested: including or excluding the calibrated *PID* response for the final states particles in D^0 decay, and using two different BDT boosting approaches, i.e. Adaptive (ada) and Gradient (grad) boosting. The final multivariate selection has been optimised in all the cases: if the *PID* variables is excluded from the list of discriminating variables used to obtain the MVA classifier, the optimization is achieved through simultaneous cut on the MVA classifier and the *PID* variables.

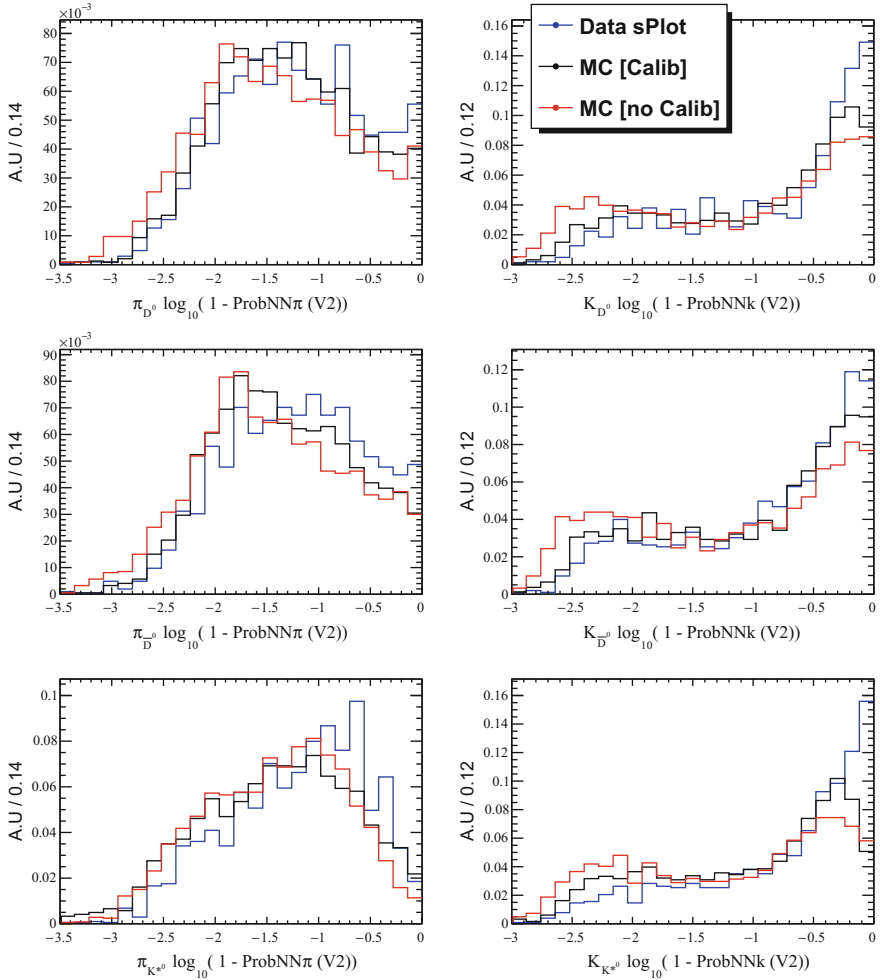[2]Note that also in the data driven method the same dependency is used in LHCb.

Fig. 6.5 Comparison of the relevant *ProbNN* variables used for this analysis. In blue the *PID* distribution for the signal events in $B^0 \to D^{*-} D^0 K^+$, in black (red) the *ProbNN* distribution in signal Monte Carlo simulation after (before) `Meerkat` resampling

The output classifier for the first stage is used as input variable for the second-stage BDT for both D^0 and $\overline{D}^0$ including and excluding also in this case within the input variables the calibrated *PID* variables for the K^{*0} (or pseudo-K^{*0} in $B^0 \to D^{*-} D^0 K^+$) decay products. An overview of multivariate analysis techniques is provided in Sect. 6.3.6 and a description of the two-staged BDT selection is provided in Sect. 6.3.8.

6.3.6 Boosted Decision Trees: Overview

The most important ingredient in discriminating a given data species to another is the identification of variables. Let's assume we have identified N discriminating variables. This set of variables defines a N dimensional space over which one can simply apply rectangular selections. At the end of this serie of cuts, the space generated by the N variables is reduced to an hyper-cubic region. The optimization of the rectangular selections is done maximizing a Figure Of Merit (FoM) which quantifies the enhancement of signal over background due to the cuts. The selections applied are, by construction, decorrelated one to another and they are called "*rectangular cuts*". If the N variables are correlated one to another, rectangular cuts is a sub-optimal selection. The goal of multivariate analysis techniques is to find the optimal selections, given the N discriminating variables accounting for correlations between variables. An illustration of a typical 2-D classification problem with two variables can be found in Fig. 6.6 together with different solutions and methods which can be used.

Multivariate analysis techniques rely and are based on machine learning. The fundamental steps of *machine learning* methods are:

- Training phase: it is performed on samples where signal and background events are known. The step aims at "*teaching*" the algorithm how to discriminate signal from background.
- Testing phase: it is performed on statistically-independent samples with respect to samples used to train the discriminating algorithm. This phase is necessary in order to check if the algorithm has been trained in the correct way. Testing allows to spot signals from what is called overtraining. Overtrained MVA classifiers are classifiers which recognize as important features in the signal or background their statistical fluctuation. This effect can be suppressed using a $k - fold$ technique in the training and testing phase.
- The MVA classifier is applied to the relevant data sample.

The first step for the training phase is to identify two samples: a signal-like and a background-like one. These two samples, together with the N discriminating variables define the basic ingredients for the development of the algorithm of discrimination based on machine learning.

Other two datasets (background and signal-like) are provided allowing to test the performance of the algorithm. This is usually achieved splitting randomly the signal like and background like samples in two sub datasets: one used for training, one for testing. Once the algorithm is trained and tested, it provides a single output classifier which is calculated taking into account the multi-dimensional $(N-$-D)informations coming from the N-D variables space. This classifier spans the N dimensional phase-space and assigns a value indicating if the specific point of the N-D space in which the event falls is signal-like or background-like.

Several MVA algorithms are available and they are based on different approaches: *Kernel-based Methods, Neutral Networks (NN), Grid Searches, Linear Methods,*
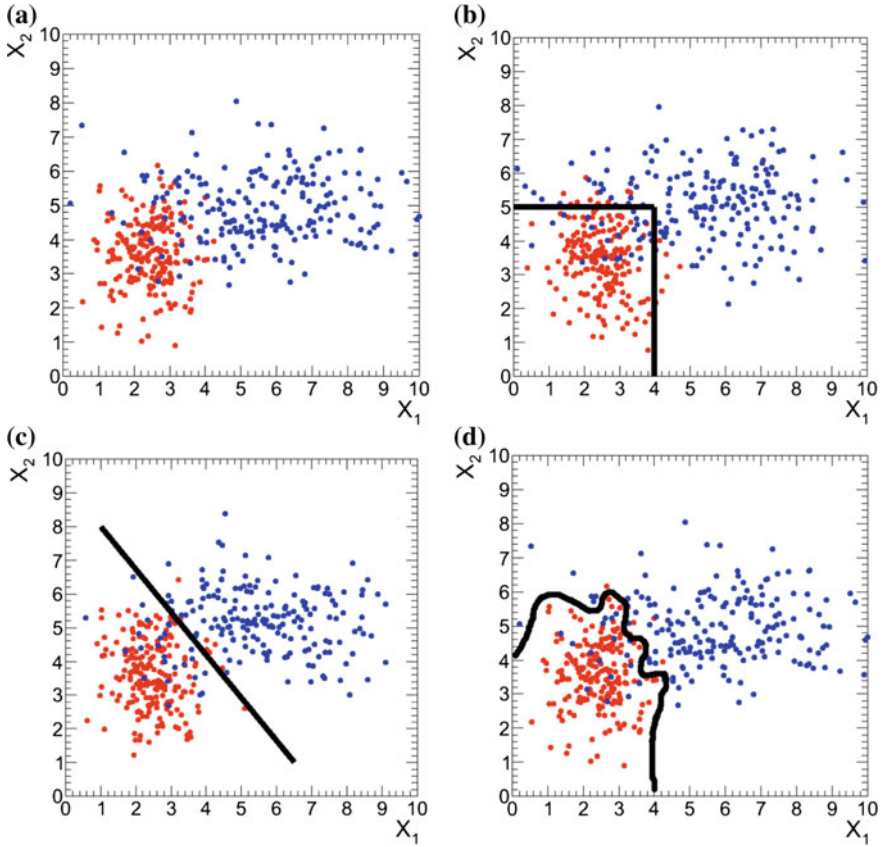
Fig. 6.6 2-dimensional (X_1, X_2) classification problem. Various solutions to the classification are shown: **a** X_1 versus X_2 distributions, **b** Rectangular cuts for classification, **c** Linear methods for classification (Fisher Method), **d** Multivariate analysis methods. The red dots corresponds to signal-like events while black one to background-like events

Bayes or Likelihood Discriminants, Multi Layer Perceptrons (MLP) and Boosted Decision Trees (BDTs). These methods have been employed in the last 30 years in High Energy Physics in order to solve *classification* problems. Among the various methods, Boosted Decision Trees have been found to be more efficient, despite being relatively simple. The main reason of the BDTs success is related to its insensitivity to irrelevant variables and its tolerance to missing variables in training and testing samples. In this analysis, all the *MVA* techniques have been used and the *BDT* method has been chosen. The software used is the TMVA Tool-kit for MultiVariate Analysis [7] and an introduction to MVA techniques can be found in [8–13].

BDTs are machine learning based classifiers. The fundamental unit of a BDT is the Decision Tree (DT). A Decision Tree is a classifier structured as a binary tree where sequential rectangular cuts are applied and for each step the best cut on variables is found. The effect of these sequential cuts is to divide the N-D space defined by the

input variables into sub-partitions. Additional selections are found and optimized within the generated sub-partitions. The procedure of division in sub-partitions is iteratively applied. The root node is the starting point and at that stage the entire sample is analysed. The following steps, called branch nodes, smaller partitions of the N dimensional space are analysed as soon as all the space is partitioned and classified. For any branch node the criteria used to separate the sample is the reduction of impurity in the sample. This is encoded in the so-called *Gini Index* which is defined as

$$G = P(1 - P)$$

where $P = \dfrac{s}{s+b}$ is the signal purity (s is the amount of signal while b is the amount of background). The partitioning process of the N dimensional space ends when no further impurity reduction can be achieved. Different criteria can be used, e.g. the maximization of the statistical significance, minimization of the misclassification error or the minimization of the cross entropy.

The last nodes of a *Decision Tree* (DT) are called leaves and they point to a specific partition of the N dimensional space. A value is assigned to each partition indicating if the corresponding N-D volume is background-like or signal-like.

The general structure of a single Decision Tree (DT) used in Boosted Decision Tree (BDT) algorithm is shown in Fig. 6.7. Some important drawbacks arise when using a single decision tree is employed to solve the classification problem:

- the classifier in real data can be different from the training sample (which we remind is in this analysis a MC sample), in this case the classifier is said to be *biased*;
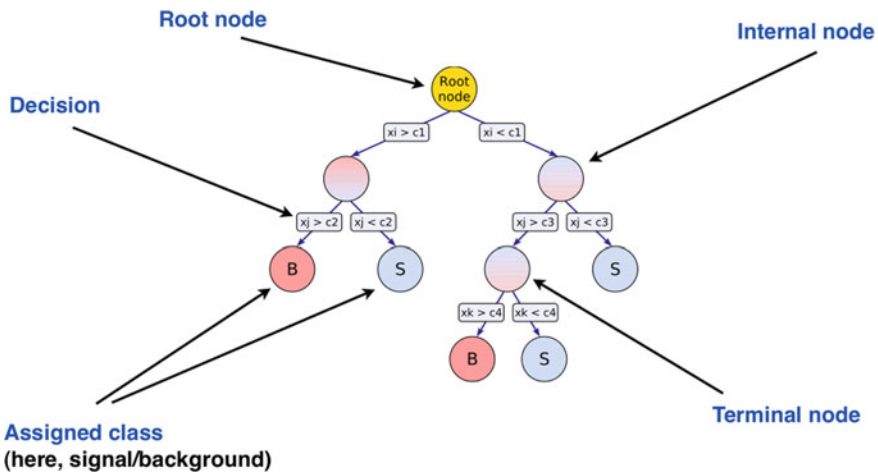

Fig. 6.7 Structure of a single Decision Tree where rectangular cuts are applied to the x_i variables ($i = 1, ..., N$). The final blob with S and B belongs to a specific volume of the N dimensional space for which the signal- or background-like behaviour is evaluated

- the classifier obtained from the training is too sensitive (sensitivity is parametrized by the variance) to the input data sample: naively it means that the classifier is well trained only for the training samples.

In order to overcome these problems, instead of a single Decision Tree, an ensemble of DT is considered for the classification problem. Thus the classifier output is taken as the average of the single DT response in the specific region of the N dimensional phase space. The logic behind this is basically related to the fact that in order to provide a "single doctor exceptional diagnosis" for a given "illness", one can use several "mediocre doctors diagnosis" for the same "case" and reach the a very efficient diagnosis. In other words, if single *DTs* of modest quality are combined together, it is possible to generate a very efficient classifier, i.e. a *collective boosted* decision is taken.

The most successful boosting algorithms are the Adaptive (AdaBoost) and Gradient Boosting which employ different strategies in the learning phase. Both of them have been tested in this analysis. Given a BDT made of M DTs, the AdaBoost [14] algorithm makes uses of weights (assigned to each event) for misclassified DTs composing in the training phase of the BDT. This allows to obtain harder training moving from one DT to the next one for the events which are harder to classify. Given the ith DT, events misclassified by the previous DT are weighted (called *boost weight* according to the following:

$$\alpha_i = \frac{1 - \varepsilon_m^{i-1}}{\varepsilon_m^i},$$

where ε_m^{i-1} is the misclassification rate of the previous *DT* and α_i is the *boost weight* assigned to the misclassified events for the training of the ith DT. For a given N dimensional tuple of discriminating variables, the output of the ith classifier is a scalar labelled as $h_i(\vec{x})$ ($\vec{x}$ is a vector in the N-Dimensional space) and its value is equal to -1 (background-like) or 1 (signal-like).

The final BDT output classifier for a given event is then built as a weighted average of all the single DTs output, i.e:

$$BDT(\vec{x}) = \frac{1}{M} \sum_{i=1}^{M} \ln(\alpha_i) h_i(\vec{x}). \tag{6.2}$$

In (6.2), M is the number of DTs used for the BDT and the final BDT classifier is a number ranging from –1 (background) to 1 (signal).

The baseline idea behind the gradient boosting is the same as in AdaBoost, except that it does not use the weights in the training phase. More details concerning the gradient boosting technique can be found in Ref. [7].

Both algorithms aims at boosting the performance of a simple base learner by iteratively shifting the focus towards problematic observations that are difficult to predict. AdaBoost performs the shift by up-weighting observations that were mis-

classified before. Gradient boosting identifies difficult observations by large residuals computed in the previous iterations.

Usually the BDT classifier cut is optimized using data samples in such a way to maximize the significance, defined as

$$\mathscr{S} = \frac{\mathscr{N}_s}{\sqrt{\mathscr{N}_s + \mathscr{N}_b}}$$

where $\mathscr{N}_s$ and $\mathscr{N}_b$ are the numbers of signal and background events which survive after the *BDT* classifier cut. The BDT algorithm can be tuned changing some options and the most important ones are:

- *Number of DTs*: number of *DTs* to take into account for the final "*boosted*" (weighted) decision;
- *Maximum Depth*: maximum depth of nodes allowed for each *DT*;
- *Number of Cuts*: number of grid points in the variable range used for finding optimal cuts at every node splitting;
- *Pruning Method*: if activated, it allows to remove statistically insignificant branches after the *DT* creation.[3]

6.3.7 *k − Folding of Data Samples to Maximise Statistics*

One of the limitation in MVA technique is the low statistics available for the training samples. Indeed, this is the case for the training performed in $B^0 \rightarrow D^0 \overline{D}^0 K^{*0}$, where only 30,000 signal events are used. The statistics is generally further reduced by the fact that the performance of the algorithm is evaluated on a second data sample which has not been used by the algorithm for the training phase. Such testing sample allows to spot and ensure that the algorithm is not biased by the statistical fluctuations of the training sample. The full dataset is splitted in $k = 10$ different subset and 10 different BDTs are trained and tested using only 9/10 of the statistics. The BDT classifier is then applied to the remaining 1/10 excluded from the training and testing. Thus a total of 10 statistically independent BDT classifiers are obtained aiming at covering the full datasets statistics. In this way, all of the available background and signal sample events are used for training but may also be used in subsequent stages of the analysis without bias to optimise the BDT and evaluate efficiencies. The 10-folding procedure is shown schematically in Fig. 6.8.

---

[3]*Pruning* method is a technique in *machine learning* that reduces the size of *decision trees* by removing sections of the tree that provide little power to the classification of the instances. The goals of *pruning* are the reduction of the complexity in the final classifier and the achievement of a better predictive accuracy. This is done thanks to the reduction of over-fitting and removal of sections of a classifier that may be based on noisy or erroneous data.
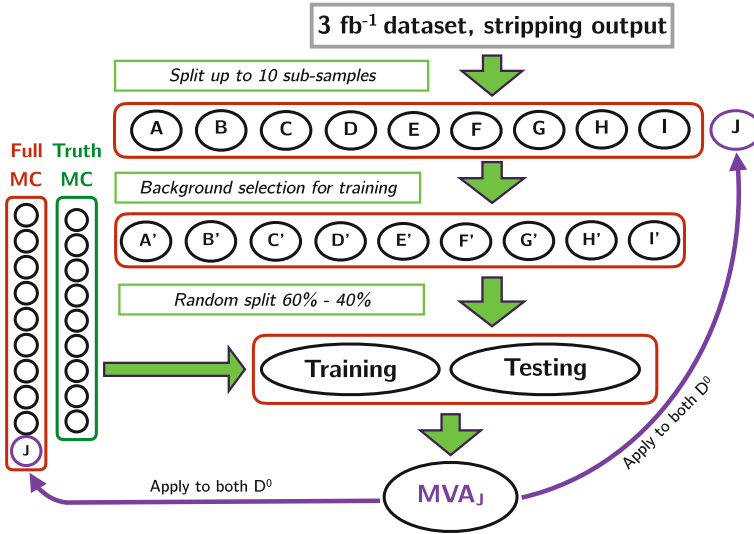
Fig. 6.8 Working principle of the $k - folding$ technique used for the analysis. In this case, it shows the application of the technique for the D_{fromB} BDT

6.3.8   Two Staged BDT Classifier

6.3.8.1   First Stage BDT: $D^0/\overline{D}^0$ Training

The first stage BDT (called D_{fromB}) is trained using kinematic and topology variables of D^0 and of the K_{D^0} and π_{D^0}. Variables are chosen to be not correlated to the B properties. The samples used for the training are the following:

1. Signal sample: Monte Carlo events matched to true signal after stripping and pre-selection.
2. Background sample: data after stripping and a partial pre-selection aiming at selecting events in D^0 sidebands, $\overline{D}^0$ signal region and B^0 signal region.

Concerning the background sample used for the D_{fromB}, we train the BDT against D^0 lying in the D^0 sidebands, i.e. $|m(D^0) - m_{PDG}| > 40\,\mathrm{MeV/c^2}$, but having all the remaining particles in the signal region $|m(\overline{D}^0) - m_{PDG}(\overline{D}^0)| < 40\,\mathrm{MeV/c^2}$ and $|m(B^0) - m_{PDG}(B^0)| < 100$ MeV/c^2. The background sample selection used for the training is shown in Fig. 6.9.

The list of the input variables used for the training is summarised in Table 6.6. The variables in Table 6.6 represent the following:

- D^0 χ^2_{ENDVTX} represents the χ^2 (i.e. the quality) of the reconstructed decay vertex of the D^0.
- D^0 $FD_{OWNPV}\chi^2$ is the flight distance significance of the reconstructed D^0 with respect the primary vertex PV.
- D^0 $IP_{OWNPV}\chi^2$ is the significance of the impact parameter of the reconstructed D^0 with respect to the primary vertex PV. The larger is the impact parameter, the
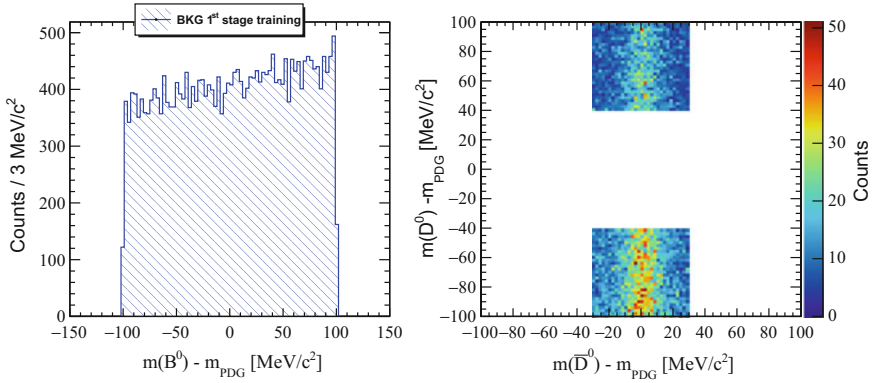
Fig. 6.9 The background sample for the first stage BDT training is extracted from data. Candidates are selected to lie in the B^0 invariant mass signal region (left). Only the variables of one the 2 D mesons are used for the training. The D meson is selected to have an invariant mass outside the signal region, but the other D meson is selected to be in the signal region (right)

Table 6.6 List of variables used to train the first stage. Different *PID* variables are used leading to different D_{fromB} classifier versions as well as different boosting strategies: adaptive boosting (ada) or gradient boosting (grad). A total of 6 different versions of the D_{fromB} BDT have been tested

Particle	Input Variable
D^0	χ^2_{ENDVTX}
	p
	p_T
	$FD_{OWNPV}\chi^2$
	$IP_{OWNPV}\chi^2$
	$doca_{\pi K}$
π_{D^0}	p
	p_T
	$IP_{OWNPV}\chi^2$
	$ProbNN\pi$ (V2 or V3 or none)
K_{D^0}	P
	P_T
	$IP_{OWNPV}\chi^2$
	$ProbNNk$ (V2 or V3 or none)
$D^0/\overline{D}^0$ classifier	$D_{fromB}^{NOPID/V3/V2}$ (grad/ada boost)

worse is the χ^2, since such value represents the compatibility of the IP with a value equal to zero. The same variable for the π_{D^0} and K_{D^0} is used as input variable for the BDT training. Generally, the $IP\chi^2$ for a track with respect to a primary vertex is defined as the difference between the χ^2 of the PV reconstructed with and without the track under consideration.

- $doca_{\pi K}$ is the distance of closest approach of the π and K used to reconstruct the D^0.
- A single $ProbNN$ variable for the π_{D^0} ($ProbNN\pi$) and the K_{D^0} ($ProbNNk$) is used for the D^{V2}_{fromB} and D^{V3}_{fromB} BDT. Also a BDT where no PID information is used has been trained (D^{NOPID}_{fromB}).
- The total momentum p and transverse momentum p_T of the D^0, K_{D^0} and π_{D^0} are used in the training of the BDT.

The D^{V2}_{fromB} (D^{V3}_{fromB}) uses the V2 (V3) tuning of the $ProbNN$ for the K and π final states particles. The two tunings are obtained using different samples for the training as described in Sect. 2.4.4.

It is important to underline that the PID variables in MC ($ProbNN$) have been used after re-sampling their distribution according to the particles kinematic to reproduce the data. Indeed, in LHCb large differences are observed between simulation and data for PID distributions. We take them into account using the re-sampled distributions through the kernel density estimator approach (performed by the `Meerkat` package) described in Sect. 6.3.4. Since the re-sampling strategy can be applied for a single PID variable per track, otherwise correlations would be completely destroyed, we used a single PID input variable per track. Indeed, two different tracks would maintain the proper correlations also in terms of PID variables as soon as the resampled PID variables of two different tracks are correlated to the corresponding kinematics of the tracks.
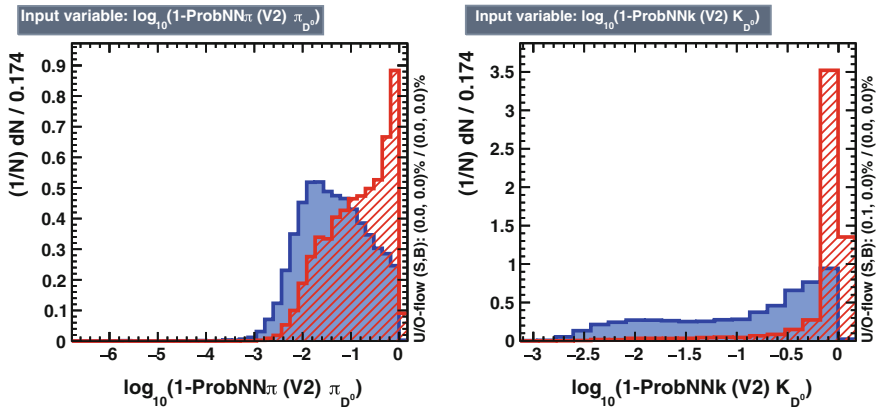

Fig. 6.10 Distribution of input variables used for the first stage BDT (D^{V2}_{fromB}) (grad). In red the input variables distribution in the background sample and in blue the same distribution for the signal sample used in the training. Plots obtained for the fifth fold of the training
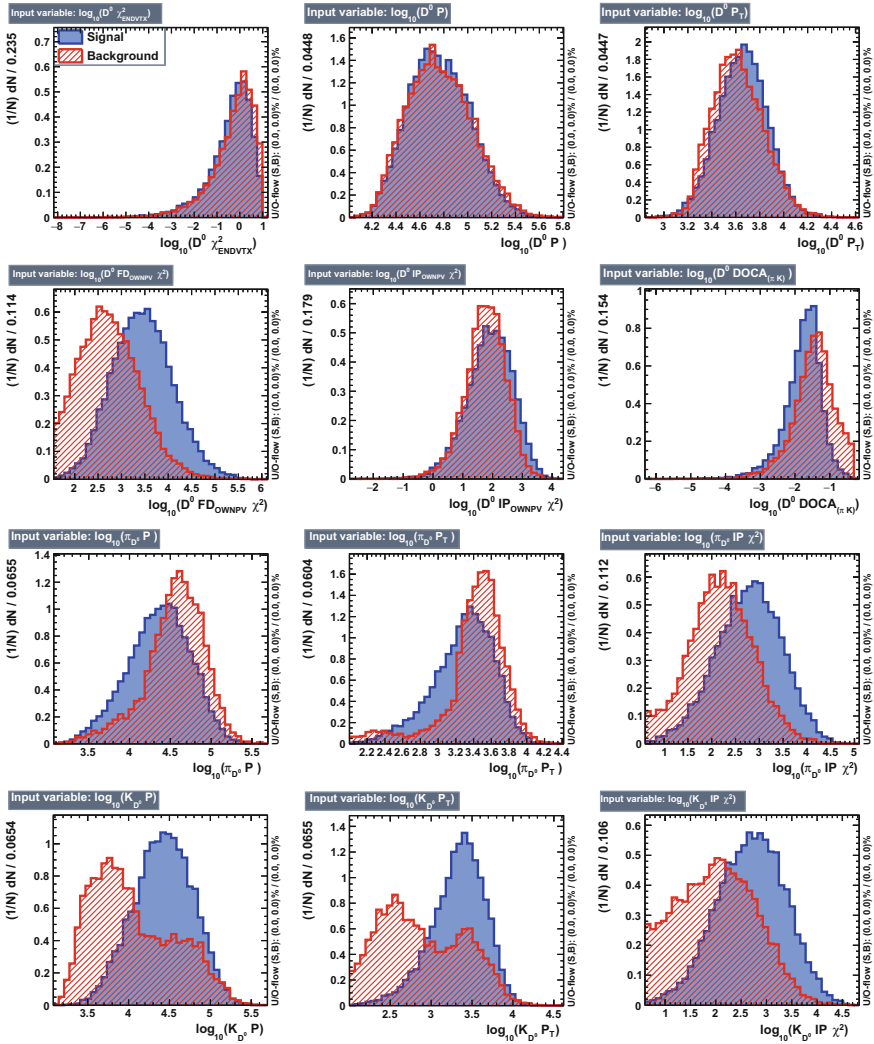
Fig. 6.11 Distribution of input variables used for the first stage BDT (D_{fromB}^{V2}) (grad). In red the input variables distribution in the background sample and in blue the same distribution for the signal sample used in the training

According to the final selection (see Sect. 6.3.10), the list of input variables used for the training in the signal sample and background sample are shown in Figs. 6.10 and 6.11.

The various BDTs performances are evaluated on the testing sample. Figure 6.14 shows the background rejection on the background sample against the signal efficiencies evaluated on the signal sample. The background rejection is defined as $1 - \varepsilon_{bkg}$, where ε_{bkg} is the ratio between the number of background events (in the
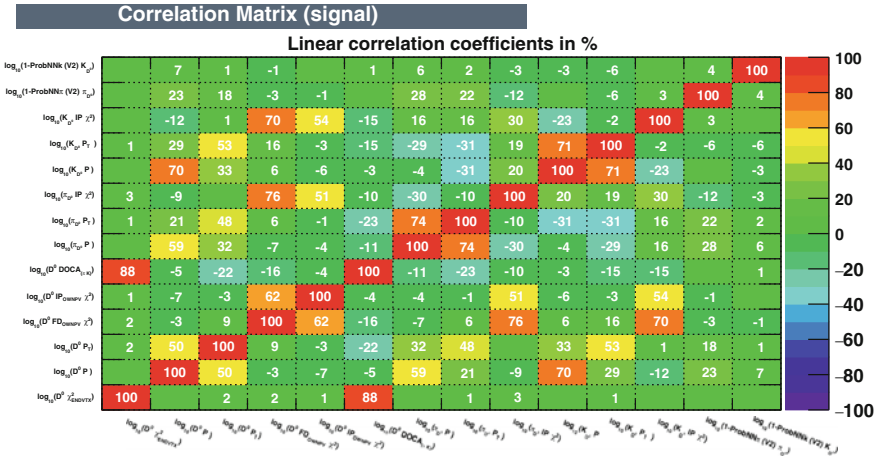
Fig. 6.12 Linear correlation of input variables in the signal sample for the first stage D^{V2}_{fromB} (grad) BDT
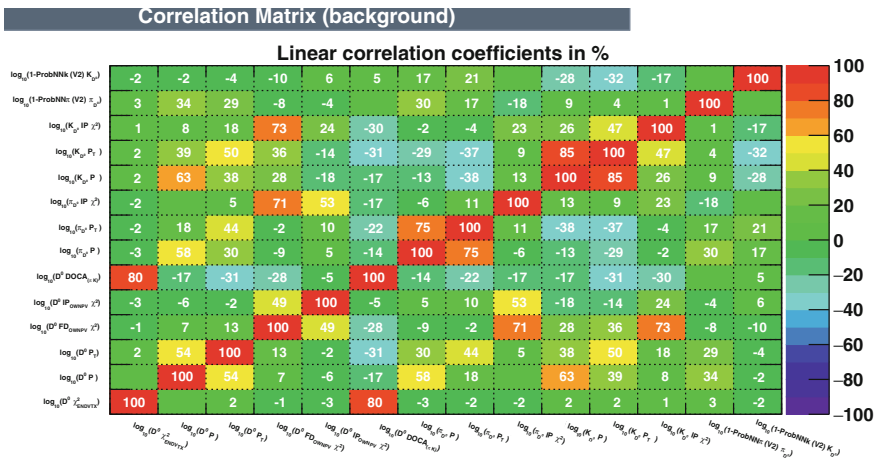

Fig. 6.13 Linear correlation of input variables in the signal sample for the first stage D^{V2}_{fromB} (adaptative boosting) BDT

background sample) after the BDT cut and the number of background events without any cut applied. The larger is the area underneath the curve, called Receiving Operator Curve (ROC curve), the better the performance. From Fig. 6.14 it is indeed hard to tell if the $V2$ performs better than $V3$ or the $NOPID$ when combined to rectangular cuts on the $ProbNN$ variables of the K_{D^0} and π_{D^0}. Thus, we keep all the cases as well as the versions trained with Gradient boosting and with Adaptive boosting (Figs. 6.12 and 6.13).

The BDTs classifier output is evaluated on the data and Monte Carlo samples looking at the $\overline{D}^0$, leading to the corresponding $\overline{D}^0 D_{fromB}$ output classifier variable.

Table 6.7 Input variables used for the second stage BDT training

Particle	Input variable
B^0	$IP\chi^2_{OWNPV}$
	p
	$DTF\chi^2/ndof$
	p_T
	$FD\chi^2_{OWNPV}$
	$DOCAMAX$
	$log_{10}(1 - |DIRA_{OWNPV}|) \cdot sign(DIRA_{OWNPV})$
$D^0 \& \overline{D}^0$	$D^{V2/V3/NOPID}_{fromB}$
	$FD\chi^2_{ORIVX}$
	$log_{10}(1 - |DIRA_{ORIVX}|) \cdot sign(DIRA_{ORIVX})$
K^{*0}	$K_{K^{*0}} ProbNNk$(V2 / V3 / none)
	$DOCA_{K\pi}$
	$\pi_{K^{*0}} ProbNN\pi$ (V2 / V3 / none)
Final classifier	$First_{V2,V3,NOPID} - Second_{V2,V3,NOPID}$(grad-grad/ada-ada)

6.3.8.2 Second Stage BDT: B^0 Selection

The outcome of the first stage BDT is used to train a second BDT. The second BDT aims at finding the B^0 candidates and the list of variables used for the training is listed in Table 6.7. The signal sample used for training is the $B^0 \to D^0\overline{D}^0 K^{*0}$ Monte Carlo signal sample with pre-selection applied. The background sample is taken from real data after pre-selections selecting events for which $m(B^0) - m_{PDG}(B^0) > 200$ MeV/c^2. All the pre-selections are applied for the background sample including the $|m(\overline{D}^0\pi^-) - m(\overline{D}^0)|$ cut aiming at selecting $B^0 \to D^0\overline{D}^0 K^{*0}$ (Sect. 6.3.2). No selections are applied for the background sample on both D invariant masses. The background training sample is shown in Fig. 6.15.

The input variables used in the training of the second BDT are an admixture of kinematic and topological variables. The variables have been selected in such a way that the BDT is independent as much as possible from $m(K^{*0})$. Indeed, no kinematic variables for the $\pi_{K^{*0}}$, $K_{K^{*0}}$ and K^{*0} have been used.

The variables in Table 6.7 represents the following:

- B^0 $IP\chi^2_{OWNPV}$, is the impact parameter χ^2 of the reconstructed B^0 candidate with respect to the primary vertex.
- B^0 $DTF\chi^2/ndof$ is the χ^2 per degrees of freedom of the Decay Tree refit applying only the constraint on the K^{*0} vertex.
- B^0 $FD\chi^2_{OWNPV}$ is the flight distance significance of the reconstructed B^0 with respect to the primary vertex.
- B^0 $DOCAMAX$ is the maximal distance of closest approach between the three particles D^0, $\overline{D}^0$ and K^{*0}. For example, if $doca_{D^0\overline{D}^0} < doca_{D^0 K^{*0}} < doca_{\overline{D}^0 K^{*0}}$, $DOCAMAX$ corresponds to $doca_{\overline{D}^0 K^{*0}}$
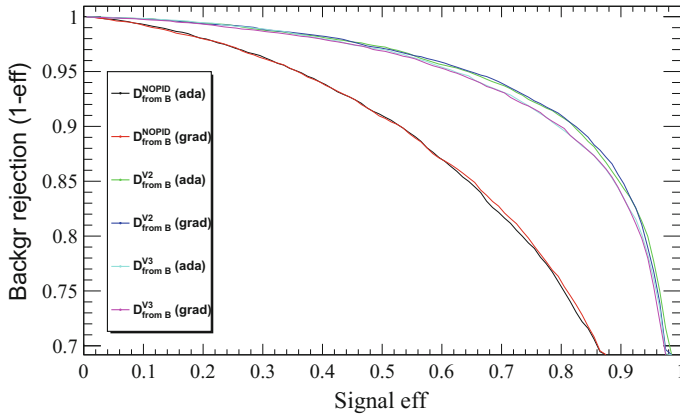
Fig. 6.14 Receiving Operator Curves for the various D_{fromB} trained BDTs. Plots obtained from the 7th fold trained BDT
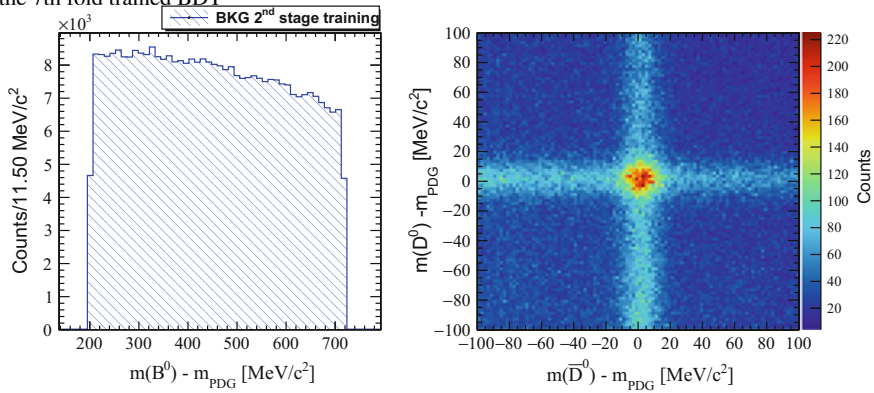

Fig. 6.15 Background selected events used for the second stage BDT training

- $B^0\ DIRA_{OWNPV}$ measures the cosine of the angle between the momentum of the particle and the direction vector define by the primary vertex and the B^0 decay vertex. The transformation of the variable to $log_{10}(1 - |DIRA_{OWNPV}|) \cdot sign(DIRA_{OWNPV})$ aims at smoothing the input variable and accounting for the sign of the $DIRA_{OWNPV}$.
- D^0 and $\overline{D}^0\ FD\chi^2_{ORIVX}$ is the flight distance significance of the D^0 and $\overline{D}^0$ with respect to the decay vertex of the B^0.
- $D^0(\overline{D}^0)\ |DIRA_{ORIVX}|$ is the cosine of the angle between the momentum of the reconstructed $D^0(\overline{D}^0)$ and the vector joining the B^0 decay position and the $D^0(\overline{D}^0)$ one.
- D^0 and $\overline{D}^0\ D_{fromB}^{V2/V3/NOPID}$ is the output classifier of the first stage BDT.
- A single *PID* variable per K^{*0} daughter is used, namely the $K_{K^{*0}}\ ProbNNk$ and $\pi_{K^{*0}}\ ProbNN\pi$. Also the case where no *PID* is included among the training variables has been tested.
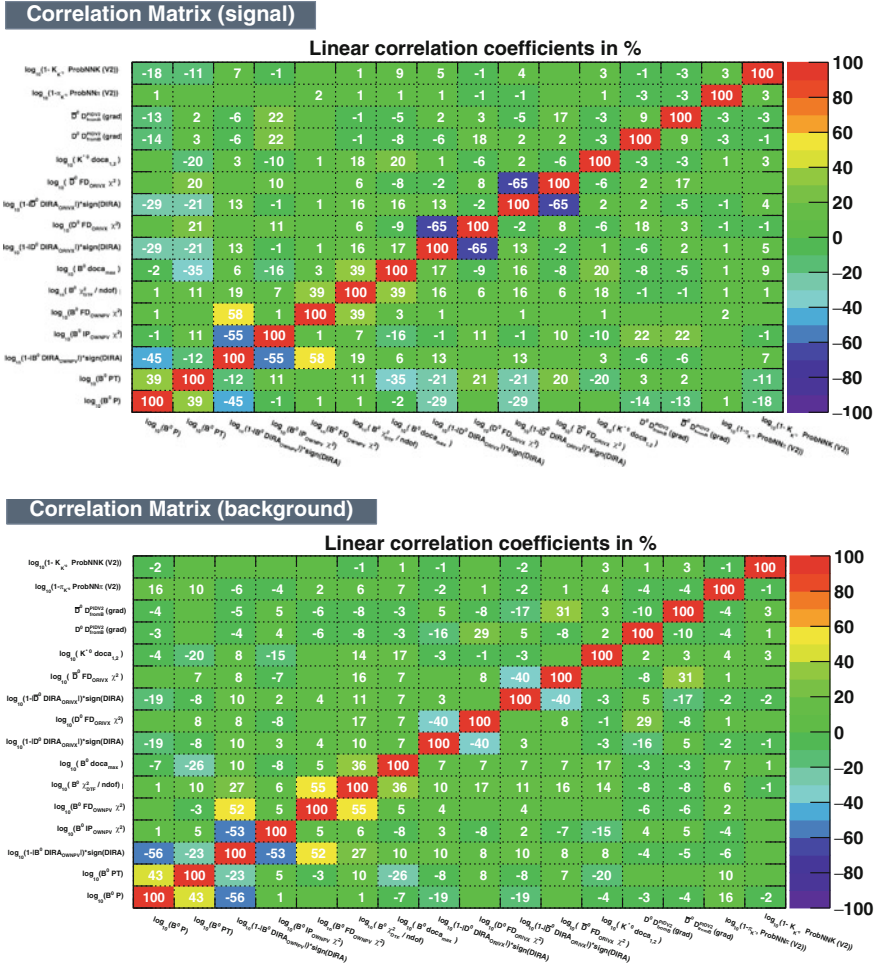
Fig. 6.16 (top) Linear correlation of input variables in the signal sample for the $First_{V2} - Second_{V2}$ (grad-grad) BDT. (bottom) Linear correlation of input variables in the background sample for the $First_{V2} - Second_{V2}$ (grad-grad) BDT

Eight different BDTs have been trained: the one including the $V3$ tuning of the $ProbNN$ variables, called $First_{V3} - Second_{V3}$, the one including the $V2$ tuning of the $ProbNN$, called $First_{V2} - Second_{V2}$ and the case without any K_{K*0} and π_{K*0} PID variables which is called $First_{NOPID} - Second_{NOPID}$ (Figs. 6.16 and 6.17).

The various configurations are obtained without mixing the various cases: if the first stage BDT was trained using π/K_{D^0} $ProbNN\pi/k$ (V2) as input variables and the gradient boosting, the second stage BDT uses $D^0/\overline{D}^0$ D_{fromB}^{V2} (ada) and π/K_{K*0} $ProbNN\pi/k$ (V2) as input variables and gradient boosting (Figs. 6.17, 6.18 and 6.19).
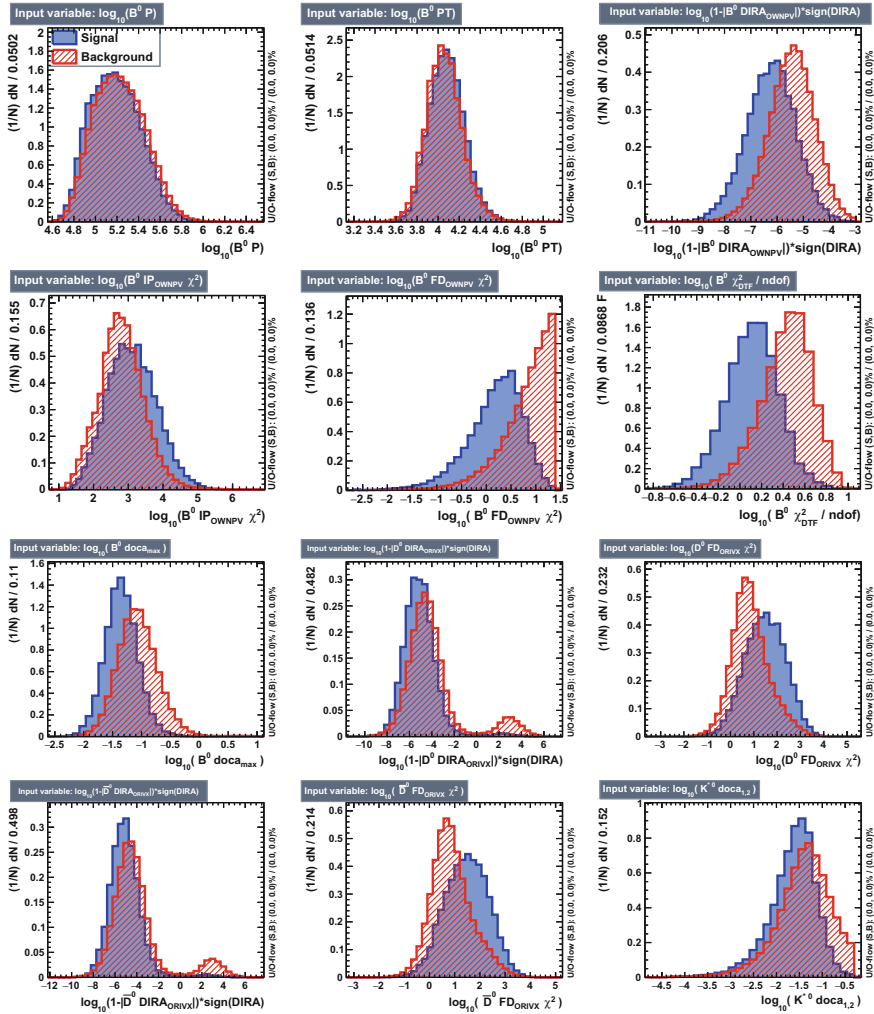
Fig. 6.17 Input variables distributions in signal (blue) and background (red) training samples for the $First_{V2} - Second_{V2}$ (grad-grad) BDT

6.3.9   Background From Single Charmless and Double Charmless Decays

The charmless background arises when the D meson candidates are not required to be well separated from the decay vertex of the B mesons. In $B^0 \to D^0 \overline{D}^0 K^{*0}$, single charmless background originates when only one D meson candidate is not flying a significant distance from the B decay position while double charmless originates when both D meson candidates are not flying a significant distance. In
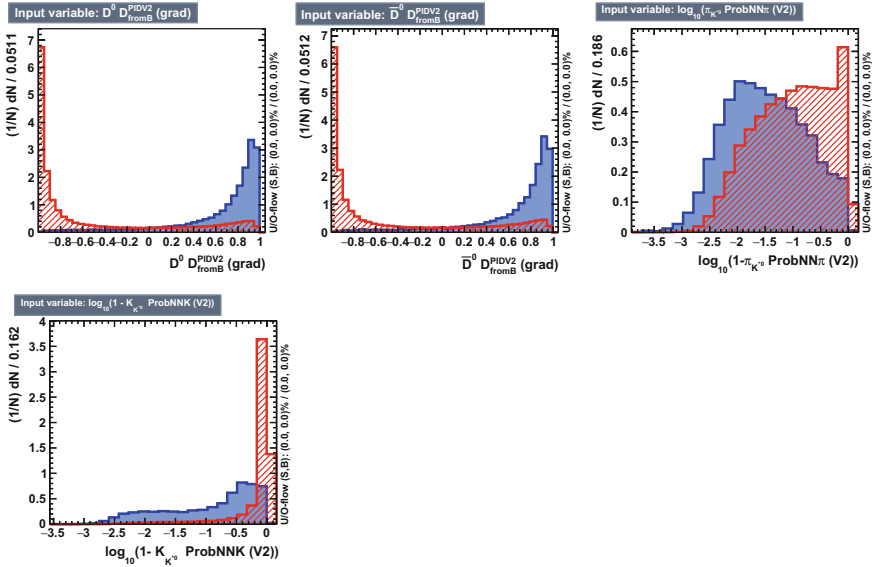
Fig. 6.18 Input variables distributions in signal (blue) and background (red) training samples for the $First_{V2} - Second_{V2}$ (grad-grad) BDT
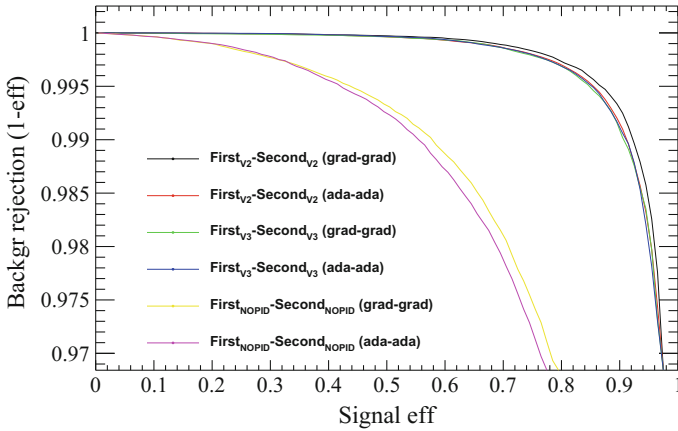

Fig. 6.19 Receiving Operator Curves for the various second stage $First_{XX} - Second_{XX}$ trained BDTs. Plots obtained from the 2nd fold trained BDT

$B^0 \to D^{*-}D^0K^+$, the contamination is expected to be mostly originating from the D mesons not used to reconstruct the D^{*-}. Indeed, $B^0 \to D^{*-}D^0K^+$ has a strong kinematic constraint for the $D^0\pi_{K^{*0}}$ system and it strongly suppresses the double charmless contamination. We can therefore describe such peaking background components as follows:

- Single charmless:

  1. In $B^0 \to D^0 \overline{D}^0 K^{*0}$, it is due to $B^0 \to D^0 \pi K \pi K$ decays where the $2K2\pi$ system can also arrange among themselves to form any strongly decaying resonant structure.
  2. In $B^0 \to D^{*-} D^0 K^+$, single charmless background is associated to $B^0 \to D^{*-} K \pi K$ decays, where the $2K\pi$ system can also arrange among themselves to form any strongly decaying resonant structure.

- Double charmless:

  1. In $B^0 \to D^0 \overline{D}^0 K^{*0}$, it is associated to $B^0 \to K\pi K\pi K\pi$ decays, where the $3K3\pi$ system can also arrange among themselves to form any strongly decaying resonant structure.
  2. In $B^0 \to D^{*-} D^0 K^+$, double charmless decay are strongly suppressed from the D^{*-} reconstruction requirement, thus at least one D^0 is well reconstructed.

In order to fight such kind of background, among the pre-selection cuts, we require for the D^0 and $\overline{D}^0$ that $\dfrac{\text{DecayLength}_{signed}}{\sigma_{\text{DecayLength}}} > 0$. The decay length is evaluated as the distance of the D^0 or $\overline{D}^0$ reconstructed decay vertex and the position where the $K_{K^{*0}}$ and $\pi_{K^{*0}}$ intersect each other, i.e. the decay vertex of the B^0.[4] The *signed* in DecayLength$_{signed}$ means that a plus (minus) sign is assigned if the D^0 (or $\overline{D}^0$) decays upstream (downstream) the decay vertex of the B^0.

The cut selection has been found looking at the B^0 candidates in different regions of $m(D^0)$ and $m(\overline{D}^0)$. We identified the following categories:

1. Double charmless: both D^0 and $\overline{D}^0$ are in the sidebands. The amount of charmless background is estimated counting the number of B^0 candidates when looking at the `!CrossBox` region (see the green region Fig. 6.20). The `!CrossBox` region is identified as follows:

   - $40\,\text{MeV/c}^2 < |m(D^0) - m_{PDG}(D^0)| < 100\,\text{MeV/c}^2$ and $40\,\text{MeV/c}^2 < |m(\overline{D}^0) - m_{PDG}(D^0)| < 100\,\text{MeV/c}^2$, green region in Fig. 6.20.

2. Single charmless: only one between D^0 and $\overline{D}^0$ is in the sidebands:

   - $40\,\text{MeV/c}^2 < |m(D^0) - m_{PDG}(D^0)| < 100\,\text{MeV/c}^2$ or $40\,\text{MeV/c}^2 < |m(\overline{D}^0) - m_{PDG}(D^0)| < 100\,\text{MeV/c}^2$, blue region in Fig. 6.20.

3. Signal region: both D^0 and $\overline{D}^0$ are in signal region:

   - $|m(D^0) - m_{PDG}(D^0)| < 30\,\text{MeV/c}^2$ and $|m(\overline{D}^0) - m_{PDG}(D^0)| < 30\,\text{MeV/c}^2$, red in Fig. 6.20.

The number of B^0 candidates in the double charm region ($\mathcal{N}_{!CrossBox}$) is measured fitting for a Gaussian with a fixed width and fixed mean plus an exponential the corresponding invariant mass spectrum of B^0 candidates (bottom right green distribution

---

[4]The signed decay length of the D mesons is obtained after constraining the K^{*0} vertex in the DTF.
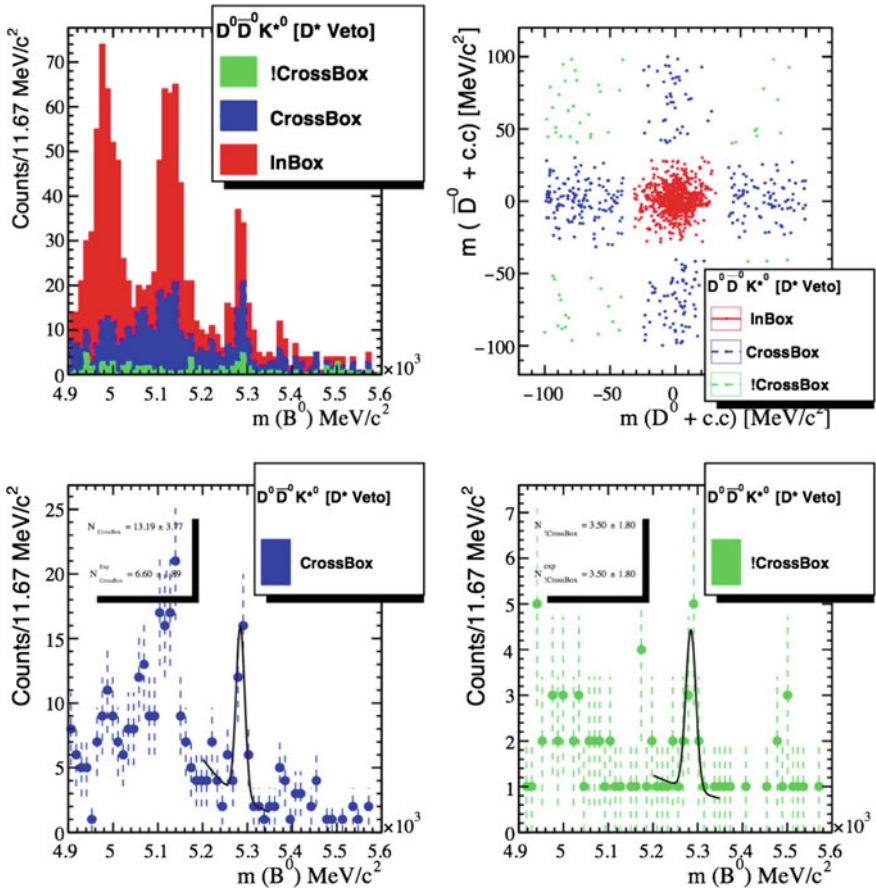
Fig. 6.20 In red, the signal region for the contamination from single and double charm studies. In blue the single charm region and the corresponding B^0 candidates (bottom left). In green the double charm region and the corresponding B^0 candidates (bottom right). In the top left plot the 2D plot of the D^0 and $\bar{D}^0$ showing the various regions definition. On the top right, the distributions of the various components

in Fig. 6.20). The number of B^0 candidates in the single charm region ($\mathcal{N}_{CrossBox}$) is measured fitting for a Gaussian fixed width and fixed mean plus an exponential the corresponding invariant mass spectrum of B^0 candidates (bottom left blue distribution in Fig. 6.20). The number of B^0 signal candidates in the signal region ($\mathcal{N}_{InBox}$) is measured counting the number of events in the signal region (30 MeV/c^2 window around both the D and B nominal invariant mass) corresponding to the red spot region in the top right plot in Fig. 6.20.

The optimization of the D^0 and $\bar{D}^0$ flight distance cut has been achieved estimating the contamination of single charmless and double charmless looking only at the upper sideband of the D^0 and $\bar{D}^0$ (upper right quadrant in the top right plot of Fig. 6.20).

The estimation is evaluated extrapolating the number of candidates expected in signal region from single ($N_{CrossBox}^{InBox}$) and double charmless ($N_{!CrossBox}^{InBox}$) regions using the ratio of the corresponding surfaces in the $m(D^0)$ versus $m(\overline{D}^0)$ plot covered by the various region $\mathscr{A}_{CrossBox}$ (single charmless), $\mathscr{A}_{!CrossBox}$ (double charmless) and $\mathscr{A}_{InBox}$ (signal).

For each selection cut on the flight distance we estimated the contamination as

$$\mathscr{N}_{backg}/(\mathscr{N}_{InBox} + \mathscr{N}_{backg}),$$

where

$$\mathscr{N}_{backg} = \mathscr{N}_{CrossBox}^{InBox} + \mathscr{N}_{!CrossBox}^{InBox},$$

with

$$\mathscr{N}_{CrossBox}^{Signal} = \left(\mathscr{N}_{CrossBox} - N_{!CrossBox} \cdot \frac{\mathscr{A}_{CrossBox}}{\mathscr{A}_{!CrossBox}} \right) \times \frac{\mathscr{A}_{InBox}}{\mathscr{A}_{CrossBox}}$$

and

$$\mathscr{N}_{!CrossBox}^{Signal} = \mathscr{N}_{!CrossBox} \times \frac{\mathscr{A}_{InBox}}{\mathscr{A}_{!CrossBox}}$$

The situation is shown in Fig. 6.20 when looking to all the sidebands. For this study, only the upper sidebands ($m(D) - m_{PDG}(D) > 40\,\text{MeV/c}^2$ for `CrossBox` and `!CrossBox`) have been used.

The cut value for the flight distance signed significance on the D^0 and $\overline{D}^0$ has been obtained performing a 2D scan on the flight distance signed significance. The first cut value is applied to both D^0 and $\overline{D}^0$. The second cut value is applied to the D meson having the larger signed flight distance significance. The contamination and selection efficiencies of the scan are shown in Fig. 6.21 using the $B^0 \to D^0 \overline{D}^0 K^{*0}$ Monte Carlo sample and a first iteration of the BDT selection. A good compromise between contamination (2%) and signal efficiencies (80%) is achieved requiring for both D to have a signed flight distance significance greater than 0. After this study, the cut has been added to the pre-selection cut.

The final contamination from charmless background after the full selection chain (pre-selections with the flight distance cut included, BDT selection and trigger selection) has been evaluated. The expected number of single and double charmless B^0 candidates has been evaluated looking at the whole D sideband regions and the same approach described in this section has been applied. The expected number of single and double charmless background has been estimated to be zero in $B^0 \to D^{*-} D^0 K^+$ as it can be observed in Fig. 6.22. From the fit shown in Fig. 6.22:

- $\mathscr{N}_{CrossBox} = 14.3 \pm 4.4$.
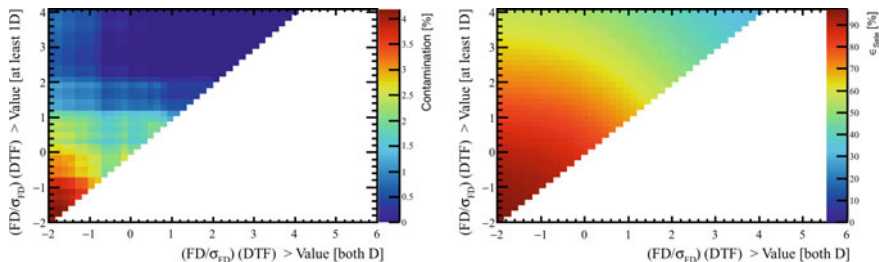- $\mathscr{N}_{!CrossBox} = 3.5 \pm 1.9$.

Fig. 6.21 On the left, the contamination in % of single and double charm as a function of the signed flight distance significance (after constraining the K^{*0} vertex) and the maximum value among the two D of the signed flight distance significance. On the right the selection efficiencies as a function of the flight distance signed significance (after constraining the K^{*0} vertex) and the maximum value among the two D of the signed flight distance significance

Therefore, the $\mathcal{N}_{CrossBox}^{Signal} = 2 \pm 1$, and $\mathcal{N}_{!CrossBox}^{Signal} = 0.9 \pm 0.5$. For this evaluation, the $\mathscr{A}_{InBox}$ is provided by the final invariant mass selection for D^0 and $\overline{D}^0$ (i.e. 30 MeV/c^2 window around the nominal PDG value), while the $\mathscr{A}_{CrossBox}$ and $\mathscr{A}_{!CrossBox}$ is considering both the D sidebands (cut optimization done only with the upper one).

6.3.10 BDT Optimisation

The various BDTs have been optimised separately for both $B^0 \to D^{*-} D^0 K^+$ and $B^0 \to D^0 \overline{D}^0 K^{*0}$ making scans of cut value on the classifier output. The optimisation is performed evaluating the expected number of signal events $\mathcal{N}_s$ and measuring in data the number of background events. The figure of merit that has been optimised is the significance defined as:

$$\mathscr{S} = \frac{\mathcal{N}_S}{\sqrt{\mathcal{N}_B + \mathcal{N}_S}}. \tag{6.3}$$

The expected number of signal events in $B^0 \to D^0 \overline{D}^0 K^{*0}$ is obtained using the following formula:

$$\mathcal{N}_S^{expected}(B^0 \to D^0 \overline{D}^0 K^{*0}) = \int \mathscr{L} \times \sigma_{b\bar{b}} \times 2 \times f_d$$

$$\times \varepsilon_{Acceptance} \times \varepsilon_{Stripping|Acceptance} \times \varepsilon_{Preliminary|Stripping} \times \varepsilon_{BDT|Preliminary} \tag{6.4}$$

$$\times \mathscr{B}(B^0 \to D^0 \overline{D}^0 K^{*0}) \times \mathscr{B}(D^0 \to K^- \pi^+)^2 \times \mathscr{B}(K^{*0} \to K\pi)$$
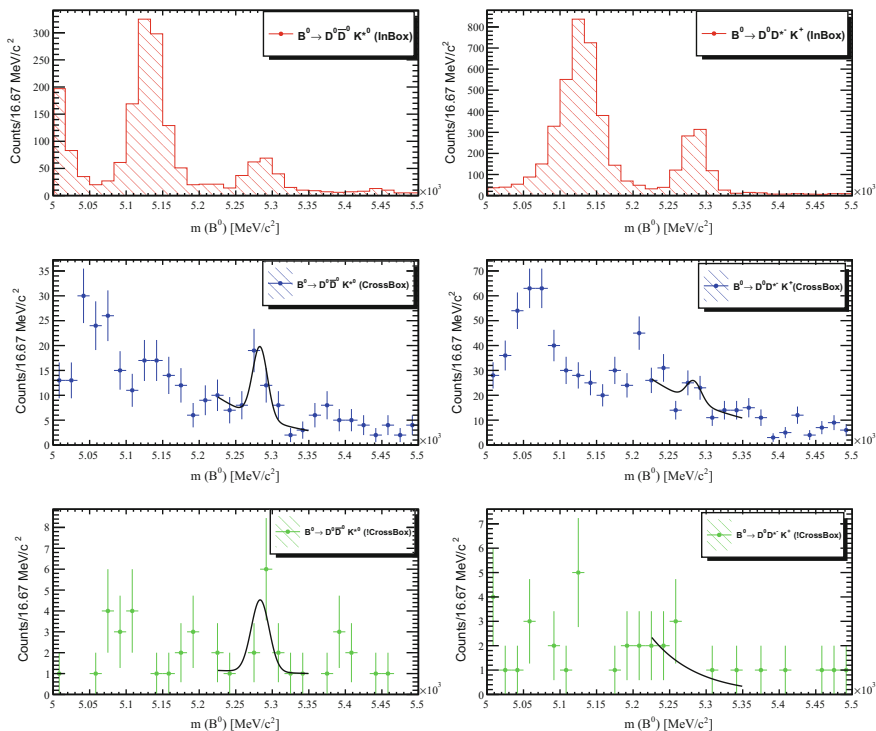
Fig. 6.22 On the left (right) column the invariant mass distribution of the B^0 candidates in $B^0 \rightarrow D^0 \overline{D}^0 K^{*0}$ ($B^0 \rightarrow D^{*-} D^0 K^+$) after all selections (stripping, pre-selection, BDT and trigger requirements. On the first row (red distributions) the B^0 candidates are obtained looking at $|m(D^0) - m_{PDG}(D^0)| < 30 \, \text{MeV/c}^2$ and $|m(\overline{D}^0) - m_{PDG}(\overline{D}^0)| < 30 \, \text{MeV/c}^2$. On the second row (blue distributions), the B^0 candidates are obtained when looking at the single charmless background, i.e. one D meson in the signal region (40 MeV/c^2 window around the D^0 PDG mass is used for this) and the other one in the sidebands $|m(D^0) - m_{PDG}(D^0)| > 40 \, \text{MeV/c}^2$. On the third row (green distribution), the B^0 candidates are obtained when looking to double charmless background, i.e. both the D mesons candidates reconstructed invariant mass is in the sidebands $|m(D^0 \& \overline{D}^0) - m_{PDG}(D^0)| > 40 \, \text{MeV/c}^2$. The fitted values of peaking B^0 candidates in the single and double charmless case has been used to estimate the contamination of charmless background

The expected number of signal events in $B^0 \rightarrow D^{*-} D^0 K^+$ is obtained using the following formula:

$$\mathcal{N}_S^{expected}(B^0 \rightarrow D^{*-} D^0 K^+) = \int \mathcal{L} \times \sigma_{b\bar{b}} \times 2 \times f_d$$

$$\times \varepsilon_{Acceptance} \times \varepsilon_{Stripping|Acceptance} \times \varepsilon_{Preliminary|Stripping} \times \varepsilon_{BDT|Preliminary} \quad (6.5)$$

$$\times \mathcal{B}(B^0 \rightarrow D^{*-} D^0 K^+) \times \mathcal{B}(D^0 \rightarrow K^- \pi^+)^2 \times \mathcal{B}(D^{*-} \rightarrow \overline{D}^0 \pi^-)$$

Table 6.8 Summary of the parameters used for the second stage BDT cut optimization

Parameter	$B^0 \to D^{*-}D^0K^+$	Value $B^0 \to D^0\overline{D}^0K^{*0}$
$\int \mathcal{L}$	3000 pb^{-1}	3000 pb^{-1}
$\sigma_{b\bar{b}}$	284 µb	284 µb
$\varepsilon_{Acceptance}$	14.91%	14.74%
$\varepsilon_{Stripping\vert Acceptance}$	0.615%	1.025%
$\varepsilon_{Preliminary\vert Stripping}$	76.60%	78.08%
$\mathcal{B.R.}(DDh)$	$2.47 \cdot 10^{-3}$(measured)	$2.4 \cdot 10^{-4}$ (expected)
$\mathcal{B.R.}(D^0 \to K\pi)$	3.93%	3.93%
$\mathcal{B.R.}(D^{*-} \to D^0\pi^-)$	67.7%	–
$\mathcal{B.R.}(K^{*0} \to K^+\pi^-)$	–	66.6%

The parameters used in (6.4) and (6.5) and summarised in Table 6.8 are:

- $\int \mathcal{L} = 3000$ pb^{-1} is the integrated luminosity in Run I LHCb data.
- $\sigma_{pp\to b\bar{b}X} = (284 \pm 20 \pm 49)$ µb is the cross section production of $b\bar{b}$ in proton proton collisions at $\sqrt{s} =$ 7 TeV [15].
- $f_d = 40\%$ is the hadronization probability of a b quark into a B^0. The factor two is used since we are considering both cases B^0 and $\overline{B}^0$.
- $\varepsilon_{Acceptance}$ is the geometrical efficiency of the decay defined as the probability to observe the whole decay chain inside the LHCb acceptance. This value is evaluated from generator level simulation.
- $\varepsilon_{Stripping\vert Acceptance}$ is the selection efficiency from the stripping selections given the decay products being in the geometrical acceptance. This value is evaluated from Monte Carlo simulation.
- $\varepsilon_{Preliminary\vert Stripping}$ is the pre-selection efficiency evaluated with respect the events passing the stripping selections. This value is evaluated from Monte Carlo simulation.
- $\varepsilon_{BDT\vert Preliminary}$ is the efficiency of a given cut on the BDT classifier response. A 1D scan on the BDT value is performed in the cases where the *PID* variables are used for the training. For the cases where no *PID* information are used within the BDT training, a multi dimensional cut is applied. In more detail, for the case $First_{NOPID} - Second_{NOPID}$ BDT a five dimensional optimization is performed scanning through the BDT classifier response simultaneously to the $K_{D^0/\overline{D}^0}$ $ProbNNk$ (V2 or V3) and $\pi_{D^0/\overline{D}^0}$ $ProbNN\pi$ (V2 or V3) as well as the $\pi_{K^{*0}}$ $ProbNN\pi$ and the $K_{K^{*0}}$ $ProbNNk$.
- $\mathcal{B}(B^0 \to D^0\overline{D}^0K^{*0}) \sim 2.4 \cdot 10^{-4}$ is estimated. The value is estimated using the following relation:

$$\frac{\mathcal{B}(B^0 \to D^0\overline{D}^0K^{*0})}{\mathcal{B}(B^0 \to D^0\overline{D}^0K^0)} = \frac{\mathcal{B}(B^0 \to D^0K^{*0})}{\mathcal{B}(B^0 \to D^0K^0)}, \tag{6.6}$$

where $\mathscr{B}(B^0 \to \overline{D}^0 D^0 K^0)$ is measured to be $(0.27 \pm 0.10) \times 10^{-3}$, $\mathscr{B}(B^0 \to D^0 K^0)$ is measured to be $(5.2 \pm 0.7) \times 10^{-5}$ and $\mathscr{B}(B^0 \to D^0 K^{*0})$ is measured to be $(4.5 \pm 0.6) \times 10^{-5}$.

- $\mathscr{B}(D^0 \to K^- \pi^+)$ is known and its value is $(3.93 \pm 0.03) \times 10^{-2}$.
- $\mathscr{B}(D^{*-} \to \overline{D}^0 \pi^-)$ is measured to be 0.677 ± 0.005 and also $\mathscr{B}(K^{*0} \to K^+ \pi^-) = 2/3$.

The number of background events ($\mathscr{N}_B$) is evaluated fitting for a line ($a + b \cdot m(B^0)$) the invariant mass spectrum of the B^0 (with DTF and $D^0/\overline{D}^0$ mass constraints applied) in the $m(B^0) \in [5380, 5800]$ MeV/c^2 region. The parameters from the line fit are used to estimate $\mathscr{N}_B$ integrating the line fit into the B^0 mass signal region $(m_{PDG}(B^0) \pm 50$ MeV/c$^2)$ as follows:

$$\mathscr{N}_B = \int_{m_{PDG}(B^0) - 50\,\text{MeV/c}^2}^{m_{PDG}(B^0) + 50\,\text{MeV/c}^2} (a + b \cdot m)dm \tag{6.7}$$

A scan through the BDT cut value is performed computing at each iteration the efficiency $\varepsilon_{BDT|Preliminary}$, the expected purity $\frac{S}{B} = \frac{\mathscr{N}_S}{\mathscr{N}_B}$ and significance $\mathscr{S} = \frac{\mathscr{N}_s}{\sqrt{\mathscr{N}_s + \mathscr{N}_b}}$. The performances of the various BDT are quite similar: the one allowing for a good compromise between purity and significance has been chosen for both $B^0 \to D^0 \overline{D}^0 K^{*0}$ and $B^0 \to D^{*-} D^0 K^+$. The results of the BDT optimization is shown in Table 6.9. The optimization strategy in $B^0 \to D^0 \overline{D}^0 K^{*0}$ ($B^0 \to D^{*-} D^0 K^+$) for the selected BDT ($First_{V2} - Second_{V2}$ (grad-grad)) is shown in Fig. 6.23 (Fig. 6.24).

6.3.11 Trigger Selection and Trigger Requirements

The data selected from the BDT undergo a further selection, the trigger selection. Trigger requirements are applied in this case to model the efficiencies in a proper way. Indeed, events for which the candidates are found because the trigger selection is applied on other particles which do not belong to the signal candidate need a special treatment in terms of efficiencies evaluation. The trigger selections for the $B^0 \to D^0 \overline{D}^0 K^{*0}$ and $B^0 \to D^{*-} D^0 K^+$ are summarised in Table 6.10. The composition in $B^0 \to D^0 \overline{D}^0 K^{*0}$ and $B^0 \to D^{*-} D^0 K^+$ in terms of trigger categories is shown in Fig. 6.25.

The selected dataset is divided in different categories named as follows:

1. L0Hadron_TIS (L0h_{TIS}): the hardware level trigger for hadron selection is fired by particles which are not present in the decay chain of the reconstructed $B^0 \to D^0 \overline{D}^0 K^{*0}$ or $B^0 \to D^{*-} D^0 K^+$.
2. L0Hadron_TOS (L0h_{TOS}): the hardware level trigger for hadron selection is fired by particles which are present in the decay chain of the reconstructed $B^0 \to D^0 \overline{D}^0 K^{*0}$ or $B^0 \to D^{*-} D^0 K^+$.

Table 6.9 Summary of the BDT performances optimization for the various trained BDT. In bold font the BDT selected for the analysis. The optimization is performed separately for $B^0 \to D^0 \overline{D}^0 K^{*0}$ and $B^0 \to D^{*-} D^0 K^+$ and the optimal cut value of the BDT is found maximising the significance $\mathscr{S}$ figure of merit. Concerning the First$_{NOPID}$-Second$_{NOPID}$, the BDT performance optimization has not been performed in $B^0 \to D^{*-} D^0 K^+$ since the corresponding maximal significance achievable in $B^0 \to D^0 \overline{D}^0 K^{*0}$ is sensibly smaller than the other cases

BDT type	Mode	Max $\mathscr{S}$	$\varepsilon_{BDT\|Preliminary}$ (%)	$\frac{S}{B}$
First$_{V2}$-Second$_{V2}$ (ada)	$B^0 \to D^0 \overline{D}^0 K^{*0}$	9.41	61.7	2.42
	$B^0 \to D^{*-} D^0 K^+$	33.99	95.31	23.65
First$_{V2}$-Second$_{V2}$ (grad)	$B^0 \to D^0 \overline{D}^0 K^{*0}$	**9.05**	**55.6**	**2.64**
	$B^0 \to D^{*-} D^0 K^+$	**33.95**	**94.4**	**29.3**
First$_{V3}$-Second$_{V3}$ (ada)	$B^0 \to D^0 \overline{D}^0 K^{*0}$	9.23	61.3	2.17
	$B^0 \to D^{*-} D^0 K^+$	33.93	96.2	18.0
First$_{V3}$-Second$_{V3}$ (ada)	$B^0 \to D^0 \overline{D}^0 K^{*0}$	8.93	61.1	1.80
	$B^0 \to D^{*-} D^0 K^+$	33.88	94.03	29.0
First$_{NOPID}$-Second$_{NOPID}$ (ada)	$B^0 \to D^0 \overline{D}^0 K^{*0}$	6.72	28.83	2.51
	$B^0 \to D^{*-} D^0 K^+$	–	–	–
First$_{NOPID}$-Second$_{NOPID}$ (grad)	$B^0 \to D^0 \overline{D}^0 K^{*0}$	7.14	69.54	0.52
	$B^0 \to D^{*-} D^0 K^+$	–	–	–

3. `L0Muon_TIS` ($L0\mu_{TIS}$): the hardware level trigger for $\mu^{\pm}$ selection is fired by particles which are not present in the decay chain of the reconstructed $B^0 \to D^0 \overline{D}^0 K^{*0}$ or $B^0 \to D^{*-} D^0 K^+$.

4. `L0` : we define this category as the logical or between $L0h_{TIS}$, $L0h_{TOS}$ and $L0\mu_{TIS}$.

5. `HLT1`: `Hlt1TrackAllL0Decision_TOS`: the first software level trigger selection named `Hlt1TrackAllL0Decision` is passed by at least one particle present in the decay chain of the reconstructed $B^0 \to D^0 \overline{D}^0 K^{*0}$ or $B^0 \to D^{*-} D^0 K^+$.

6. `HLT2`: the reconstructed B^0 candidate (in $B^0 \to D^0 \overline{D}^0 K^{*0}$ or $B^0 \to D^{*-} D^0 K^+$) decay chain products passes the Bonsai Boosted Decision Tree cut defined for the topological lines. Namely the `HLT2` trigger requirements is the or between the three topological triggers: `Hlt2Topo2BodyBBDT_TOS` or `Hlt2Topo3 BodyBBDT_TOS` or `Hlt2Topo4BodyBDDT_TOS`.

7. `TRIG` Category: ($L0h_{TIS}$ or $L0h_{TOS}$ or $L0\mu_{TIS}$) & `HLT1` & `HLT2`.

8. `CAT1` Category: this category is given by `HLT1` trigger and `HLT2` trigger and $L0h_{TOS}$. This category is the one which is well modelled in simulation, since all decisions are taken based on the information of the decay products of the $B^0 \to D^0 \overline{D}^0 K^{*0}$ and $B^0 \to D^{*-} D^0 K^+$ decay.

9. `CAT2` Category: this category is given by exclusive `L0Hadron_TIS` candidates. The logical condition applied for this category is defined as `CAT2` = `HLT1` & `HLT2` & (!$L0h\_TOS$ & $L0h_{TIS}$).
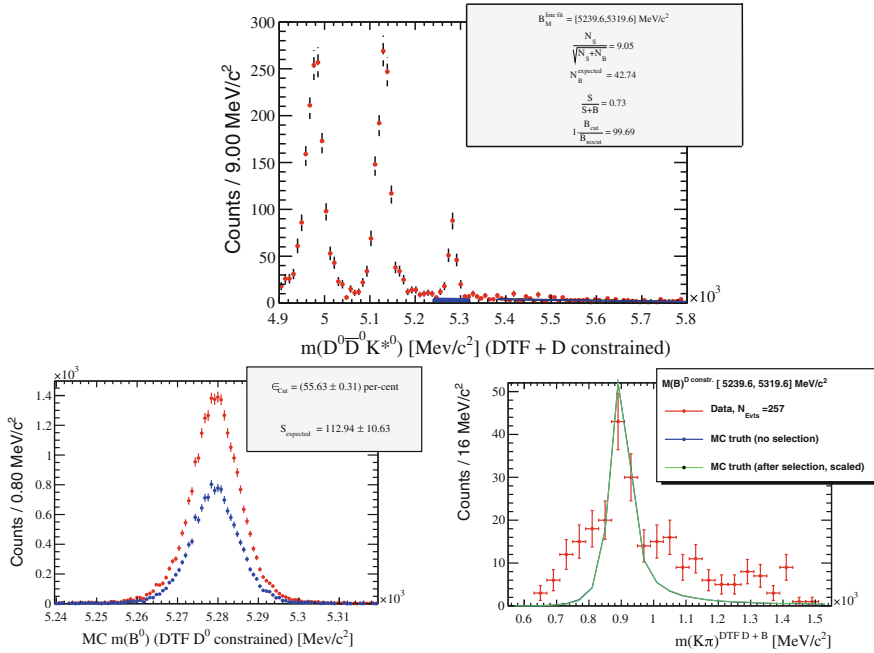
Fig. 6.23 Optimisation strategy for $B^0 \rightarrow D^0\overline{D}^0 K^{*0}$ ($First_{V2} - Second_{V2}$ (grad-grad) case). A cut is applied to the BDT classifier, $\mathcal{N}_B$ is evaluated fitting the $m(B^0)$ invariant mass (top plot) with a straight line in the upper sideband and integrating the projection of the line into the $m(B^0)$ range corresponding to $m_{PDG} \pm 50$ MeV/c^2. From MC, the efficiency $\varepsilon_{BDT|Preliminary}$ is computed (bottom left plot, where the blue distribution is after the BDT cut and in red before the cut). On the bottom right, the comparison between the $m(K^{*0})$ in the $B^0 \rightarrow D^0\overline{D}^0 K^{*0}$ data selected in the B^0 mass range of $m_{PDG}(B^0) \pm 40$ MeV/c^2 (red) and the Monte Carlo distribution of the K^{*0} before the BDT cut (blue) and after (green). The blue and green distributions overlap each other, pointing towards the fact that the BDT selection efficiency is not dependent on the $m(K_{K^{*0}}\pi_{K^{*0}})$ value

10. CAT3 Category: this category is given by exclusive $L0\mu_{TIS}$ candidates. The logical condition applied for this category is defined as CAT3 = HLT1 & HLT2 & ($L0h_{TOS}$ & !$L0h_{TIS}$ & $L0\mu_{TIS}$.

6.3.11.1 `Hlt1TrackAllL0Decision` Trigger Decisions

The HLT1 decision lines used in this analysis rely on the properties of single tracks and not on the information of the complete event. The Hlt1TrackAllL0Decision requires for a track the following:

- The track has to be composed of at least 9 VELO hits used in track reconstruction ensuring that it is build with a sufficient number of VELO hits.
- The number of OT (n_{OT}) and IT (n_{IT}) hits on the track is required to be $n_{OT} + 2 \times n_{IT} > 16$.
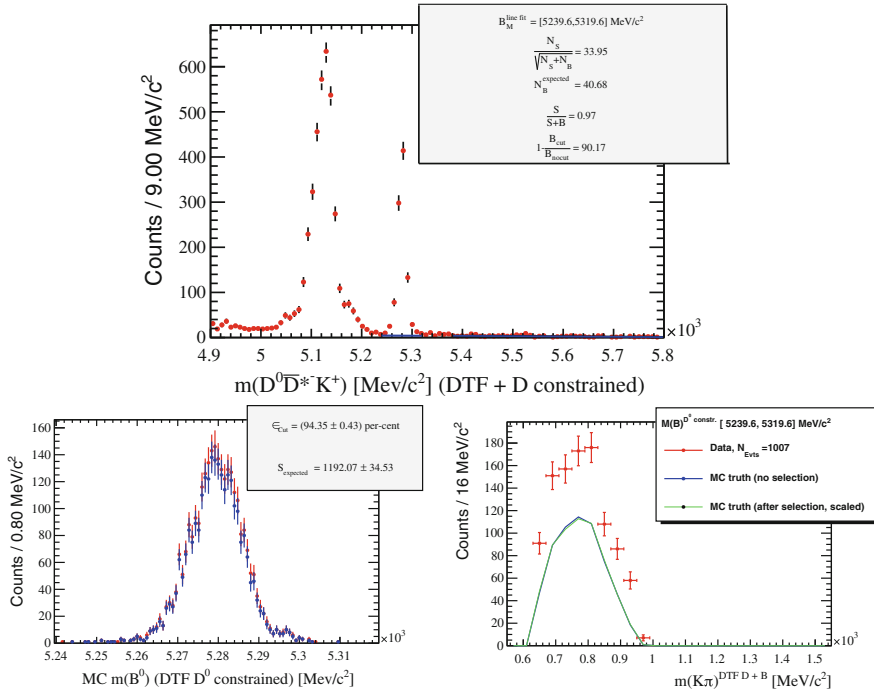
Fig. 6.24 Optimisation strategy for $B^0 \to D^0 \overline{D}^0 K^{*0}$ ($First_{V2} - Second_{V2}$ (grad-grad) case). A cut is applied to the BDT classifier, $\mathcal{N}_B$ is evaluated fitting the $m(B^0)$ invariant mass (top plot) with a straight line in the data B^0 mass upper sideband and integrating the projection of the line into the $m(B^0)$ range corresponding to $m_{PDG} \pm 50\,\mathrm{MeV}/c^2$. From simulated $B^0 \to D^{*-} D^0 K^+$ decays, the efficiency $\varepsilon_{BDT|Preliminary}$ is computed (bottom left plot, the blue (red) distribution is the $m(B^0)$ after (before) the BDT cut). On the bottom right the comparison between the $m(K^{*0})$ in the $B^0 \to D^0 \overline{D}^0 K^{*0}$ data selected in the B^0 mass range of $m_{PDG}(B^0) \pm 40\,\mathrm{MeV}/c^2$ (red) and the Monte Carlo truth distribution of the K^{*0} invariant mass before the BDT cut (blue) and after (green). The blue and green distributions overlap each other, pointing towards the fact that the BDT selection efficiency is not dependent on the $m(K_{K^{*0}} \pi_{K^{*0}})$ value

- The impact parameter with respect to the primary vertex has to be $> 0.1\,\mathrm{mm}$ and $IP\chi^2_{PV} > 16$ ensuring that the track is well separated from the primary vertex.
- Different thresholds on p, p_T and $\chi^2/ndof$ for the track have been used during data taking and they are reproduced in the Monte Carlo simulation.

6.3.11.2 `HLT2TopoNBodyBBDT` Trigger Decisions

The HLT2 topological trigger decisions for two, three, four body decays are used to select the events. These trigger selections are inclusive trigger lines based on decisions from a Bonsai Boosted Decision Tree (BBDT) [16] which uses as input variables kinematic and topological variables to select inclusively $B \to N$ body decays, where N can be 2, 3 or 4.

Table 6.10 Trigger requirements for the event selection

Trigger Level	Requirement
L0	L0 Hadron TOS (L0h_{TOS})
	OR
	L0 Muon TIS (L0μ_{TIS})
	OR
	L0 Hadron TIS (L0h_{TIS})
HLT1	HLT1 Track TOS
HLT2	HLT2 Topological 2-body TOS
	OR
	HLT2 Topological 3-body TOS
	OR
	HLT2 Topological 4-body TOS

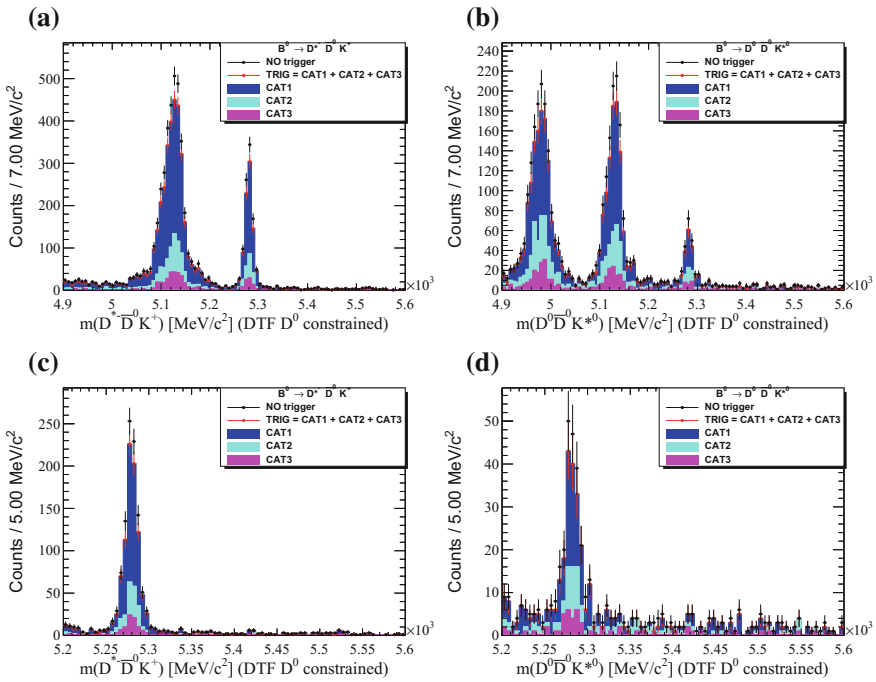**(a)**

(b)

(c)

(d)

Fig. 6.25 Invariant mass spectrum (with DTF and $D^0/\overline{D}^0$ mass constraint) of the B^0 candidate split by exclusive trigger categories of the selected $B^0 \to D^0\overline{D}^0 K^{*0}$ [figures (**b**) and (**d**)] and $B^0 \to D^{*-} D^0 K^+$ [figures (**a**) and (**c**)]. All the candidates after the BDT selection are shown in black. The TRIG category (in red) is the sum of the three exclusive trigger categories: CAT1 category (dark blue), CAT2 in cyan and CAT3 in purple

6.4 Mass Fit

In order to perform the mass fit we excluded the partially reconstructed components in the $m(D^0 \overline{D}^0 K^+ \pi^-)$ mass spectrum fitting for the signal yields in the following mass range: $5235\,\mathrm{MeV/c^2} < m(B^0)(DTF + D^0\mathrm{constrained}) < 5600\,\mathrm{MeV/c^2}$ as shown in Fig. 6.26.

The partially reconstructed components in $B^0 \to D^{*-}D^0K^+$ correspond to charged and neutral B candidates decaying into the same final states as $B^0 \to D^{*-}D^0K^+$ (D^0, D^{*-} and K^+) plus a missing particle. The missing particle can be either not being reconstructed at all or present in the event but not being used to reconstruct $B^0 \to D^0\overline{D}^0K^+\pi^-$. In $B^0 \to D^{*-}D^0K^+$, the higher branching ratio modes leading to a missing particle are the ones where one excited D meson is present in the decay chain decaying into D^0 plus γ or π^0 or π^+. The known decays com-
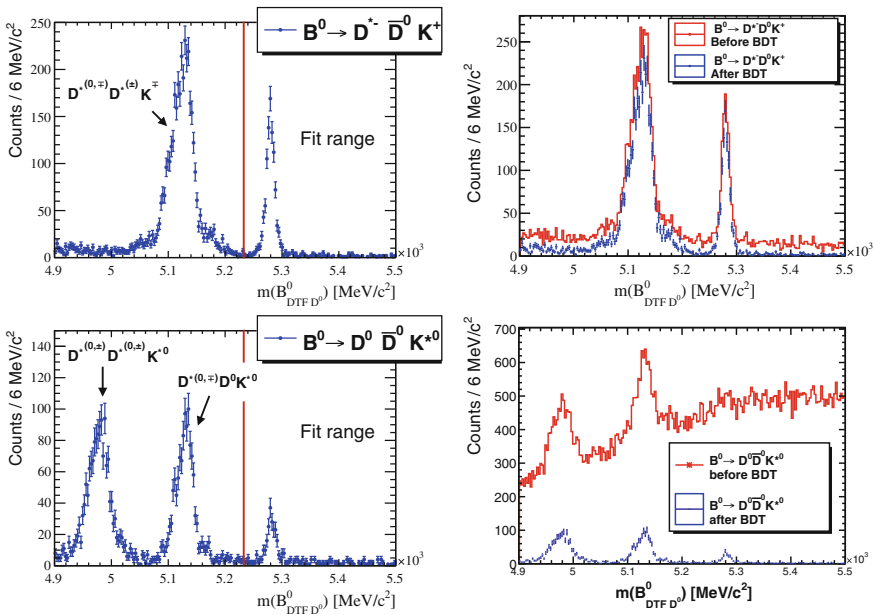

Fig. 6.26 On the top (bottom) row, the resulting invariant mass spectrum for the selected $B^0 \to D^{*-}D^0K^+$ ($B^0 \to D^0\overline{D}^0K^{*0}$) candidates. On the left column the details of the sources of partially reconstructed decay modes which are removed for the mass fit. On the right column the effect of the BDT cut showing the distribution before applying the BDT selection (red) and after (blue). It can be noted that in $B^0 \to D^0\overline{D}^0K^{*0}$ the BDT selection is able to find $B^0 \to D^0\overline{D}^0K^{*0}$ candidates which were not even visible before applying the cut (red). For $B^0 \to D^{*-}D^0K^+$, the BDT selection is very efficient since the D^{*-} invariant mass selection is able to strongly constrain the B^0 candidates

posing the partially reconstructed structure on the left-hand side of the B^0 nominal mass peak in $B^0 \to D^{*-}D^0 K^+$ (see Fig. 6.26) are:

- $B^0 \to D^{*-}K^+(D^{*0} \to D^0[\pi^0]_{miss})$.
- $B^0 \to D^{*-}K^+(D^{*0} \to D^0[\gamma]_{miss})$.
- $B^+ \to D^{*-}K^+(D^{*+} \to D^0[\pi^+]_{miss})$.

In principle also the $B \to DD^{**}K$ decay can contribute to the partially reconstructed peak, but with even lower mass and is expected to be broader.

Concerning the $B^0 \to D^0\overline{D}^0 K^{*0}$, the same arguments as in $B^0 \to D^{*-}D^0 K^+$ are valid, but also the two missing particles case is possible. Concerning the one missing particle case in $B^0 \to D^0\overline{D}^0 K^{*0}$, the first peak on the left-hand side of the nominal B^0 mass is given by $(B \to \overline{D}^* D^0 K\pi + B \to D^* \overline{D}^0 K\pi)$ where $D^* \to D^0[\pi^0, \pi^-, \gamma]_{miss}$. The two missing particle case is instead associated to B decays where two excited D mesons are present, i.e. $B \to \overline{D}^* D^* K^+ \pi^-$ and both slow particles from the decaying D^* and $\overline{D}^*$ are missed. Also in this case the $B \to D^{(*)}D^{**}K$ decay can contribute to the partially reconstructed peak (one π used to build the K^{*0} and one or two extra particles missed from the D^{**} decay), but with even lower mass and is expected to be broader.

The invariant B^0 mass spectrum fitted for in data is obtained applying the DTF and constraining the D^0 and $\overline{D}^0$ to their nominal mass and is called $m(B^0_{\text{DTF } D^0})$. Furthermore, since the partially reconstructed candidates and the signal candidates (lying around the nominal B^0 mass) are well separated, we decided to remove the partially reconstructed components from the fit selecting only the candidates having $m(B^0_{\text{DTF } D^0}) > 5235\,\text{MeV/c}^2$ and $m(B^0_{\text{DTF } D^0}) < 5600\,\text{MeV/c}^2$. Before performing the fit, multiple candidates (which are at a negligible level of $< 2\%$) in the fit range are removed randomly in both $B^0 \to D^0\overline{D}^0 K^{*0}$ and $B^0 \to D^{*-}D^0 K^+$. Multiple candidates are produced within the same event when a different combination of particles (producing the various intermediate state) are able to produce a B meson candidate and the corresponding decay chain is passing all the selections. For example, a multiple candidate can be produced in $B^0 \to D^0\overline{D}^0 K^{*0}$ when two different $\pi_{K^{*0}}$ can be used to produce a B candidate passing all the selections described so far. The model used for the fit is rather simple due to the high purity of samples achieved in both $B^0 \to D^0\overline{D}^0 K^{*0}$ and $B^0 \to D^{*-}D^0 K^+$ after selection: a double sided Crystal-Ball (DSCB) for the signal candidates and a simple line for the background ($c_0 + c_1 \cdot x$).

The double sided Crystal-Ball function is an extension of the single side Crystal-Ball (CB) function [17]. The function consists of a Gaussian core and a left-side and right-side power law to describe the tails of the distribution. The double sided Crystal-Ball function belongs to the $\mathscr{C}^1$ class (continuously differentiable function) with two free parameters for the Gaussian core ($\bar{x}$, σ_{core}), two free parameters for the left side power law (α_L and n_L) and two free parameters for the right side power law (α_R and n_R) defined as follows:

$$f(x; \alpha_L, \alpha_R, n_R, n_L, \bar{x}, \sigma_{core}) = \begin{cases} \left(\dfrac{n_L}{|\alpha_L|}\right)^{n_L} e^{-\frac{|\alpha_L|^2}{2}} \left(\dfrac{n_L}{|\alpha_L|} - |\alpha_L| - \dfrac{x - \bar{x}}{\sigma_{core}}\right)^{-n_L} & \text{for } \dfrac{x - \bar{x}}{\sigma_{core}} \leq -\alpha_L \\[2em] e^{-\frac{1}{2}\left(\frac{x - \bar{x}}{\sigma_{core}}\right)^2} & \text{for } -\alpha_L < \dfrac{x - \bar{x}}{\sigma_{core}} < \alpha_R \\[2em] \left(\dfrac{n_R}{|\alpha_R|}\right)^{n_R} e^{-\frac{|\alpha_R|^2}{2}} \left(\dfrac{n_R}{|\alpha_R|} - |\alpha_R| + \dfrac{x - \bar{x}}{\sigma_{core}}\right)^{-n_R} & \text{for } \dfrac{x - \bar{x}}{\sigma_{core}} \geq \alpha_R \end{cases}$$

The unbinned maximum likelihood fit is performed separately to the TRIG, CAT1, CAT2, CAT3 and the sum of CAT2 and CAT3 trigger categories. For the low statistics $B^0 \to D^0\overline{D}^0 K^{*0}$ trigger categories (CAT2 and CAT3), the σ_{core} parameter is fixed to the value obtained from the fit to the MC sample.

6.4.1 Signal Yields

The signal yields ($\mathcal{N}_S$) from the fit to the $B^0 \to D^0\overline{D}^0 K^{*0}$ and $B^0 \to D^{*-} D^0 K^+$ data in the various trigger categories of interest are summarised in Table 6.11.

The fit to the data falling in TRIG category in $B^0 \to D^{*-} D^0 K^+$ and $B^0 \to D^0\overline{D}^0 K^{*0}$ are shown in Fig. 6.27 and Fig. 6.28, respectively.

The fit to the data falling in CAT1 category in $B^0 \to D^{*-} D^0 K^+$ and $B^0 \to D^0\overline{D}^0 K^{*0}$ are shown in Fig. 6.29 and Fig. 6.30, respectively.

The fit to the data falling in CAT2 category in $B^0 \to D^{*-} D^0 K^+$ and $B^0 \to D^0\overline{D}^0 K^{*0}$ are shown in Fig. 6.31 and Fig. 6.32, respectively.

The fit to the data falling in CAT3 category in $B^0 \to D^{*-} D^0 K^+$ and $B^0 \to D^0\overline{D}^0 K^{*0}$ are shown in Fig. 6.33 and Fig. 6.34, respectively.

The fit to the data falling in the sum of CAT2 and CAT3 in $B^0 \to D^{*-} D^0 K^+$ and $B^0 \to D^0\overline{D}^0 K^{*0}$ are shown in Fig. 6.35 and Fig. 6.36, respectively.

Table 6.11 Signal yields from the fit to the data in $B^0 \to D^{*-} D^0 K^+$ and $B^0 \to D^0\overline{D}^0 K^{*0}$ splitted by trigger categories

	$B^0 \to D^{*-} D^0 K^+$	$B^0 \to D^0\overline{D}^0 K^{*0}$
$\mathcal{N}_S$ (TRIG)	821 ± 31	157 ± 15
$\mathcal{N}_S$ (CAT1)	612 ± 27	107 ± 14
$\mathcal{N}_S$ (CAT2)	144 ± 12	37.7 ± 7.0
$\mathcal{N}_S$ (CAT3)	81.9 ± 9.4	23.0 ± 5.4
$\mathcal{N}_S$ (CAT2+CAT3)	229 ± 16	60.8 ± 8.9

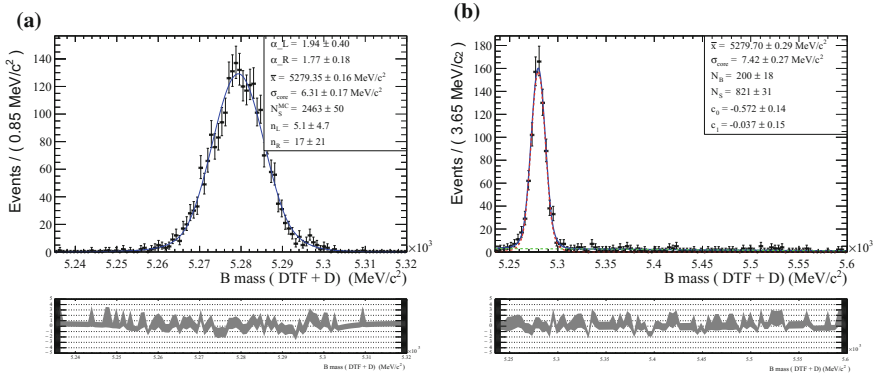**Fig. 6.27** **a** TRIG category $B^0 \to D^{*-}D^0K^+$ fit to the simulation to fix tails parameters. **b** TRIG category $B^0 \to D^{*-}D^0K^+$ fit to the data

Fig. 6.28 **a** TRIG category $B^0 \to D^0\overline{D}^0K^{*0}$ fit to the simulation to fix tails parameters. **b** TRIG category $B^0 \to D^0\overline{D}^0K^{*0}$ fit to the data

Fig. 6.29 **a** CAT1 category $B^0 \to D^{*-}D^0K^+$ fit to the simulation to fix tails parameters. **b** CAT1 category $B^0 \to D^{*-}D^0K^+$ fit to the data
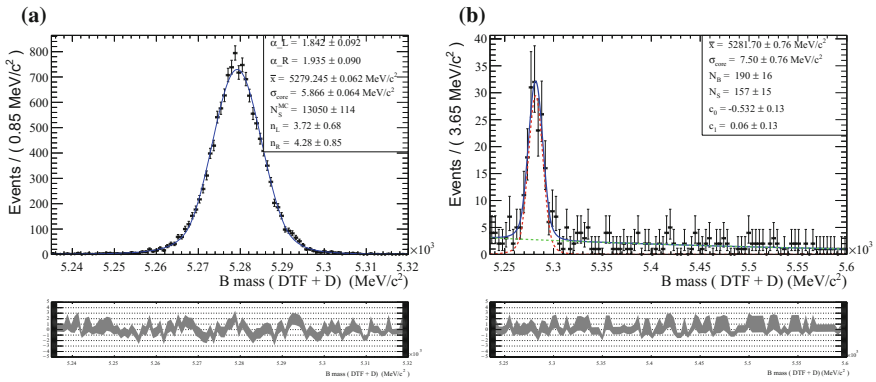
(a)

(b)

Fig. 6.30 **a** `CAT1` category $B^0 \to D^0\overline{D}^0 K^{*0}$ fit to the simulation to fix tails parameters. **b** `CAT1` category $B^0 \to D^0\overline{D}^0 K^{*0}$ fit to the data
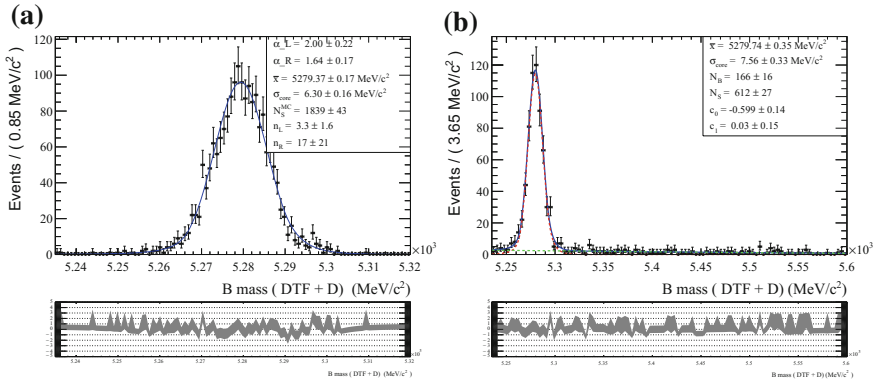
(a)

(b)

Fig. 6.31 **a** `CAT2` category $B^0 \to D^{*-}D^0 K^+$ fit to the simulation to fix tails parameters. **b** `CAT2` category $B^0 \to D^{*-}D^0 K^+$ fit to the data
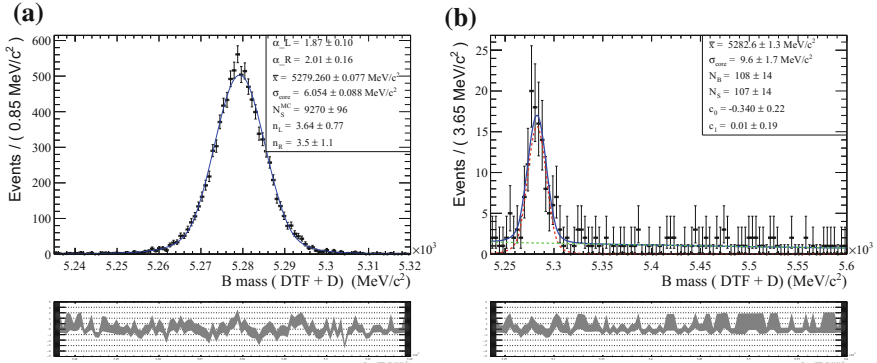
(a)

(b)
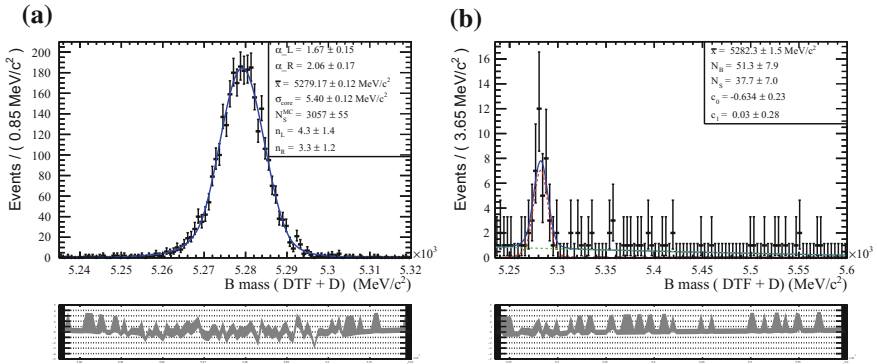
Fig. 6.32 **a** `CAT2` category $B^0 \to D^0\overline{D}^0 K^{*0}$ fit to the simulation to fix tails parameters. **b** `CAT2` category $B^0 \to D^0\overline{D}^0 K^{*0}$ fit to the data

(a)

(b)
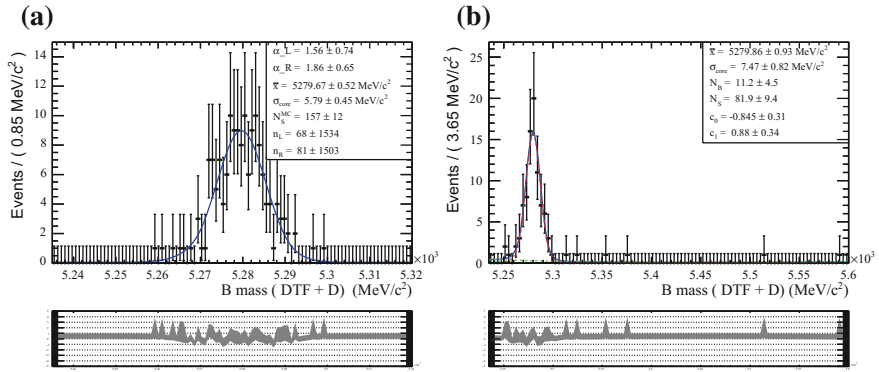
Fig. 6.33 **a** CAT3 category $B^0 \to D^{*-} D^0 K^+$ fit to the simulation to fix tails parameters. **b** CAT3 category $B^0 \to D^{*-} D^0 K^+$ fit to the data
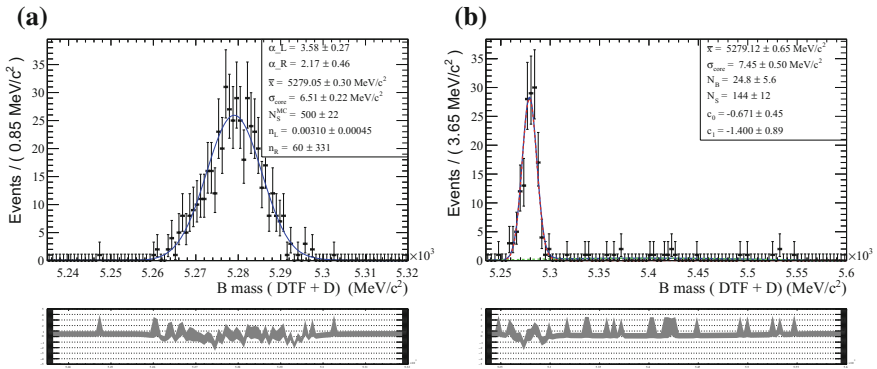
(a)

(b)

Fig. 6.34 **a** CAT3 category $B^0 \to D^{*-} D^0 K^+$ fit to the simulation to fix tails parameters. **b** CAT3 category $B^0 \to D^{*-} D^0 K^+$ fit to the data

(a)

(b)

Fig. 6.35 **a** CAT3+CAT2 category $B^0 \to D^{*-} D^0 K^+$ fit to the simulation to fix tails parameters. **b** CAT3+CAT2 category $B^0 \to D^{*-} D^0 K^+$ fit to the data

(a)

(b)

Fig. 6.36 **a** `CAT3+CAT2` category $B^0 \rightarrow D^{*-} D^0 K^+$ fit to the simulation to fix tails parameters. **b** `CAT3+CAT2` category $B^0 \rightarrow D^{*-} D^0 K^+$ fit to the data
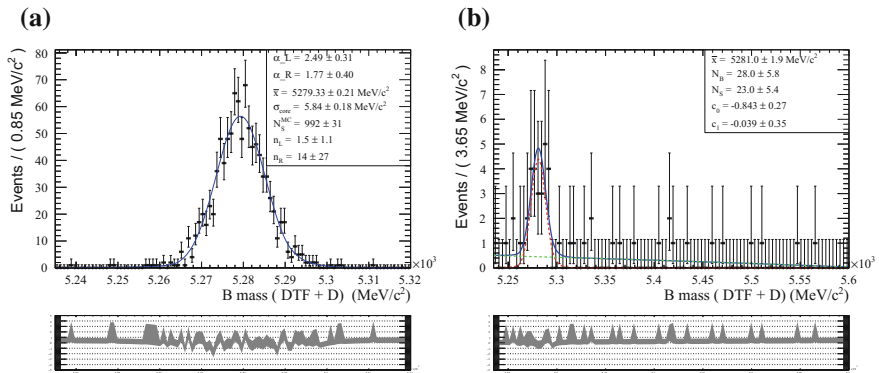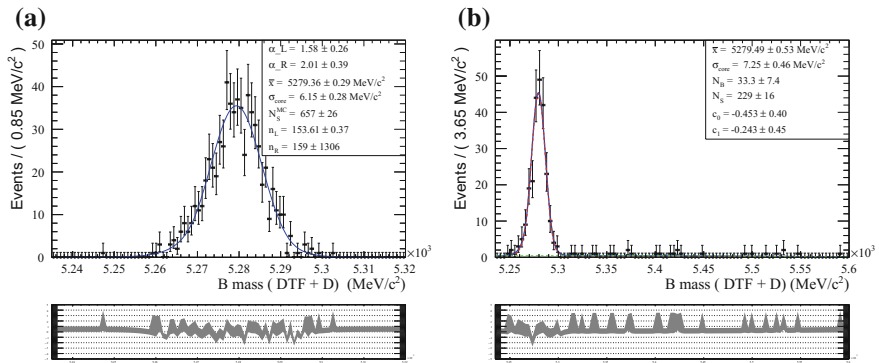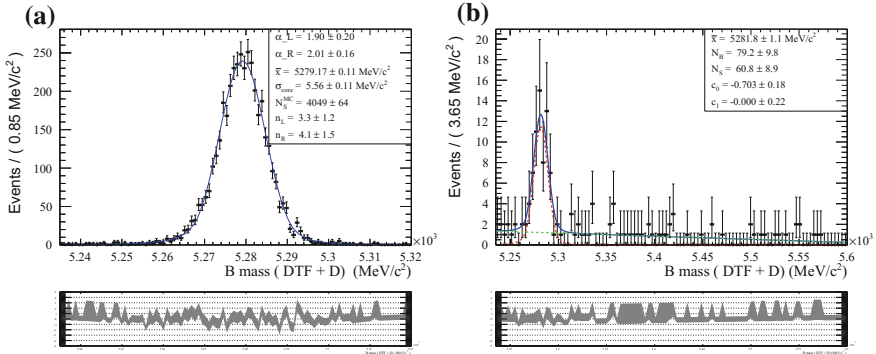
6.5 Efficiencies and Preliminary Results

The ratio of branching fractions has been measured using the following formula:

$$
\mathcal{R} = \frac{\mathcal{N}(B^0 \rightarrow D^0 \overline{D}^0 K\pi)}{\mathcal{N}(B^0 \rightarrow D^{*-} \overline{D}^0 K^+)} \times \frac{\mathcal{B}(D^{*-} \rightarrow D^0 \pi^-)}{1} \frac{\varepsilon_{geo}^{ref}}{\varepsilon_{Acceptance}^{sig}} \times \frac{\varepsilon_{Stripping|Acceptance}^{ref}}{\varepsilon_{Stripping|Acceptance}^{sig}} \frac{\varepsilon_{Presele/BDT/Trigger*}^{ref}}{\varepsilon_{Presele/BDT/Trigger*}^{sig}},
\tag{6.8}
$$

Since the $B^0 \rightarrow D^0 \overline{D}^0 K^{*0}$ dataset does not include any K^{*0} invariant mass selection, we remove from the formula the $\mathcal{B}(K^{*0} \rightarrow K^+ \pi^-)$. Indeed, the fitted value for $\mathcal{N}_S(B^0 \rightarrow D^0 \overline{D}^0 K^{*0})$ is actually related to the $B^0 \rightarrow D^0 \overline{D}^0 K^+ \pi^-$. Only a full amplitude analysis would be able to precisely extract the K^{*0} component. Some assumptions are made to obtain the preliminary results showed in Table 6.12:

- The efficiency for $B^0 \rightarrow D^{*-} D^0 K^+$ and $B^0 \rightarrow D^0 \overline{D}^0 K^{*0}$ can be extracted from Monte Carlo simulation.
- The efficiencies evaluated in the simulated $B^0 \rightarrow D^0 \overline{D}^0 K^{*0}$ sample are the same as in $B^0 \rightarrow D^0 \overline{D}^0 K^+ \pi^-$. It is assumed that the selections applied to select $B^0 \rightarrow D^0 \overline{D}^0 K^{*0}$ does not depend on the value of $m(K\pi)$. Such hypothesis must be tested in future using fully simulated $B^0 \rightarrow D^0 \overline{D}^0 K^+ \pi^-$ events.

The preliminary results on the ratio of branching fractions are provided in Table 6.12.

From Table 6.11, it is clear that the statistical error is completely dominated by the low signal yield in $B^0 \rightarrow D^0 \overline{D}^0 K^{*0}$. The values of the various efficiencies used to obtain the results in Table 6.12 are described in Sect. 6.5.1.

Table 6.12 Preliminary results from the fit to the data divided by trigger categories with statistical errors only

Category	$\mathcal{R} = \dfrac{\mathcal{B}(B^0 \to D^0\overline{D}^0K\pi)}{\mathcal{B}(B^0 \to D^{*-}\overline{D}^0K^+)}$ [%] (stat)
TRIG	13.25 ± 1.40
CAT1	12.83 ± 1.80
CAT2	16.47 ± 4.53
CAT3	16.51 ± 4.46
CAT2+3	15.92 ± 2.67

6.5.1 Break-Down of the Various Efficiencies and Efficiency Estimation

The various conditional efficiencies are evaluated in $B^0 \to D^0\overline{D}^0K^{*0}$ and $B^0 \to D^{*-}D^0K^+$:

- $\varepsilon_{Acceptance}$ is the probability that the whole decay chain of $B^0 \to D^0\overline{D}^0K^{*0}$ and $B^0 \to D^{*-}D^0K^+$ is produced in the LHCb acceptance. It is also called geometrical efficiency.
- $\varepsilon_{Stripping|Acceptance}$ is the Stripping selection (see Sect. 6.3.1) efficiencies evaluated with respect to the candidates produced in the LHCb acceptance.
- $\varepsilon_{Preliminary|Stripping}$ is the pre-selection efficiencies (see Sect. 6.3.2) evaluated with respect to the candidates passing the Stripping selections.
- $\varepsilon_{BDT|Preliminary}$ is the BDT selection efficiency (see Sect. 6.3.8) evaluated with respect to the events passing the pre-selections.
- $\varepsilon_{Trigger|BDT}$ is the efficiency of trigger selections (see Sect. 6.3.11) evaluated with respect to the events surviving the BDT selection. Here the subscript $Trigger$ stands for the various trigger categories defined in Sect. 6.3.11.

The value of $\varepsilon_{Acceptance}$ in $B^0 \to D^0\overline{D}^0K^{*0}$ and $B^0 \to D^{*-}D^0K^+$ is measured producing $\mathcal{N}_{Generated}$ events and counting the events in the LHCb acceptance $\mathcal{N}_{Generated}^{Acceptance}$, i.e. $\varepsilon_{Acceptance} = \dfrac{\mathcal{N}_{Generated}^{Acceptance}}{\mathcal{N}_{Generated}}$. The LHCb acceptance is defined for each final state particles in the decays of interests and it corresponds to $\theta \in [10, 400]$ mrad, where θ is the polar angle of the track.

The samples used to evaluate the geometrical efficiency are produced according to the phase space model which obviously do not reproduce the real distributions in data for the Dalitz plane. $B^0 \to D^0\overline{D}^0K^{*0}$ and $B^0 \to D^{*-}D^0K^+$ Monte Carlo samples used in this analysis are generated simulating $B^0 \to D^0\overline{D}^0K^{*0}$ covering all the possible phase space (PHSP model) without accounting for intermediate resonant particles and angular distributions $L = 1, 2, ..$ between particles. The $K^{*0} \to K^+\pi^-$ and the $D^{*-} \to \overline{D}^0\pi^-$ are generated simulating the two-body final states to be produced in $p - wave$, through the $V \to SS$ (vector to scalar scalar) model implemented in the LHCb simulation. A possible small variation in the geometrical acceptance value for

the $B^0 \to D^0 \overline{D}^0 K^{*0}$ and $B^0 \to D^{*-} D^0 K^+$ can occur if one would account for the correct Dalitz plane structure.

The value of $\varepsilon_{Stripping|Acceptance}$ is obtained counting the number of produced events in the LHCb acceptance ($\mathscr{N}'_{Acceptance}$) and the ones passing the stripping selections ($\mathscr{N}'^{Stripping}_{Generated|Acceptance}$). Those events differ from the ones used for the evaluation of $\varepsilon_{Acceptance}$ and they are labelled with a prime.

The value of $\varepsilon_{Preliminary|Stripping}$ is obtained from the ratio between the number of simulated events passing the pre-selections ($\mathscr{N}^{Preliminary}_{Stripping}$) and $\mathscr{N}'^{Stripping}_{Generated|Acceptance}$ defined above.

The value of $\varepsilon_{BDT|Preliminary}$ is obtained from the ratio between the number of events passing the BDT selection ($\mathscr{N}^{Preliminary}_{BDT}$) and $\mathscr{N}^{Preliminary}_{strip}$.

Finally the trigger efficiencies for the various categories is evaluated from the ratio between the number of events in the specific trigger category ($\mathscr{N}^{\mathtt{cat}\star}_{BDT}$) and $\mathscr{N}^{Preliminary}_{BDT}$.

All the efficiencies except $\varepsilon_{Acceptance}$ are evaluated using the $B^0 \to D^0 \overline{D}^0 K^{*0}$ and $B^0 \to D^{*-} D^0 K^+$ Monte Carlo samples, thus the final efficiency can be simply defined as $\varepsilon_{\mathtt{TRIG}|Acceptance}$, i.e. the ratio between the final number of events after trigger, BDT, preliminary and stripping selections and the $\mathscr{N}'^{Stripping}_{Generated|Acceptance}$. The values of the various efficiencies described above and the final values of $\varepsilon_{\mathtt{TRIG}\star|Acceptance}$ used for the evaluation of $\mathscr{R}$ are summarised in Table 6.13.

6.5.2 Background Subtraction Using sPlot

The fitted PDF for the various trigger categories described in Sect. 6.4 is used to apply the *sPlot* technique [18], which is a statistical tool to unfold data distributions. In the context of this analysis we use the *sPlot* to plot the background subtracted distributions of other interesting variables. The tool assigns to each candidate used for the fit to the data a signal weight. The signal weight can be used to plot the distributions of other variables in data. Such approach works only if the other variables are uncorrelated to the variable on which the fit has been performed, in this case $m(B^0)$ with DTF and $D^0/\overline{D}^0$ constrained to the nominal mass.

6.5.2.1 MC/Data Comparison Checks

The *sPlot* technique has been used to unfold the distributions of the input variables used for the two-stage BDT training. This check is important to ensure a proper MC/Data agreement and the reliability of the efficiencies estimation, especially for the BDT selection. The relevant 1-D distributions of the training variables for D^0 and $\overline{D}^0$ related to the D^{V2}_{fromB} (grad) BDT are then compared between Monte Carlo and s-weighted data as well as the training variables for the second stage BDT ($First_{V2} - Second_{V2}$ (grad-grad)).

Table 6.13 Summary of statistics in the various selection steps and the corresponding efficiencies. All errors are calculated using the binomial error formula

	$B^0 \to D^{*-}D^0 K^+$	$B^0 \to D^0\overline{D}^0 K^{*0}$
$\mathcal{N}_{gen}$	2,000,002	1,940,001
$\mathcal{N}_{gen}^{acc}$	298,276	285,888
$\varepsilon_{Acceptance}$	$(14.91 \pm 0.03)\%$	$(14.74 \pm 0.03)\%$
$\mathcal{N}'_{Acceptance|Generated}$	597,487	3,231,411
$\mathcal{N}'^{Stripping}_{Acceptance|Generated}$	3,676	33,152
$\varepsilon_{Stripping|Acceptance}$	$(0.615 \pm 0.010)\%$	$(1.025 \pm 0.006)\%$
$\mathcal{N}^{Preliminary}_{Stripping}$	2,816	25,884
$\varepsilon_{Preliminary|Stripping}$	$(76.61 \pm 0.70)\%$	$(78.08 \pm 0.03)\%$
$\mathcal{N}^{Preliminary}_{BDT}$	2,657	14,400
$\varepsilon_{BDT|Preliminary}$	$(94.4 \pm 0.4)\%$	$(55.63 \pm 0.31)\%$
$\mathcal{N}^{TRIG}_{BDT}$	2,502	13,376
$\mathcal{N}^{CAT1}_{BDT}$	1,844	9,309
$\mathcal{N}^{CAT2}_{BDT}$	500	3,069
$\mathcal{N}^{CAT3}_{BDT}$	158	998
$\mathcal{N}^{CAT2+CAT3}_{BDT}$	658	4,067
$\varepsilon_{TRIG|BDT}$	$(94.17 \pm 0.46)\%$	$(92.89 \pm 0.21)\%$
$\varepsilon_{CAT1|BDT}$	$(69.40 \pm 0.89)\%$	$(64.65 \pm 0.40)\%$
$\varepsilon_{CAT2|BDT}$	$(18.82 \pm 0.76)\%$	$(21.31 \pm 0.34)\%$
$\varepsilon_{CAT3|BDT}$	$(5.95 \pm 0.46)\%$	$(6.93 \pm 0.21)\%$
$\varepsilon_{CAT2+CAT3|BDT}$	$(24.76 \pm 0.84)\%$	$(28.24 \pm 0.38)\%$
$\varepsilon_{TRIG|Generated}$	$(0.419 \pm 0.008)\%$	$(0.414 \pm 0.004)\%$
$\varepsilon_{CAT1|Generated}$	$(0.309 \pm 0.007)\%$	$(0.289 \pm 0.003)\%$
$\varepsilon_{CAT2|Generated}$	$(0.084 \pm 0.004)\%$	$(0.095 \pm 0.002)\%$
$\varepsilon_{CAT3|Generated}$	$(0.026 \pm 0.002)\%$	$(0.031 \pm 0.001)\%$
$\varepsilon_{CAT2+CAT3|Generated}$	$(0.110 \pm 0.004)\%$	$(0.126 \pm 0.002)\%$

The *sPlot* of the input variables for the D^{V2}_{fromB} (grad) BDT used to select the $B^0 \to D^0\overline{D}^0 K^{*0}$ for the D^0 is shown in Fig. 6.39 and the one for the $\overline{D}^0$ is shown in Fig. 6.40. The *sPlot* of the input variables for the D^{V2}_{fromB} (grad) BDT used to select the $B^0 \to D^{*-}D^0 K^+$ for the D^0 is shown in Fig. 6.37 and the one for the $\overline{D}^0$ is shown in Fig. 6.38.

The *sPlot* of the input variables for the $First_{V2} - Second_{V2}$ (grad-grad) BDT used to select the $B^0 \to D^0\overline{D}^0 K^{*0}$ is shown in Fig. 6.42 and the one for the $B^0 \to D^{*-}D^0 K^+$ is shown in Fig. 6.41. The *sPlot* of the input variables for the $First_{V2} - Second_{V2}$ (grad-grad) BDT used to select the $B^0 \to D^{*-}D^0 K^+$ for the D^0 is shown in Fig. 6.37 and the one for the $\overline{D}^0$ is shown in Fig. 6.38.

A good agreement between Monte Carlo distributions and background subtracted signal events in data is observed.

Fig. 6.37 In blue the $B^0 \to D^{*-} D^0 K^+$ CAT1 *sPlot* distributions of the input variables used to evaluate the $D^0 D_{fromB}^{V2}$ (grad). In red the $B^0 \to D^{*-} D^0 K^+$ CAT1 Monte Carlo simulation distributions of the input variables used to evaluate the $D^0 D_{fromB}^{V2}$ (grad)
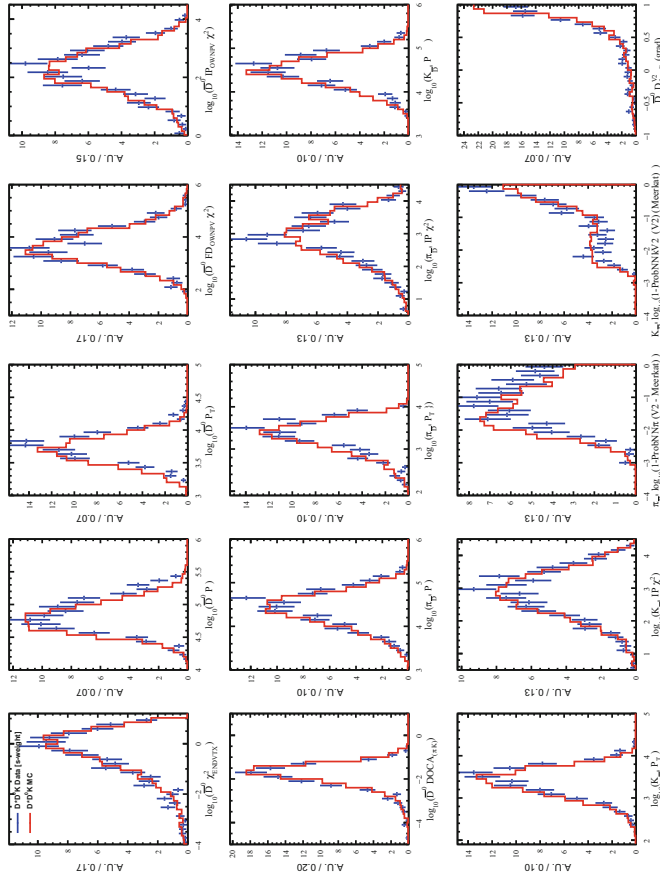
Fig. 6.38 In blue the $B^0 \rightarrow D^{*-} D^0 K^+$ CAT1 $sPlot$ distributions of the input variables used to evaluate the $\overline{D}^0 D_{from B}^{V2}$ (grad). In red the $B^0 \rightarrow D^{*-} D^0 K^+$ CAT1 Monte Carlo simulation distributions of the input variables used to evaluate the $\overline{D}^0 D_{from B}^{V2}$ (grad)
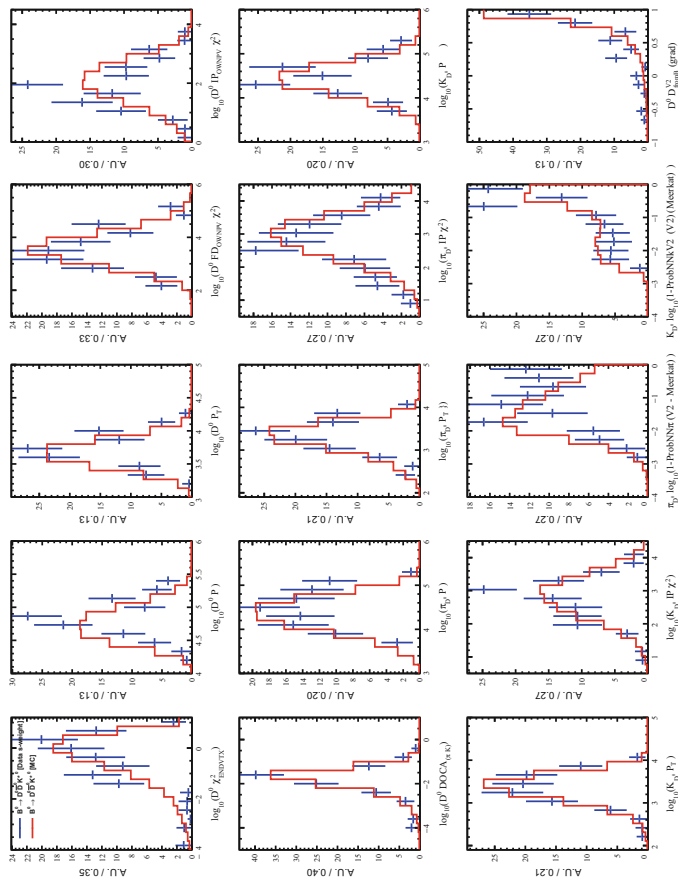
Fig. 6.39 In blue the $B^0 \rightarrow D^0\overline{D}^0 K^{*0}$ CAT1 *sPlot* distributions of the input variables used to evaluate the D^0 D_{fromB}^{V2} (grad). In red the $B^0 \rightarrow D^0\overline{D}^0 K^{*0}$ CAT1 Monte Carlo simulation distributions of the input variables used to evaluate the D^0 D_{fromB}^{V2} (grad)

Fig. 6.40 In blue the $B^0 \rightarrow D^0\overline{D}^0 K^{*0}$ CAT1 *sPlot* distributions of the input variables used to evaluate the $\overline{D}^0$ D^0_{fromB} (grad). In red the $B^0 \rightarrow D^0\overline{D}^0 K^{*0}$ CAT1 Monte Carlo simulation distributions of the input variables used to evaluate the $\overline{D}^0$ D^0_{fromB} (grad)

Fig. 6.41 In blue the $B^0 \to D^{*-} D^0 K^+$ CAT1 *sPlot* distributions of the input variables used to evaluate the $First_{V2} - Second_{V2}$ (grad-grad) BDT. In red the $B^0 \to D^{*-} D^0 K^+$ CAT1 Monte Carlo simulation distributions of the input variables used to evaluate the $First_{V2} - Second_{V2}$ (grad-grad) BDT
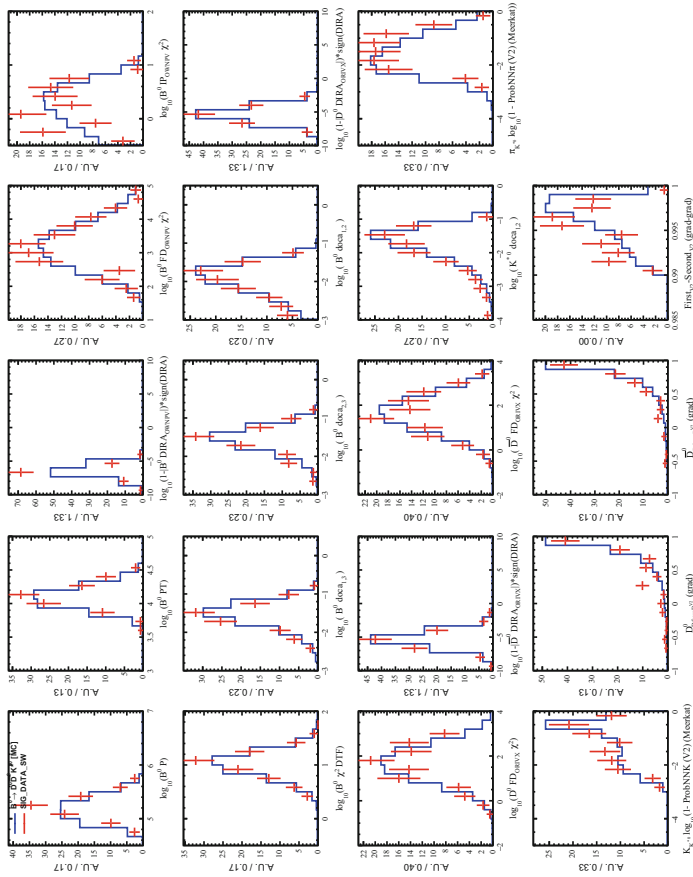
Fig. 6.42 In blue the $B^0 \to D^0 \overline{D}^0 K^{*0}$ CAT1 *sPlot* distributions of the input variables used to evaluate the $\overline{D}^0 \ D^{V2}_{fromB}$ (grad). In red the $B^0 \to D^0 \overline{D}^0 K^{*0}$ CAT1 Monte Carlo simulation distributions of the input variables used to evaluate the $\overline{D}^0 \ D^{V2}_{fromB}$ (grad)

6.5.2.2 MC/Data Dalitz Projections Checks

The *sPlot* of the invariant mass spectrum for the K^{*0} and the various invariant mass pairs projections in $B^0 \to D^0 \overline{D}^0 K^{*0}$ for the CAT1 trigger category is shown in Fig. 6.44. It can be observed in Fig. 6.44, that a clear $\psi(3770) \to D^0 \overline{D}^0$ intermediate resonance is present as well as a peaking structure in the $D^0 K^+_{K^{*0}}$ around 2850 MeV/c^2. Also a clear K^{*0} component is present. It is not clear if also a $X(3872)$ is present in the invariant mass spectrum of $D^0 \overline{D}^0$. Only a full amplitude analysis would be able to properly describe the resonant structure of the $B^0 \to D^0 \overline{D}^0 K \pi$ decay (Fig. 6.43).

The *sPlot* of the invariant mass spectrum for the K^{*0} and the various invariant mass pairs projections in $B^0 \to D^{*-} D^0 K^+$ for the CAT1 trigger category is shown in Fig. 6.43. From Fig. 6.43, a clear and broad $D_s^*(2700)^+$ is observed. Less clear is the presence or not of other resonant structures in the low and high mass region of $D^{*-} D^0$.

6.6 Source of Systematics and Estimation of K^{*0} Fraction in $B^0 \to D^0 \overline{D}^0 K^+ \pi^-$

Various systematic uncertainties will be evaluated. We provide here a list of them, their expectation and the strategy that will be used to address them. The fact that $B^0 \to D^0 \overline{D}^0 K^{*0}$ and $B^0 \to D^{*-} D^0 K^+$ share the same exact amount of final states and the fact that we quote the final result as a ratio of branching ratios allows to simplify the estimation of systematics uncertainties. The only systematic uncertainties to include in the analysis are related to the efficiencies evaluation.

- HLT trigger systematics: we rely on the fact that the TOS category is well modelled in MC, thus they are expected to cancel. Concerning the TIS categories, re-weighting the MC in both decay modes according to the B kinematics and detector occupancy (n_{SPD}) will allow to properly evaluate the efficiencies in data. The statistical error on the computed trigger efficiency will be used to estimate the systematics uncertainties.
- Stripping and selection efficiency across the Dalitz Plane: a large Monte Carlo sample of $B^0 \to D^0 \overline{D}^0 K^+ \pi^-$ (PHSP model) will be used and a study of Dalitz Plane efficiencies dependences in slices of $m(K_{K^{*0} \pi_{K^{*0}}})$. The dependence of the whole selection efficiency (stripping, pre-selection, BDT and trigger) across the $m(K_{K^{*0} \pi_{K^{*0}}})$ value in $B^0 \to D^0 \overline{D}^0 K^{*0}$ and $B^0 \to D^{*-} D^0 K^+$ will be accounted to correct the central value of the efficiency ratio. The maximal variation of efficiencies in $B^0 \to D^{*-} D^0 K^+$ and $B^0 \to D^0 \overline{D}^0 K^{*0}$ across the Dalitz plane will be used to evaluate the corresponding systematics uncertainty.
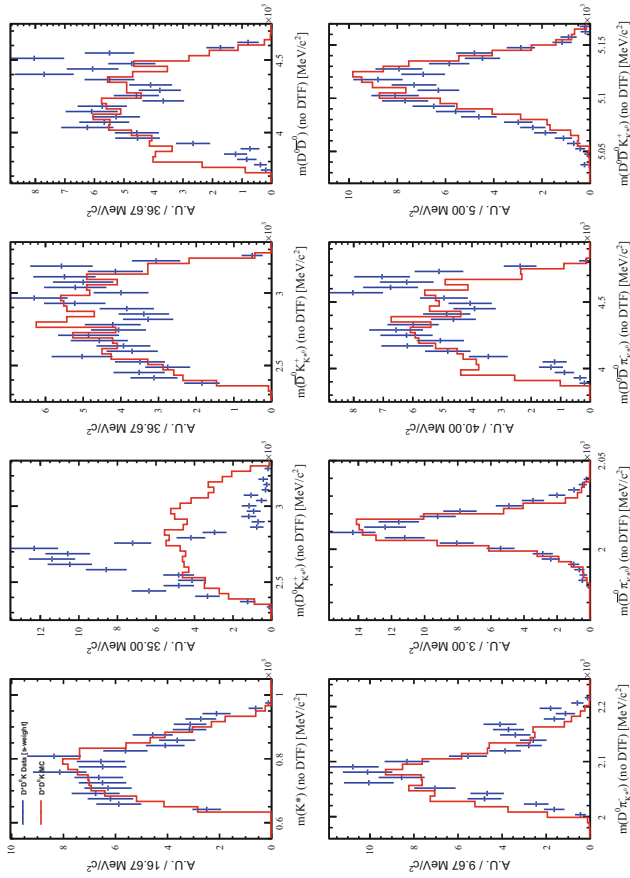
Fig. 6.43 In blue the $B^0 \to D^{*-} D^0 K^+$ CAT1 $sPlot$ distributions of the various invariant mass projections for $B^0 \to D^0 \overline{D}^0 K^+ \pi^-$. In red the $B^0 \to D^{*-} D^0 K^+$ CAT1 Monte Carlo phase space simulation distributions of the various invariant mass projections for $B^0 \to D^0 \overline{D}^0 K^+ \pi^-$

Fig. 6.44 In blue the $B^0 \to D^0\overline{D}^0K^{*0}$ CAT1 *sPlot* distributions of the various invariant mass projections for $B^0 \to D^0\overline{D}^0K^+\pi^-$. In red the $B^0 \to D^0\overline{D}^0K^{*0}$ CAT1 Monte Carlo phase space simulation distributions of the various invariant mass projections for $B^0 \to D^0\overline{D}^0K^+\pi^-$
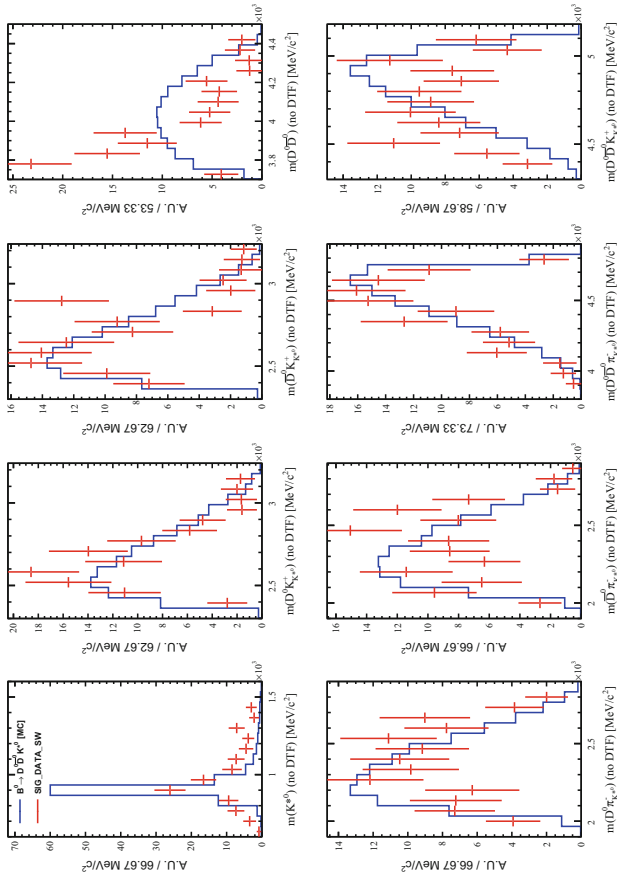
- Fit model: a check to the fit stability will be performed generating toys according to the fitted shape. The generated toys will be fitted with the same fit model and systematics will be addressed looking at the 1-σ level of the fitted mean value of signal yield in $B^0 \to D^{*-} D^0 K^+$ and $B^0 \to D^0 \overline{D}^0 K^{*0}$. Additional systematics will be evaluated changing the background model from polynomial to exponential in both $B^0 \to D^0 \overline{D}^0 K^{*0}$ and $B^0 \to D^{*-} D^0 K^+$. A simple Gaussian model will also be used for the signal to evaluate the corresponding systematics. Additional systematics can be measured including in the fit model the partially reconstructed background which would help to further constraint the combinatorial background shape.
- Loose cuts on *PID* for the pre-selection: the standard tools from LHCb will be used. Systematics can be evaluated taking into account the multi-final states (6 in total for this analysis) kinematic properties. This method relies in using look-up tables built using standard candle decay modes $B \to D \to (K\pi)\pi$ from which the *PID* response can be extracted as a function of the tracks p_T and pseudorapidity.
- Tracking efficiencies: the tracking efficiencies are embedded in the stripping selection. We expect them to cancels between $B^0 \to D^0 \overline{D}^0 K^{*0}$ and $B^0 \to D^{*-} D^0 K^+$, nevertheless we will correct the stripping efficiency accounting for them. The reason why tracking efficiencies matters in terms of systematic uncertainty is mainly due to the different kinematic of the slow pion in $B^0 \to D^{*-} D^0 K^+$ with respect to $B^0 \to D^0 \overline{D}^0 K^+ \pi^-$. A flat systematics of 1% per track is usually assigned and several efficiency ratio can be estimated using a large amount of different tables, leading to the final systematics uncertainty.
- `Meerkat` *PID* re-sampling: the weighted $ProbNN$ is used to train the BDT and evaluate the corresponding efficiencies. The random re-sampling is unbinned. Several *PID* responses can be generated in $B^0 \to D^{*-} D^0 K^+$ and $B^0 \to D^0 \overline{D}^0 K^{*0}$ and the new final BDT response can be produced.
- Vertexing: in the BDT we use as input variable the DTF χ^2. Such value differs in Data and MC, but we expect to have a negligible effects.
- Charmless contamination: the estimation of charmless background has be evaluated looking to the D meson sideband. The corresponding estimated contamination and its error will be used to address the systematic uncertainties.
- Truth matching in MC: a different truth matching algorithm will be employed and the new efficiency ratio will be evaluated again and a systematic uncertainties will be added.

The estimation of the amount of K^{*0} in the reconstructed $B^0 \to D^0 \overline{D}^0 K^+ \pi^-$ will be performed fitting the *sPlot* of the K^{*0} invariant mass with a relativistic Breit–Wigner (for the K^{*0} line shape) and a polynomial for the remaining contents. Further studies are needed to properly account for the resonant structure of $B^0 \to D^0 \overline{D}^0 K^+ \pi^-$ in $D^0 \overline{D}^0$ as well as in DK and $D\pi$ as well as potential exotics in DDK or $DD\pi$. A full modelling of the $K\pi$ spectrum and a precise extraction of K^{*0} component can only be achieved through a full amplitude analysis, which goes beyond the goal of the presented analysis.

6.7 Conclusions and Future Plans

This chapter presented the measurement of the branching fraction of $B^0 \to D^0\overline{D}^0 K^{*0}$ with respect to the $B^0 \to D^{*-}D^0 K^+$. No K^{*0} mass requirements are applied. The preliminary value we trust more in terms of efficiencies corresponds to the value obtained using the $L0h_{TOS}$ trigger category:

$$\mathscr{R} = \frac{\mathscr{B}(B^0 \to D^0\overline{D}^0 K^+\pi^-)}{\mathscr{B}(B^0 \to D^{*-}D^0 K^+)} = (12.83 \pm 1.80(\text{stat}))\% \qquad (6.9)$$

We use only the CAT1 in this estimation because trigger efficiencies evaluated using tracks contained in the decay chain (all TOS category for L0, HLT1 and HLT2) of the B candidates is reliable in Monte Carlo. Concerning the TIS categories, one must use data driven methods or apply corrections to the Monte Carlo concerning the B kinematics (the kinematic of the other B produced in the decay is correlated to the B used as signal) and detector occupancy (n_{SPD}).

Concerning the CAT2 and CAT3, a reweighting of the efficiency ratio as a function of the B mass kinematic (B^0 p_T, η) and the occupancy in the SPD detector (used for L0 trigger decision) has to be applied since the Trigger Independent On Signal depends on the other B meson in the event. Furthermore we need to take into account the fact that the Dalitz structure of $B^0 \to D^0\overline{D}^0 K^+\pi^-$ is unknown, and for this a systematic uncertainty will be added.

Additional work is planned in order to fit the *sPlot* of the K^{*0} mass spectrum simulating various resonant structures in the $B^0 \to D^0\overline{D}^0 K^+\pi^-$ decay. Additional checks are expected to be performed to validate the fact that the selection is flat across the Dalitz plane, as it should be since the variables used in the BDT are independent on the presence of a K^{*0}. Indeed, no kinematic variables from the $\pi_{K^{*0}}$ and $K_{K^{*0}}$ are used to train the BDTs.

Although we obtained only a preliminary result in this thesis, we can make a rough prediction of the contribution to the charm counting from $B \to D^{(*)}D^{(*)}K\pi$ decays. Assuming the following:

$$\frac{\mathscr{B}(B^0 \to D^0\overline{D}^0 K\pi)}{\mathscr{B}(B^0 \to D^0\overline{D}^0 K^0)} = \frac{\sum \mathscr{B}(B \to D^{(*)}\overline{D}^{(*)}K\pi)}{\sum \mathscr{B}(B \to D^{(*)}\overline{D}^{(*)}K)}, \qquad (6.10)$$

where

$$\mathscr{B}(B^0 \to D^0\overline{D}^0 K\pi) = (12.83 \pm 1.80)\% \quad \times \quad \mathscr{B}(B^0 \to D^{*-}D^0 K^+) = (3.17 \pm 0.46) \times 10^{-4}. \qquad (6.11)$$

According to (6.10), we can estimate that $\sum \mathscr{B}(B^0 \to D^{(*)}\overline{D}^{(*)}K\pi) = (4.8 \pm 1.9)\%$. The addition of Run II data would help to increase the signal yields of more than a factor two and it would allow to perform a full amplitude analysis for $B^0 \to D^0\overline{D}^0 K^+\pi^-$ decay.

References

1. BaBar, P. del Amo Sanchez et al., Measurement of the $B \rightarrow \overline{D}^{(*)} D^{(*)} K$ branching fractions. Phys. Rev. **D83**, 032004 (2011). http://dx.doi.org/10.1103/PhysRevD.83.032004, arXiv:1011.3929
2. Particle Data Group, C. Patrignani et al., Review of particle physics. Chin. Phys. **C40**(10) 100001 (2016). http://dx.doi.org/10.1088/1674-1137/40/10/100001
3. LHCb, R. Aaij et al., Precision luminosity measurements at LHCb. JINST **9**(12) P12005 (2014). http://dx.doi.org/10.1088/1748-0221/9/12/P12005, arXiv:1410.0149
4. W.D. Hulsbergen, Decay chain fitting with a Kalman filter. Nucl. Instrum. Meth. **A552**, 566 (2005). http://dx.doi.org/10.1016/j.nima.2005.06.078, arXiv:physics/0503191
5. A. Poluektov, Kernel density estimation of a multidimensional efficiency profile. JINST **10**(02) P02011 (2015). http://dx.doi.org/10.1088/1748-0221/10/02/P02011, arXiv:1411.5528
6. A. Hocker et al., TMVA - toolkit for multivariate data analysis. PoS **ACAT**, 040 (2007). arXiv:physics/0703039
7. A. Hoecker et al., TMVA - toolkit for multivariate data analysis. Physics (2007), arXiv:physics/0703039
8. P.C. Bhat, Multivariate analysis methods in particle physics. Ann. Rev. Nucl. Part. Sci. **61**, 281 (2011). http://dx.doi.org/10.1146/annurev.nucl.012809.104427
9. C. Bishop, *Neural Network for Pattern Recognition* (Oxford University Press, Oxford, 1955)
10. C.M. Bishop, *Pattern Recognition and Machine Learning* (Springer Science Business Media, New York, 2007)
11. V.N. Vapnik, *Statistical Learning Theory*
12. J. Friedman, T. Hastie, R. Tibshirani, *The Elements of Statistical Learning: Data Mining, Inference, and Prediction*
13. J. Friedman, L. Brieman, *Classificaton and Regression Trees* (Springer, New York, 2000)
14. R.E. Schapire, Y. Freund, A decision-theoretic generalization of on-line learning and an application to boosting. J. Comput. Syst. Sc. **55**, 119 (1997). http://dx.doi.org/10.1006/jcss.1997.1504
15. LHCb Collaboration, R. Aaij et al., Measurement of $\sigma(pp \rightarrow b\bar{b}X)$ at $\sqrt{s} = 7$ TeV in the forward region. Phys. Lett. **B694**, 209 (2010). http://dx.doi.org/10.1016/j.physletb.2010.10.010, arXiv:1009.2731
16. V.V. Gligorov, M. Williams, Efficient, reliable and fast high-level triggering using a bonsai boosted decision tree. JINST **8**, P02013 (2013). http://dx.doi.org/10.1088/1748-0221/8/02/P02013, arXiv:1210.6861
17. T. Skwarnicki, A study of the radiative CASCADE transitions between the Upsilon-Prime and Upsilon resonances. Ph.D thesis, Cracow, INP (1986)
18. M. Pivk, F.R. Le Diberder, sPlot: A statistical tool to unfold data distributions. Nucl. Instrum. Meth. **A555**, 356 (2005). http://dx.doi.org/10.1016/j.nima.2005.08.106, arXiv:physics/0402083

Curriculum Vitae

Employment and Education

- **CNRS, France**: PostDoc, Oct 2017 – present
- **University of Bristol, Bristol, UK & University of Paris Sud, Orsay, France**: Ph.D. in co-tutel

  – DPhil in Physics July 2014–Oct 2017 (both institutes)
  Advisers: Dr. Jonas Rademacker and Dr. Patrick Robbe.
  Thesis title: Study of double charm B decays with the LHCb experiment at CERN and track reconstruction for the LHCb upgrade. (http://cds.cern.ch/record/2296404.)

- **University of Paris Sud, Orsay, France & University of Ferrara, Ferrara, Italy**: Double master degree in physics

  – Master 2 NPAC (M2 Nuclei, Particles, Astroparticles and Cosmology), Sept 2013–July 2014.
  Final grade: *bien*.
  – Master degree in Physics, Sept 2012–Sept 2014.
  Voto laurea: 110/110 cum laude
  Advisers: Dr. Patrick Robbe and Drs. Eleonora Luppi.
  Thesis title: Study of double charm B decays with the LHCb experiment.

- **University of Ferrara, Ferrara, Italy**

  – Bachelor degree in Physics and Astrophysics, Sept 2009–July 2012.
  Voto laurea: 110/110 cum laude
  Advisers: Dr. Wander Baldini.
  Thesis title: Study of the Performance of a Prototype for the Muon Detector of SuperB. (http://inspirehep.net/record/13381267ln)

- **SLAC National Accelerator Laboratory**, Menlo Park (CA), USA: DOE/INFN Summer Exchange Program.

  – Adviser: Dr. Justin Vandenbroucke.

- **Liceo scientifico Leonardo Da Vinci, Jesi (AN), Italy**: high-school degree. Final grade 99/100.

Awards

- Springer Thesis award 2017. My Ph.D. thesis has been selected and will be published in "Springer Thesis" series recognizing outstanding Ph.D. research.
- LHCb early career scientist award (2017) (https://home.cern/cern-people/updates/2017/07/lhcb-early-career-scientist-awards).
- "Ferrara School of Physics" award for the path of excellence for students within an international environment.
- Double master degree scholarship between University of Ferrara and University of Paris Sud (2013–2014).
- Winner of the contest "I problemi dell'Universo", editions 2012 and 2011, reserved to undergraduate students of the Physics department of University of Ferrara for the best resolution of problems in physics.

Publications

My h_{HEP} index is 37, I have 202 publications according to the Inspire Author Profile, here are the most significant ones where I contributed significantly.

- **"Status of HLT1 sequence and path towards 30 MHz"**
  CERN-LHCb-PUB-2018-003 CDS entry

- **"Upgrade trigger & reconstruction strategy: 2017 milestone"**
  CERN-LHCb-PUB-2018-005 CDS entry

- **"Upgrade trigger: Biannual performance update"**
  CERN-LHCb-PUB-2017-005 CDS entry

- **"Novel real-time alignment and calibration of LHCb detector for Run II and tracking for the upgrade"**
  J. Phys. Conf. Ser. 762 (2016) no.1, 012046 Inspire entry

- **"Summary of the 2015 LHCb workshop on multi-body decays of D and B mesons"**
  ArXiv:1605.03889 Inspire entry

- **"Study of double charm B decays with the LHCb experiment at CERN and track reconstruction for the LHCb upgrade"**
  CERN-THESIS-2017-254 CDS entry

- **"A stand-alone track reconstruction algorithm for the scintillating fibre tracker at the LHCb upgrade"**
  Poster-2017-584 CDS entry

- **"TARGET 5: a new multi-channel digitizer with triggering capabilities for gamma-ray atmospheric Cherenkov telescopes"**
  arXiv:1607.02443 ArXiv entry

- **"SciFi - A large Scintillating Fibre Tracker for LHCb"**
  Poster-2016-546 CDS entry

- **"Study of the Performance of a Prototype for the Muon Detector of SuperB"**
  Thesis Inspire entry

Conferences/Talks/Posters

- **"Connecting the Dots 2017"**
  Talk: *Tracking for LHCb upgrade, using a full software trigger at* 30 MHz
  Poster: *A stand-alone track reconstruction algorithm for the scintillating fibre tracker at the LHCb upgrade*

- **International Conference on High Energy Physics 2016**
  Poster: *SciFi - A large Scintillating Fibre Tracker for LHCb*

- **Advanced Computing and Analysis Technique 2015**
  Talk: *Novel real-time alignment and calibration of LHCb detector for Run II and tracking for the upgrade*

- **LHCC 2017**
  Poster: *A stand-alone track reconstruction algorithm for the scintillating fibre tracker at the LHCb upgrade*

- **Pheniics Days 2016**
  Talk: *Study of double charm B decays and track reconstruction for the LHCb upgrade*

- **Journes de Rencontres Jeunes Chercheurs 2015**
  Talk: *Study of double charm B decays and track reconstruction for the LHCb upgrade*

Research Interests and Experience

My primary research interest is the understanding of discrepancies between theories and experimental evidences in the domain of high-energy physics. The elementary particles of the Standard Model and their interaction are all observed experimentally and they describe the nature with an excellent precision. Nevertheless, the Standard Model is not sufficient to explain the asymmetry of matter and anti-matter in the universe in which we are all living nowadays (among others other issues). My research has been mainly carried within the LHCb collaboration (since 2014) trying to answer these questions.

1 Data Analysis at LHCb

Since October 2017, I am working on the study of lepton universality violation using the data produced by the LHCb and the developments of the trigger strategy for the Run III data taking aiming to perform real-time analysis. The analysis consists in measuring the ratio of branching ratios between $b \rightarrow se^+e^-$ and $b \rightarrow s\mu^+\mu^-$ decay modes. Indeed, recent LHCb results on $R(K^{*0})$, the ratio of the branching fractions of $B \rightarrow K^{*0}\mu^+\mu^-$ to that of $B^0 \rightarrow K^{*0}e^+e^-$, for the dilepton invariant mass bins $q^2 = m_{ll}^2 = [0.0451.1]$ GeV/c^2 and $[0.045\ 1.1]$ GeV/c^2 show approximately 2.5 σ deviations from the corresponding Standard Model prediction in each of the bins.

This, when combined with the measurement of R(K)($q^2 = [1\ 6]\,\text{GeV}/c^2$), a similar ratio for the decay to a pseudo scalar meson, highly suggests for lepton non-universal new physics in semi-leptonic B meson decays. I have a central role in that analysis as developer of the analysis framework for the data selection for Run 1 and Run 2, efficiency corrections and fitting to data. That framework is designed to measure simultaneously $R(K)$ and $R(K^{*0})$ and it has been designed to be flexible enough to easily integrate any $R(X)$ measurement.

During my Ph.D., I worked on the analysis for the branching ratio measurement of the decay $B^0 \to D^0\overline{D}^0 K^{*0}$ using Run I data at LHCb. The mode has never been observed so far (lack of statistics in BaBar and Belle). The mode is of particular interest to study the presence of intermediate short-lived resonances decaying into $D^0\overline{D}^0$ which cannot be explained as a standard charmonium state. I am the main and unique contributor to the analysis and I have worked on the development of the event selection, to the data mass fit, and to the determination of efficiencies and systematics for Run I. That analysis is not yet published and currently Run II data are analized. That analysis would have a natural follow up in the study of the Dalitz structures (in $D^0\overline{D}^0 K\pi$) including Run II data. The dalitz analysis is also of particular interest in order to understand charm-loops and charmonium effects in $b \to sl^+l^-$.

2   Trigger and Data Processing for the LHCb Upgrade

In addition to the analysis interest, I am interested also in the triggering and data processing for HEP experiments. The amount of data processed by the LHC experiments has no precedent, but the storage resources are limited. Therefore, any HEP experiment needs to implement an efficient, robust and flexible trigger strategy. Moreover, the event selection must fulfill the computing resources available for the experiment. This multivariate issue of HEP experiments is of great interest and since my Ph.D. to nowadays I am strongly involved in the preparation of the data taking and algorithms developments for the LHCb upgrade. The LHCb upgrade trigger will employ a fully software based event reconstruction and selection at the pp collision rate (40 MHz). The key aspect of the trigger strategy of the LHCb experiment is the track reconstruction which must be able to find and identify tracks displaced from the primary vertices to fully identify if an event contains or not a b hadron.

I am the author and maintainer of the upgrade Vertex Locator (the detector placed closer to the interaction point) track finding algorithms, which is the fist and most crucial algorithm that will be executed in the tracking sequence of the LHCb upgrade. I am also the author and maintainer of the upgrade Scintillating Fibre tracker track finding algorithm which, used together with the Vertex Locator track finding algorithm enables to find and assign a momentum to the reconstructed tracks which later are combined to form the daughters of the B candidates of the physics analysis. Both algorithm have been fully designed and developed by me and they have superseded the ones used for the Technical Design Report of the LHCb upgrade. Overall those two algorithms are capable to find with an extremely high efficiency the tracks of physics interest for the LHCb upgrade physics program, rejecting efficiently the fake

tracks and more important (for the trigger strategy) gaining several factors (>3) in terms of throughput. The work performed in this area has been awarded by the LHCb collaboration in 2017 with the LHCb early career scientist award.

In addition to algorithm developments and design, I am currently the maintainer of the throughput measurement system for the LHCb upgrade trigger. This role is important to keep track of developments and push the priority towards future optimizations of the different steps of the trigger reconstruction. Together with the maintenance activities I am currently covering a key role in the developments for the upgrade trigger strategy being almost the only one within the LHCb collaboration understanding the different pieces composing the tracking sequence and what are the bottlenecks and areas to improve.

As a member of the LHCb collaboration, I presented status reports of data analysis, updates and status summary of the software track reconstruction for the LHCB upgrade, summaries of the working group talks during LHCb collaboration weeks. I also participated to several LHCb computing workshops and various conferences (Connecting the Dots 2017, ICHEP 2016, ACAT 2016). In addition, I helped to port the algorithms to the new LHCb software framework, designed to fully exploit the potentiality of parallel event processing.

3   CTA Experiment

During the DOE/INFN Summer Exchange Program I took part to the development and test of the TARGET 5 chip: a new multi-channel digitizer with triggering capabilities for gamma-ray atmospheric Cherenkov telescopes. During that period I have been responsible of the experimental setup to measure the dependencies of the performance as a function of the temperature and the FPGA settings. The work done during the 3 months internship has demonstrated the feasibility of using for the first time of ASICs for triggering purposes for an Imaging Air Cherenkov Telescopes, providing one development path for readout electronics in the forthcoming Cherenkov Telescope Array (CTA).

4   SuperB Experiment

During the bachelor degree thesis period I have studied the performances and feasibility of using scintillating fibres coupled to scintillating detectors for the muon system of the SuperB experiment and more generally for flavour physics experiments using e^+e^- collisions.

Responsability Roles Covered

- Maintainer and developer of the infrastructure to measure the throughput of the event reconstruction for the LHCb upgrade.
- Responsible and developer of the fit strategy for the $R(X)$ analysis.
- Supervisioning Ph.D. students on the $R(X)$ analysis and $B \rightarrow DDK^{*0}$ analysis using Run II data.

- Maintainer, developer and author of the Vertex LOcator and Scintillating Fibre tracker track reconstruction algorithms for the LHCb upgrade.
- Maintainer and developer of performance checking tools for the LHCb upgrade track reconstruction.
- "Tracking liaison" for the B decaying to Open Charm working group (2015–2016). The responsibilities of this role is to ensure a correct communication between the analysis working group and the tracking and alignment working group.

Other Skills

- Computing area:
  - Advanced C++, python, SVN, Git.
  - LHCb software expert.
- Language:
  - Fluent in english (TOEFL) and french. Italian native speaker.

Other Professional Experiences

- **2009**: Internship in Strasbourg (France) with the *Project ISIV-Leonardo 2007/2008* as technical assistant in a computing support center.
- **2008**: Internship in an architecture studio working on 3-D and 2-D design modeling (AutoCad).
- **2009–2014**: Part-time private lectures in physics and math for high school and engineering students.